7-2015

Surface Modification of Noble Metal Nanostructures toward Biomedical Applications

Samir V. Jenkins
University of Arkansas, Fayetteville

Surface Modification of Noble Metal Nanostructures toward Biomedical Applications

Surface Modification of Noble Metal Nanostructures toward Biomedical Applications

A dissertation submitted in partial fulfillment
Of the requirements for the degree of
Doctor of Philosophy in Chemisty

by

Samir Jenkins
Yale University
Bachelor of Science in Chemistry, 2008

July 2015
University of Arkansas

This dissertation is approved for recommendation to the Graduate Council

_____
Professor Jingyi Chen
Dissertation Director

_____
Professor Dan Davis
Committee Member

_____
Professor Roger Koeppe
Committee Member

_____
Professor Suresh Thallapuranam
Committee Member

_____
Professor Ryan Tian
Committee Member

Abstract

Noble metal nanostructures have seen a steady increase in biomedical application over the last several decades; new diagnostic and therapeutic modalities are under intense investigation. Many of these applications are possible because of post-synthetic modifications to the particle surface. These modifications take a variety of forms and can significantly affect the pharmacokinetics of these particles. In this work, various surface modifications were investigated. Particle agglomeration, which occurs when particle surfaces remain in contact, can significantly affect the toxicity and efficacy of a nanomedicine. Darkfield microscopy and single-particle ICP-MS were developed as complementary methods to detect agglomeration in blood, with the long-range goal being to establish regulatory mechanisms for nanomedicine. Two novel constructs were developed for such theranostic applications. A hydrophobic photosensitizer was introduced to the surface of poly(ethylene glycol), and its potential was investigated as a photothermal transducer, a photoacoustic contrast agent, and as a delivery vehicle. Relative to the free drug, the construct was found to increase tumor accumulation of the drug in mice and to make the drug more effective as a photodynamic therapeutic. Further surface modification and laser irradiation were able to impart additional control of the release of the drug from the conjugate. Noncovalent interactions were also applied to load and deliver a hydrophilic antibiotic using polydopamine-coated Au nanostructures as a platform. This construct was conjugated with a targeting agent and was then shown to be effective at killing methicillin-sensitive and –resistant strains of *S. aureus*. Finally, the effect of the anchoring group on $AuCu_3$ nanorod catalysis was investigated using several model reactions and surface ligands, and it was determined that more strongly bound ligands inhibit the catalytic reactions.

Acknowledgement

I would like to thank my advisor, Professor Jingyi Chen, for her energetic support and guidance. Her patience and open-mindedness allowed me to develop into who I am today. I would like to thank my committee members Profs. Dan Davis, Roger Koeppe, and Suresh Thallapuranam for their helpful suggestions, encouragement, and advice. I offer my sincerest thanks to all of my labmates for their patience and insight. I must thank Dr. Yongbin Zhang for mentoring me during the 2013 summer at the National Center for Toxicological Research, and I must also thank Drs. Paul Howard, Thilak Mudalige, and Taylor Ingle, Ms. Yvonne Jones, and Mr. Bill Monroe for their helpful guidance during the same summer. I appreciate Prof. Min Zou for providing the opportunity and subsequent financial support to develop the nanomaterials lab module. I thank Profs. Tim Muldoon and Julie Stenken for their professional and financial support. I would like to thank Prof. Mark Smeltzer and Mr. Daniel Meeker for the patience, faith, and hard work. I also thank all of my numerous coauthors for their contributions to this text. I would also like to thank Drs. Denise Greathouse, Srinivas Jayanthi, and Geoff Keeler for their expertise and technical advice.

Dedication

This dissertation is dedicated to my mother for her unwavering support and my father for his inspring memory.

Table of Contents

List of Abbreviations

$^1O_2$	Singlet oxygen
AgNC	Ag nanocube
AgNP	Citrate-capped Ag nanoparticle
$AuCu_3NR$	$AuCu_3$ nanorod
AuNC	Au nanocage
AuNC@/Dap$_{xx}$-PDA	AuNC@PDA loaded with daptomycin at xx ppm
AuNC@Dap-PDA-SPA	AuNC@PDA loaded with daptomycin, conjugated with anti-SPA
AuNC@PDA	AuNC coated with polydopamine
AuNC@PDA-SPA	AuNC@PDA conjugated with anti-SPA
AuNC-PEG	AuNC conjugated with PEG
AuNC$_{XXX}$-HPPH	AuNC-PEG noncovalently conjugated with HPPH
AuNP	Au nanoparticles
AuNP-cit	Citrate-capped Au nanoparticles
BSA	Bovine serum albumin
CCM	Cell-culture medium
CFU	Colony forming units
cRM	Confocal Raman microscopy
Dap	Daptomycin
DAPI	4',6-diamidino-2-phenylindole
DDA	Discrete dipole approximation
dh	Hydrodynamic diameter
DLS	Dynamic light scattering
DMSO	Dimetylsulfoxide

EM	Electon microscopy
EPR	Enhanced permeability and retention
EtOH	Ethanol
FAAS	Flame atomic aborbance spectroscopy
FBS	Fetal bovine serum
FTIR	Fourier transform infrared
GNM	Au nanomaterial
HPPH	3-devinyl-3-(1'-hexyloxyethyl)pyropheophorbide
hsDFM	Darkfield microscopy with hyperspectral imaging
IC_{50}	Half-maximal inhibitory concentration
K_d	Dissociation constant
LSPR	Localized surface plasmon resonance
m.w.	Molecular weight
MeOH	Methanol
MIC	Minimum inhibitory concentration
MRSA	Methicillin-resistant *Staphylococcus aureus*
MSSA	Methicillin-sensitive *S taphylococcus aureus*
NanoEL	Nanomaterial-induced-endothethial leakage
NIR	Near-infrared
NIST-XX	NIST standard AuNP-cit with XX nm diameter
NP	Nanoparticle (generic)
NTA	Nanoparticle tracking analysis
OCT	Optical coherence tomography
PA	Photoacoustic
PAT	Photoacoustic tomography

PBS	Phosphate buffered saline
PDA	Polydopamine
PDT	Photodynamic therapy
PEG	Poly(ethylene glycol)
PEI_{XX}	Poly(ethyleneimine) (m.w. = XX Da)
pNiPAAm	Poly(N-isopropyl acrylamide)
PT	Photothermal
PTT	Photothermal therapy
SERS	Surface enhanaced Raman spectroscopy
SOSG	Singlet oxygen sensor green
SPA	Staphyloccocal protein A
sp-ICP-MS	Single particle inductively-coupled plasma mass spectrometry
STEM	Scanning-tunneling electron microscopy
TEM	Transmission electron microscopy
TSA	Tryptic soy agar
TSB	Tryptic soy broth
UPLC	Ultraperformance liquid chromatography.
UV-Vis	Ultraviolet-visible
XRD	X-ray diffraction
$XX-PEG_{ZZ}-YY$	Heterobifunctional PEG (XX, and YY) (m.w. = ZZ)

List of Tables and Figures

Chapter V

Chapter VI

List of Published Articles.

Gold Nanocage-Photosensitizer Conjugates for Dual-Modal Image-Guided Enhanced Photodynamic Therapy. Srivastan, A.;[*] Jenkins, S.V.;[*] Jeon, M.;[*] Wu, Z.; Kim, C.; Chen J.; Pandey, R. *Theranostics,* **2014**, 4, 163-74 ([*]equal contribution).

Rapid Determination of Plasmonic Nanoparticle Agglomeration Status in Blood. Jenkins, S.V.; Qu, H.; Mudalige, T.; Ingle, T.; Wang, R.; Wang F.; Howard, P.C.; Chen, J.; Zhang, Y. Biomater **2015**, 51, 226-37.

Gold-Copper Alloyed Nanorods for Metal-catalyzed Organic Reactions: Implication of Surface Ligands on Nanoparticle-based Heterogeneous Catalysis. Jenkins, S.V.; Chen, S.; Chen, J. *TetLett* **2015**, 23, 3368-72.

Chapter I. **Introduction**

Nanomaterials are typically defined as materials with some dimension in the 1-100 nm range and possess unique properties due to their size. These properties exist between molecular properties and bulk properties. Nanomaterials can be made out of a variety of components including metals, oxides, ceramics, polymers, lipids, organic dendrimers, and even aggregates of proteins or small molecules. Gold, silver, and copper nanoparticles exhibit brilliant coloration due to the localized surface plasmon resonance (LSPR). The conduction electrons in a small metal particle oscillate in resonance with particular wavelengths of light, resulting in absorption and scattering of some wavelengths and transmission of others. These particles were (unknowingly) used to stain glass for centuries, with colloids forming during the casting of the glass. The Lycurgus Cup, a fourth century Roman relic currently housed in the British Museum, is made of dichroic glass that contains Au nanoparticles, so it appears red or green depending on the direction of the incident light.

Noble metals have a long history of biomedical use. Ancient Indian, Chinese, and Egyptian medicine treated arthritis through the oral use of a gold-salt based paste.[1, 2] Ultimately the salts formed colloids *in situ* in the synovial fluid.[3] More recently, intrasynovial injection of AuNPs has been shown to reduce inflammation and arthritis score.[4] This effect has been attributed to the interaction between cysteines in pro-inflammatory cytokines and the Au surface. Signaling proteins conjugate to the particle surface, reducing the inflammatory signal and thereby the inflammation.[4] Gold-based therapeutics were also unsuccessfully applied to treat tuberculosis, lupus, epilepsy, and migraines.[2] Similarly, silver nitrate was used to treat wounds, as a purgative, and to treat ocular infections,[5] and many ancient civilizations transported water in Ag containers, unknowingly tapping into the antimicrobial properties of the metal.

1

Modern study of Au nanoparticles began with Michael Faraday in 1857. Faraday synthesized extremely stable ruby-red gold colloids[6] that are still on display in the Faraday Museum. The understanding and application of these materials has advanced significantly in the intervening years. Tight morphological control has been accomplished through the development of advanced synthetic methods. Additional metals and organic materials can be conjugated to the particles to increase functionality. The systems can even be engineered to respond to environmental changes.[7] In this chapter the role of the nanoparticle surface is considered in the context of biomedical applications. The origin, nature, and application of the optical properties of noble metal nanostructures is considered in depth. Surface modification techniques are then discussed, with emphasis on potential avenues for drug delivery. Finally the role of the surface in toxicity, biodistribution, and catalysis is considered.

The Localized Surface Plasmon Resonance (LSPR)

When metal nanomaterials are appreciably smaller than the wavelength of incident light, the oscillations of the conduction electrons resonate with the incident electromagnetic wave. This effect is known as the localized surface plasmon resonance (LSPR),[8] illustrated in **Fig. 1A**. Adjusting the solvent or the surface coating will cause a shift in the LSPR position because the dielectric constant around the particle has changed. This subtle shift is the basis of many plasmon-based sensing modalities. For biomedical applications, the various components in an organism cause opacity. The "tissue-transparent window" is the spectral region where light penetration is the greatest. The first spectral window ranges between 650 and 900 nm;[9] the second NIR window exists between 1,000 and 1,350 nm.[10] As such, shifting the LSPR to these regions will allow for greater optical penetration for *in vivo* work.

The morphology of a nanostructure plays an important role in the LSPR position.[11] Discrete

dipole approximation (DDA) has become a popular method for calculation of the LSPR of advanced geometries, which have shown remarkable agreement with experimental results.[12] A variety of advanced Au structures exist;[13] the four most commonly studied complex geometries are nanorods, nanocages, nanoshells, and agglomerates of spherical particles. A robust synthetic route for Au nanorods was developed concurrently by Murphy's[14] and El-Sayed's[15] groups. As the aspect ratio (length: diameter) of the rods increases, a second LSPR peak emerges (**Fig. 1B**). As the length of the rod increases, the resonant energy decreases, so the LSPR shifts to longer wavelengths (lower energy).[16] Xia's group developed the synthesis of gold nanocages whereby Ag nanocubes are synthesized as a sacrificial template; Au salt is added to the colloids, and a galvanic replacement occurs, which gradually leads to deposition of Au on the surface and dissolution of Ag resulting in a hollow structure. Increasing the amount of gold redshifts the LSPR and decreases wall thickness (**Fig. 1C**).[17] Au nanoshells, first developed by Halas's group, are made by coating a thin film of Au on a dielectric core nanoparticle. Increasing the deposition of Au increases the thickness of the shells, blueshifting the LSPR (**Fig. 1D**).[18] This phenomenon is similar to AuNC wall thickness, but synthetically proceeds in the opposite direction. Agglomeration also results in redshifting of the LSPR as a plasmon from the ensemble of particles will exhibit a unique LSPR from a single particle.[19]
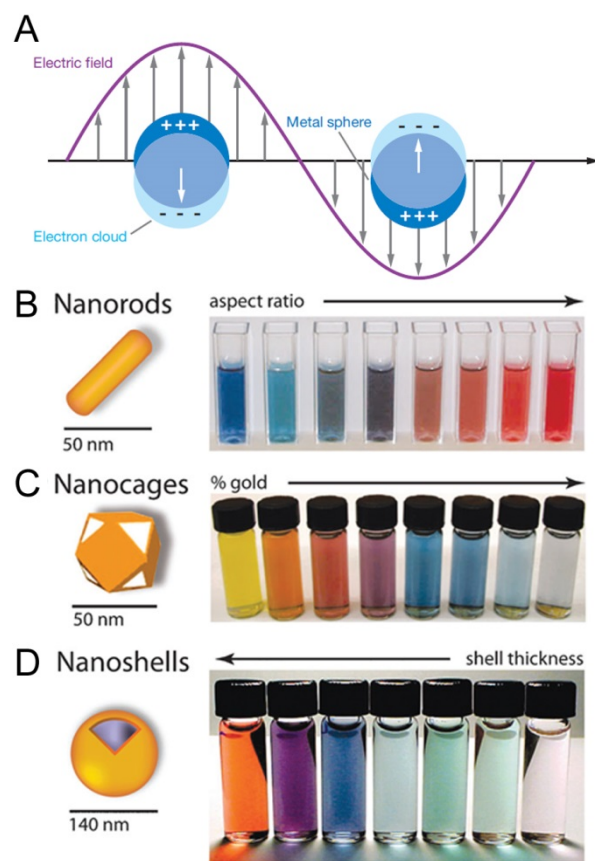
Fig. 1. (A) Schematic illustration of the interaction of electromagnetic wave with a metal nanosphere, resulting in the LSPR. Illustration and photograph of (B) Au nanorod, (C) Au nanocage, and (D) Au nanoshells with varying morphologies. Adapted with permission from (A) reference 8 and (B-D) reference 11.

The LSPR contains both an absorption and a scattering component. Absorption is the process by which the photon energy is absorbed into the nanomaterial's overall electronic structure. Several interesting phenomena arise as a result of absorption. The most well-studied is photothermal heating, whereby the excitation energy is released as thermal energy, resulting in localized heating.[20, 21] Additionally, absorption by the LSPR can cause quenching of nearby fluorophores, in a Forster type (*i.e.* dipole-dipole) process,[22] though the process can occur directly to the metal surface in the absence of an LSPR.[23] The quenching efficiency of plasmonic particles has been shown to have a $1/d^6$ distance dependence.[24] Absorption can also result in photoluminescence (emission) by the particle itself, which is distinct from scattering in that the photon is absorbed by the LSPR and emitted after a short period of time, and the wavelength of the emitted photon is shifted relative to the exciting light. For metallic structures, *d* band holes are generated by the excitation. These holes recombine with *sp* electrons in the metal releasing a particle plasmon that then decays radiatively.[25] A milestone efficiency of 10^{-4} (i.e. 1 photon emitted for every 10^4 absorbed) has been achieved using nanoparticles, while emission from bulk metals is practically nonexistent (~10^{-10}).[26] The luminescence efficiency of this process is quite low, but the LSPR enhances photoluminescence by increasing the frequency of excitations.

Scattering is the process by which the incident photon is reflected in a random direction after a nearly instantaneous interaction with the particle. Alternatively, plasmonic scattering generates regions of very high electromagnetic field strength in the local area of a nanoparticle. The plasmon results in scattering of resonant light, so plasmonic nanomaterials can be readily detected by their increased scattering at the LSPR.[21] Additionally, the LSPR can enhance the optical properties of nearby and adsorbed dye molecules. The most-studied example is surface enhanced Raman spectroscopy (SERS). Raman scattering by molecules is an inelastic process

wherein a molecule is excited to a virtual state (between two electronic states, in nonresonance Raman), changes vibrational states, and relaxes by emission of a photon slightly shifted from the incident (Rayleigh) wavelength. [27] Raman cross sections are extremely small, but the plasmon acts like a two-way antenna: enabling more light flux on a single molecule thereby increasing the number of transient absorptions and amplifying the scattered Raman signal.[28] This process is called electromagnetic enhancement.[29] Electromagnetic enhancement[30] has also been used to enhance fluorescence of local dye molecules.[31] The LSPR enhances emission by increasing the excitation rate, thereby increasing the frequency of excitations; by increasing the rate of radiative decay, causing emission to occur more readily from the excited state of the fluorophore; and by engaging in far-field coupling with the emitted photon, increasing the likelihood of emission.[32] Interestingly, the LSPR can enhance both singlet and triplet state phenomena, such as phosphorescence,[33] and singlet oxygen generation,[34] by stabilizing the excited state. This phenomenon has also been shown to enhance the phosphorescent signal from the decay of singlet oxygen leading to lower detection limits.[35] Various studies have further demonstrated that the maximum stabilization of the triplet state can be achieved by matching the LSPR with the wavelength of phosphorescent emission.[36]

The properties of the LSPR have led to development of many sensing, imaging, diagnostic, and therapeutic modalities.[7] Darkfield microscopy makes use of the resonance scattered light from nanomaterials and can be readily used to identify the location of particles in a biological sample.[37] Similarly, multiphoton luminescence can be used to generate a signal from nanoparticles while reducing the background of biomolecules for easy identification.[38] Additionally, mapping the Raman signal of a sample can be used to identify SERS active substrates. Photoacoustic imaging results from absorption by the nanoparticle followed by

6

thermal relaxation, which generates acoustic waves that can be readily detected.[39] The generation

of heat has also been used to induce cell death in both tumors[40] and bacteria.[41] This heat has also

been harnessed for a variety of drug delivery applications (*vide infra*).

Particle Surface Effects on Biomedical Properties

One of the great challenges of nanomedicine is successful delivery to the desired site. Two

primary mechanisms can be used to deliver materials: passive targeting and active targeting; the

primary distinction between the two is the use of targeting moieties. Passive targeting relies on

the natural mechanisms at play within an organism to deliver the material. The best known

example is the enhanced permeability and retention (EPR) effect observed in tumors.[42] The leaky

vasculature in a tumor allows for increased uptake of nanomaterials, while the inflammation

associated with a tumor leads to increased retention time in the interstitium.[43] Active targeting

makes use of targeting moieties on the particle surface to provide specific interactions; small

molecules, peptides, antigens, aptamers, and antibodies have all been used as targeting moieties

with varying success.[44] Active targeting leads to a significant increase in tumor uptake as well as

a decrease of particle concentration in other organs.[45] Because of the high local density of the

moieties on a particle's surface, multiple receptors can bind to a single particle, which causes

invagination of the membrane and formation of an endosome.[46] Even nontargeted particles are

typically taken up *via* endocytosis and reside in small vesicles within the cytosol.[47] It was

demonstrated using MDA-MB-435 cells that 30 and 60 nm Au nanoparticles will have a

significant increase in uptake with the use of a targeting ligand while 15 and 100 nm particles did

not show significant changes in uptake.[48] Additionally, cell penetrating peptides can be

conjugated to the surface, which results in particles passing through the membrane to the cytosol

without being encapsulated in a vesicle.[49]

Careful engineering of the surface, however, can be readily compromised by the formation of a protein corona in a biological environment, like the bloodstream. Two types of protein corona exist: the soft corona and the hard corona. The soft corona forms almost immediately, but is characterized by the rapid adsorption and desorption of proteins on the surface. Because of the transient nature of this binding, the soft corona tends to not disrupt the specific interactions engineered into a material.[50] The hard corona, however, consists of relatively permanently bound proteins on the surface.[51] The hard corona develops over an extended period of time as the tightly binding proteins replace proteins in the soft corona.[52] The hard corona is not readily removed from the particle surface and it can significantly affect the particle's fate. For instance, adsorbed proteins can disrupt the targeted interactions at a particle surface, leading to a loss of active targeting; proteins affect the surface charge and particle size, which influences cellular uptake.[53] Additionally, adsorption of proteins like IgG and complement factors will lead to phagocytosis by the immune cells,[54] causing the particles to be sequestered in the spleen and liver. The association constants for particular proteins change with particle morphology and surface chemistry, indicated the protein corona has a highly variable makeup.[55] The variety and variability of the interactions between proteins and nanoparticles complicates predictions and generalizations.

The particle surface also plays a significant role in the organismic toxicity of nanomaterials.[56] At present, toxicity studies suffer from high variability across experimenters. Dosages, size constraints, and even initial cell counts vary widely.[56] Similarly, the protein composition of the media used affects the corona composition, thereby affecting particle uptake and toxicity.[56] As such, careful study of the toxicity of these materials is still needed. The surface coating may actually be the origin of toxicity, rather than the particle itself, as was the case with surfactant-

coated Au nanorods.[56] It has been shown that particle toxicity can be dependent on the cell line used and even the ligand used to target the same receptor.[57] One interesting pattern that has been demonstrated is the increased level of toxicity associated with nanoparticles presenting a cationic rather than an anionic surface.[58] Similarly, heat responsive, poly(N-isopropylacrylamide) coated nanoparticles have shown higher toxicity than their poly(ethylene glycol) coated counterparts.[59] The presented features of the surface play a significant role in any toxicity exhibited by nanoparticles.[60]

Agglomeration

Particle agglomeration is an important surface consideration, as agglomeration affects the LSPR position and the pharmacokinetic profile of the particles. Agglomeration results from the high surface energy of nanoscale particles.[61] Reducing the surface area of a particle is energetically favorable, which can be accomplished by putting the surfaces together. Agglomeration is prevented through the use of electrostatic and steric stabilization. Electrostatic stabilization is the result of charged moieties on the surface of one particle repelling the like charges on the surface of another particle. Steric stabilization results from the surface coating on a particle physically interfering with the metal surface of two particles interacting.[62] Agglomeration occurs when these stabilization mechanisms are negated by environmental conditions.

Agglomeration can have significant effects on nanoparticle pharmacokinetics. For instance, particle agglomeration was shown to decrease uptake by HeLa cells and A549 cells but increase uptake by MDA-MB-435 cells.[63] Additionally, it has been shown that monocyte-like macrophages will uptake individual particles, while more mature macrophages will cause particle agglomeration during uptake.[64] Another size dependent phenomenon is nanomaterial-induced endothelial leakage (NanoEL). Nanomaterials bypass the cell membrane by disrupting

adherens junctions; agglomerates leak less efficiently from cells.[65] The EPR effect is also heavily size dependent, with excessively large particles accumulating poorly within the tumor.[66] It is worth noting that particles can be engineered so they function properly upon agglomeration in a particular environment.

Surface Modification

The optical properties of plasmonic nanostructures are quite robust. Particles composed of noble metals also exhibit high stability and robust surface chemistry. In particular, the Au-thiol bond is extremely strong, on the order of a hydrogen bond.[67] Whitesides's group performed much of the pioneering work in self-assembled monolayers on gold films using alkanethiols.[68] Interestingly, disulfides and thioethers and even amines can also be used to functionalize the Au surface.[69] Thiol moieties can be introduced to a wide variety of molecules, enabling nearly limitless possibilities for ligands and functional groups (**Fig. 2**). The binding strength can be used to modulate the surface coverage and release of the ligand.[70] Additionally, mixed monolayers can be generated that include multiple components in controllable compositions.[71] PEG is one of the most common surface ligands because of its ability to repel proteins and increase circulation lifetimes.[72] Heterobifunctional PEG allows the potential for a thiol to serve as an anchor to an Au nanoparticle and the exposed terminus to serve as a functional handle for further conjugation. Indeed, many fluorophores, therapeutics, markers, and targeting moieties have been conjugated to the surface of various nanostructures. The surface of a material is extremely important for *in vivo* and *in vitro* studies, as the biological response is dictated by what the cell perceives, and that perception is determined by the surface chemistry.
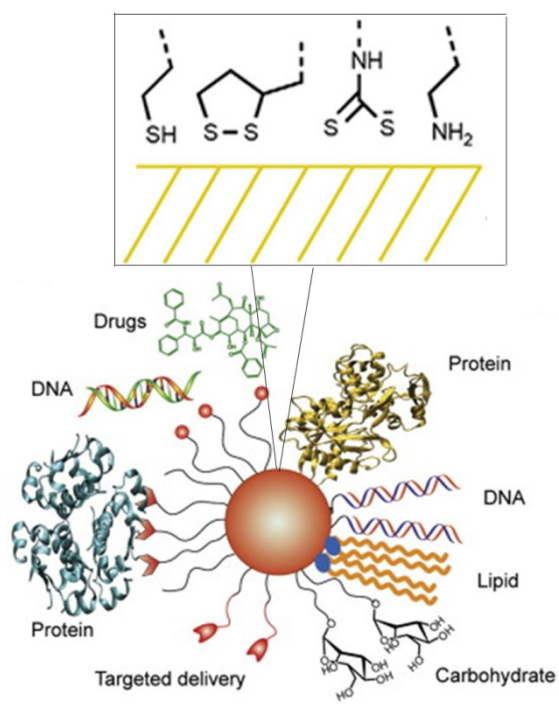
Fig.2. Illustration of molecules that can be conjugated to the surface of Au nanoparticles with blow-up of surface conjugating moieties. Adapted with permission from references 97 and (blow-up) 73

Covalent Conjugation

Direct conjugation of drug molecules to the surface, without the use of a linker molecule, has been demonstrated in a variety of systems. Antibiotics have been directly conjugated to AuNP surfaces, typically through available amine groups.[73] The close-packing of vancomycin on the AuNP surface mimicked the mechanism of action of the drug, fundamentally removing the entropic contribution to the activation. As such, this conjugate more readily enabled the antibiotic to oligomerize at the cell membrane, lowering the MIC for the antibiotic.[74] Similarly, cefaclor,[75] quinolone,[76] aminoglycosides (-mycins),[77] ampicillin,[78] and even pyrimidines (which lack antibacterial activity),[79] conjugated AuNPs have shown efficacy against both gram negative and gram positive bacteria. Photosensitizers have also been successfully conjugated and show a 4-fold decrease in MIC relative under white light illumination.[80] AuNPs conjugated with vitamin E derivatives have been demonstrated as a powerful radical scavengers and antioxidants.[81] Conjugation with a mimetic HIV fusion inhibitor led to a significant decrease in viral activity in cultures, because the high density of the peptide at the surface more effectively oligomerizes with the virus.[82] Antigens can also be conjugated to the surface of nanoparticles and introduced to the immune system, which increases antibody production enabling the potential for immunization without the use of deactivated or live viruses.[83] Rather than direct conjugation to the surface, a nearly limitless library of coupling techniques exist that can covalently link a surface bound molecule to a drug molecule of interest.[84]

Noncovalent conjugation

A number of strategies have been utilized to noncovalently tether drugs to metal nanoparticles. Electrostatic interactions can be used to encapsulate the drug within polyelectrolyte layers, and additional wrapping can lead to high loading and multiple shell layers.[85] These systems utilize

oppositely charged polymers and ligands to incorporate the ligand between the particle surface and the polymer shell. Lipids can be used to encapsulate drugs through the use of vesicles[86] and liposomes,[87] though these methods suffer from limitations regarding the stability of the lipid structure and the loading capacity of the system. Alternatively, a "hydrophobic pocket" can be used to drive molecules toward the particle surface through hydrophobic interactions.[88] These hydrophobic interactions are increased with increasing ionic strength, making these conjugates particularly stable in saline solutions. Au nanostructures can be embedded in heat-responsive matrices.[89] Similarly, replacing the bulky matrix with a monolayer coating has demonstrated the capability for on-demand release from the interior of hollow, porous Au nanocages (AuNCs) with the polymers (e.g. pNIPAAm derivatives) serving as a gate at the surface pores.[90, 91]

Plasmonic nanostructures also show great promise for gene delivery and gene therapy. The two primary conjugation strategies for genetic material are to anchor the terminus to the surface so the oligonucleotide is roughly perpendicular to the surface or to use electrostatic interactions between the anionic, phosphate backbone and cationic particles, which results in the strand being roughly parallel to the surface. The two most commonly delivered genetic materials are deoxyribonucleic acid (DNA) and small interfering ribonucleic acid (siRNA). AuNPs provide a significant increase in transfection efficiency relative to free DNA because they are resistant to DNAses[92] and can be targeted to the nucleus.[93] The LSPR can be used to heat a construct, causing melting of double-stranded DNA, which releases a single strand that can be used for translation.[94] Alternatively, siRNAs, RNAs that help control protein expression levels by turning various functions off and on, and can also be delivered using AuNP conjugation.[95]

Controlled release systems for drug delivery have been developed and studied for more than three decades.[96] Many efforts have been devoted to the fabrication of "smart" delivery systems

that integrate responsive macromolecules with Au nanostructure platforms.[97] These systems respond to changes of the intrinsic, physiological environment such as pH, temperature, or concentration of a biomolecule. Because of the LSPR, Au nanostructures enable the delivery systems to respond to external stimuli, particularly light. Halas's group first demonstrated that the photothermal effect of Au nanoshells initiated a conformational change to a drug-loaded hydrogel matrix, provoking release of the payload.[98] Xia's group shrank the size of the system to below 100 nm by using a monolayer of heat-responsive polymer or phase-change material to lock the molecules inside the Au nanocage (AuNC).[90, 99] The release of the molecules from the nanocages could be both temporally and spatially controlled by a NIR laser. Additionally, Li's group photothermally released doxorubicin from poly(ethylene glycol) (PEG) coated hollow Au nanoshells,[100] and Murphy's group demonstrated that release of dye molecules from layers of polyelectrolytes wrapped around Au nanorods could be achieved with NIR light.[101] Further, a number of systems have utilized photothermal response of DNA to control the release of molecules that are grooved on the DNA strands.[102 103]

In Situ catalysis

Due to its high surface energy, the nanoparticle surface can be harnessed for catalysis of organic reactions in aqueous media. Stabilizing ligands can leave atomic vacancies on the particle surface that can be quite catalytically active.[104] Noble metal nanoparticles have been demonstrated for a wide variety of reactions, though most of these rely on the presence of Pd or Pt.[105] There are a handful of Au, Ag, and Cu reactions that have been demonstrated with nanostructures.[104] Much catalytic activity derives from the crystal facets exposed at the surface, as such particle design is an important factor in designing nanocatalysts.[106] For instance, azide-alkyne cycloaddition, which is typically catalyzed by Cu^I salts, has been achieved on the Au

(111) surface.[107]Additionally, the surface ligand plays an important role in catalytic activity, with thiol groups having been shown to inactivate certain Au catalysts.[108] Additionally, the LSPR can be harnessed to aid in catalysis. Aside from localized heating, which would increase reaction rates, the LSPR can also generate a "hot" electron, which can be a reactive partner during reactions such as nitro coupling to yield a di-azo group.[109] Efforts are being made to use nanoparticle catalysts for *in situ* activation of prodrugs at the target site.

Outlook

The surface of a nanoparticle is a crucial consideration for biomedical applications. The surface dictates how the particle will be distributed, what cells it interacts with, and its toxicity profile. Additionally, the surface electrons give rise to the optical properties of noble metal materials, which have been harnessed for a wide range of diagnostic and therapeutic modalities. In particular the surface can be used to deliver chemotherapeutics. This dissertation seeks to understand and manipulate the surface of noble metal nanoparticles toward theranostic ends. In Chapter 2, a series of complementary methods are developed for the detection of particle agglomeration in blood. The most valuable data was provided by darkfield microscopy with hyperspectral imaging and single-particle inductively-coupled plasma mass spectrometry. Chapters 3 and 4 focus on the development, characterization, and application of Au nanocages coated with poly(ethylene) glycol and loaded with a photosensitizer for photodynamic treatment of tumors. The conjugate was found to be more effective *in vivo* than the free drug, and the release rate can be controlled with surface modification or laser irradiation. Chapter 5 covers the development, characterization, and application of Au nanocages coated with polydopamine, loaded with an antibiotic, and conjugated with a targeting molecule to treat planktonic *Staphylococcus aureus.* This system was shown to effectively kill both methicillin-sensitive and

methicillin-resistant strains through the synergy of photothermal and antibiotic therapy. Finally in Chapter 6, the catalytic properties of AuCu$_3$ nanorods are investigated using several model reactions. The anchoring group of the ligand on the particle surface was found to significantly affect the catalytic properties of the particle.

References

1.   Thakor, A. S.; Jokerst, J.; Zavaleta, C.; Massoud, T. F.; Gambhir, S. S., Gold Nanoparticles: A Revival in Precious Metal Administration to Patients. *Nano Letters* **2011,** *11* (10), 4029-4036.

2.   Whitehouse, M. W., Therapeutic gold. Is it due for a come-back? *Inflammopharmacology* **2008,** *16* (3), 107-9.

3.   Brown, C. L.; Bushell, G.; Whitehouse, M. W.; Agrawal, D.; Tupe, S.; Paknikar, K.; Tiekink, E. R., Nanogold-pharmaceutics. *Gold Bulletin* **2007,** *40* (3), 245-250.

4.   Tsai, C.-Y.; Shiau, A.-L.; Chen, S.-Y.; Chen, Y.-H.; Cheng, P.-C.; Chang, M.-Y.; Chen, D.-H.; Chou, C.-H.; Wang, C.-R.; Wu, C.-L., Amelioration of collagen-induced arthritis in rats by nanogold. *Arthritis & Rheumatism* **2007,** *56* (2), 544-554.

5.   Alexander, J. W., History of the medical use of silver. *Surg Infect (Larchmt)* **2009,** *10* (3), 289-92.

6.   Faraday, M., The Bakerian Lecture: Experimental Relations of Gold (and Other Metals) to Light. *Philosophical Transactions of the Royal Society of London* **1857,** *147*, 145-181.

7.   Jenkins, S. V.; Muldoon, T. J.; Chen, J., Plasmonic Nanostructures for Biomedical and Sensing Applications. In *Metallic Nanostructures*, Xiong, Y.; Lu, X., Eds. Springer International Publishing: 2015; pp 133-173.

8.   Wilets, K. A.; Duyne, R. P. V., Localized Surface Plasmon Resonance Spectroscopy and Sensing. *Annu. Rev. Phys. Chem.* **2007,** *58*, 267-97.

9.   Weissleder, R., A clearer vision for in vivo imaging. In *Nat Biotechnol*, United States, 2001; Vol. 19, pp 316-7.

10.   Smith, A. M.; Mancini, M. C.; Nie, S., Bioimaging: second window for in vivo imaging. *Nat Nanotechnol* **2009,** *4* (11), 710-1.

11.   Dreaden, E. C.; Alkilany, A. M.; Huang, X.; Murphy, C. J.; El-Sayed, M. A., The golden age: gold nanoparticles for biomedicine. *Chem. Soc. Rev.* **2012,** *41*, 2740-2779.

12.   Zhao, J.; Pinchuk, A. O.; McMahon, J. M.; Li, S.; Ausman, L. K.; Atkinson, A. L.; Schatz, G. C., Methods for Describing the Electromagnetic Properties of Silver and Gold

Nanoparticles. *Accounts of Chemical Research* **2008,** *41* (12), 1710-1720.

13. Xia, Y.; Xiong, Y.; Lim, B.; Skrabalak, S. E., Shape-Controlled Synthesis of metal Nanocrystals: Simple Chemistry Meets Complex Physics. *Angewandte Chemie International Edition* **2009,** *48*, 60-103.

14. Jana, N. R.; Gearheart, L.; Murphy, C. J., Wet chemical synthesis of high aspect ratio cylindrical gold nanorods. *The Journal of Physical Chemistry B* **2001,** *105* (19), 4065-4067.

15. Nikoobakht, B.; El-Sayed, M. A., Preparation and growth mechanism of gold nanorods (NRs) using seed-mediated growth method. *Chemistry of Materials* **2003,** *15* (10), 1957-1962.

16. Lee, K.-S.; El-Sayed, M. A., Dependence of the Enhanced Optical Scattering Efficiency Relative to That of Absorption for Gold Metal Nanorods on Aspect Ratio, Size, End-Cap Shape, and Medium Refractive Index. *The Journal of Physical Chemistry B* **2005,** *109* (43), 20331-20338.

17. Sun, Y.; Xia, Y., Mechanistic Study on the Replacement Reaction between Silver Nanostructures and Chloroauric Acid in Aqueous Medium. *Journal of the American Chemical Society* **2004,** *126* (12), 3892-3901.

18. Pham, T.; Jackson, J. B.; Halas, N. J.; Lee, T. R., Preparation and characterization of gold nanoshells coated with self-assembled monolayers. *Langmuir* **2002,** *18* (12), 4915-4920.

19. Basu, S.; Ghosh, S. K.; Kundu, S.; Panigrahi, S.; Praharaj, S.; Pande, S.; Jana, S.; Pal, T., Biomolecule induced nanoparticle aggregation: Effect of particle size on interparticle coupling. *Journal of Colloid and Interface Science* **2007,** *313* (2), 724-734.

20. Chen, J.; Glaus, C.; Laforest, R.; Zhang, Q.; Yang, M.; Gidding, M.; Welch, M. J.; Xia, Y., Gold Nanocages as Photothermal Transducers for Cancer Treatment. *Small* **2010,** *6*, 811-817.

21. Wax, A.; Sokolov, K., Molecular imaging and darkfield microspectroscopy of live cells using gold plasmonic nanoparticles. *Laser & Photonics Reviews* **2009,** *3* (1-2), 146-158.

22. Yun, C. S.; Javier, A.; Jennings, T.; Fisher, M.; Hira, S.; Peterson, S.; Hopkins, B.; Reich, N. O.; Strouse, G. F., Nanometal Surface Energy Transfer in optical rulers, breaking the FRET Barrier. *Journal of the American Chemical Society* **2005,** *127*, 3115-9.

23. Jennings, T. L.; Singh, M. P.; Strouse, G. F., Fluorescent Lifetime Quenching Near d = 1.5 nm Gold Nanoparticles: Probing NSET validity. *J. Am. Chem. Soc.* **2006,** *128*, 5462-7.

24. Li, M.; Cushing, S. K.; Wang, Q.; Shi, X.; Hornak, L. A.; Hong, Z.; Wu, N., Size-Dependent Energy Transfer Between CdSe/ZnS Quantum Dots and Gold Nanoparticles. *The Journal of Phsyical Chemistry Letters* **2011,** *2*, 2125-9.

25.   Mooradian, A., Photoluminescence of Metals. *Physical Review Letters* **1969,** *22* (5), 185-187.

26.   Mohamed, M. B.; Volkov, V.; Link, S.; El-Sayed, M. A., The `lightning' gold nanorods: fluorescence enhancement of over a million compared to the gold metal. *Chemical Physics Letters* **2000,** *317* (6), 517-523.

27.   Raman, C. V.; Krishnan, K. S., A new type of secondary radiation. *Nature* **1928,** *121* (3048), 501-502; Raman, C. V., A new radiation. *Indian Journal of physics* **1928,** *2*, 387-398; Skoog, D. A.; West, D. M., *Principles of instrumental analysis*. Saunders College Philadelphia: 1980.

28.   Saikin, S. K.; Chu, Y.; Rappoport, D.; Crozier, K. B.; Aspuru-Guzik, A., Separation of Electromagnetic and Chemical Contributions to Surface-Enhanced Raman Spectra on Nanoengineered Plasmonic Substrates. *The Journal of Physical Chemistry Letters* **2010,** *1* (18), 2740-2746.

29.   Xu, H.; Aizpurua, J.; Kall, M.; Apell, P., Electromagnetic contributions to single-molecule sensitivity in surface-enhanced raman scattering. *Phys Rev E Stat Phys Plasmas Fluids Relat Interdiscip Topics* **2000,** *62* (3 Pt B), 4318-24.

30.   Metiu, H.; Das, P., The electromagnetic theory of surface enhanced spectroscopy. *Annual Review of Physical Chemistry* **1984,** *35* (1), 507-536.

31.   Bardhan, R.; Grady, N. K.; Cole, J. R.; Joshi, A.; Halas, N. J., Fluorescence Enhancement by Au Nanostructure: Nanoshells and Nanorods. *ACS Nano* **2009,** *3* (3), 744-52.

32.   Tamican, T. H.; Stefani, F. D.; Segerink, F. B.; Hulst, N. F. v., Optical Antennas Direct Single Molecule Emission. *Nature Photonics* **2008,** *2*, 234-7.

33.   Pan, S.; Wang, Z.; Rothberg, L. J., Photoluminescent Enhancement of Ruthenium Complex Monolayers by Surface Plasmon Resonance of Silver Nanoparticles. *MRS Online Proceedings Library* **2004,** *818*, null-null.

34.   Zhang, Y.; Aslan, K.; Previte, M. J. R.; Geddes, C. D., Metal-Enhanced Singlet Oxygen Generation: A Consequence of Plasmon Enhanced Triplet Yields. *Journal of Fluorescence* **2007,** *17*, 345-9; Srivatsan, A.; Jenkins, S. V.; Jeon, M.; Wu, Z.; Kim, C.; Chen, J.; Randey, R., Gold nanocage-photosensitizer conjugates for dual-modal image-guided enhanced photodynamic therapy. *Theranostics* **2013**, in press.

35.   Toftegaard, R.; Arnbjerg, J.; Cong, H.; Agheli, H.; Sutherland, D. S.; Ogilby, P. R., Metal nanoparticle-enhanced radiative transitions: Giving singlet oxygen emission a boost. *Pure and Applied Chemistry* **2011,** *83* (4), 885-898.

36.   Zhang, Y.; Aslan, K.; Previte, M. J. R.; Malyn, S. N.; Geddes, C. D., Metal-Enhanced Phosphorescence: Interpretation in Terms of Triplet-Coupled Radiating Plasmons. *The Journal of Physical Chemistry B* **2006,** *110* (49), 25108-25114; Previte, M. J. R.; Aslan, K.; Zhang, Y.; Geddes, C. D., Metal-Enhanced Surface Plasmon-Coupled

Phosphorescence. *J. Phys. Chem. C* **2007,** *111*, 6051-6059.

37. Rothen-Rutishauser, B. M.; Schürch, S.; Haenni, B.; Kapp, N.; Gehr, P., Interaction of Fine Particles and Nanoparticles with Red Blood Cells Visualized with Advanced Microscopic Techniques†. *Environmental Science & Technology* **2006,** *40* (14), 4353-4359.

38. Powless, A. J.; Jenkins, S. V.; McKay, M. L.; Chen, J.; Muldoon, T. J. In *Molecule-specific darkfield and multiphoton imaging using gold nanocages*, 2015; pp 93390B-93390B-6.

39. Jeon, M.; Jenkins, S.; Oh, J.; Kim, J.; Peterson, T.; Chen, J.; Kim, C., Nonionizing photoacoustic cystography with near-infrared absorbing gold nanostructures as optical-opaque tracers. *Nanomedicine* **2013**, 1-10.

40. Huang, X.; Jain, P.; El-Sayed, I.; El-Sayed, M., Plasmonic photothermal therapy (PPTT) using gold nanoparticles. *Lasers in Medical Science* **2008,** *23* (3), 217-228.

41. Zharov, V. P.; Mercer, K. E.; Galitovskaya, E. N.; Smeltzer, M. S., Photothermal nanotherapeutics and nanodiagnostics for selective killing of bacteria targeted with gold nanoparticles. *Biophys J* **2006,** *90* (2), 619-27.

42. Nie, S., Understanding and overcoming major barriers in cancer nanomedicine. *Nanomedicine* **2010,** *5* (4), 523-528.

43. Wang, A. Z.; Langer, R.; Farokhzad, O. C., Nanoparticle Delivery of Cancer Drugs. *Annual Review of Medicine* **2012,** *63* (1), 185-198.

44. Verma, A.; Stellacci, F., Effect of Surface Properties on Nanoparticle–Cell Interactions. *Small* **2010,** *6* (1), 12-21.

45. Choi, C. H. J.; Alabi, C. A.; Webster, P.; Davis, M. E., Mechanism of active targeting in solid tumors with transferrin-containing gold nanoparticles. *Proceedings of the National Academy of Sciences* **2010,** *107* (3), 1235-1240.

46. Chithrani, B. D.; Chan, W. C. W., Elucidating the Mechanism of Cellular Uptake and Removal of Protein-Coated Gold Nanoparticles of Different Sizes and Shapes. *Nano Letters* **2007,** *7* (6), 1542-1550.

47. Brandenberger, C.; Mühlfeld, C.; Ali, Z.; Lenz, A.-G.; Schmid, O.; Parak, W. J.; Gehr, P.; Rothen-Rutishauser, B., Quantitative Evaluation of Cellular Uptake and Trafficking of Plain and Polyethylene Glycol-Coated Gold Nanoparticles. *Small* **2010,** *6* (15), 1669-1678.

48. Sykes, E. A.; Chen, J.; Zheng, G.; Chan, W. C. W., Investigating the Impact of Nanoparticle Size on Active and Passive Tumor Targeting Efficiency. *ACS Nano* **2014,** *8* (6), 5696-5706.

49.   McNeil, S. E., Nanotechnology for the biologist. *J Leukoc Biol* **2005,** *78* (3), 585-94.

50.   Monopoli, M. P.; Aberg, C.; Salvati, A.; Dawson, K. A., Biomolecular coronas provide the biological identity of nanosized materials. *Nat Nano* **2012,** *7* (12), 779-786.

51.   Liu, W.; Rose, J.; Plantevin, S.; Auffan, M.; Bottero, J.-Y.; Vidaud, C., Protein corona formation for nanomaterials and proteins of a similar size: hard or soft corona? *Nanoscale* **2013,** *5* (4), 1658-1668.

52.   Casals, E.; Pfaller, T.; Duschl, A.; Oostingh, G. J.; Puntes, V., Time Evolution of the Nanoparticle Protein Corona. *ACS Nano* **2010,** *4* (7), 3623-32.

53.   Tenzer, S.; Docter, D.; Kuharev, J.; Musyanovych, A.; Fetz, V.; Hecht, R.; Schlenk, F.; Fischer, D.; Kiouptsi, K.; Reinhardt, C.; Landfester, K.; Schild, H.; Maskos, M.; Knauer, S. K.; Stauber, R. H., Rapid formation of plasma protein corona critically affects nanoparticle pathophysiology. *Nat Nano* **2013,** *8* (10), 772-781.

54.   Leroux, J.-C.; De Jaeghere, F.; Anner, B.; Doelker, E.; Gurny, R., An investigation on the role of plasma and serum opsonins on the evternalization of biodegradable poly(D,L-lactic acid) nanoparticles by human monocytes. *Life Sciences* **1995,** *57* (7), 695-703.

55.   Lacerda, S. H. D. P.; Park, J. J.; Meuse, C.; Pristinski, D.; Becker, M. L.; Karim, A.; Douglas, J. F., Interaction of Gold Nanoparticles with Common Human Blood Proteins. *ACS Nano* **2009,** *4* (1), 365-379.

56.   Alkilany, A.; Murphy, C., Toxicity and cellular uptake of gold nanoparticles: what we have learned so far? *J. Nanoparticle Res.* **2010,** *12*, 2313-2333.

57.   Wang, J.; Tian, S.; Petros, R. A.; Napier, M. E.; DeSimone, J. M., The Complex Role of Multivalency in Nanoparticles Targeting the Transferrin Receptor for Cancer Therapies. *Journal of the American Chemical Society* **2010,** *132* (32), 11306-11313.

58.   Goodman, C. M.; McCusker, C. D.; Yilmaz, T.; Rotello, V. M., Toxicity of Gold Nanoparticles Functionalized with Cationic and Anionic Side Chains. *Bioconjugate Chemistry* **2004,** *15* (4), 897-900.

59.   Wadajkar, A.; Koppolu, B.; Rahimi, M.; Nguyen, K., Cytotoxic evaluation of N-isopropylacrylamide monomers and temperature-sensitive poly(N-isopropylacrylamide) nanoparticles. *Journal of Nanoparticle Research* **2009,** *11* (6), 1375-1382.

60.   Walczyk, D.; Bombelli, F. B.; Monopoli, M. P.; Lynch, I.; Dawson, K. A., What the Cell "Sees" in Bionanoscience. *Journal of the American Chemical Society* **2010,** *132*, 5761-8.

61.   Nanda, K. K.; Maisels, A.; Kruis, F. E.; Fissan, H.; Stappert, S., Higher Surface Energy of Free Nanoparticles. *Physical Review Letters* **2003,** *91* (10), 106102.

62.   Jiang, J.; Oberdörster, G.; Biswas, P., Characterization of size, surface charge, and agglomeration state of nanoparticle dispersions for toxicological studies. *Journal of*

Nanoparticle Research **2009,** *11* (1), 77-89.

63. Albanese, A.; Chan, W. C. W., Effect of Gold Nanoparticle Aggregation on Cell Uptake and Toxicity. *ACS Nano* **2011,** *5* (7), 5478-5489.

64. Wang, H.; Wu, L.; Reinhard, B. M., Scavenger Receptor Mediated Endocytosis of Silver Nanoparticles into J774A.1 Macrophages Is Heterogeneous. *ACS Nano* **2012,** *6* (8), 7122-7132.

65. Setyawati, M. I.; Tay, C. Y.; Chia, S. L.; Goh, S. L.; Fang, W.; Neo, M. J.; Chong, H. C.; Tan, S. M.; Loo, S. C. J.; Ng, K. W.; Xie, J. P.; Ong, C. N.; Tan, N. S.; Leong, D. T., Titanium dioxide nanomaterials cause endothelial cell leakiness by disrupting the homophilic interaction of VE–cadherin. *Nat Commun* **2013,** *4*, 1673.

66. Fang, J.; Nakamura, H.; Maeda, H., The EPR effect: Unique features of tumor blood vessels for drug delivery, factors involved, and limitations and augmentation of the effect. *Adv. Drug Delivery Rev.* **2011,** *63*, 136-151.

67. Grönbeck, H.; Curioni, A.; Andreoni, W., Thiols and Disulfides on the Au(111) Surface: The Headgroup−Gold Interaction. *Journal of the American Chemical Society* **2000,** *122* (16), 3839-3842.

68. Bain, C. D.; Biebuyck, H. A.; Whitesides, G. M., Comparison of self-assembled monolayers on gold: coadsorption of thiols and disulfides. *Langmuir* **1989,** *5* (3), 723-727.

69. Love, J. C.; Estroff, L. A.; Kriebel, J. K.; Nuzzo, R. G.; Whitesides, G. M., Self-Assembled Monolayers of Thiolates on Metals as a Form of Nanotechnology. *Chemical Reviews* **2005,** *105* (4), 1103-69.

70. Cheng, Y.; Samia, A. C.; Li, J.; Kenney, M. E.; Resnick, A.; Burda, C., Delivery and Efficacy of a Cancer Drug as a Function of the Bond to the Gold Nanoparticle Surface. *Langmuir* **2009,** *26* (4), 2248-2255.

71. Bain, C. D.; Whitesides, G. M., Formation of monolayers by the coadsorption of thiols on gold: variation in the length of the alkyl chain. *Journal of the American Chemical Society* **1989,** *111* (18), 7164-7175; Bain, C. D.; Evall, J.; Whitesides, G. M., Formation of monolayers by the coadsorption of thiols on gold: variation in the head group, tail group, and solvent. *Journal of the American Chemical Society* **1989,** *111* (18), 7155-7164.

72. Lipka, J.; Semmler-Behnke, M.; Sperling, R. A.; Wenk, A.; Takenaka, S.; Schleh, C.; Kissel, T.; Parak, W. J.; Kreyling, W. G., Biodistribution of PEG-modified gold nanoparticles following intratracheal instillation and intravenous injection. *Biomaterials* **2010,** *31* (25), 6574-6581.

73. Vigderman, L.; Zubarev, E. R., Therapeutic platforms based on gold nanoparticles and their covalent conjugates with drug molecules. *Advanced Drug Delivery Reviews* **2013,** *65* (5), 663-676.

74. Gu, H.; Ho, P. L.; Tong, E.; Wang, L.; Xu, B., Presenting Vancomycin on Nanoparticles to Enhance Antimicrobial Activities. *Nano Letters* **2003,** *3* (9), 1261-1263.

75. Rai, A.; Prabhune, A.; Perry, C. C., Antibiotic mediated synthesis of gold nanoparticles with potent antimicrobial activity and their application in antimicrobial coatings. *Journal of Materials Chemistry* **2010,** *20* (32), 6789-6798.

76. Grace, A. N.; Pandian, K., Quinolone Antibiotic-Capped Gold Nanoparticles and Their Antibacterial Efficacy Against Gram Positive and Gram Negative Organisms. *Journal of Bionanoscience* **2007,** *1* (2), 96-105.

77. Nirmala Grace, A.; Pandian, K., Antibacterial efficacy of aminoglycosidic antibiotics protected gold nanoparticles—A brief study. *Colloids and Surfaces A: Physicochemical and Engineering Aspects* **2007,** *297* (1–3), 63-70.

78. Brown, A. N.; Smith, K.; Samuels, T. A.; Lu, J.; Obare, S. O.; Scott, M. E., Nanoparticles functionalized with ampicillin destroy multiple-antibiotic-resistant isolates of Pseudomonas aeruginosa and Enterobacter aerogenes and methicillin-resistant Staphylococcus aureus. *Appl Environ Microbiol* **2012,** *78* (8), 2768-74.

79. Zhao, Y.; Tian, Y.; Cui, Y.; Liu, W.; Ma, W.; Jiang, X., Small Molecule-Capped Gold Nanoparticles as Potent Antibacterial Agents That Target Gram-Negative Bacteria. *Journal of the American Chemical Society* **2010,** *132* (35), 12349-12356.

80. Narband, N.; Tubby, S.; Parkin, I. P.; Gil-Tomas, J.; Ready, D.; Nair, S. P.; Wilson, M., Gold Nanoparticles Enhance the Toluidine Blue-Induced Lethal Photosensitisation of Staphylococcus aureus. *Current Nanoscience* **2008,** *4* (4), 409-414.

81. Nie, Z.; Liu, K. J.; Zhong, C.-J.; Wang, L.-F.; Yang, Y.; Tian, Q.; Liu, Y., Enhanced radical scavenging activity by antioxidant-functionalized gold nanoparticles: A novel inspiration for development of new artificial antioxidants. *Free Radical Biology and Medicine* **2007,** *43* (9), 1243-1254.

82. Bowman, M.-C.; Ballard, T. E.; Ackerson, C. J.; Feldheim, D. L.; Margolis, D. M.; Melander, C., Inhibition of HIV Fusion with Multivalent Gold Nanoparticles. *Journal of the American Chemical Society* **2008,** *130* (22), 6896-6897.

83. Chen, Y. S.; Hung, Y. C.; Lin, W. H.; Huang, G. S., Assessment of gold nanoparticles as a size-dependent vaccine carrier for enhancing the antibody response against synthetic foot-and-mouth disease virus peptide. *Nanotechnology* **2010,** *21* (19), 195101; Niikura, K.; Matsunaga, T.; Suzuki, T.; Kobayashi, S.; Yamaguchi, H.; Orba, Y.; Kawaguchi, A.; Hasegawa, H.; Kajino, K.; Ninomiya, T.; Ijiro, K.; Sawa, H., Gold Nanoparticles as a Vaccine Platform: Influence of Size and Shape on Immunological Responses in Vitro and in Vivo. *ACS Nano* **2013,** *7* (5), 3926-3938.

84. Hermanson, G. T., *Bioconjugate Techniques*. Elsevier Science: 2010.

85. Angelatos, A. S.; Radt, B.; Caruso, F., Light-Responsive Polyelectrolyte/Gold

Nanoparticle Microcapsules. *The Journal of Physical Chemistry B* **2005,** *109*, 3071-3076; Skirtach, A. G.; Muñoz Javier, A.; Kreft, O.; Köhler, K.; Piera Alberola, A.; Möhwald, H.; Parak, W. J.; Sukhorukov, G. B., Laser-Induced Release of Encapsulated Materials inside Living Cells. *Angew. Chem. Int. Ed.* **2006,** *45*, 4612-4617.

86. Niikura, K.; Iyo, N.; Matsuo, Y.; Mitomo, H.; Ijiro, K., Sub-100 nm Gold Nanoparticle Vesicles as a Drug Delivery Carrier enabling Rapid Drug Release upon Light Irradiation. *ACS Applied Materials & Interfaces* **2013,** *5* (9), 3900-3907.

87. Wu, G.; Mikhailovsky, A.; Khant, H. A.; Fu, C.; Chiu, W.; Zasadzinski, J. A., Remotely Triggered Liposome Release by Near-Infrared Light Absorption via Hollow Gold Nanoshells. *J. Am. Chem. Soc.* **2008,** *130*, 8175-8177; Agarwal, A.; Mackey, M. A.; El-Sayed, M. A.; Bellamkonda, R. V., Remote Triggered Release of Doxorubicin in Tumors by Synergistic Application of Thermosensitive Liposomes and Gold Nanorods. *ACS Nano* **2011,** *5*, 4919-4926.

88. Kim, C. K.; Ghosh, P.; Pagliuca, C.; Zhu, Z.-J.; Menichetti, S.; Rotello, V. M., Entrapment of Hydrophobic Drugs in Nanoparticle Monolayers with Efficient Release into Cancer Cells. *J. Am. Chem. Soc.* **2009,** *131*, 1360-1361.

89. Sershen, S. R.; Westcott, S. L.; Halas, N. J.; West, J. L., Temperature-Sensitive Polymer–Nanoshell Composites for Photothermally Modulated Drug Delivery. *J. Biomed. Mater. Res.* **2000,** *51*, 293-298; Bikram, M.; Gobin, A. M.; Whitmire, R. E.; West, J. L., Temperature-Sensitive Hydrogels with SiO_2–Au Nanoshells for Controlled Drug Delivery. *J. Controlled Release* **2007,** *123*, 219-227.

90. Yavuz, M. S.; Cheng, Y.; Chen, J.; Cobley, C. M.; Zhang, Q.; Rycenga, M.; Xie, J.; Kim, C.; Song, K. H.; Schwartz, A. G.; Wang, L. V.; Xia, Y., Gold nanocages covered by smart polymers for controlled release with near-infrared light. *Nat. Mater.* **2009,** *8*, 935-939.

91. Xia, X.; Yang, M.; Oetjen, L. K.; Zhang, Y.; Li, Q.; Chen, J.; Xia, Y., An Enzyme-Sensitive Probe for Photoacoustic Imaging and Fluorescence Detection of Protease Activity. *Nanoscale* **2011,** *3*, 950-3.

92. Rosi, N. L.; Giljohann, D. A.; Thaxton, C. S.; Lytton-Jean, A. K. R.; Han, M. S.; Mirkin, C. A., Oligonucleotide-Modified Gold Nanoparticles for Intracellular Gene Regulation. *Science* **2006,** *312* (5776), 1027-1030.

93. Ghosh, P. S.; Kim, C.-K.; Han, G.; Forbes, N. S.; Rotello, V. M., Efficient Gene Delivery Vectors by Tuning the Surface Charge Density of Amino Acid-Functionalized Gold Nanoparticles. *ACS Nano* **2008,** *2* (11), 2213-2218.

94. Barhoumi, A.; Huschka, R.; Bardhan, R.; Knight, M. W.; Halas, N. J., Light-induced release of DNA from plasmon-resonant nanoparticles: Towards light-controlled gene therapy. *Chemical Physics Letters* **2009,** *482* (4–6), 171-179.

95. Bonoiu, A. C.; Mahajan, S. D.; Ding, H.; Roy, I.; Yong, K.-T.; Kumar, R.; Hu, R.;

Bergey, E. J.; Schwartz, S. A.; Prasad, P. N., Nanotechnology approach for drug addiction therapy: Gene silencing using delivery of gold nanorod-siRNA nanoplex in dopaminergic neurons. *Proceedings of the National Academy of Sciences* **2009**.

96. Peer, D.; Karp, J. M.; Hong, S.; Farokhzad, O. C.; Margalit, R.; Langer, R., Nanocarriers as an emerging platform for cancer therapy. *Nat Nano* **2007,** *2* (12), 751-760.

97. Ghosh, P.; Han, G.; De, M.; Kim, C. K.; Rotello, V. M., Gold nanoparticles in delivery applications. *Adv. Drug Delivery Rev.* **2008,** *60*, 1307-1315; Rana, S.; Bajaj, A.; Mout, R.; Rotello, V. M., Monolayer Coated Gold Nanoparticles for Delivery Applications. *Adv. Drug Del. Rev.* **2012,** *64*, 200-216.

98. Sershen, S. R.; Westcott, S. L.; Halas, N. J.; West, J. L., Temperature-sensitive polymer–nanoshell composites for photothermally modulated drug delivery. *Journal of Biomedical Materials Research* **2000,** *51* (3), 293-298.

99. Moon, G. D.; Choi, S.-W.; Cai, X.; Li, W.; Cho, E. C.; Jeong, U.; Wang, L. V.; Xia, Y., A New Theranostic System Based on Gold Nanocages and Phase-Change Materials with Unique Features for Photoacoustic Imaging and Controlled Release. *Journal of the American Chemical Society* **2011,** *133* (13), 4762-4765.

100. You, J.; Zhang, G.; Li, C., Exceptionally High Payload of Doxorubicin in Hollow Gold Nanospheres for Near-Infrared Light-Triggered Drug Release. *ACS Nano* **2010,** *4* (2), 1033-1041.

101. Huang, J.; Jackson, K. S.; Murphy, C. J., Polyelectrolyte Wrapping Layers Control Rates of Photothermal Molecular Release from Gold Nanorods. *Nano Letters* **2012,** *12* (6), 2982-2987.

102. Alexander, C. M.; Maye, M. M.; Dabrowiak, J. C., DNA-capped nanoparticles designed for doxorubicin drug delivery. *Chemical Communications* **2011,** *47* (12), 3418-3420.

103. Xiao, Z.; Ji, C.; Shi, J.; Pridgen, E. M.; Frieder, J.; Wu, J.; Farokhzad, O. C., DNA Self-Assembly of Targeted Near-Infrared-Responsive Gold Nanoparticles for Cancer Thermo-Chemotherapy. *Angewandte Chemie International Edition* **2012,** *51* (47), 11853-11857.

104. Zhang, Y.; Cui, X.; Shi, F.; Deng, Y., Nano-Gold Catalysis in Fine Chemical Synthesis. *Chemical Reviews* **2012,** *112* (4), 2467-2505.

105. Yan, N.; Xiao, C.; Kou, Y., Transition metal nanoparticle catalysis in green solvents. *Coordination Chemistry Reviews* **2010,** *254* (9–10), 1179-1218.

106. Donoeva, B. G.; Ovoshchnikov, D. S.; Golovko, V. B., Establishing a Au Nanoparticle Size Effect in the Oxidation of Cyclohexene Using Gradually Changing Au Catalysts. *ACS Catalysis* **2013,** *3* (12), 2986-2991.

107. Díaz Arado, O.; Mönig, H.; Wagner, H.; Franke, J.-H.; Langewisch, G.; Held, P. A.; Studer, A.; Fuchs, H., On-Surface Azide–Alkyne Cycloaddition on Au(111). *ACS Nano*

2013, *7* (10), 8509-8515.

108. Biswas, M.; Dinda, E.; Rashid, M. H.; Mandal, T. K., Correlation between catalytic activity and surface ligands of monolayer protected gold nanoparticles. *Journal of Colloid and Interface Science* **2012,** *368* (1), 77-85.

Chapter II. Rapid Determination of the Agglomeration Status of Plasmonic Nanoparticles in Blood[*]

Abstract

Plasmonic nanomaterials as drug delivery or bio-imaging agents are typically introduced to biological systems through intravenous administration. However, the potential for agglomeration of nanoparticles in biological systems could dramatically affect their pharmacokinetic profile and toxic potential. Development of rapid screening methods to evaluate agglomeration is urgently needed to monitor the physical nature of nanoparticles as they are introduced into blood. Here, we establish novel methods using darkfield microscopy with hyperspectral detection (hsDFM), single particle inductively-coupled plasma mass spectrometry (spICP-MS), and confocal Raman microscopy (cRM) to discriminate gold nanoparticles (AuNPs) and their agglomerates in blood. Rich information about nanoparticle agglomeration *in situ* is provided by hsDFM monitoring of the plasmon resonance of primary nanoparticles and their agglomerates in whole blood; cRM is an effective complement to hsDFM to detect AuNP agglomerates in minimally manipulated samples. The AuNPs and the particle agglomerates were further distinguished in blood for the first time by quantification of particle mass using spICP-MS with excellent sensitivity and specificity. Furthermore, the agglomeration status of synthesized and commercial NPs incubated in blood was successfully assessed using the developed methods. Together, these complementary methods enable rapid determination of the agglomeration status of plasmonic nanomaterials in biological systems, specifically blood.

Introduction

Nanomaterial-containing commercial products are under intense development by the pharmaceutical industry for imaging, diagnosis, prevention, and treatment of disease [1]. The safety of these new, nanomaterial-containing products remains a concern to scientists and the public [2]. The toxicity of nanomaterials depends strongly on their physiochemical properties (*e.g.* size, size distribution, shape, surface charge, crystal structure, hydrophobicity, surface reactivity, solubility, aggregation and purity) and material composition itself [3-5]. The United States Food and Drug Administration (FDA) has developed a nanotechnology regulatory science program to enhance research in nanomaterial characterization, *in vitro* and *in vivo* modeling, and product-focused disposition and toxicity [6]. One priority is the development of the analytical tools to detect and characterize nanomaterials in commercial products, food matrices, and biological systems. The challenge facing biomedical research is the poor understanding of the agglomeration status and biological fate of nanomaterials once they are introduced into the blood stream.

Gold nanomaterials (GNMs) are particularly appealing candidates as new diagnostic and therapeutic agents because of their relative bioinertness, tightly controllable morphology, facile surface functionalization, and unique optical properties [7-10]. Some GNM-based medicines are in clinical trials. As an example, Aurimune® is a nanomedicine with tumor necrosis factor (rhTNFa) covalently conjugated to PEGylated gold nanoparticles that has been approved for phase II clinical trials for cancer therapy [11]. AuroLase®, which is also in clinical trials, utilizes gold nanoshells and laser technology as a new photothermal treatment modality for refractory head and neck cancer [12]. In practice, GNM-based medicine is generally administered intravenously, i.e. directly into the blood stream. Blood is a complex fluid with significant

concentrations of proteins, salts, and blood cells. Nanoparticles interact with blood proteins; adsorption onto the materials' surface results in the formation of a protein corona [13,14]. The change in surface properties introduced by blood ionic strength can induce nanoparticle agglomeration [15], and thus significantly alter the cellular interactions, biodistribution [16], and toxicity profile of the particles [17]. Additionally, nanomaterials retard cell motility [18], and nanomaterial induced endothelial leakage (NanoEL), wherein nanomaterials bypass the cell membrane by disrupting through adherens junction, has also shown a strong correlation to the hydrodynamic size of the particle [19]. Due to their potential for agglomeration, *in situ* monitoring of nanoparticles in blood is crucial to fully understand *in vivo* effects of GNM-materials targeted for human theranostics.

There are many well-developed methods to characterize GNMs; however, characterizing GNMs in blood is complicated by the complex environment, *e.g.* plasma proteins and various blood cells. Electron microscopy (EM) is considered the most accurate method to measure the size of nanoparticles and the most widely used method of assessing nanoparticle morphology. However, EM requires considerable sample manipulation, which introduces artifacts; it provides only a static image of the GNMs, typically in thin, dry sections of tissues or matrices (e.g. 50-100 nm), and cannot readily distinguish agglomerates from primary particles located in close proximity [20-23]. Recently, cellular uptake of 30 nm, spherical AuNPs has been visualized using scanning transmission electron microscopy (STEM) imaging of liquids, yet at this point the technique suffers from low resolution [24]. Chromatographic techniques, such as size-exclusion chromatography, ultracentrifugation, and electrophoresis, have been shown to separate primary and agglomerated nanoparticles based on shape, size, or charge [25]. One considerable disadvantage is that these techniques often require extensive sample preparation, which may

affect particle agglomeration status. Dynamic light scattering (DLS) has been used to estimate particle concentration in blood [26]; however, DLS is limited due to (1) its requirement that the blood cells to be lysed prior to measurement, which could affect the agglomeration status of nanomaterials; (2) the presence of proteins and cells in blood interferes with nanoparticle signal; and (3) larger particles which are overrepresented in polydisperse samples [27]. UV-Vis and Raman spectroscopy can readily distinguish primary and agglomerated plasmonic nanoparticles [28,29], but the signal is compromised by the extremely high optical density and opacity of blood. Accordingly, we are unable to find a simple and robust methodology for in situ characterization of nanoparticle agglomeration in blood and other complex biological environments.

In this work, complementary and rapid *in situ* methods have been developed to monitor the agglomeration status of plasmonic nanoparticles in *ex vivo* blood. These methods include darkfield microscopy with hyperspectral imaging (hsDFM), confocal Raman microscopy (cRM), and single particle inductively-coupled plasma mass spectrometry (spICP-MS). The first two methods are based on the optical properties of GNMs, that is, the localized surface plasmon resonance (LSPR) [30]. The LSPR is extremely sensitive to particle morphology with agglomeration of GNMs resulting in a shift of the LSPR to lower energy [31]. The hsDFM can monitor this shift of scattered photons from GNMs, thereby distinguishing light scattered by the cellular environment from that scattered by nanoparticles [32-36], and this instrument has been used to distinguish macrophage maturity based on silver nanoparticle (AgNPs) uptake [37]. Scattering also gives rise to enhancement of the fluorescence and Raman scattering properties of molecules close to the GNMs [38]. The areas of high curvature or between adjacent AuNPs at agglomeration sites create localized "hot spots" that enhance Raman signals, similar to a

roughened metal surface [38], with enhancement factors that can be 10^8 or greater [39].

Surface enhanced Raman spectroscopy (SERS) has been used to identify circulating tumor cells in blood [40] and detect tumor cells *in vivo* [41], as well as a wide-range of other chemical detection and sensing applications [42,43]. We have applied SERS *via* cRM to directly monitor nanoparticle agglomeration as a label-free detection method in this study.

In addition to the optical techniques, spICP-MS provides a high-resolution technique to detect individual particle events for characterization of a variety of engineered nanomaterials [44]. Unlike traditional ICP-MS, which provides bulk elemental analysis of homogenized metallic species, spICP-MS provides a measure of individual particles in suspension. At sufficiently low particle concentrations, particles are introduced individually for atomization and ionization in the plasma, creating a packet of ions that are detected as a discrete signal. This quantifiable spike in intensity due to single particle events enables individual nanoparticles to be distinguished from the background ionic current [45]. The signal intensity is proportional to the number of atoms in an individual event, so larger particles produce higher signal intensity. Similarly, particle agglomeration can be detected by monitoring the increase in signal intensity [46]. By collecting a large number of data points, the particle size and distribution can be determined [44,46-48].

In this report, we have validated and applied the spICP-MS technique to analyze the agglomeration status of nanoparticles in blood as a complement to the optical methods. AuNPs and agglomerates were synthesized and characterized using well-developed methods like UV-Vis, Raman spectroscopy, TEM, DLS, nanoparticle tracking analysis (NTA), and discrete dipole approximation (DDA) calculations. Detection of particle agglomeration was validated in a variety of simple biological media. The promising methods were then used to detect agglomerates in blood, with hsDFM and spICP-MS as the primary methodologies. Finally,

30

citrate-capped NPs were incubated in blood, and their agglomeration was monitored using the developed methods. Together, hsDFM, cRM, and spICP-MS provide a rapid and robust means to analyze nanoparticle agglomeration in biological systems with minimal sample preparation. These diverse, label-free methods can distinguish primary particles from agglomerates in blood. Identification of the interactions between nanoparticles and components in biological systems is, in turn, critically important for rational design and implementation of nanomedicine.

Results and discussion

Synthesis and characterization of nanoparticles and agglomerates

The AuNPs synthesized *via* the citrate reduction method (AuNP-cit) [49] had a diameter of 44.5 ± 9.2 nm from TEM measurements (**Fig. 1A** inset, **Fig S1**). Based on DLS, the d_H was 50.1 ± 0.7 nm and the zeta potential was -35.2 ± 0.9 mV. NTA indicated a mode diameter of 51.3 ± 2.3 nm. The size difference between TEM and DLS/NTA measurements is expected because TEM is used to determine the size of the metal core, while DLS and NTA measure d_H, which reflects the size of the metal particle and the citrate stabilizer in solution. AuNP-cit exhibited an LSPR maximum at 537 nm (**Fig. 1A**) and appeared wine-red in color. The simulated spectrum of a 45 nm diameter Au nanosphere showed an extinction peak at 534 nm, similar to that of the measured spectrum (**Fig. 1E**).

Citrate-capped AuNPs have long been known to agglomerate following an increase in the ionic strength in the suspensions [50]. Agglomerates of increasing size were generated by addition of increasing volumes of saturated NaCl to AuNP-cit suspensions. After 10 min reaction, BSA solution (40 mg/mL) was added to the suspension to arrest agglomeration as described previously [17], and the samples in various agglomeration states were collected *via* centrifugation. The transmitted color of the suspension visibly changed from its initial wine-red

to purple and then purple-black. The UV-Vis spectra of primary, BSA-coated AuNPs and agglomerates showed that as the NaCl concentration increased the LSPR red-shifted from 539 to 545 nm and a shoulder, red-shifted from the LSPR, emerged and resolved to a peak in the NIR (**Fig S2**). The morphology of the agglomerates was assessed with TEM (**Fig S3**).

From these BSA-coated samples, "primary AuNPs," "small agglomerates," and "large agglomerates" were defined as the samples agglomerated with 0, 2.5, and 7.5 μL of saturated NaCl, respectively. These samples were used as standards for further experiments. Primary AuNPs (**Fig. 1**B) showed no agglomeration and had an LSPR maximum at 539 nm. Small agglomerates (**Fig. 1C**) consisted of trimers to pentamers with an LSPR peak at 541 nm and a visible shoulder at ~600 nm. Large agglomerates (**Fig. 1D**) were typically composed of between 10 and 25 AuNPs per agglomerate and showed LSPR peaks at 545 and 780 nm. The emergence and separation of these two peaks is often observed during controlled agglomeration of nanoparticles and results from the plasmon resonance of the particle ensembles, while the peak attributed to individual particles remains [53]. The particle size, orientation, and interparticle distance can all affect the position of the LSPR that results from the ensemble of particles [29,31,54].

The discrete dipole approximation (DDA) method was used to simulate the optical spectra of primary AuNPs and their agglomerates. The simulated spectra of a BSA-coated primary AuNP shows an extinction peak at 543 nm (**Fig. 1F**), slightly red-shifted from that of a citrate-coated particle (534 nm) due to the increase of refractive index from 1.33 for citrate to 1.46 for BSA. For small agglomerates, spectra of several configurations were simulated according to visualization in TEM, as shown in Fig S4. These spectra were averaged and plotted in **Fig. 1G**, indicating an extinction peak at ~540 nm and a shoulder at ~670 nm, which is comparable to the

measured spectrum. In the case of large agglomerates, a representative configuration was chosen for simulation (**Fig. 1H**) because it was not practical to integrate all the configurations that 10-25 particles could stochastically adopt in the sample. The simulated spectrum shows two peaks at ~550 nm and ~750 nm with a board shoulder in between, which indicates a similar trend as the measured spectrum despite the discrepancy due to different configurations in the actual sample. It is important to note that the scattering efficiency increases in the order of primary AuNPs, small agglomerates, and large agglomerates.
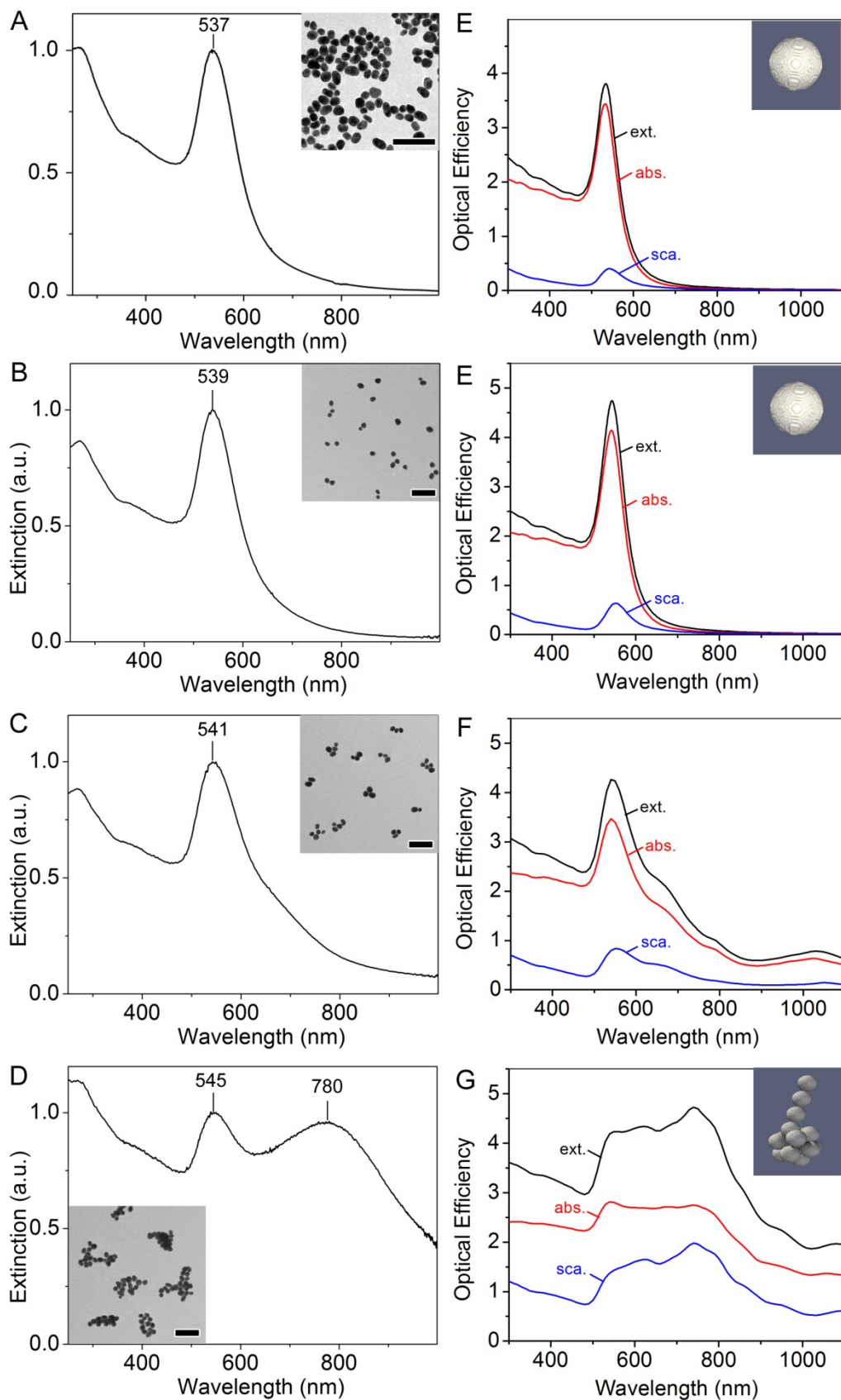
Fig. 1. Characterization of AuNPs and agglomerates synthesized as described in the methods: (left) UV-Vis spectra of samples with inset TEM images (200 nm scale bar) and (right) corresponding spectra simulated by discrete dipole approximation with inset geometric illustrations: (A, E) citrate-capped AuNPs; (B, F) BSA-capped primary AuNPs, (C, G) small agglomerates; and (D, H) large agglomerates. The spectra in (G) are averages from six possible geometries as shown in **Fig. S3**.

The trend of increasing agglomeration was further confirmed by DLS, NTA, and zeta potential measurements (**Table 1**). A rapid increase of hydrodynamic diameter (d_H) was observed by DLS during the progression from primary AuNPs (53.7 ± 0.4 nm) to small agglomerates (142.3 ± 0.4 nm), and large agglomerates (176.5 ± 3.1 nm). This result was further confirmed by NTA with respective mode diameters of 63.0 ± 1.0, 86.0 ± 13.0, and 177.0 ± 27.4nm. Additionally, the zeta potential changed from -19.5 ± 1.5mV for primary AuNPs to -20.8 ± 1.1 and -28.3 ± 1.2mV, suggesting that the primary AuNPs and agglomerates were coated with BSA, in agreement with other studies under similar conditions [55,56]. The initial discrepancy between DLS and NTA can be ascribed to the different measurements of the instrument. DLS is weighted by signal intensity, so a greater contribution to the d_H is made by larger components than smaller components, which can artificially inflate d_H values; NTA measures many particles individually but produces a diameter based on population intensity, rather than signal intensity, which may artificially deflate d_H values. Further, agglomerates of 3-5 particles can be expected to show high variability, as their overall geometry can be expected to change the most from the stochastic arrangement (see **Fig. S4** for some examples). Both of these techniques rely on the velocity of particles in solution, and indicate that as the agglomerates become larger, they travel more slowly through the solution.

Table 1 Summary of characterization of Au nanoparticles and their agglomerates.

AuNPs per Agglomerate	LSPR (nm)	d_H (DLS) (nm)	d_H (NTA) (nm)	Zeta Potential (mV)	Designation
Citrate	537	50.1 ± 0.7	51.3 ± 2.3	-35.2 ± 0.9	AuNP-Cit
1	539	53.7 ± 0.4	63.0 ± 1.0	-19.5 ± 1.5	Primary AuNPs
3-5	542	142.3 ± 0.4	86.0 ± 13.0	-20.8 ± 1.1	Small agglomerate
10-25	545, 780	176.5 ± 3.1	177.0 ± 27.4	-28.3 ± 1.2	Large agglomerate

Establishment of the hsDFM method for identification of agglomeration

The hsDFM has been used as analytical tool to detect certain nanomaterials in cells [57,58]. For instance, a recent study demonstrated the combination of the plasmonic Au dimer probes and hyperspectral imaging is capable of quantitatively imaging single mRNA splices in live cells [59]. In this study, primary AuNPs and their agglomerates can be easily seen using hsDFM because of their large scattering cross-sections. Primary AuNPs appeared green on the microscope (**Fig. 2A**) and moved around extremely quickly due to Brownian motion (*i.e.* diffusion). The agglomerates appeared yellow and the particle motion decreased substantially (**Fig. 2, C** and **E**). Hyperspectral maps were acquired for the various samples. From these spectra, the most intense spectra were accumulated to represent typical spectral output. The scattering peak of primary AuNPs appeared at ~550-560 nm (**Fig. 2B**). For small agglomerates, the peak shifted to ~580 nm (**Fig. 2D**); for large agglomerates, the peaks were observed at ~550 nm and ~660-700 nm (**Fig. 2F**). Importantly, the signal intensity increased from primary AuNPs to small and large agglomerates, as would be expected for a scattering-based process. The signal from agglomerates is significantly brighter than that of primary AuNPs, therefore the presence of agglomerates can be readily detected by the relative intensity difference of their scattering spectra. Agglomeration can be qualitatively monitored based on the color of the scattered light as seen in the microscope and by the particle diffusion velocity, which can then be further confirmed using the hyperspectral camera to identify the change in wavelength and intensity.
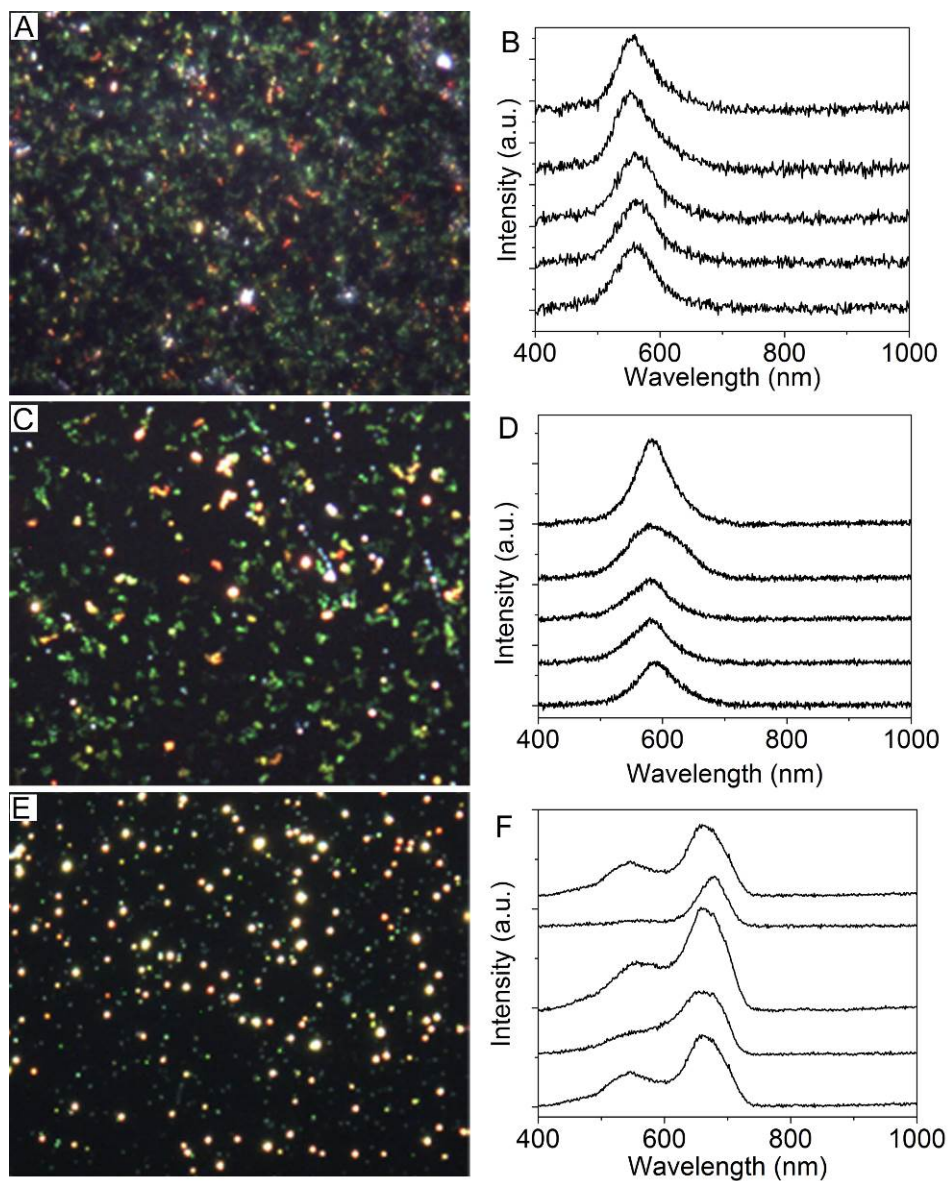
Fig. 2. Darkfield images of typical hyperspectral scattering spectra of (A, B) primary AuNPs; (C, D) small agglomerates; and (E, F) large agglomerates, which correspond to the samples in **Fig. 1**.

Having demonstrated the capacity to distinguish agglomerates, hsDFM was applied to identify the status of AuNP-cit in different media (*i.e.* H_2O, PBS, cell-culture medium (CCM), and serum) and compared with UV-Vis spectra as shown in **Fig. 3**. In **Fig. 3 A** and **D**, the hsDFM showed scattering maxima at ~550-560 nm for H_2O, and the true color images show mainly green, fast-moving particles, suggesting that the AuNP-cit did not agglomerate in these media. In agreement with these results, the UV-Vis spectra showed no significant changes in either medium. In contrast, hyperspectral plots of AuNP-cit incubated in PBS and CCM showed two typical peaks, one located in the 550-580 nm region and the other in the 630-700 nm region. True color, darkfield imaging displayed primarily bright yellow, slow-moving spots, suggesting that AuNP-cit agglomerates detectably in PBS and CCM. This result was confirmed by UV-Vis spectroscopy, which showed the emergence of a second peak ~680 nm, suggesting the formation of medium to large agglomerates (**Fig. 3 B** and **C**). These results clearly demonstrate that the hsDFM method can detect and monitor agglomeration of AuNPs in simple media.
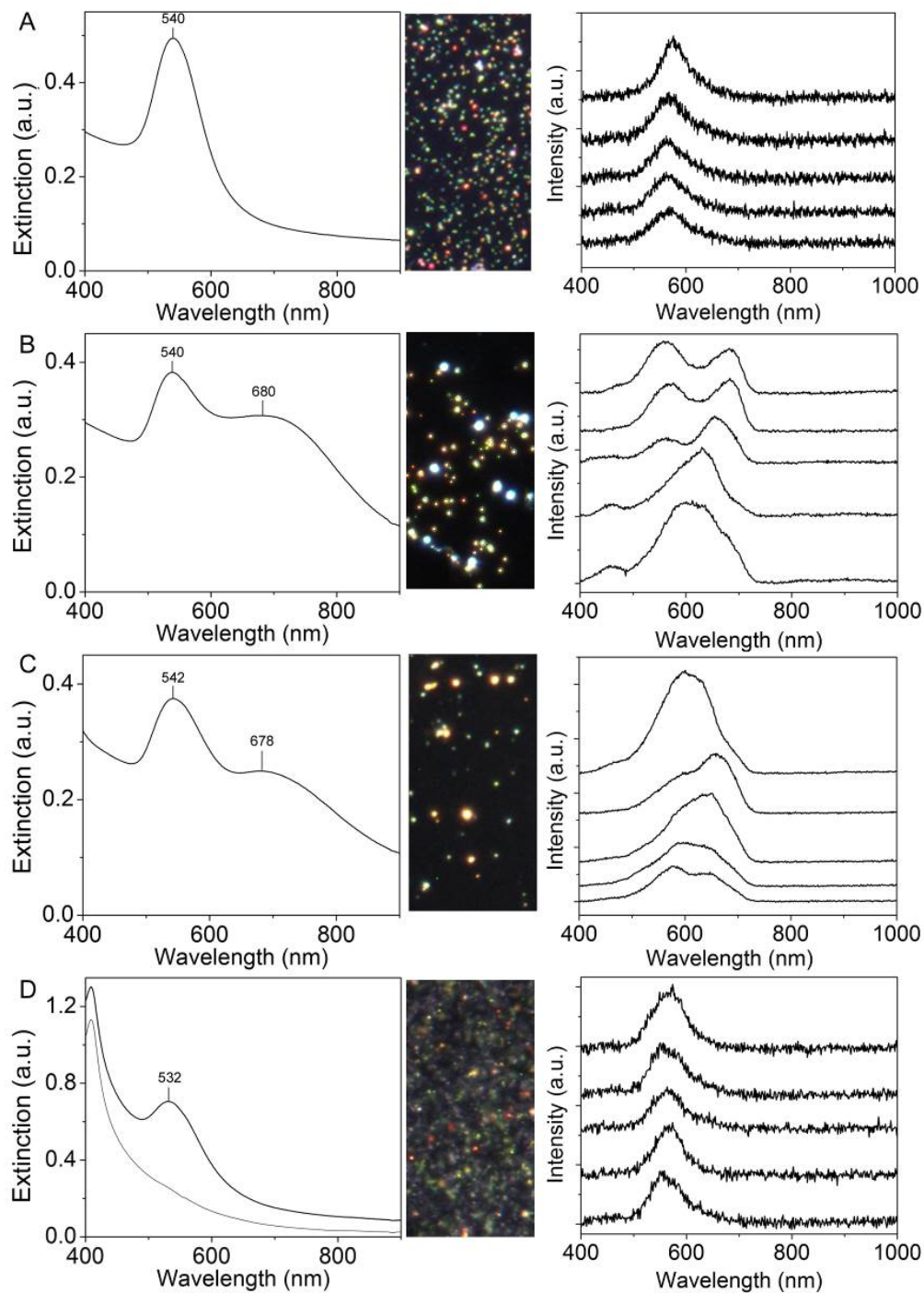
Fig. 3. The agglomeration behavior of citrate-capped AuNPs in four aqueous media: (A) H$_2$O; (B) phosphate-buffered saline; (C) cell-culture medium; and (D) fetal bovine serum (black) with and (gray) without AuNPs. (Left) UV-Vis spectra; (Center) darkfield image; and (Right) typical hyperspectral scattering spectra.

Raman studies of agglomeration

The cRM has been applied as a fast and label-free analytical approach to detect carbon-based nanomaterials in biological system [60]. GNMs' use as an agent for SERS has attracted much attention in recent years [61]. In this study, cRM was used to characterize agglomeration as a compliment to hsDFM. The surface coatings, citrate and BSA, can serve as indicators of the agglomeration of AuNPs because the gaps between agglomerated AuNPs can enhance Raman signal by up to 10^8-fold relative to primary particles [62]. **Fig. 4A** shows this same trend with large agglomerates having more intense spectral features than small agglomerates. BSA-coated, primary AuNPs produced the same spectrum as pure H_2O with Raman shift at ~1640 cm^{-1} [63]. As the size of the agglomerates increased, the Raman shift of H_2O was replaced by several informative peaks. The peak at ~225 cm^{-1} may be the result of Au-N bond stretching [64] from the protein adsorbed to the particle surface. Additionally, a number of peaks emerge in the range of 1000-1600 cm^{-1} that are likely associated with stretching of the citrate carbonyls or aromatic vibrations and carbonyl stretching within the protein structure [65]. The strongest peak to emerge, however, is ~2900 cm^{-1} and can be attributed to C-H stretching [65]. Monitoring for the emergence of these peaks, particularly the C-H stretch, can be used to track the degree of agglomeration. Interestingly, the intensity of the peaks begins to decrease at higher agglomeration levels (**Fig. S5**), which could be the result of the agglomerate not being completely irradiated, thereby producing less signal [66], LSPR shift reducing the resonant absorption needed for enhancement [67], or the structure of the agglomerate resulting in less enhancement [68].

Raman spectroscopy was used to complement the study of the various media, and the response of AuNP-cit to incubation in H_2O, PBS, CCM, and serum was measured (**Fig. 4B**). Similar to the

42

hsDFM and UV-Vis results, no significant change was seen between solvent spectra and Au containing spectra for water or serum, suggesting that the AuNP-cit remains nonagglomerated. On the other hand, incubation of AuNP-cit in CCM or PBS leads to the emergence of several Raman peaks attributed to citrate, particularly the C=O and C-H stretches. The emergence of these peaks further confirms the agglomeration of AuNP-cit in both of these media, and demonstrates the complementary nature of Raman spectroscopy for detection of agglomeration.
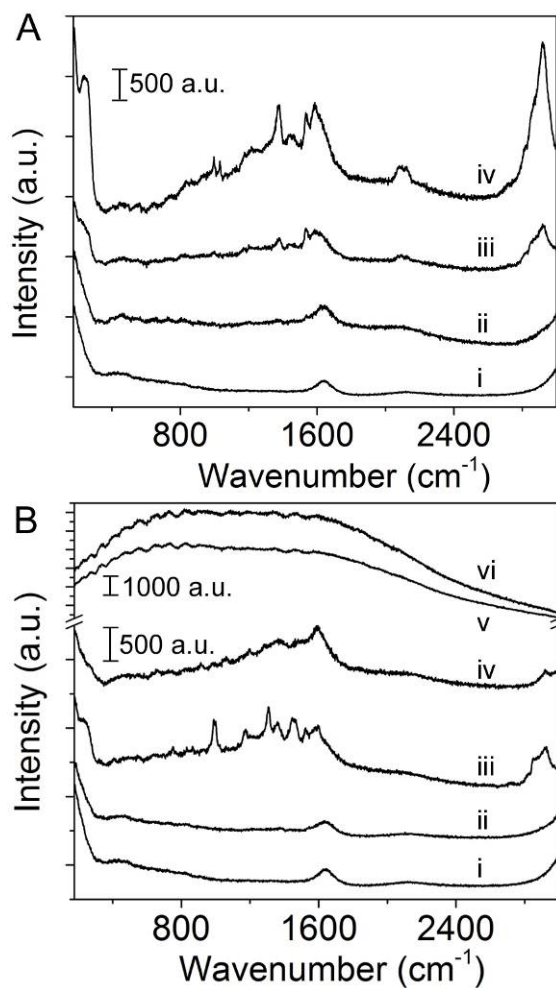
Fig. 4. Raman spectra taken from (A) (i) H_2O and albumin-capped (ii) primary AuNPs, (iii) small agglomerates, and (iv) large agglomerates and (B) (i) H_2O and citrate-capped AuNPs after 10 min incubation in (ii) H_2O, (iii) phosphate-buffered saline, (iv) cell-culture medium, and (vi) fetal bovine serum with (v) normal fetal bovine serum as a reference.

Detection and evaluation of Au particle agglomeration in blood by hsDFM

The primary AuNPs and their agglomerates were added to whole rat blood to model the behavior of the particles following intravenous injection. The optical density of blood limited the use of Raman and UV-Vis spectroscopy to monitor agglomeration, and the medium's complexity additionally ruled out the use of many traditional characterization methods such as electron microscopy and light scattering [69]. **Fig. 5** shows darkfield images and typical hyperspectral plots (hsDFM) of primary AuNPs and large agglomerates following 5 min incubation in blood prior to slide preparation. The primary AuNPs and agglomerates can be visually distinguished using the hsDFM as they appear green and yellow, respectively, as shown by the respective spectra, and with different levels of brightness. The peak does not identically match the peaks observed in simpler media, which may be attributed to the optical interference by the blood. The peak location ~600 nm for primary particles shifts to ~800 nm for agglomerates. These data clearly demonstrate primary AuNPs can be distinguished from agglomerates amongst the blood cells by using the hsDFM technique.
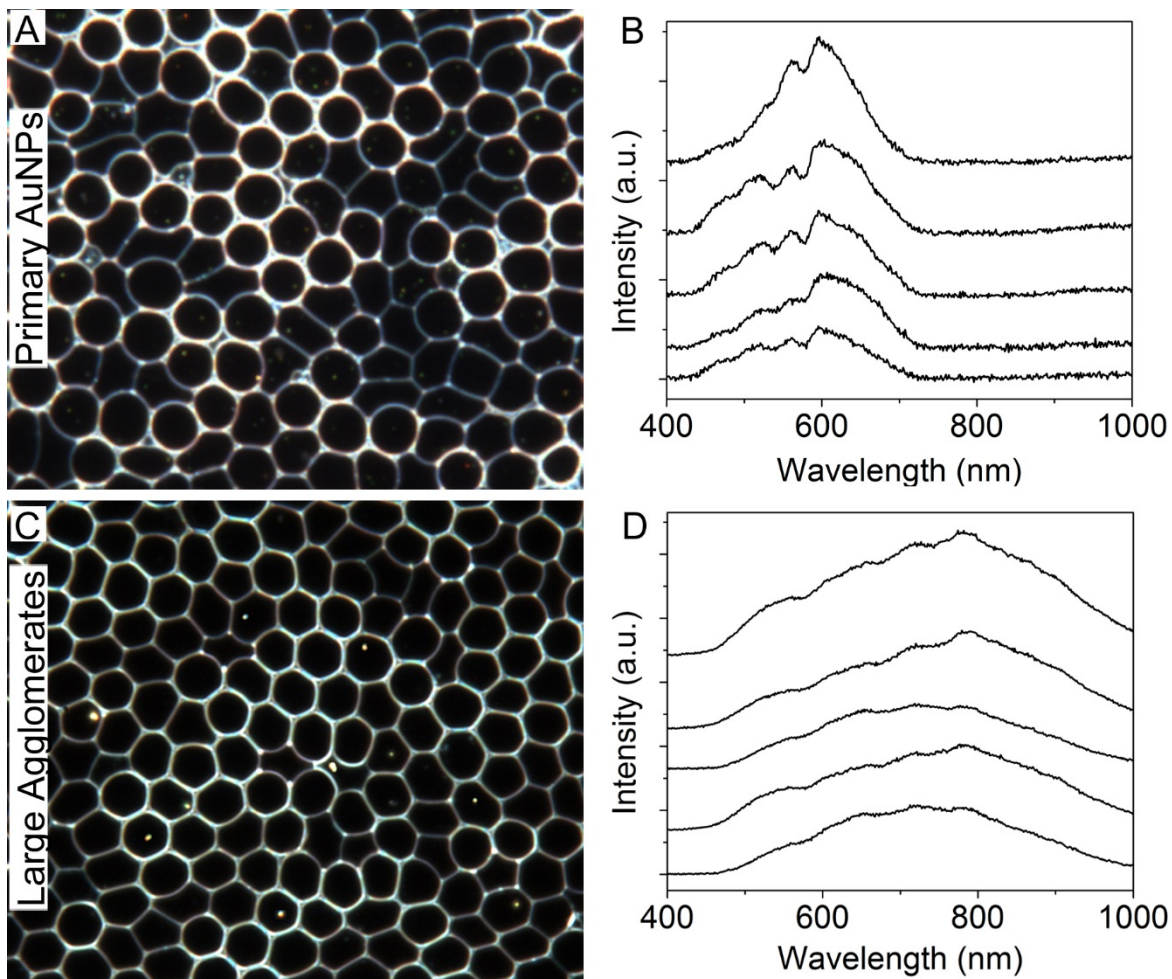
Fig 5. Characterization of prepared AuNPs in the blood: (A) darkfield image and (B) typical hyperspectral scattering spectra of primary AuNPs; (C) darkfield image and (D) typical hyperspectral scattering spectra of large agglomerates.

The hsDFM method was further used to monitor the agglomeration status of AuNP-cit in blood, as shown in **Fig. 6**. AuNP-cit were incubated in blood for 5 min and 18 h. After 5 min incubation, the hyperspectral plots showed maxima primarily ~600 nm, indicating the presence of primary AuNPs. A slight red-shift to ~620 nm was observed after 18 h incubation, suggesting there may be some slight modification of the particles. This agglomeration could be the result of restructuring of the protein corona during incubation [70] or an artifact of the incubation itself. The typical blood half-life for AuNPs is on the order of hours, though with proper surface coating it can be extended to days [71]. As such, it is likely that the sanguine concentration of AuNPs *in vivo* would be low after 18 h, which would reduce the likelihood of agglomeration. Nonetheless, the power of hyperspectral imaging of individual particles using darkfield microscopy is demonstrated and can be further explored to identify changes in the surface of the nanoparticles (*i.e.* agglomeration).

For the most part, AuNP-cit did not agglomerate during incubation in blood, and cell morphology appeared unperturbed, though several anomalies should be remarked upon. First, once the blood sample is prepared, the sample must be imaged quickly to observe an accurate representation of the blood cell morphology. As the specimen remains on the microscope stage, the blood cells begin to deform over the course of 30 min. Presumably this cell disfiguration is the result of evaporation, leading to an increase in salinity and deformation of the blood cells. Blood cells presented typical morphology immediately following sample preparation even after the blood had been stored in a refrigerator for several days. Additionally, slides that had been prepared 30 min prior to imaging began to show evidence of the formation of opalescent particles visible by hsDFM that were likely the initial stages of thrombus formation.
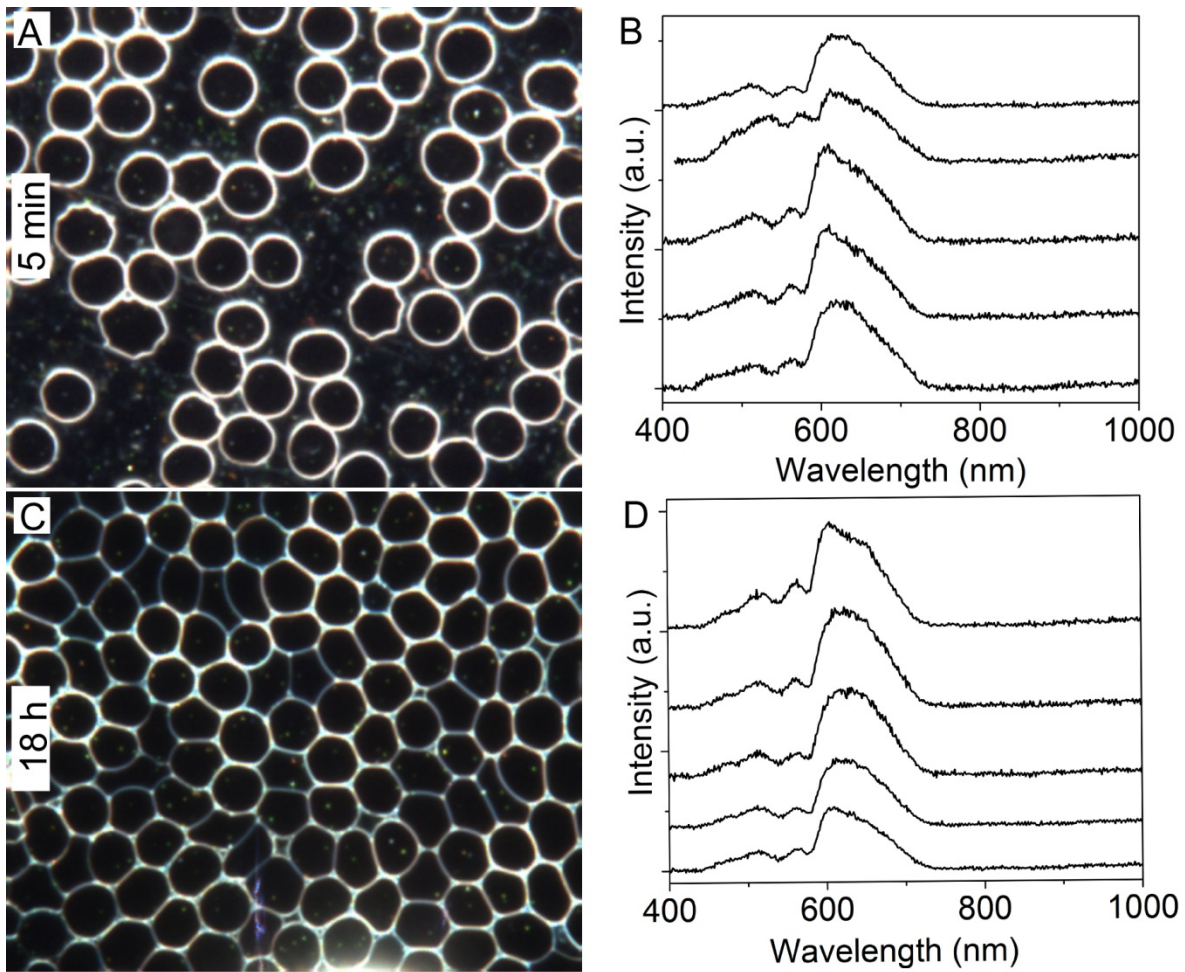
47

Fig. 6. The agglomeration behavior of the citrate-capped AuNPs in the blood after incubation for different time periods: (A) darkfield image and (B) typical hyperspectral scattering spectra at 5 min; (C) darkfield image and (D) typical hyperspectral scattering spectra at 18 h.

Detection of Au nanoparticle agglomeration in blood by single particle ICP-MS

The spICP-MS was applied to discriminate the size of various primary AuNPs in whole rat blood. Whole rat blood was used as a matrix blank to monitor the background counts, and the results showed that majority of the events exhibited counts smaller than 20. Typical pulse intensity versus time output can clearly distinguish primary AuNPs, small agglomerates and large agglomerates in blood (**Fig. 7A**). Citrate-capped NIST AuNP reference materials with 30 nm and 60 nm diameter were coated with BSA (NIST-30 and NIST-60, respectively) and used as standards against which to compare to the primary AuNPs. The measurements for each sample were performed three times and the results were reported as a summation. **Fig. 7B** clearly shows that a large population of events from our primary AuNPs fell between NIST-30 and NIST-60, consistent with the size of the primary AuNPs (45 nm diameter) obtained from TEM studies. Previous studies have suggested that in spICP-MS, signal intensity is proportional to particle size for diameters <80 nm [44]. Since the intensity of each event is proportional to the number of detected ions, the intensity ratio of different particle sizes should be the same as their volume ratio. To simplify the process, samples were normalized to the bin with maximum number of events. As a result, the intensity ratio between our primary AuNPs and the NIST standards were 3.40 for NIST-30 and 0.42 for NIST-60, which are very close to their volume ratios using 45 nm particles ($V_{45}/V_{30} = 3.38$; $V_{45}/V_{60} = 0.42$).

The capability of spICP-MS to distinguish primary AuNPs, small agglomerates and large agglomerates in blood was further examined. Typical measurements of primary particles, small agglomerates, and large agglomerates after incubation in blood are shown in **Fig. 7C**. Relative to primary AuNPs, small agglomerates presented a broader intensity range; a large portion of events had counts higher than 400/event. There were also a considerable number of events with

even higher pulse intensities, suggesting a range of agglomerate masses. When large agglomerates were analyzed, the intensity distribution broadened further. As the intensity increased, the frequency of events decreased relative to small agglomerates, further indicating a much greater degree of agglomeration. These results demonstrate that spICP-MS can be readily utilized to monitor agglomeration of AuNPs in blood.
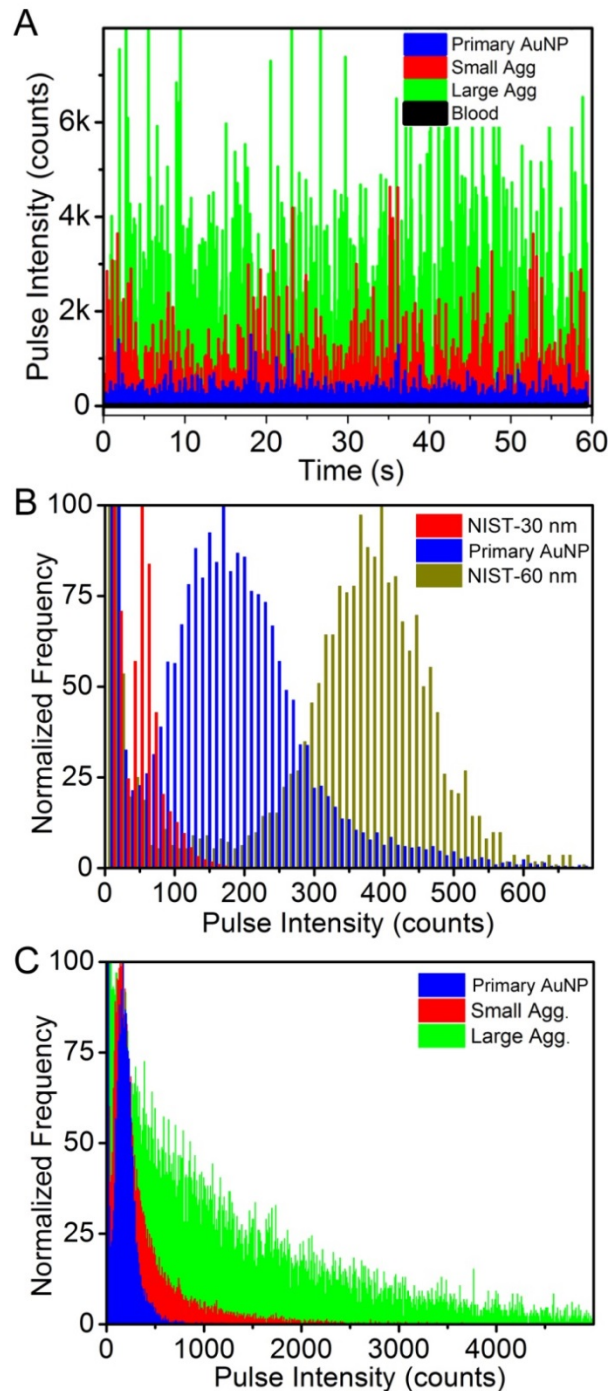
Fig. 7. Single particle ICP-MS analysis of various AuNPs in whole rat blood: (A) Typical pulse intensity versus time output from ICP-MS in single particle mode for blood without AuNPs (black), or incubated with primary AuNPs (blue), small agglomerates (red), or large agglomerates (green), (B) primary AuNPs in whole rat blood using 30 nm (red) and 60 nm (gold) diameter NIST standard citrate-capped AuNPs stabilized with albumin and in-house synthesized, albumin stabilized primary AuNPs (blue), small agglomerates (red), and large agglomerates (green) in whole rat blood.

Evaluation of Ag nanoparticle agglomeration status in blood by hsDFM

Similar to AuNPs, AgNPs are also in development as potential therapeutics with strong plasmonic properties [72]. To test the robustness of the hsDFM method, AgNPs were subjected to similar analysis as AuNPs. Citrate-capped AgNPs were agglomerated by NaCl resulting in a change in LSPR. BSA-capped primary and agglomerated AgNPs were introduced to blood and imaged using darkfield microscopy (**Fig. 8, A** and **B**). Primary AgNPs scattered a cyan color associated with rapidly moving particles, while agglomerates appeared as slow-moving yellow spots. Due to either the size of the AgNPs (~75 nm) or the optical properties of AgNPs, the signal is significantly brighter than that of AuNPs. Hyperspectral plots confirm this change in color and intensity with primary AgNPs scattering ~500 nm and agglomerates scattering ~600-700 nm, sometimes displaying multiple peaks. Having demonstrated that agglomeration of AgNPs can be detected, citrate-capped AgNPs were incubated in isolated, heparinized rat blood for 5 min and 18 h. After 5 min, the signal returned is primarily between 500 and 540 nm, with the typical spectrum of the primary particles (**Fig. 8, C** and **D**). There appears to be some background signal from the blood, though it presents less interference than for AuNPs, which is attributable to the increased signal intensity of the AgNPs. After 18 h in blood, a mixture of signals was obtained (representative signals shown in **Fig. 8 E** and **F**) with agglomerated AgNP showing emissions at 550-600 nm (upper two spectra) and primary particles at 500-540 nm (lower three spectra). Interestingly, the increased brightness of the AgNPs mitigated some of the obscuring effects of the blood on the hyperspectral plot as was seen with AuNPs.
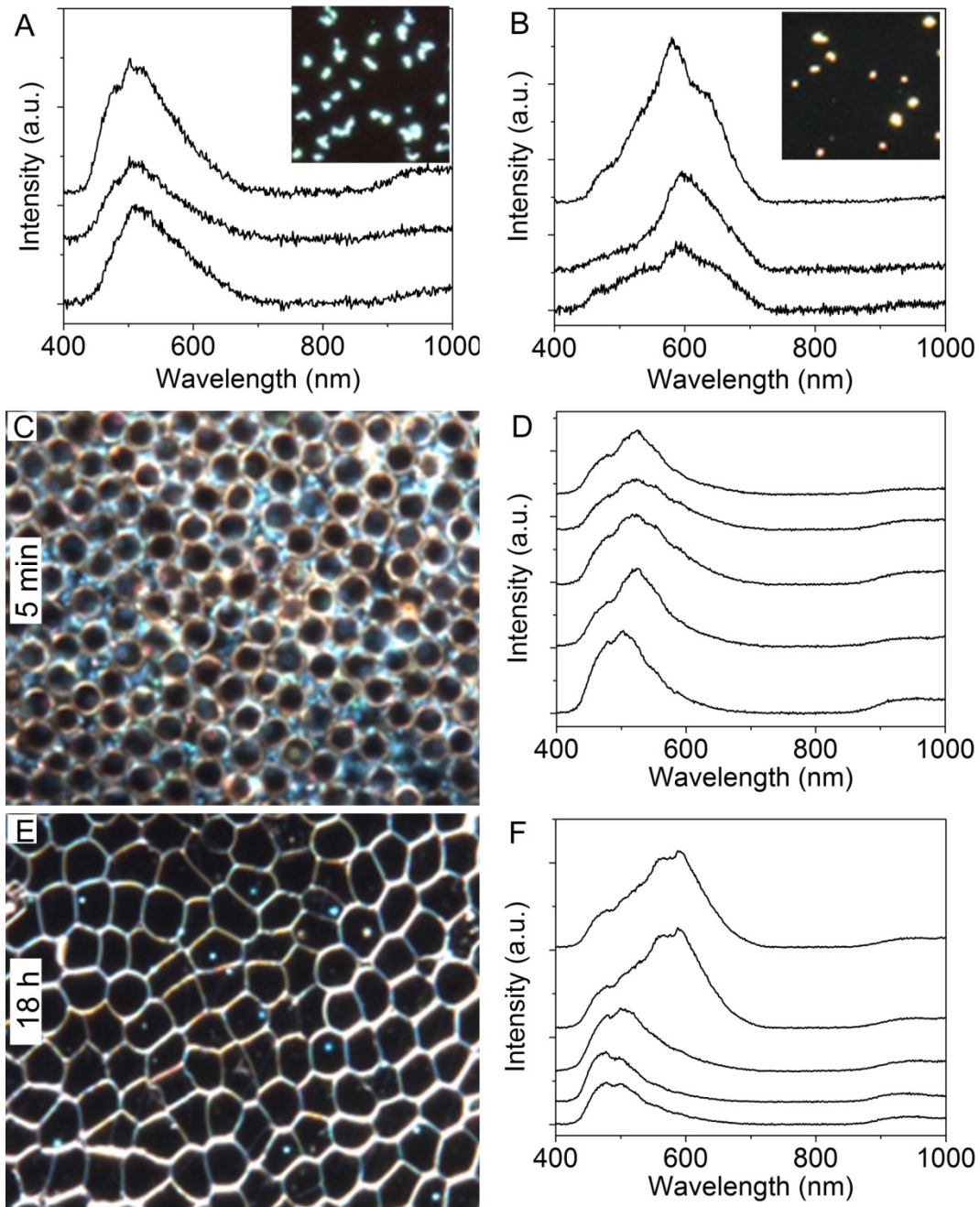
Fig. 8. Characterization of Ag nanomaterials in isolated, whole rat blood with typical hyperspectral scattering spectra with inset darkfield image of albumin-stabilized (A) primary Ag nanoparticles and (B) agglomerates. The agglomeration behavior of citrate-capped nanoparticles in isolated whole rat blood after incubation for different time periods: (C) darkfield image and (D) typical hyperspectral scattering spectra at 5 min; (E) darkfield image and (F) typical hyperspectral scattering spectra at 18 h.

Conclusions

Three complementary methods, hsDFM, cRM, and spICP-MS, have been demonstrated for the first time for rapid characterization of plasmonic nanomaterials in blood with minimal sample preparation. These methods were capable of distinguishing primary nanoparticles and agglomerates in simple media, which was validated by the standard methods such as TEM, UV-Vis, DLS and NTA. More importantly, hsDFM and spICP-MS demonstrated the unique capability to distinguish primary particles and agglomerates in blood. As a test, AuNPs and AgNPs were incubated in whole rat blood and these methods were used to monitor for the agglomeration of particles. The methods are anticipated to be adaptable to a wide variety of particle morphologies, surface coatings, and biological matrices. Furthermore, these methods could be applicable to blood and tissue extracted from animals following *in vivo* nanomedicine administration. These methods provide biological and pharmacokinetic information important for the development of nanomedicine, as well as analytical approaches for the assessment of nanomaterial-based products.

Materials and methods

Chemicals

Tetrachloroauric acid trihydrate (HAuCl$_4$•3H$_2$O) and trisodium citrate heptahydrate (Na$_3$-Cit; Na$_3$C$_6$H$_5$O$_7$•7H$_2$O) were acquired from Alfa Aesar (Ward Hill, MA). Phosphate buffered saline (PBS), fetal bovine serum (FBS), and Eagle medium were acquired from Corning Cellgro (Manassas, VA). The reference AuNPs with nominal diameters of 10 nm (RM8010), 30 nm (RM8012), and 60 nm (RM8013), were purchased from the National Institute of Standards and Technology (NIST). Citrate-capped 75-nm AgNPs were obtained from NanoComposix (San Diego, CA). Sodium chloride (NaCl) and bovine serum albumin (BSA) were obtained from Sigma Aldrich (St. Louis, MO). All chemicals were used as received.

Synthesis of AuNPs and agglomerates

Citrate-capped AuNPs (AuNP-cit) were synthesized *via* the Turkevich method as previously described [49]. Briefly, 10.6 mg HAuCl$_4$ was dissolved in 99 mL 18 MΩ H$_2$O and heated to boiling. To this solution, 0.9 mL of 10 mg/mL Na$_3$Cit was quickly injected. After 20 min, a deep wine-red color was observed, indicating the formation of AuNPs. The suspension was removed from heat and allowed to cool to room temperature. Prior to use, the excess precursors were removed by centrifuging at 20,800 *g* for 20 min at 20 °C, and the AuNP-cit was redispersed in 18 MΩ H$_2$O.

Agglomerates were generated by adding 0, 2.5, 5, 7.5, 10, 20, or 50 μL of saturated NaCl solution to 1 mL of the AuNP-cit suspension, immediately followed by thoroughly mixing for 5 s. After 10 min, 50 μL BSA (40 mg/mL, 18 MΩ H$_2$O) was added to arrest agglomeration [50]. The solution was immediately mixed and allowed to incubate without further mixing for 30 min at room temperature. Agglomerates were isolated by centrifugation at 20,800 *g* for 20 min at 20

°C. The pellet was redispersed in 18 MΩ H_2O, centrifuged a second time (20,800 g, 20 min, 20 °C), redispersed in 18 MΩ H_2O, and stored at room temperature. Samples were redispersed by brief (<2 s) bath sonication (Branson 5510, Branson Ultrasonics, Danbury, CT) prior to use. No appreciable changes in the UV-Vis spectra or hydrodynamic diameter of agglomerates used were observed after 1 month of storage at room temperature in the dark.

Introduction of nanoparticles into blood

Adult Fisher 344 rats were obtained from the National Center for Toxicological Research (NCTR) Breeding Colony (Jefferson, AR). Whole blood samples from the rats were collected *via* cardiac puncture into plastic whole blood collection tube (Becton, Dickinson, Franklin Lakes, NJ) for the study. The animal procedures followed the guidelines of the "Guide for the Care and Use of Laboratory Animals" and were approved by the NCTR Institutional Animal Care and Use Committee. AuNP-cit (100 μL; 80 ppm) was incubated directly with 1.5 mL fresh whole blood in a blood collection tube. Alternatively, primary AuNPs and agglomerates (80 ppm) were redispersed by bath sonication (~2 s) prior to use. A 20 mL sample was added to 200 mL of fresh, nanoparticle-free blood, followed by mixing for 2 s (final concentration ~8 ppm). To prepare samples for imaging, 3 mL of blood was applied to a clean-room-grade glass microscope slide (Schott, Elmsford, NY), smeared, and a coverslip applied immediately prior to acquisition of hsDFM images. An identical process was followed to introduce AgNPs to blood.

Transmission electron microscopy (TEM)

TEM images were recorded using a JEOL JEM-1400 (JEOL, Tokyo, Japan) with accelerating voltage of 80 keV. Samples (3 mL) were applied onto a 200 mesh carbon-coated copper grid, followed by addition of 3 mL isopropyl alcohol and air dried. Images were acquired using XR41 4mp TEM CCD system (AMT, Woburn, MA) and the particle size was then measured using

ImageJ software (National Institute of Health, Bethesda, MD).

Dynamic light scattering (DLS) and nanoparticle tracking analysis (NTA)

Hydrodynamic diameter (d_H) and zeta potential were determined using a ZetaPALS instrument (Brookhaven, Holtzville, NY). The sample was prepared by diluting 20 mL of primary AuNPs or agglomerates to 2 mL with 1 mM of KCl after brief sonication (<5 s) of the sample (~800 ppb). AuNP-cit was diluted 100-fold in 18 MΩ H_2O. The d_H was measured by performing three consecutive 60 s runs while the zeta potential was measured at 10 runs of 5 cycles each. Average hydrodynamic size was determined using nanoparticle tracking analysis (NTA), and was performed using NanoSight LM-10 (Malvern Instruments Inc, MA, USA). The sample was prepared by diluting 10 mL of sample to 10 mL with 18 MΩ H_2O (80 ppb) after brief sonication (<5 s) of the sample. The diameter corresponding to the mode of the sample was used to represent the most prominent nanoparticle size in solution. Triplicate measurements were acquired for each sample.

UV-Vis spectroscopy

Extinction spectra were acquired on an Agilent HP8453 UV-Vis spectrometer (Agilent Technologies, Santa Clara, CA) using a quartz cuvette with 1-cm path length and 18 MΩ H_2O as a blank. Samples were sonicated for <5 s and diluted 10-fold to 8 ppm with 18 MΩ H_2O prior to measurement.

Confocal Raman microscopy (cRM)

Raman spectra were acquired using a Horiba Jobin Yvon high-resolution LabRam Raman microscope system (Horiba, Edison, NJ) equipped with a charge-coupled detector and a spectrometer with a grating of 600 lines/mm. The systems were set up with a 150-mm entrance slit and a 400-mm pinhole. The 633-nm laser excitation was provided by a HeNe laser operating

at 5 mW. Raman shift calibration was performed using the 521 cm^{-1} line of a silicon wafer. Raman samples were prepared by diluting 100 mL of AuNPs, or agglomerates, to 1 mL with 18 MΩ H$_2$O (8 ppm) after brief sonication (<5 s) of the sample. The diluted sample was then transferred to a 50 mL, 10 mm path length quartz cuvette. Signal was acquired for 10 s and three acquisitions were averaged per spectrum to improve signal-to-noise ratio.

Darkfield microscopy with hyperspectral detection (hsDFM)

Darkfield microscopy images and hyperspectral plots were acquired using enhanced darkfield transmission optical microscope (Olympus BX41) equipped with hyperspectral imaging spectrophotometer (Headwall, CytoViva Inc, Auburn, AL). This system is capable of recording high quality spectra (high signal-to-noise ratio) in the visible and near infrared wavelength range (400-1000 nm). Hyperspectral images were acquired using a 0.25 s collection time and a white light source. Images were acquired using a 100x oil immersion lens.

Single particle inductively-coupled plasmon mass spectrometry (spICP-MS)

The nanoparticles or agglomerates were stored at 4 °C in the dark prior to analysis. Samples were warmed to room temperature, then mixed and sonicated briefly prior to dilution to ensure full dispersion without disrupting agglomeration. Nanoparticles or agglomerates (0.1 mg/mL) were briefly incubated with fresh blood, and then diluted into 10 mL 18 MΩ water. Single particle analysis was performed using an Agilent 7700X ICP-MS (Agilent, Santa Clara, CA) which was tuned daily to optimal sensitivity and resolution. A MicroMist glass concentric nebulizer was used with nickel composite sample and skimmer cones. Argon was used as a carrier gas at a flow rate of 1.05 mL/min. Peristaltic pump speed was set at 0.1 rpm. Samples were analyzed in selected time resolved analysis (TRA)/full quantification mode with a sampling period of 0.01 s and an acquisition time of 180 s. Between each acquisition, the instrument was

first flushed with a solution containing 10% HNO_3 and 10% HCl in water at a pump speed of 0.5 rpm for 3 min to eliminate the AuNPs that were trapped inside the sampling tube from prior measurement. Then the system was rinsed with water for another 3 min to purge the acid. Every sample was measured in triplicate. Agilent's MassHunter Workstation software was used for data analysis.

Calculation of optical properties

The optical properties were calculated according to the discrete dipole approximation (DDA) using the DDSCAT 7.3 program [51]. In this formalism, the particles are represented by an array of dipole moments residing within the volume of the nanoparticles. The nanoparticles were represented as a dielectric continuum with the complex dielectric response function of bulk Au [52]. The optical efficiency, Q, is reported as the ratio of the respective optical cross section to $\pi*\alpha_{eff}^2$, where the effective radius, α_{eff}, is defined as the radius of a sphere whose volume is equal to that of the nanoparticle. The optical cross sections were averaged over two orthogonal polarization directions of the incident light.

References

[1] Kim BYS, Rutka JT, Chan WCW. Current concepts: nanomedicine. N Eng J Med 2010;363:2434-43.

[2] Zhang Y, Ferguson SA, Watanabe F, Jones Y, Xu Y, Biris AS, et al. Silver nanoparticles decrease body weight and locomotor activity in adult male rats. Small 2013;9:1715-20.

[3] Nel A, Xia T, Madler L, Li N. Toxic potential of materials at the nanolevel. Science 2006;311:622-7.

[4] Zhang Y, Ali SF, Dervishi E, Xu Y, Li Z, Casciano D, et al. Cytotoxicity effects of graphene and single-wall carbon nanotubes in neural phaeochromocytoma-derived PC12 cells. ACS Nano 2010;4:3181-6.

[5] Karmakar A, Zhang Q, Zhang Y. Neurotoxicity of nanoscale materials. J Food Drug Anal 2014;22:147-60.

[6] Hamburg MA. FDA's approach to regulation of products of nanotechnology. Science 2012;336:299-300.

[7] Dreaden EC, Alkilany AM, Huang X, Murphy CJ, El-Sayed MA. The golden age: gold nanoparticles for biomedicine. Chem Soc Rev 2012;41:2740-79.

[8] Bardhan R, Lal S, Joshi A, Halas NJ. Theranostic nanoshells: from probe design to imaging and treatment of cancer. Acc Chem Res 2011;44:936-46.

[9] Xia Y, Li W, Cobley CM, Chen J, Xia X, Zhang Q, et al. Gold nanocages: from synthesis to theranostic applications. Acc Chem Res 2011;44:914-24.

[10] Jenkins SV, Muldoon TJ, Chen J. Plasmonic nanostructures for biomedical and sensing applications. In: Xiong Y, Lu X, editors. Metallic nanostructures. Springer International Publishing; 2015. p. 133-73.

[11] Libutti SK, Paciotti GF, Byrnes AA, Alexander Jr HR, Gannon WE, Walker M, et al. Phase I and pharmacokinetic studies of CYT-6091, a novel PEGylated colloidal gold-rhTNF nanomedicine. Clin Cancer Res 2010;16:6139-49.

[12] Pilot study of AuroLase(tm) therapy in refractory and/or recurrent tumors of the head and neck. 2010 ed. National Institute of Health; 2013.

[13] Rivera-Gil P, Jimenez De Aberasturi D, Wulf V, Pelaz B, Del Pino P, Zhao Y, et al. The challenge to relate the physicochemical properties of colloidal nanoparticles to their cytotoxicity. Acc Chem Res 2012;46:743-9.

[14] Casals E, Pfaller T, Duschl A, Oostingh GJ, Puntes V. Time evolution of the nanoparticle protein Corona. ACS Nano 2010;4:3623-32.

[15] Lacerda SHDP, Park JJ, Meuse C, Pristinski D, Becker ML, Karim A, et al. Interaction of gold nanoparticles with common human blood proteins. ACS Nano 2009;4:365-79.

[16] Keene AM, Peters D, Rouse R, Stewart S, Rosen ET, Tyner KM. Tissue and cellular distribution of gold nanoparticles varies based on aggregation/ agglomeration status. Nanomed Lond U K 2012;7:199-209.

[17] Chithrani BD, Chan WCW. Elucidating the mechanism of cellular uptake and removal of protein-coated gold nanoparticles of different sizes and shapes. Nano Lett 2007;7:1542-50.

[18] Tay CY, Cai P, Setyawati MI, Fang W, Tan LP, Hong CHL, et al. Nanoparticles strengthen intracellular tension and retard cellular migration. Nano Lett 2013;14:83-8.

[19] Setyawati MI, Tay CY, Chia SL, Goh SL, Fang W, Neo MJ, et al. Titanium dioxide nanomaterials cause endothelial cell leakiness by disrupting the homophilic interaction of VEecadherin. Nat Commun 2013;4:1673.

[20] Woehl TJ, Park C, Evans JE, Arslan I, Ristenpart WD, Browning ND. Direct observation of aggregative nanoparticle growth: kinetic modeling of the size distribution and growth rate. Nano Lett 2013;14:373-8.

[21] Nativo P, Prior IA, Brust M. Uptake and intracellular fate of surface-modified gold

nanoparticles. ACS Nano 2008;2:1639-44.

[22] Dykman LA, Khlebtsov NG. Uptake of engineered gold nanoparticles into Mammalian cells. Chem Rev 2013;114:1258-88.

[23] Qiu Y, Liu Y, Wang L, Xu L, Bai R, Ji Y, et al. Surface chemistry and aspect ratio mediated cellular uptake of Au nanorods. Biomaterials 2010;31:7606-19.

[24] Peckys DB, de Jonge N. Visualizing gold nanoparticle uptake in live cells with liquid scanning transmission electron microscopy. Nano Lett 2011;11: 1733-8.

[25] Liu FK. Analysis and applications of nanoparticles in the separation sciences: a case of gold nanoparticles. J Chromatogr A 2009;1216:9034-47.

[26] Xie H, Gill-Sharp KL, O'Neal DP. Quantitative estimation of gold nanoshell concentrations in whole blood using dynamic light scattering. Nanomed Nanotechnol Biol Med 2007;3:89-94.

[27] Hinterwirth H, Wiedmer SK, Moilanen M, Lehner A, Allmaier G, Waitz T, et al. Comparative method evaluation for size and size-distribution analysis of gold nanoparticles. J Sep Sci 2013;36:2952-61.

[28] Shipway AN, Lahav M, Gabai R, Willner I. Investigations into the electrostatically induced aggregation of Au nanoparticles. Langmuir 2000;16:8789-95.

[29] Wustholz KL, Henry A-I, McMahon JM, Freeman RG, Valley N, Piotti ME, et al. Structure-Activity Relationships in gold nanoparticle dimers and trimers for surface-enhanced Raman spectroscopy. J Am Chem Soc 2010;132:10903-10.

[30] Wilets KA, Duyne RPV. Localized surface plasmon resonance spectroscopy and sensing. Annu Rev Phys Chem 2007;58:267-97.

[31] Ghosh SK, Pal T. Interparticle coupling effect on the surface plasmon resonance of gold nanoparticles: from theory to applications. Chem Rev 2007;107:4797-862.

[32] Fairbairn N, Christofidou A, Kanaras AG, Newman TA, Muskens OL. Hyperspectral darkfield microscopy of single hollow gold nanoparticles for biomedical applications. Phys Chem Chem Phys 2013;15:4163-8.

[33] Badireddy AR, Wiesner MR, Liu J. Detection, characterization, and abundance of engineered nanoparticles in complex waters by hyperspectral imagery with enhanced darkfield microscopy. Environ Sci Technol 2012;46:10081-8.

[34] Rothen-Rutishauser BM, Schürch S, Haenni B, Kapp N, Gehr P. Interaction of fine particles and nanoparticles with red blood cells visualized with advanced microscopic techniques. Environ Sci Technol 2006;40:4353-9.

[35] Aaron J, Travis K, Harrison N, Sokolov K. Dynamic imaging of Molecular assemblies in live cells based on nanoparticle plasmon resonance coupling. Nano Lett 2009;9:3612-8.

[36] Yu X, Wang J, Feizpour A, Reinhard BM. Illuminating the lateral organization of cell-

surface CD24 and CD44 through plasmon coupling between Au nanoparticle immunolabels. Anal Chem 2013;85:1290-4.

[37] Wang H, Wu L, Reinhard BM. Scavenger receptor mediated endocytosis of silver nanoparticles into J774A.1 macrophages is heterogeneous. ACS Nano 2012;6:7122-32.

[38] Haynes CL, McFarland AD, Duyne RPV. Surface-enhanced raman spectroscopy. Anal Chem 2005;77. 338 A-46 A.

[39] Valley N, Greeneltch N, Van Duyne RP, Schatz GC. A look at the origin and magnitude of the chemical contribution to the enhancement mechanism of surface-enhanced Raman spectroscopy (SERS): theory and experiment. J Phys Chem Lett 2013;4:2599-604.

[40] Wang X, Qian X, Beitler JJ, Chen ZG, Khuri FR, Lewis MM, et al. Detection of circulating tumor cells in human peripheral blood using surface-enhanced Raman scattering nanoparticles. Cancer Res 2011;71:1526-32.

[41] Qian X, Peng XH, Ansari DO, Yin-Goen Q, Chen GZ, Shin DM, et al. In vivo tumor targeting and spectroscopic detection with surface-enhanced Raman nanoparticle tags. Nat Biotechnol 2008;26:83-90.

[42] Jans H, Huo Q. Gold nanoparticle-enabled biological and chemical detection and analysis. Chem Soc Rev 2012;41:2849-66.

[43] Shah NB, Dong J, Bischof JC. Cellular uptake and nanoscale localization of gold nanoparticles in Cancer using label-free confocal Raman microscopy. Mol Pharm 2010;8:176-84.

[44] Liu J, Murphy KE, MacCuspie RI, Winchester MR. Capabilities of single particle inductively coupled plasma mass spectrometry for the size measurement of nanoparticles: a case study on gold nanoparticles. Anal Chem 2014;86: 3405-14.

[45] Laborda F, Jimenez-Lamana J, Bolea E, Castillo JR. Selective identification, characterization and determination of dissolved silver(i) and silver nanoparticles based on single particle detection by inductively coupled plasma mass spectrometry. J Anal At Spectrom 2011;26:1362-71.

[46] Rakcheev D, Philippe A, Schaumann GE. Hydrodynamic chromatography coupled with single particle-inductively coupled plasma mass spectrometry for investigating nanoparticles agglomerates. Anal Chem 2013;85:10643-7.

[47] Mitrano DM, Barber A, Bednar A, Westerhoff P, Higgins CP, Ranville JF. Silver nanoparticle characterization using single particle ICP-MS (SP-ICP-MS) and asymmetrical flow field flow fractionation ICP-MS (AF4-ICP-MS). J Anal At Spectrom 2012;27:1131-42.

[48] Zook J, Long S, Cleveland D, Geronimo C, MacCuspie R. Measuring silver nanoparticle dissolution in complex biological and environmental matrices using UVevisible absorbance. Anal Bioanal Chem 2011;401:1993-2002.

[49] Frens G. Controlled Nucleation for the Regulation of the particle size in Monodisperse gold suspensions. Nature Lond Phys Sci 1973;241:20-2.

[50] Dominguez-Medina S, Blankenburg J, Olson J, Landes CF, Link S. Adsorption of a protein monolayer via hydrophobic interactions prevents nanoparticle aggregation under harsh environmental conditions. ACS Sustain Chem Eng 2013;1:833-42.

[51] Draine BT, Flatau PJ. Discrete-dipole approximation for scattering calculations. J Opt Soc Am A 1994;11:1491-9.

[52] Johnson PB, Christy RW. Optical constants of the noble metals. Phys Rev B Condens Matter Mater Phys 1972;6:4370-9.

[53] Basu S, Ghosh SK, Kundu S, Panigrahi S, Praharaj S, Pande S, et al. Biomolecule induced nanoparticle aggregation: effect of particle size on interparticle coupling. J Colloid Interface Sci 2007;313:724-34.

[54] Halas NJ, Lal S, Chang WS, Link S, Nordlander P. Plasmons in strongly coupled metallic nanostructures. Chem Rev 2011;111:3913-61.

[55] Chithrani BD, Stewart J, Allen C, Jaffray DA. Intracellular uptake, transport, and processing of nanostructures in cancer cells. Nanomed Nanotechnol Biol Med 2009;5:118-27.

[56] Dominguez-Medina S, McDonough S, Swanglap P, Landes CF, Link S. In situ measurement of bovine serum albumin interaction with gold nanospheres. Langmuir 2012;28:9131-9.

[57] Eustaquio T, Leary JF. Nanobarcoding: detecting nanoparticles in biological samples using in situ polymerase chain reaction. Int J Nanomed 2012;7: 5625-39.

[58] Smith BR, Ghosn EEB, Rallapalli H, Prescher JA, Larson T, Herzenberg LA, et al. Selective uptake of single-walled carbon nanotubes by circulating monocytes for enhanced tumour delivery. Nat Nanotechnol 2014;9:481-7.

[59] Lee K, Cui Y, Lee LP, Irudayaraj J. Quantitative imaging of single mRNA splice variants in living cells. Nat Nanotechnol 2014;9:474-80.

[60] Zhang Y, Xu Y, Li Z, Chen T, Lantz SM, Howard PC, et al. Mechanistic toxicity evaluation of uncoated and PEGylated single-walled carbon nanotubes in neuronal PC12 cells. ACS Nano 2011;5:7020-33.

[61] Qian X, Zhou X, Nie S. Surface-enhanced raman nanoparticle beacons based on bioconjugated gold nanocrystals and long range plasmonic coupling. J Am Chem Soc 2008;130:14934-5.

[62] Zhu Z, Zhu T, Liu Z. Raman scattering enhancement contributed from individual gold nanoparticles and interparticle coupling. Nanotechnology 2004;15:3574-664.

[63] Barker EF, Sleator WW. The infrared spectrum of heavy water. J Chem Phys 1935;3:660-3.

[64] Jang NH. The coordination chemistry of DNA nucleosides on gold nanoparticles as a probe

by SERS. Bull Korean Chem Soc 2002;23:1790-800.

[65] Tuma R. Raman spectroscopy of proteins: from peptides to large assemblies. J Raman Spectrosc 2005;36:307-19.

[66] Margueritat J, Gehan H, Grand J, Lévi G, Aubard J, Fe'lidj N, et al. Influence of the number of nanoparticles on the enhancement properties of surface-enhanced raman scattering active area: sensitivity versus repeatability. ACS Nano 2011;5:1630-8.

[67] Yan B, Thubagere A, Premasiri WR, Ziegler LD, Dal Negro L, Reinhard BM. Engineered SERS substrates with multiscale signal enhancement: nanoparticle cluster arrays. ACS Nano 2009;3:1190-202.

[68] Fraire JC, Pe'rez LA, Coronado EA. Cluster size effects in the surface-enhanced Raman scattering response of Ag and Au nanoparticle aggregates: experimental and theoretical insight. J Phys Chem C 2013;117:23090-107.

[69] Shah Neha B, Bischof John C. Blood protein and blood cell interactions with gold nanoparticles: the need for in vivo studies. Bionanomaterials 2013;14:65.

[70] Rivera Gil P, Oberdo₵rster G, Elder A, Puntes V, Parak WJ. Correlating physico-chemical with toxicological properties of nanoparticles: the present and the future. ACS Nano 2010;4:5527-31.

[71] Dreaden EC, Austin LA, Mackey MA, El-Sayed MA. Size matters: gold nanoparticles in targeted cancer drug delivery. Ther Deliv 2012;3:457-78.

[72] Arvizo RR, Bhattacharyya S, Kudgus RA, Giri K, Bhattacharya R, Mukherjee P. Intrinsic therapeutic applications of noble metal nanoparticles: past, present and future. Chem Soc Rev 2012;41:2943-70.

Appendix A: Supplemental Information

Table S1 Summary of characterization of Citrate-capped Au NPs, albumin capped Au NP and their agglomerates.

Agglomerate (number of AuNPs)	LSPR (nm)	d_H, fresh (DLS) (nm)	d_H, 1 mo. (DLS) (nm)	d_H (NTA) (nm)	Zeta Potential (mV)	Designation
AuNP – Citrate	537	50.1 ± 0.7	50.4 ± 0.8	51.3 ± 2.3	-35.2 ± 0.9	Citrate-capped
1	539	53.7 ± 0.4	53.2 ± 0.9	63.0 ± 1.0	-19.5 ± 1.5	Primary
1-3	541	72.6 ± 2.0	76.1 ± 2.1	N/A	-21.2 ± 1.2	
3-5	542	142.3 ± 0.4	144.1 ± 0.6	86.0 ± 13.0	-20.8 ± 1.1	Sm. Agg
5-10	545, 732	165.8 ± 2.9	164.1 ± 2.9	114 ± 5.2	-27.4 ± 1.2	
10-25	545, 780	176.5 ± 3.1	181.2 ± 1.7	177 ± 27.4	-28.3 ± 1.2	Lg. Agg
>25	546, 848	216.8 ± 1.9	212.1 ± 3.3	N/A	-29.9 ± 1.0	
>50	546, 863	227.3 ± 4.8	235.8 ± 5.4	N/A	-28.9 ± 1.5	
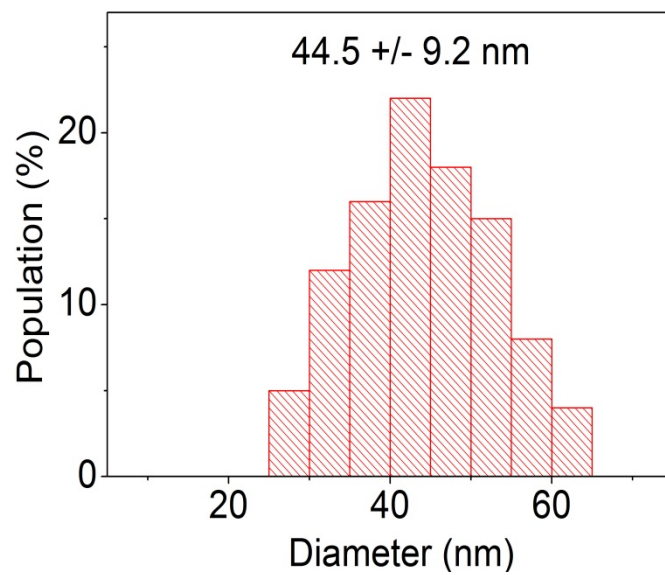
Figure S1. Histogram of particle diameter of citrate-capped AuNPs based on transmission electron microscope measurements of 200 nanoparticles.
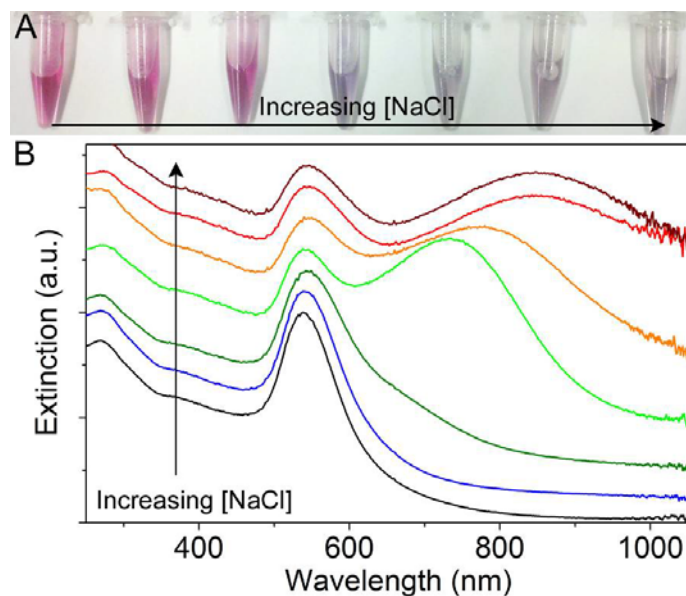
Figure S2. (A) Photograph of isolated AuNPs at various agglomeration states from left to right corresponding to A-F in **Figure S3**. From left to right, agglomerates were generated by addition of 0, 2.5, 5, 7.5, 10, 20, or 50 µL saturated NaCl to 1 mL of citrate-capped gold nanoparticles. (B) UV-Vis spectra of agglomerates in (A). The spectra were normalized to LSPR maximum and offset for clarity.
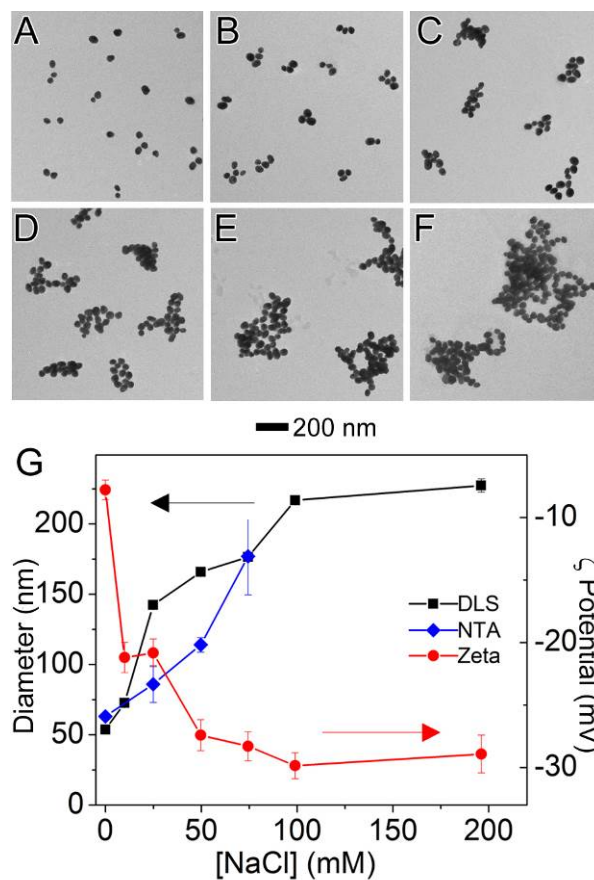
Figure S3. (A-F) TEM characterization of agglomerates shown in **Figure S2**. Agglomerates were generated by addition of 0, 2.5, 5, 7.5, 10, or 20 μL saturated NaCl to 1 mL of citrate-capped gold nanoparticles. The scale bar is 200 nm. (G) Hydrodynamic diameter as measured by dynamic light scattering (black, left axis) and nanoparticle tracking analysis (blue, left axis) and zeta potential (red, right axis) of isolated agglomerates.
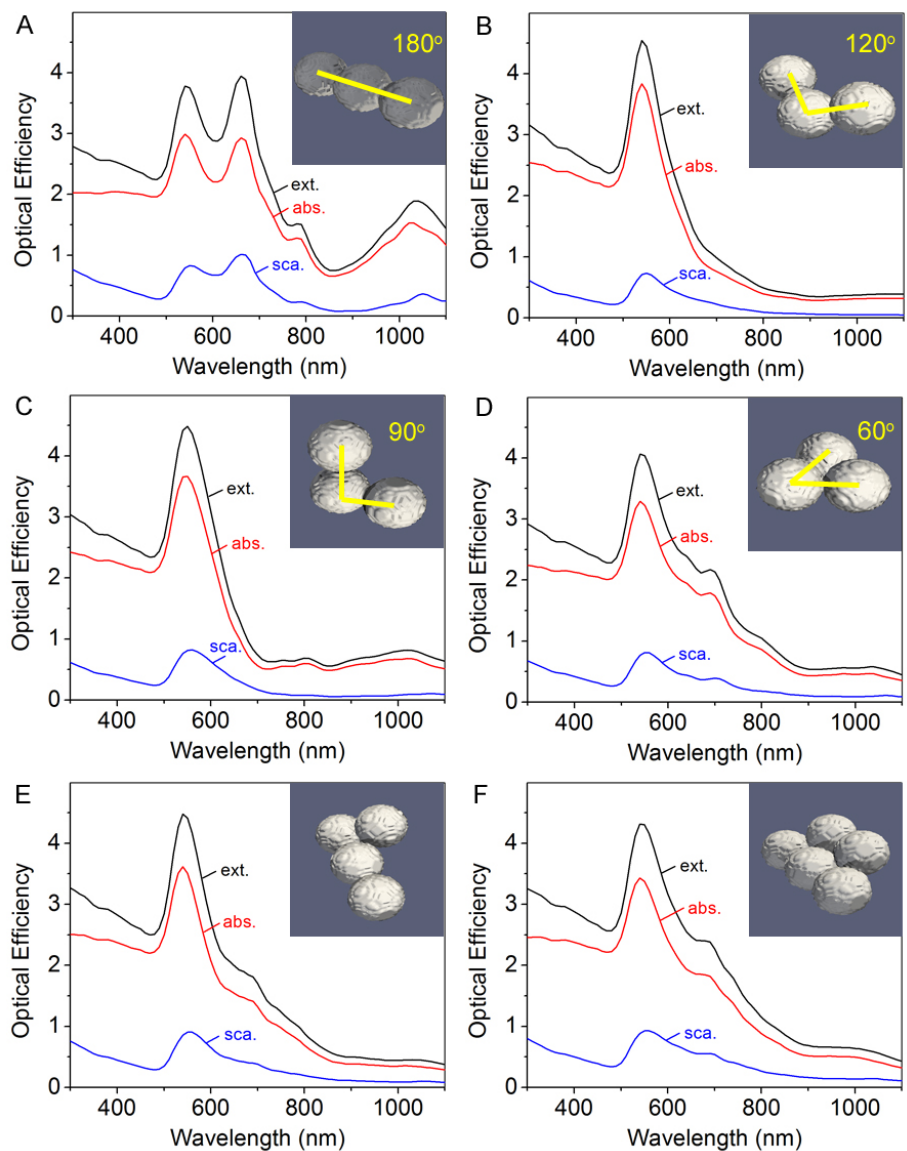
Figure S4. Simulated extinction, absorption, and scattering spectra of small agglomerates of AuNPs in various geometries. The inset shows the corresponding geometry.
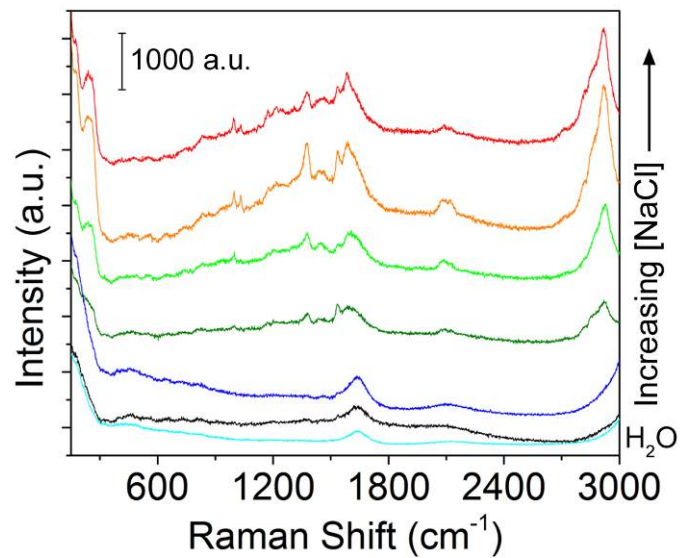
Figure S5. (A) Raman spectra of H$_2$O (cyan) and increasingly agglomerated AuNPs corresponding to **Figure S2**. Agglomerates were generated by addition of 0, 2.5, 5, 7.5, 10, or 20 μL saturated NaCl to 1 mL of citrate-capped gold nanoparticles. Spectra are shifted for clarity but unscaled.

Chapter III. Gold Nanocage-Photosensitizer Conjugates for Dual-Modal Image-Guided Enhanced Photodynamic Therapy[*]

Abstract

We have demonstrated that gold nanocage-photosensitizer conjugates can enable dual image-guided delivery of photosensitizer and significantly improve the efficacy of photodynamic therapy in a murine model. The photosensitizer, 3-devinyl-3-(1'-hexyloxyethyl)pyropheophorbide (HPPH), was noncovalently entrapped in the poly(ethylene glycol) monolayer coated on the surface of gold nanocages. The conjugate is stable in saline solutions, while incubation in protein-rich solutions leads to gradual unloading of the HPPH, which can be monitored optically by fluorescence and photoacoustic imaging. The slow nature of the release in turn results in an increase in accumulation of the drug within implanted tumors due to the passive delivery of gold nanocages. Furthermore, the conjugate is found to generate more therapeutic singlet oxygen and have a lower IC_{50} value than the free drug alone. Thus the conjugate shows significant suppression of tumor growth as compared to the free drug *in vivo*. Short-term study showed neither toxicity nor phenotypical changes in mice at therapeutic dose of the conjugates or even at 100-fold higher than therapeutic dose of gold nanocages.

Introduction

Gold nanostructures are an emerging class of promising multifunctional platforms for cancer theranostics due to their superior optical properties, chemically modifiable surface, and biological inertness.(1-3) They strongly scatter and absorb light at a tunable resonance frequency, known as localized surface plasmon resonance (LSPR). The LSPR enables enhanced contrast for a variety of optical imaging modalities including optical coherent tomography (OCT),(4-7) multi-photon photoluminescence imaging,(8-11) and photoacoustic tomography (PAT).(12-16) Furthermore, they can act directly as therapeutic agents by converting the light into heat for photothermal treatment of diseases.(17-19) When combined with drug molecules, Au nanostructures are widely applicable carriers for delivery of therapeutics to the target region, both passively and actively.(20-22) Drug molecules can be conjugated to the surface of Au nanostructures covalently or non-covalently *via* chemical bonds or intermolecular interactions, respectively. The latter is particularly appealing because the drug molecules remain unmodified, thereby minimizing the potential for alterations in drug efficacy and pharmacokinetics.(23) Hydrophobic interactions are an effective strategy to noncovalently incorporate lipophilic drug molecules within nanoparticle surface coating for drug delivery. Different types of surface coating have been demonstrated for this purpose including amphiphilic molecules(24) and polymers containing non-polar groups (*e.g.* poly(ethylene glycol), PEG).(25-27) Herein, we incorporate a hydrophobic photosensitizer, 2-devinyl-2-(1-hexyloxyethyl)pyropheophorbide (HPPH), into PEG covered on Au nanocages (AuNCs) as a theranostic agent for enhanced photodynamic therapy (PDT).

Photodynamic therapy is a known therapeutic modality that relies on the use of light to excite a photosensitizer molecule which in turn transfers the energy to local O_2 molecules, changing

them from the ground, triplet state to an excited, singlet state ($^1O_2$). The $^1O_2$ molecules are highly sensitive to the environment and have an intracellular lifetime on the order of 3 μs.(28, 29) At the therapeutic dosage, their reaction with biomolecules leads to apoptosis and necrosis of cells.(30) Because of its transient nature, effective generation of $^1O_2$ at the target site is important for the success of PDT. Several methods to improve PDT efficacy have been developed that use nanocarrier-based delivery, including liposomes,(31) polymeric micelles,(32, 33) pure nanocrystal forms,(34) silica nanoparticles,(35, 36) and polymeric nanoparticles.(37, 38) Recently, PEGylated Au nanoparticles have been demonstrated as nanocarriers to efficiently deliver photosensitizers for PDT.(25, 27) The hydrophobic photosensitizers were entrapped inside the PEG monolayer close to the surface of the Au nanoparticles and released rapidly at the tumor site within hours. In this case, the Au nanoparticles were used only as delivery vehicles because their LSPR peak was located in the visible region where light penetration is relatively superficial. By replacing spherical particles with nanorods, the LSPR maximum was shifted to the near-infrared (NIR) region where light penetrates deeper into biological tissue, enabling PDT to be coupled with photothermal therapy (PTT) to enhance the cancer treatment efficacy.(39, 40) More recently, multi-modal imaging has been demonstrated to monitor the delivery and treatment of particle-assemblies loaded with photosensitizers for cancer theranostics.(41) The loading efficiency was double that of nanorods because the hollow nature of the assemblies overcomes the limitation of the surface loading. The size of the particle-assemblies, however, was around 280 nm, which may be unfavorable for *in vivo* delivery.

In this work, we develop AuNC-HPPH conjugates that incorporate the hydrophobic HPPH into the PEG monolayer on the AuNC surface. The size of the AuNC is relatively small with edge length of ~50 nm and hollow interior. The LSPR peak of AuNCs has been tuned to the

NIR region, which enables *in vivo* tracking of the conjugate delivery by both fluorescence (FL) and photoacoustic (PA) imaging modalities. A "see and treat" approach has been established with the dual-modal imaging capability that provides complementary features to guide PDT. The FL imaging monitors the release of HPPH from the AuNC surface by distinguishing the aggregated (quenched) and non-aggregated (fluorescent) states of HPPH. The PA imaging reveals the volumetric distribution of AuNC in the tumor and monitors the therapeutic response of the treatment. More importantly, the efficacy of the PDT has been significantly improved by the presence of AuNCs because of local electromagnetic field enhancement of $^1O_2$ generation and efficient delivery of the drug. Additionally, no observable toxicity of the conjugates at therapeutic dose was found in the short-term study.

Results and Discussion

The multifunctional platform consists of AuNCs coated with a PEG layer (AuNC-PEG) in which HPPH is noncovalently loaded (AuNC-HPPH) (**Fig. 1A**). The AuNCs were synthesized using galvanic replacement between Ag nanocubes and $HAuCl_4$, resulting in a composition of 91% Au and 9% Ag by mass. The average edge length of the AuNCs was 52.6 ± 8.2 nm, and the LSPR maximum was at 801 nm after PEGylation (**Fig. 1B**). The hydrodynamic diameter of the as-prepared AuNC coated with PVP was 91.8 ± 7.1 nm and the zeta potential was -16.7 ± 1.4 mV in 1 mM KCl aqueous solution. PEGylation was accomplished using heterobifunctional PEG with a thiol group at one terminus and an amine at the other ($HS-PEG-NH_3^+$). The $HS-PEG-NH_3$ was anchored to the surface of AuNC through the Au-thiol bond, while the exposed amine formed a cationic surface that can be further functionalized. The hydrodynamic diameter of AuNC-PEG was 98.6 ± 0.9 nm and the zeta potential was positive ($+4.79 \pm 0.23$ mV) in 1 mM KCl aqueous solution, indicating the success of PEGylation. The loading mechanism is based on the

hydrophobic interaction between the porphyrin and the $-CH_2-CH_2-$ group of PEG.(46) After incorporation of HPPH, the LSPR peak was redshifted to 829 nm (**Fig. 1C**) due to the refractive index change of the surface layer.(47) The peaks at 517, 550, 624, and 684 nm, as well as the shoulder at 669 nm, were attributed to absorption by the HPPH molecules, and the slight redshifting can be attributed to a change in electron density as a result of conjugation. The hydrodynamic diameter of the HPPH incorporated AuNC-PEG (AuNC-HPPH) remains unchanged (100 ± 1.1 nm), while the zeta potential of the conjugates became negative (-25.73 ± 1.23 mV) in 1 mM KCl aqueous solution. The discrepancy in the zeta potential before and after loading of HPPH could be due to the influence of the negatively-charged carboxylate group on the HPPH at neutral pH. Quantification of AuNC concentration has been well established in our previous publications.(48, 49) The concentration of AuNCs is estimated from an extinction-concentration curve derived from measurement of the average size and the atomic Au and Ag concentration of AuNCs (Supplementary Material: **Fig. S1**). The final HPPH loading concentration was determined to be approximately 1×10^5 HPPHs per AuNC based on the recovered fluorescence after dissolution of a known amount of AuNCs using KCN (**Fig. 1D** and Supplementary Material: **Fig. S2**).
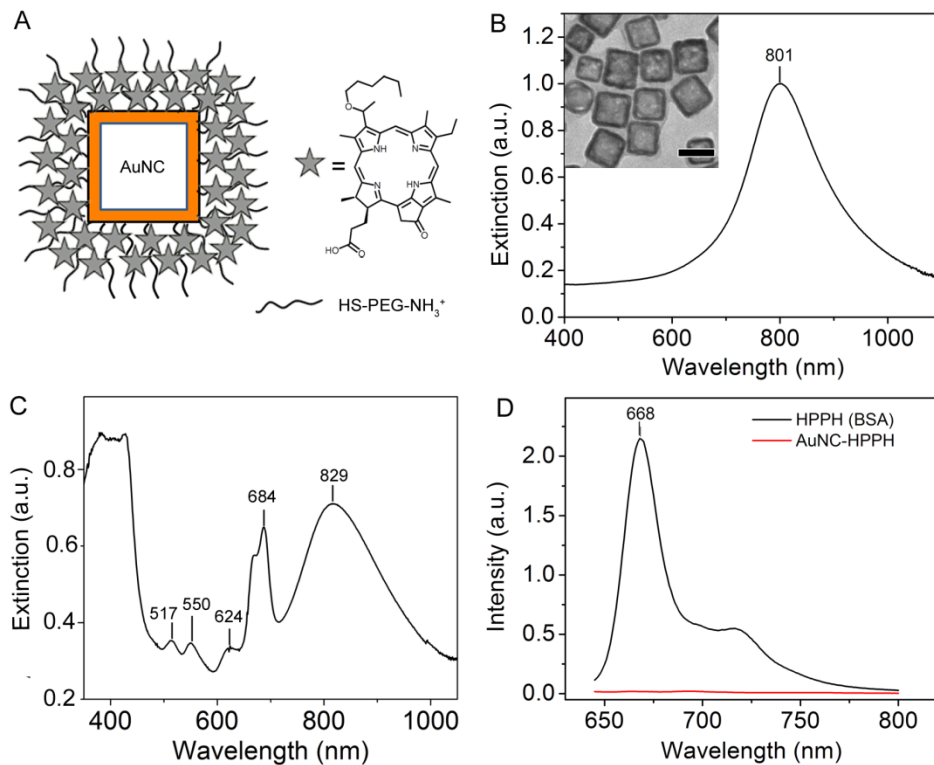
Figure 1. (A) Schematic illustration of AuNC-HPPH conjugate. The UV-Vis-NIR spectra of the AuNCs with an LSPR peak at 801 nm and an edge length of 52.6 ± 8.2 nm before (B) and after (C) loading with HPPH. Inset of (B) shows the TEM image of the AuNCs with a scale bar of 50 nm. (D) Fluorescence spectra of AuNC-HPPH before (red) and after KCN etching (black).

The release of HPPH from the AuNC-HPPH was studied in serum to better understand the conjugate's interaction with blood and interstitial environments. The AuNC-HPPH suspensions were incubated in serum or PBS over 24 h. Fluorescence was gradually recovered in the protein-containing serum (Supplementary Material: **Fig. S3A**) but barely recovered in PBS. The lack of fluorescence in PBS primarily results from HPPH aggregation.(34) For this reason, the release in PBS was also monitored by measuring the absorption spectra of the supernatant at various times (Supplementary Material: **Fig. S3B**). It was found that while over 80% of the drug was unloaded by the serum within 24 h, only 3% of the payload was released in PBS (**Fig. 2A**).

The release profile can also be monitored using PA amplitude since both AuNC and HPPH can function as exogenous PA contrast agents.(13, 50) As the amplitude of PA signal is proportional to the light absorption,(44) extinction spectra were acquired and compared with the change of PA signal during the release. The extinction spectrum of AuNC-HPPH initially included two convoluted peaks at 665 and 685 nm (**Fig. 2B**) which could be attributed to the high local concentration of HPPH,(51) metalation of the pheophorbide ring,(52) metal-HPPH interactions,(53) or a combination thereof. During release, the peak at 685 nm disappeared while the peak at 665 nm was augmented. **Figure 2, C** and **D**, shows the changes of PA signals over the period of 30 h at 665 and 685 nm in serum. As expected, the PA signal at 685 nm decreased as a function of time due to the decrease of light absorption at this wavelength. Surprisingly, the PA signal decreased over time at 665 nm in contrast to the increase of absorbance. This discrepancy is attributed to the fluorescence recovery of HPPH, which offers a competitive relaxation pathway (*i.e.* emission) to the nonradiative decay. At close proximity to AuNC, the fluorescence of HPPH was quenched through energy transfer to the metal surface. As a result, the energy dissipated nonradiatively as heat whose conversion efficiency was linearly

proportional to the amplitude of the PA pressure waves. During the release of HPPH from the metal surface, the recovery of quenched fluorescence led to the reduction of the nonradiative energy decay, and thus the decrease of PA signal. After 30 h, the signal at 685 nm decreased to less than 50%, while the signal at 665 nm leveled off at 60%. The slower decay rate of PA signal at 665 nm was the result of the near-doubling of the light absorption compared to that at 685 nm.
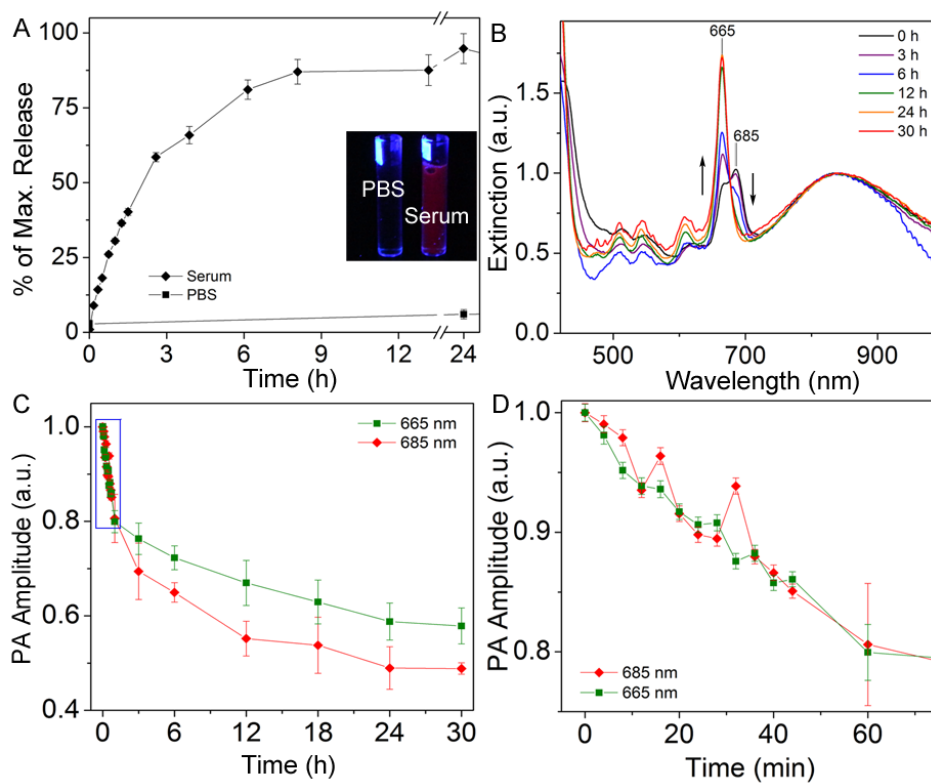
Figure 2. (A). Comparison of 24 h release kinetics of AuNC-HPPH in serum (diamonds) and PBS (squares). Inset depicts photograph of vials containing AuNC-HPPH as PBS (left) and serum (right) under UV light illumination. (B) UV-Vis-NIR spectra of AuNC-HPPH in serum at different time periods, with PA wavelengths marked. Spectra are normalized to the AuNC LSPR peak. (C) plot of normalized PA signal amplitude of AuNC-HPPH in serum as a function of time at λ = 665 nm (green square) and 685 nm (red diamond). (D) Blow-up view of the box region in (C).

Photodynamic therapy relies on photoexcited molecules to generate reactive oxygen species, mainly $^1O_2$, for destruction of malignant cells. To investigate the potential efficacy of AuNC-HPPH for PDT, SOSG was used to qualitatively measure the $^1O_2$ generation.[54] Interestingly, 73% enhancement of $^1O_2$ signal was observed for the AuNC-HPPH conjugates as compared to the same amount of free HPPH upon light irradiation at 665 nm with a fluence of 15 J/cm^2 (**Fig. 3A**). As control experiments (Supplementary Material: **Fig. S4A**), SOSG in absence of drugs shows no change in the fluorescence signal following irradiation, confirming that the sensor alone does not directly respond to the light. On the other hand, the $^1O_2$ generation from AuNC alone is negligible upon light irradiation at the 1 pM concentration. The results implied that the HPPH in proximity to AuNCs could enhance the probability of $^1O_2$ generation upon irradiation as compared to free HPPH. This enhancement is possibly due to the overlap between the LSPR of AuNCs (~800 nm) and the phosphorescence emission of HPPH (750-800 nm).[55, 56] Replacing the aqueous solution with MeOH, the enhancement fell to 26% as compared to free HPPH (Supplementary Material: **Fig. S4B**). The decrease of $^1O_2$ signal is attributed to the near-complete release of HPPH from the AuNC-HPPH conjugate in methanol. Interestingly, the $^1O_2$ signal of AuNC-HPPH and a combination of AuNC and HPPH was nearly identical; suggesting that the prescence of the AuNCs in the tumor would continue to enhance $^1O_2$ generation after HPPH is released.

The efficacy of PDT was evaluated *in vitro* using Colon-26 cell line. The cells were incubated with the free drug and the AuNC-HPPH at equimolar HPPH concentrations. After 24 h incubation, the cells were irradiated with 665 nm light at a fluence of 0.25 J/cm^2, followed by incubation for another 48 h. Cell viability was then assessed by MTT assay. **Figure 3B** shows the plot of cell viability as a function of HPPH concentration under different conditions. The

dose response curves were fitted by the method of least squares. The estimated IC_{50} concentrations were 57 and 27 nM for HPPH and AuNC-HPPH, respectively ($p < 0.05$). The relatively-high potency of the AuNC-HPPH could be the result of the increased $^1O_2$ generation and/or the increased uptake of the AuNC-HPPH by the tumor cells as compared to the free HPPH.
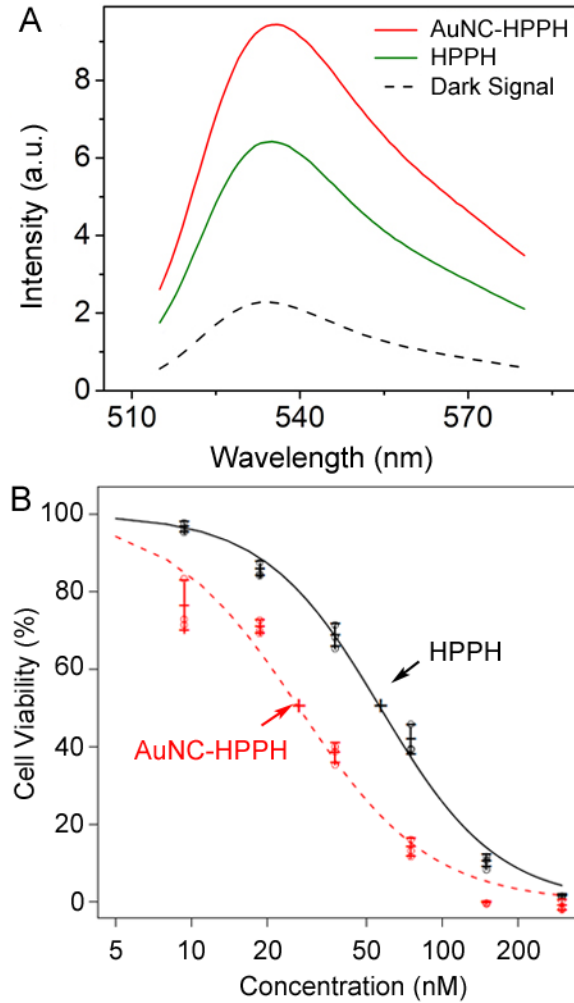
Figure 3. (A) Fluorescence spectra of SOSG in PBS/D_2O after different treatments: in the dark as a control (black dashes), and after light irradiation at 665 nm with a dose of 15 J/cm^2 and treatment with AuNC-HPPH (red) or HPPH (green). (B) Plot of cell viability as a function of concentration after treatment with free HPPH (black) and AuNC-HPPH (red), followed by light irradiation at a fluence of 0.25 J/cm^2. The dose response curves were fitted using the method of least squares ($p < 0.05$).

The delivery of HPPH to the tumor was further monitored by fluorescence imaging *in vivo* using a Colon-26 tumor-bearing mouse model. Two groups of Colon-26 tumor-bearing BALB/c mice (3 mice per group) were intravenously administered with free HPPH and AuNC-HPPH using equal HPPH amounts (0.3 µmol/kg). The fluorescence intensity of the tumor region was monitored up to 48 h post-injection. **Figure 4, A-F** and **G-L** show the fluorescence images of representative mice injected by AuNC-HPPH and HPPH, respectively. In either case, the fluorescence at the tumor region increased with time and reached a peak at 24 h post-injection. The strong fluorescence signal was mainly localized at the tumor region for the AuNC-HPPH treated mouse whereas the fluorescence intensity was relatively weak at the tumor site and elevated in other organs for the HPPH treated mouse. The fluorescence intensity of the tumor region was further plotted as a function of post-injection time for the two groups (**Fig. 4M**). A linear model is fitted to the fluorescence data, resulting in $p < 0.05$ for all time points. At 2 h post-injection, the fluorescence intensity for the HPPH was higher than that for the AuNC-HPPH. This discrepancy could be attributed to two factors: different accumulation rates for small molecules and nanoparticles and/or fluorescence quenching of HPPH at close proximity to the AuNC surface. At 8 h post-injection, the fluorescence intensity for the HPPH was significantly lower than that of the AuNC-HPPH, suggesting that the HPPH gradually released from the conjugates in agreement with the release profile in serum discussed earlier. At the same time, the AuNC-HPPH was accumulated more efficiently within the tumor as compared to the HPPH alone due to the enhanced permeability and retention (EPR) effect.(57)
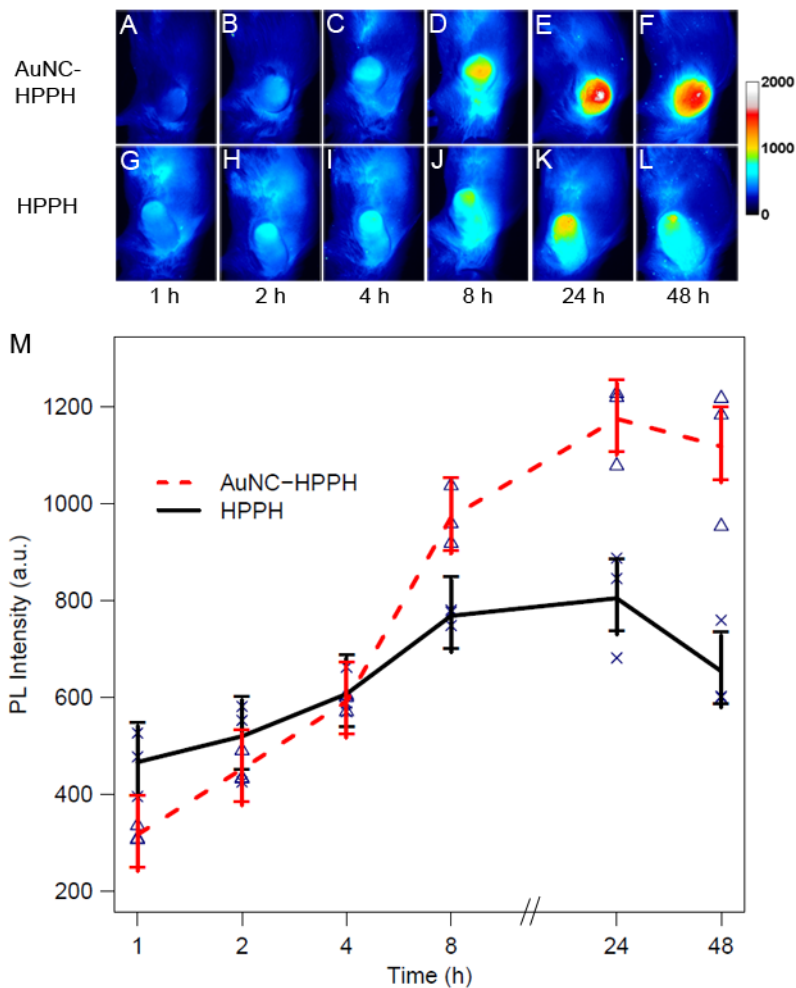
Figure 4. *In vivo* whole-body fluorescence images of Colon-26 tumor-bearing mice acquired after intravenous injection of 0.3 μmol/kg of HPPH as AuNC-HPPH (A-F) and HPPH (G-L). (M) Plot of fluorescence intensity of the tumor region as a function of time for two groups of mice (3 mice per group) intravenously administered with AuNC-HPPH (red) and HPPH (black). The mean values and the standard errors were obtained by fitting the raw data using a linear model ($p < 0.05$). The measurements at each time point were labeled for AuNC-HPPH (triangles) and HPPH (crosses).

The PDT efficacy was evaluated *in vivo* using Colon-26 tumor-bearing mouse model. Two groups of tumor-bearing mice (5 mice per group) were intravenously injected with HPPH (0.3 µmol/kg) as free HPPH or AuNC-HPPH. As a control group, 5 mice were intravenously injected with PBS. Guided by FL imaging, the mice were treated with 665-nm laser irradiation for 30 min with a total light dose of 135 J/cm^2 at 24 h post-injection when the accumulation of the conjugates reached the peak. After the PDT treatment, tumor growth was monitored by measuring the tumor size for up to 60 days. The mice were euthanized when the tumor grew to 400 mm3. **Figure 5** shows the Kaplan-Meier plot (percent survival versus time) that compares the *in vivo* PDT efficacies of three groups treated with different conditions. Of the mice treated with free HPPH, only 1 of the 5 mice remained alive with tumor size < 400 mm^3 (20% survival) at 60 days post-treatment. Of the mice treated with AuNC-HPPH, 3 of 5 mice survived with tumor size remained < 400 mm^3 (60% survival) at 60 days post-treatment. In contrast, no mouse in the control group with PBS injection survived beyond 15 days post-treatment. These results suggest that the survival rate of the AuNC-HPPH treated mice is higher than the HPPH-treated mice under the same irradiation condition, indicating the higher potency of AuNC-HPPH as compared to the equal amount of free HPPH.
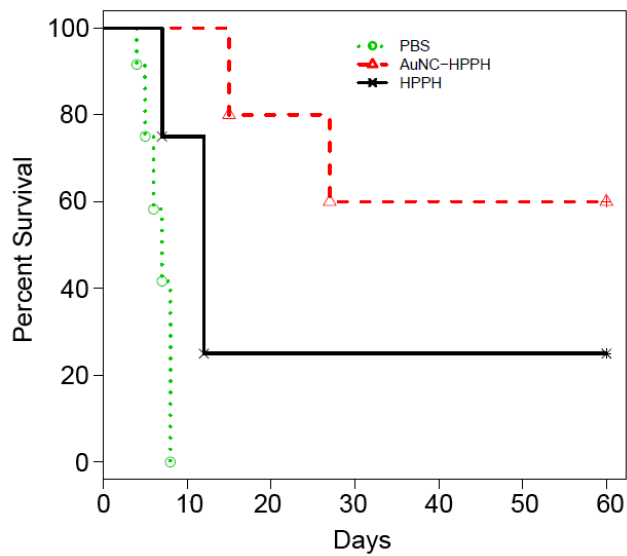
Figure 5. Kaplan-Meier plot of percent survival of Colon-26 tumor-bearing mice after intravenous injection of PBS (green), HPPH (0.3 μmol HPPH/kg, black), and AuNC-HPPH (0.3 μmol HPPH/kg, red), followed by light irradiation with a fluence of 135 J/cm^2.

The high potency of the AuNC-HPPH formulation could be attributed to the increased accumulation of HPPH to the tumor region through the EPR effect of the nanocarriers, as well as the enhanced $^1O_2$ generation in the presence of AuNC. Due to the high HPPH loading per AuNC (1×10^5 HPPHs per AuNC), the AuNC dose is on the order of 30 pM which is nearly three orders of magnitude lower than that of PTT (10 nM).[58] Under PDT conditions (75 mW/cm2 for 30 min), the temperature rise of ~0.1 nM AuNC-HPPH was negligible (Supplementary Material: **Fig. S5A**). In this case, the photothermal effect on the PDT efficacy could be ruled out. Additionally, the entrapped HPPH has essentially no influence on the photothermal capability of the AuNCs (Supplementary Material: **Fig. S5B**). Potentially, the PDT and PTT can be combined to further improve the survival rate of cancer.

Photoacoustic imaging was used to further assess the PDT efficacy *in vivo*. This method was demonstrated on a tumor-bearing BALB/c mouse which was imaged before and after intratumoral injection of AuNC-HPPH, followed by PDT treatment. **Figure 6, A-E**, shows photographs of the tumor taken before and over nine days following PDT post injection of AuNC-HPPH. Prior to intratumoral injection of AuNC-HPPH, a control PA image was acquired at an optical wavelength of 829 nm (**Fig. 6F**). The tumor boundary and tumor-feeding vasculature were clearly visualized. After injection of AuNC-HPPH, the distribution of AuNC-HPPH within the tumor was clearly mapped (**Fig. 6G**) and served as background signal of AuNCs. After PDT, a series of PA images were obtained at 3, 7 and 9 days post-treatment (**Fig. 6, H-J**). The PA amplitude increased significantly after PDT treatment, suggesting that the contrast mainly resulted from the necrotic effect due to the draining of AuNCs from the tumor region over a long period of time. Thus, mapping of the PA signal provides information about the necrotic region after PDT treatment. At 7 days post-treatment, the PA signal amplitude

further increased in the tumor necrotic region whose boundary matched well with the corresponding photograph. **Figure 6, K-O**, shows the respective depth-sensitive cross-sectional PA B-scan images of **Figure 6, F-J**. The imaging depth information of **Fig 6, K-O**, was further mapped using pseudo color as shown in **Figure 6, P-T**, respectively. The bottom of the tumor necrotic regions was around 3-4 mm from the skin surface.
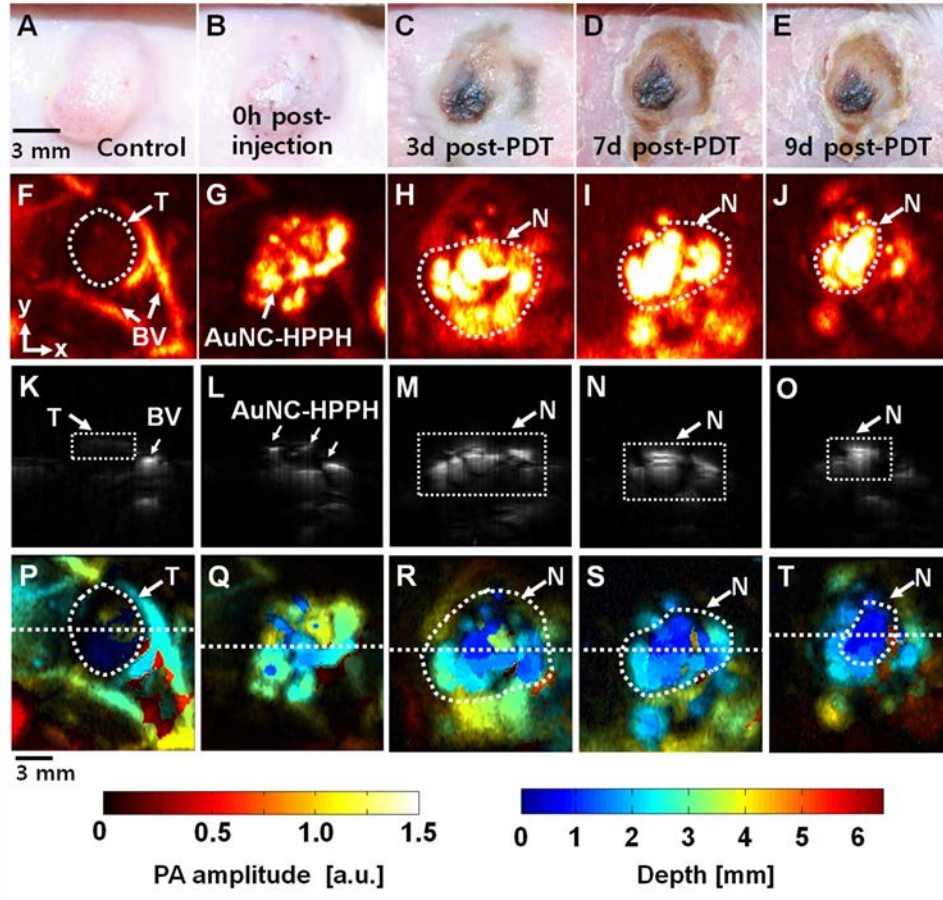
Figure 6. (A-E) Photograph of the tumor taken before and after PDT with an injection of AuNC-HPPH at various time points up to 9 days. PA images acquired (F) before intratumoral injection of AuNC-HPPH, (G) after injection, and (H-J) 3, 7, and 9 days post-treatment. (K-O) Depth-resolved PA B-scan images cut along the dotted lines in (F-J), respectively. (P-T) Depth-encoded PA images of (F-J), respectively. BV, blood vessels; T. Tumor boundary; and N, tumor necrotic region.

In order to translate the conjugate to clinic, the biocompatibility of AuNCs is important from a clinical perspective. The biosafety of AuNCs has yet to be understood or well studied in animals, although several studies have been performed on therapeutic Au-based nanoparticles such as spherical particles,(59) $SiO_2@Au$ core-shell particles,(60) and nanorods.(61) In this study, we investigate the biodistribution and short-term toxicity of AuNC-PEG at therapeutic or higher dose. AuNC is an excellent exogenous contrast agent for PA imaging with a detection limit of 4.5 pM (or ~9 × 10^{-21} mol of AuNCs per imaging voxel). We have demonstrated the use of PA to quantify the accumulation of AuNC-PEGs *ex vivo* 24 h post-injection.(13) Three groups of BALB/c mice (n = 3 per group) were intravenously injected with a dose of 100 μL AuNCs with three different concentrations, 10, 30, and 100 nM (1, 3, and 10 pmol). For comparison, the corresponding organs from untreated mice were used as controls. **Figure 7A** shows the photograph of the four excised spleens with injections of 0, 1, 3, and 10 pmol of AuNCs, and their corresponding PA images (**Fig. 7B**). The PA signal of the spleen increases with the injection dose. The PA amplitude of the spleen collected from the mouse after injection of AuNC at a dose of 10 pmol was ~740 % stronger than that from a non-treated mouse. The PA amplitude from the different organs was plotted in **Figure 7C**. The PA signal intensity is dose-dependent, and the change of signal was low at the therapeutic dose (1 pmol) as compared to the control. The AuNC-PEG mainly accumulated in the liver and spleen, which agrees well with previous data.(62)
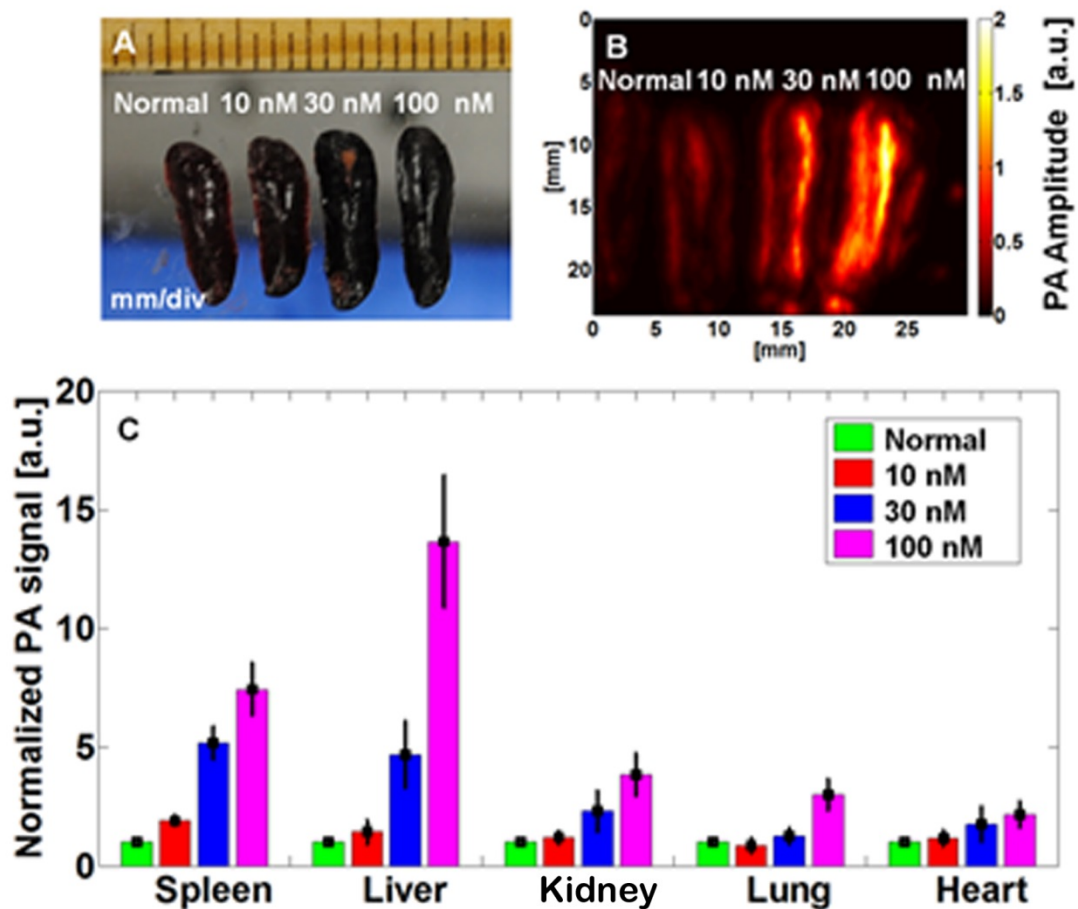
Figure 7. Biodistribution study of mice that were intravenously injected with 100 μL of AuNC-PEGs at different concentrations for 24 h. (A) Photographs of excised spleens, (B) *ex vivo* PA images of excised spleens acquired at 700 nm, and (C) biodistribution of AuNCs in different excised organs.

The short-term toxicity was also performed for both the therapeutic dose of AuNC-HPPH and high dose of AuNC-PEG. In this study, mice were monitored for 28 days after injection of therapeutic dose of AuNC-HPPH (0.3 µmol/kg HPPH) and three different doses of AuNC-PEG (1, 3, and 10 pmol) to examine any phenotypical changes. During the course of the experiment, neither weight loss nor abnormal behavior was observed in any of the mice. After 28 day post-treatment, histological analysis was performed on five organs including spleen, liver, kidney, lung, and heart (**Fig. 8**). No tissue toxicity or visible differences were found with therapeutic dose of AuNC-HPPH compared to the control mice without treatment. Similar result was found in 7 day post-treatment without any observable difference (Supplementary Material: **Fig. S6**). When the dose of AuNC-PEG (10 pmol) was increased to ~100 times of the therapeutic dose (~0.1 pmol), scattered macrophages with multiple dark granules in the cytoplasm were found, indicating the presence of AuNCs in the spleen of the mice. Macrophages are known sites for nanoparticle accumulation and actively take up various nanoparticles.(63) Similar uptake by the macrophages was observed in the liver, however, no dark granules were found in the Kupffer cells in the same mouse. No dark granules were found in the kidney, lung, and heart of the mouse at the dose of 10 pmol. These results suggest that there was no observable toxicity at the therapeutic dose of AuNC-HPPH or even at 100-fold higher than therapeutic dose of AuNC-PEG in the 28-day study.
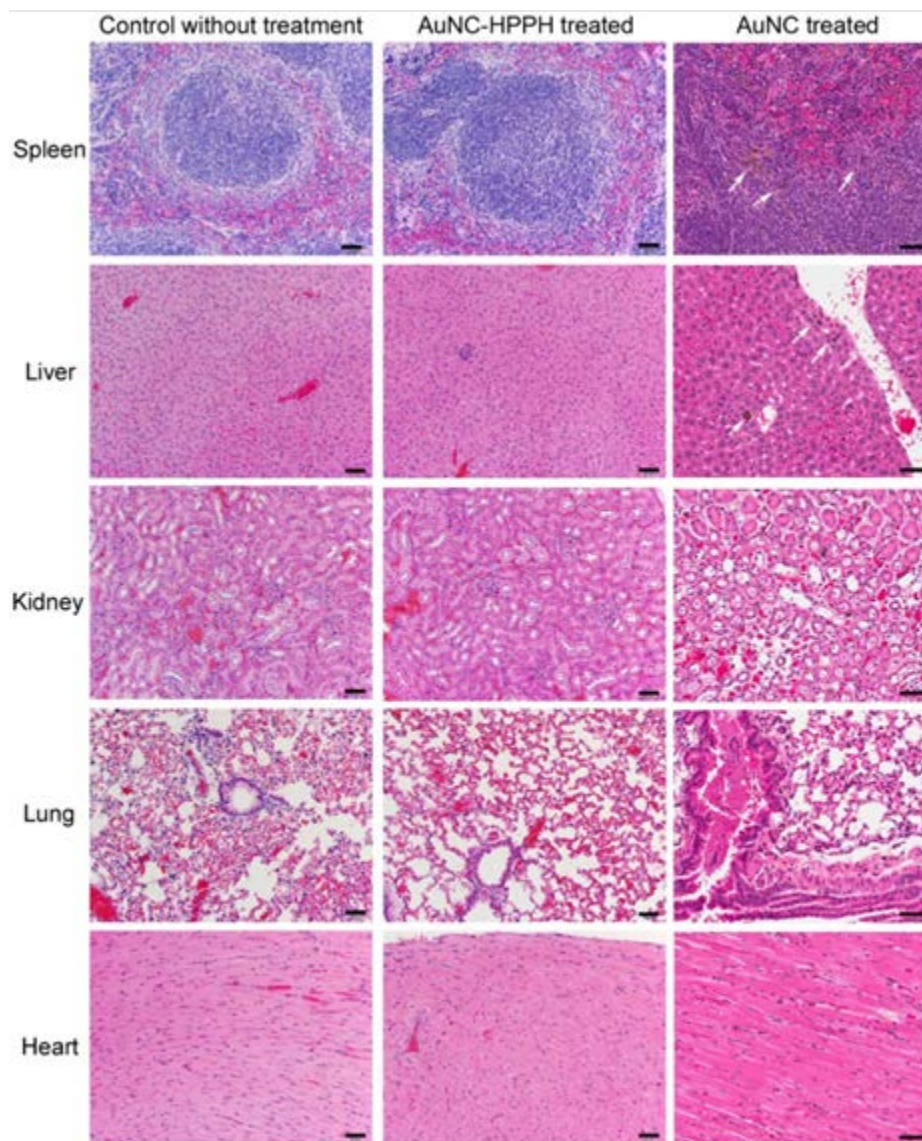
Figure 8. Photographs of representative H&E staining tissue sections of mice after 28 days of different treated conditions: Control mouse without treatment (left column), AuNC-HPPH treated at 0.3 µmol/kg of HPPH (middle column), and AuNC treated at a dose of 10 pmol (right column). The scale bars are 50 µm

Conclusions

We have demonstrated AuNC-HPPH conjugates as a multifunctional agent for enhanced PDT. HPPH entrapped within a PEG layer can be delivered more effectively to the tumor as compared to free HPPH. The presence of the AuNCs enhances the $^1O_2$ generation and the phototoxicity of the HPPH *in vitro*. The growth of the tumor *in vivo* was suppressed possibly due to the combination of the effective delivery and the enhanced phototoxicity of the AuNC-HPPH conjugates. In addition, the FL and PA imaging were demonstrated as an informative tool to monitor the progression of delivery and tumor treatment following PDT. A short-term study showed a relatively-low toxicity of the therapeutic-dose conjugates and high-dose AuNCs. This AuNC-HPPH system could potentially be translated from bench-top research to preclinical and clinical trials.

Materials and Methods

Synthesis and PEGylation of AuNCs: The AuNCs were synthesized by a two-step process using Ag cubes as a sacrificial template in the galvanic replacement reaction.(42) The LSPR peak of the AuNCs was tuned to 798 nm as monitored using a UV-Vis-NIR spectrometer (Agilent HP8453). The size of the AuNCs was estimated by TEM analysis (JEOL 100cx). The

composition of the AuNCs was measured by atomic absorption spectrometer (GBC 932). The $^{+}$ $^{+,}$

surface of the AuNCs was then derivatized with amine-terminated PEG thiol (HS-PEG-NH$_3$

M.W. = 5,000, JenKem). Briefly, 4 mg HS-PEG-NH$_3$ was dissolved in 4 mL water in a 20

mL vial. The solution was placed in an ice bath with stirring for 5 min. To this solution, 8

mL of 1 nM AuNC suspension was added dropwise over 5 min. The vial was flushed with argon

for 10 min and allowed to stir overnight in the dark. After conjugation, the excess PEG was

removed by washing the PEGylated AuNCs (AuNC-PEG) with water 3 times. The AuNC-PEG

were redispersed in phosphate buffered saline (PBS) at a concentration of ~3 nM. The

hydrodynamic diameter and zeta potential were determined using dynamic light scattering

instrument (Brookhaven ZetaPALS).

Entrapment of photosensitizers to AuNC-PEGs: The photosensitizer, 3-devinyl-3-(1'-

hexyloxyethyl) pyropheophorbide (HPPH) which was prepared in Dr. Pandey's laboratory,(43)

was used in this study. The HPPH (7 mg, 11 μmol) was dissolved in 2.5 mL DMSO at a

concentration of 4.5 mM as a stock solution. This stock solution (0.25 mL) was diluted in 4 mL

of PBS to a concentration of ~0.3 mM. The diluted HPPH solution was flushed with Ar for 5 min

and allowed to mix for an additional 5 min. The AuNC-PEG solution (3 nM, 2 mL) was added

dropwise to the HPPH solution, and the reaction was allowed to stir overnight under the

protection of argon in the dark. The product, containing noncovalently-incorporated HPPH on

AuNC-PEG (AuNC-HPPH), was then washed with PBS three times and redispersed in PBS at a

concentration of 6 nM with a loading efficiency of ~1 × 10^5 HPPHs per AuNC.

The release of HPPH was monitored by fluorescence (Horiba FluoroLog3), optical absorbance,

and PA amplitude in serum. The PA measurement was performed using a home-made PA

imaging system.(44, 45) Briefly, a tunable OPO laser (Surelite OPO PLUS, Continuum)

pumped by a Q-switched Nd:YAG laser (SLII-10, Continuum) produced laser pulses with 5 ns pulse widths at a rate of 10 Hz. The illumination was focused on a Tygon tube filled with an aqueous suspension of AuNC-HPPH conjugates with serum. The resultant PA waves were detected by a 5 MHz ultrasound transducer (V308, Panametrics-NDT). For each data point, the PA signals were averaged from 10 B-scan images of the same solution at multiple positions at wavelengths of 665 and 685 nm.

Measurement of singlet oxygen generation: The production of $^1O_2$ was monitored with singlet oxygen sensor green® (SOSG, Invitrogen). Measurements were carried out in D_2O (Cambridge Isotope Laboratories) to increase $^1O_2$ lifetime. Briefly, SOSG was dissolved in MeOH at a concentration of ~5 mM as a stock solution and then diluted in 2 mL of PBS in D_2O to give a final concentration of ~10 µM. Equimolar HPPH as free HPPH or AuNC-HPPH was added to the SOSG solution. Each sample was irradiated for 20 min by a Xenon lamp (Newport) with a 650-680 nm filter and a fluence of 15 J/cm^2. After irradiation, AuNCs were digested by addition of 10 µL of 0.5 M KCN for 10 min to advoid interference. Fluorescence spectra of SOSG were acquired using $\lambda_{ex} = 488$ nm.

Cell line and animal model: The Colon-26 cell line was cultured in RPMI medium (Invitrogen) supplemented with 10% fetal bovine serum (FBS, Hyclone) at 37 °C with 5% CO_2. BALB/c mice, aged 6-8 weeks, were obtained from the National Cancer Institute (NCI). The Colon-26 tumor model was generated by subcutaneous injection of ~1 × 10^6 Colon-26 cells in 100 µL PBS into the right rear flank. Animals used in the studies had a tumor volume of 50-60 mm^3 (typically 5-7 days after inoculation). All animal experiments were conducted in compliance with the guidelines for the care and use of research animals established by the Animal Studies Committee of Roswell Park Cancer Institute or the State University of New York

at Buffalo.

Evaluation of PDT efficacy in vitro: The Colon-26 cells were reseeded in 96-well plates at a density of 3×10^3 cells/well. After overnight incubation, equimolar HPPH as free HPPH or AuNC-HPPH were added to the wells and incubated at 37 °C with 5% CO_2 for 24 h in the dark. Before PDT treatment, the medium was replaced with fresh drug-free medium. The cells were then illuminated by the argon-pumped dye laser at a wavelength of 665 nm and a fluence of 0.25 J/cm^2. After PDT treatment, the cells were incubated for another 48 h at 37 °C with 5% CO_2 in the dark. The cell viability was assessed by 3-[4, 5-dimethylthiazol-2-yl]-2,5-diphenyltetrazoliumbromide (MTT) assay. Briefly, 10 µL of 4 mg/mL MTT in PBS was added to each well and incubated for 4 h. After incubation, the solution was completely removed, and then 100 µL DMSO was added to dissolve the formazan crystals in each well. The absorbance at 570 nm was read using a microplate reader (BioTek ELx800). Each experiment was performed with three replicates.

Fluorescence imaging in vivo: Six tumor-bearing mice (~ 20 g) were randomly divided into two groups (n = 3). The mice were anesthetized by inhalation of isoflurane (2% in 100% oxygen). The mice in Groups **1** and **2** were injected intravenously with 0.3 µmol/kg HPPH as free HPPH and AuNC-HPPH, respectively. Prior to fluorescence imaging, the hair at the tumor region was depilated using a hair-removal lotion. The mice were imaged using a Nuance optical imaging system (Cambridge Research) with excitation wavelength at 665 nm. Fluorescence images were acquired using a 700 nm long pass filter. The fluorescence intensity of the region of interest (ROI) encompassing the tumor was analyzed for each image using the Image J (NIH) software.

Evaluation of PDT efficacy in vivo: Fourteen tumor-bearing mice (~ 20 g) were randomly divided into three groups. The mice in Groups **3** (n = 4) and **4** (n = 5) were intravenously injected

with 0.3 µmol/kg HPPH as AuNC-HPPH and free HPPH, respectively. The mice in Group **5** (n = 5) were administered with 100 µL of PBS as a control. At 24 h post-injection, each mouse was positioned in a specially-designed mouse holder and exposed to laser irradiation at a wavelength of 665 nm with a fluence of 135 J/cm^2 at a rate of 75 mW/cm2 under the non-anesthetic condition. After irradiation, the tumor regrowth of each mouse was monitored. Mice were monitored up to 60 days post-treatment and euthanized once the tumor volume reached 400 mm3. The results were plotted as Kaplan-Meier curve using Graphpad Prism software.

PA monitoring of PDT in vivo: The *in vivo* PA experiments were carried out using the same system as described previously for monitoring the release kinetics. To enhance the spatial resolution, a 10-MHz-single-element ultrasound transducer was used with the resolutions of 125 µm and 140 µm in the axial and transverse directions, respectively. Each volumetric image with a field of view (FOV) of 1.4×1.4 cm^2 took ~25 min with a fluence of 1 mJ/cm^2. The mice were initially anesthetized by intraperitoneal injection of a mixture of ketamine (85 mg/kg) of body with hematoxylin and eosin (H&E) for histology studies.

References

1. Dreaden EC, Alkilany AM, Huang X, Murphy CJ, El-Sayed MA. The golden age: gold nanoparticles for biomedicine. Chem Soc Rev. 2012;41:2740-79.

2. Bardhan R, Lal S, Joshi A, Halas NJ. Theranostic Nanoshells: From Probe Design to Imaging and Treatment of Cancer. Acc Chem Res. 2011;44:936-46.

3. Xia Y, Li W, Cobley CM, Chen J, Xia X, Zhang Q, et al. Gold Nanocages: From Synthesis to Theranostic Applications. Acc Chem Res. 2011;44:914-24.

4. Loo C, Lin A, Hirsch L, Lee M-H, Barton J, Halas N, et al. Nanoshell-Enabled Photonics-Based Imaging and Therapy of Cancer. Tech Cancer Res & Treatment. 2004;3:33-40.

5. Chen J, Saeki F, Wiley BJ, Cang H, Cobb MJ, Li Z-Y, et al. Gold Nanocages: Bioconjugation and Their Potential Use as Optical Imaging Contrast Agents. Nano Lett. 2005;5:473-7.

6. Cang H, Sun T, Li Z-Y, Chen J, Wiley BJ, Xia Y, et al. Gold Nanocages as Contrast

Agents for Spectroscopic Optical Coherence Tomography. Opt Lett.2005;30:3048-50.

7. Oldenburg AL, Hansen MN, Ralston TS, Wei A, Boppart SA. Imaging Gold Nanorods in Excised Human Breast Carcinoma by Spectroscopic Optical Coherence Tomography. J Mater Chem. 2009;19:6407-11.

8. Park J, Estrada A, Sharp K, Sang K, Schwartz JA, Smith DK, et al. Two-Photon-Induced Photoluminescence Imaging of Tumors using Near-Infrared Excited Gold Nanoshells. Opt Express. 2008;16:1590-9.

9. Au L, Zhang Q, Cobley CM, Gidding M, Schwartz AG, Chen J, et al. Quantifying the Cellular Uptake of Antibody-Conjugated Au Nanocages by Two-Photon Microscopy and Inductively Coupled Plasma Mass Spectrometry. ACS Nano. 2009;4:35-42.

10. Tong L, Cobley CM, Chen J, Xia Y, Cheng J-X. Bright Three-Photon Luminescence from Gold/Silver Alloyed Nanostructures for Bioimaging with Negligible Photothermal Toxicity. Angew Chem Int Ed. 2010;49:3485-8.

11. Gao L, Fei J, Zhao J, Li H, Cui Y, Li J. Hypocrellin-Loaded Gold Nanocages with High Two-Photon Efficiency for Photothermal/Photodynamic Cancer Therapy in Vitro. ACS Nano. 2012;6:8030-40.

12. Kim C, Favazza C, Wang LV. In Vivo Photoacoustic Tomography of Chemicals: High-Resolution Functional and Molecular Optical Imaging at New Depths. Chem Rev. 2010;110:2756-82.

13. Kim C, Cho EC, Chen J, Song KH, Au L, Favazza C, et al. In Vivo Molecular Photoacoustic Tomography of Melanomas Targeted by Bioconjugated Gold Nanocages. ACS Nano. 2010;4:4559-64.

14. Akers WJ, Kim C, Berezin M, Guo K, Fuhrhop R, Lanza GM, et al. Noninvasive Photoacoustic and Fluorescence Sentinel Lymph Node Identification using Dye-Loaded Perfluorocarbon Nanoparticles. ACS Nano. 2010;5(1):173-82.

15. Lozano N, Al-Jamal WT, Taruttis A, Beziere N, Burton NC, Van den Bossche J, et al. Liposome–Gold Nanorod Hybrids for High-Resolution Visualization Deep in Tissues. J Am Chem Soc. 2012;134:13256-8.

16. Kim C, Song H-M, Cai X, Yao J, Wei A, Wang LV. In vivo photoacoustic mapping of lymphatic systems with plasmon-resonant nanostars. J Mater Chem. 2011;21:2841-4.

17. Hirsch LR, Stafford RJ, Bankson JA, Sershen SR, Rivera B, Price RE, et al. Nanoshell-mediated near-infrared thermal therapy of tumors under magnetic resonance guidance. Proc Nat Acad Sci. 2003;100:13549-54.

18. Huang X, El-Sayed IH, Qian W, El-Sayed MA. Cancer Cell Imaging and Photothermal Therapy in the Near-Infrared Region by Using Gold Nanorods. J Am Chem Soc. 2006;128(6):2115-20.

19. Chen J, Wang D, Xi J, Au L, Siekkinen A, Warsen A, et al. Immuno Gold Nanocages with Tailored Optical Properties for Targeted Photothermal Destruction of Cancer Cells. Nano Lett. 2007;7:1318-22.

20. Peer D, Karp JM, Hong S, Farokhzad OC, Margalit R, Langer R. Nanocarriers as an Emerging Platform for Cancer Therapy. Nat Nanotech. 2007;2:751-60.

21. Ghosh P, Han G, De M, Kim CK, Rotello VM. Gold nanoparticles in delivery applications. Adv Drug Delivery Rev. 2008;60:1307-15.

22. Rana S, Bajaj A, Mout R, Rotello VM. Monolayer Coated Gold Nanoparticles for Delivery Applications. Adv Drug Del Rev. 2012;64:200-16.

23. Knop K, Hoogenboom R, Fischer D, Schubert US. Poly(ethylene glycol) in Drug Delivery: Pros and Cons as Well as Potential Alternatives. Angew Chem Int Ed. 2010;49:6288-308.

24. Kim CK, Ghosh P, Pagliuca C, Zhu Z-J, Menichetti S, Rotello VM. Entrapment of Hydrophobic Drugs in Nanoparticle Monolayers with Efficient Release into Cancer Cells. J Am Chem Soc. 2009;131:1360-1.

25. Cheng YC. Samia A, Meyers JD, Panagopoulos I, Fei B, Burda C. Highly Efficient Drug Delivery with Gold Nanoparticle Vectors for in Vivo Photodynamic Therapy of Cancer. J Am Chem Soc. 2008;130:10643-7.

26. Cheng Y, Samia AC, Li J, Kenney ME, Resnick A, Burda C. Delivery and Efficacy of a Cancer Drug as a Function of the Bond to the Gold Nanoparticle Surface. Langmuir. 2009;26:2248-55.

27. Cheng Y, Meyers JD, Broome A-M, Kenney ME, Basilion JP, Burda C. Deep Penetration of a PDT Drug into Tumors by Noncovalent Drug-Gold Nanoparticle Conjugates. J Am Chem Soc. 2011;133:2583-91.

28. Kuimova MK, Yahioglu G, Ogilby PR. Singlet Oxygen in a Cell: Spatially Dependent Lifetimes and Quenching Rate Constants. J Am Chem Soc. 2008;131:332-40.

29. Egorov SY, Kamalov VF, Koroteev NI, Krasnovsky Jr AA, Toleutaev BN, Zinukov SV. Rise and decay kinetics of photosensitized singlet oxygen luminescence in water. Measurements with nanosecond time-correlated single photon counting technique. Chem Phys Lett. 1989;163:421-4.

30. Jarvi MT, Niedre MJ, Patterson MS, Wilson BC. Singlet Oxygen Luminescence Dosimetry (SOLD) for Photodynamic Therapy: Current Status, Challenges and Future Prospects. Photochem Photobiol. 2006;82:1198-210.

31. Derycke ASL, de Witte PAM. Liposomes for photodynamic therapy. Adv Drug Delivery Rev. 2004;56:17-30.

32. van Nostrum CF. Polymeric micelles to deliver photosensitizers for photodynamic therapy.

Adv Drug Delivery Rev. 2004;56:9-16.

33. Cinteza LO, Ohulchanskyy TY, Sahoo Y, Bergey EJ, Pandey RK, Prasad PN. Diacyllipid Micelle-Based Nanocarrier for Magnetically Guided Delivery of Drugs in Photodynamic Therapy. Mol Pharm. 2006;3:415-23.

34. Baba K, Pudavar HE, Roy I, Ohulchanskyy TY, Chen Y, Pandey RK, et al. New Method for Delivering a Hydrophobic Drug for Photodynamic Therapy Using Pure Nanocrystal Form of the Drug. Mol Pharm. 2007;4:289-97.

35. Ohulchanskyy TY, Roy I, Goswami LN, Chen Y, Bergey EJ, Pandey RK, et al. Organically Modified Silica Nanoparticles with Covalently Incorporated Photosensitizer for Photodynamic Therapy of Cancer. Nano Lett. 2007;7:2835-42.

36. Kim S, Ohulchanskyy TY, Pudavar HE, Pandey RK, Prasad PN. Organically Modified Silica Nanoparticles Co-encapsulating Photosensitizing Drug and Aggregation-Enhanced Two-Photon Absorbing Fluorescent Dye Aggregates for Two-Photon Photodynamic Therapy. J Am Chem Soc. 2007;129:2669-75.

37. Bechet D, Couleaud P, Frochot C, Viriot M-L, Guillemin F, Barberi-Heyob M. Nanoparticles as vehicles for delivery of photodynamic therapy agents. Trends Biotech. 2008;26:612-21.

38. Wang S, Fan W, Kim G, Hah HJ, Lee Y-EK, Kopelman R, et al. Novel Methods to Incorporate Photosensitizers Into Nanocarriers for Cancer Treatment by Photodynamic Therapy. Lasers Surg Med. 2001;43:686-95.

39. Jang B, Park J-Y, Tung C-H, Kim I-H, Choi Y. Gold Nanorod−Photosensitizer Complex for Near-Infrared Fluorescence Imaging and Photodynamic/Photothermal Therapy In Vivo. ACS Nano. 2011;5(2):1086-94.

40. Choi WI, Kim J-Y, Kang C, Byeon CC, Kim YH, Tae G. Tumor Regression In Vivo by Photothermal Therapy Based on Gold-Nanorod-Loaded, Functional Nanocarriers. ACS Nano. 2011;5(3):1995-2003.

41. Lin J, Wang S, Huang P, Wang Z, Chen S, Niu G, et al. Photosensitizer-Loaded Gold Vesicles with Strong Plasmonic Coupling Effect for Imaging-Guided Photothermal/Photodynamic Therapy. ACS Nano. 2013.

42. Skrabalak SE, Au L, Li X, Xia Y. Facile Synthesis of Ag Nanocubes and Au Nanocages. Nat Protoc. 2007;2:2182-90.

43. Pandey RK, Sumlin AB, Constantine S, Aoudia M, Potter WR, Bellnier DA, et al. Alkyl Ether Analogs of Chlorophyll-a Derivatives: Part 1. Synthesis, Photophysical Properties and Photodynamic Efficacy. Photochem Photobiol.1996;64:194-204.

44. Cho EC, Kim C, Zhou F, Cobley CM, Song KH, Chen J, et al. Measuring the Optical Absorption Cross Sections of Au−Ag Nanocages and Au Nanorods by Photoacoustic

Imaging. J Phys Chem C. 2009;113:9023-8.

45. Kim C, Jeon M, Wang LV. Nonionizing photoacoustic cystography in vivo. Opt Lett. 2011;36(18):3599-601.

46. Li Y-C, Rissanen S, Stepniewski M, Cramariuc O, Róg T, Mirza S, et al. Study of Interaction Between PEG Carrier and Three Relevant Drug Molecules: Piroxicam, Paclitaxel, and Hematoporphyrin. J Phys Chem B. 2012;116:7334-41.

47. Wilets KA, Duyne RPV. Localized Surface Plasmon Resonance Spectroscopy and Sensing. Ann Rev Phys Chem. 2007;58:267-97.

48. Chen J, Wiley B, Li ZY, Campbell D, Saeki F, Cang H, et al. Gold Nanocages: Engineering Their Structure for Biomedical Applications. Advanced Materials. 2005;17(18):2255-61.

49. Xia X, Yang M, Zheng Y, Li Q, Chen J, Xia Y. Quantifying the Coverage Density of Poly(ethylene glycol) Chains on the Surface of Gold Nanostructures. ACS Nano. 2012;6:512-22.

50. Lovell JF, Jin CS, Huynh E, Jin H, Kim C, Rubinstein JL, et al. Porphysome nanovesicles generated by porphyrin bilayers for use as multimodal biophotonic contrast agents. Nat Mater. 2011;10:324-32.

51. de Paula JC, Robblee JH, Pasternack RF. Aggregation of chlorophyll a probed by resonance light scattering spectroscopy. Biophys J. 1995;68:335-41.

52. Hartwich G, Fiedor L, Simonin I, Cmiel E, Schäfer W, Noy D, et al. Metal-Substituted Bacteriochlorophylls. 1. Preparation and Influence of Metal and Coordination on Spectra. J Am Chem Soc. 1998;120:3675-83.

53. Postlethwaite TA, Hutchison JE, Hathcock KW, Murray RW. Optical, Electrochemical, and Electrocatalytic Properties of Self-Assembled Thiol-Derivatized Porphyrins on Transparent Gold Films. Langmuir. 1995;11(10):4109-16.

54. Gollmer A, Arnbjerg J, Blaikie FH, Pedersen BW, Breitenbach T, Daasbjerg K, et al. Singlet Oxygen Sensor Green: Photochemical Behavior in Solution and in a Mammalian Cell. Photochem Photobiol. 2011;87:671-9.

55. Ostrowski JC, Mikhailovsky A, Bussian DA, Summers MA, Buratto SK, Bazan GC. Enhancement of Phosphorescence by Surface-Plasmon Resonances in Colloidal Metal Nanoparticles: The Role of Aggregates. Adv Funct Mater. 2006;16:1221-7.

56. Previte MJR, Aslan K, Zhang Y, Geddes CD. Metal-Enhanced Surface Plasmon-Coupled Phosphorescence. J Phys Chem C. 2007;111:6051-9.

57. Fang J, Nakamura H, Maeda H. The EPR effect: Unique features of tumor blood vessels for drug delivery, factors involved, and limitations and augmentation of the effect. Adv Drug Delivery Rev. 2011;63:136-51.

58. Chen J, Glaus C, Laforest R, Zhang Q, Yang M, Gidding M, et al. Gold Nanocages as Photothermal Transducers for Cancer Treatment. Small. 2010;6:811-7.

59. Goel R, Shah N, Visaria R, Paciotti GF, Bischof JC. Biodistribution of TNF-α-coated gold nanoparticles in an in vivo model system. Nanomedicine. 2009;4(4):401-10.

60. Gad SC, Sharp KL, Montgomery C, Payne JD, Goodrich GP. Evaluation of the Toxicity of Intravenous Delivery of Auroshell Particles (Gold–Silica Nanoshells). Int J Toxicol. 2012;31:584-94.

61. Alkilany A, Murphy C. Toxicity and cellular uptake of gold nanoparticles: what we have learned so far? J Nanoparticle Res. 2010;12:2313-33.

62. Zhang XD, Wu D, Shen X, Liu PX, Yang N, Zhao B, et al. Size-Dependent In Vivo Toxicity of PEG-Coated Gold Nanoparticles. Inter J Nanomed. 2011;6:2071-81.

63. Walkey CD, Olsen JB, Guo H, Emili A, Chan WCW. Nanoparticle Size and Surface Chemistry Determine Serum Protein Adsorption and Macrophage Uptake. J Am Chem Soc. 2011;134:2139-47.
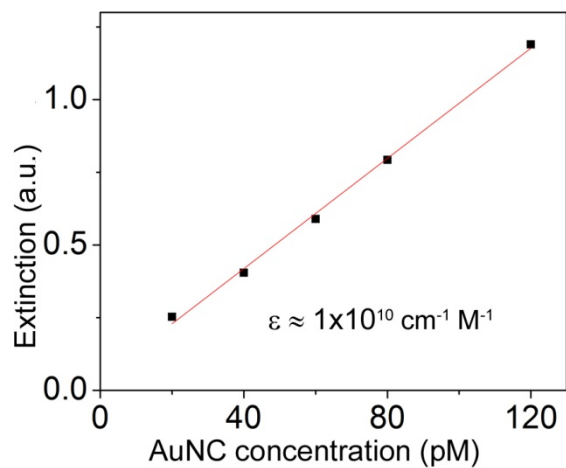
Figure S1. Plot of AuNC concentration against extinction intensity at 802 nm. The particle concentration of AuNCs was estimated from the size and composition of AuNCs directly measured from the TEM and AA analyses. Based on Beer-Lambert law, a linear fit to the data gives the slope of curve as the extinction coefficient of the AuNC to be 1×10^{10} cm^{-1}M^{-1}.
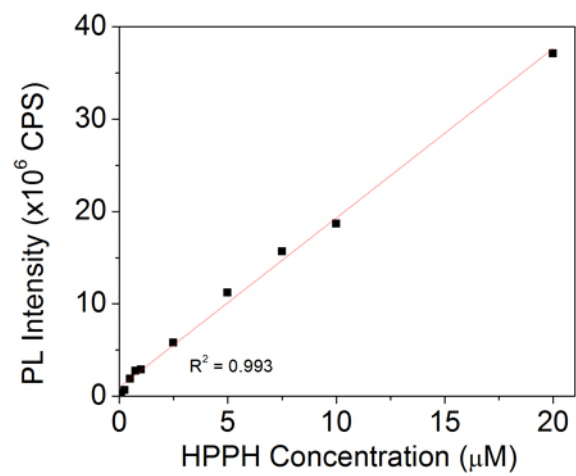
Figure S2. Plot of HPPH concentration against emission intensity at 670 nm as a calibration curve with λ_{ex} = 605 nm.
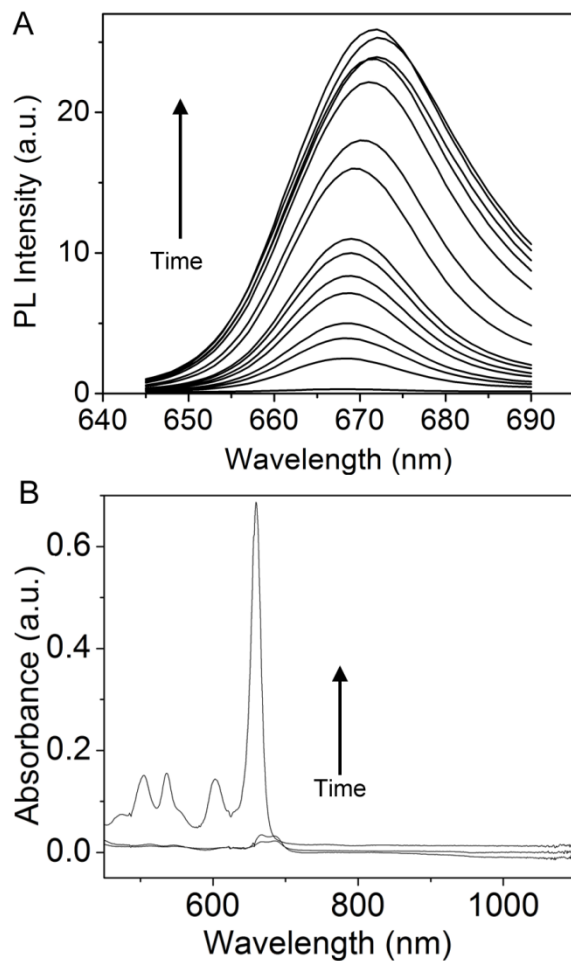
Figure S3. (A) Fluorescence spectra of AuNC-HPPH at different time points of incubation in serum. Spectra were taken after incubation for 20 s, 10, 20, 30, 45, 60, 75, 90, 120 min, 4, 6, 8, 12, and 24 h, as well as post-KCN digestion with λ_{ex} = 605 nm. (B) UV-Vis absorbance spectra of supernatants of AuNC-HPPH incubated in serum for 5 min and 24 h after 15 min centrifugation at 14,000 RPM, as well as post-KCN digestion.
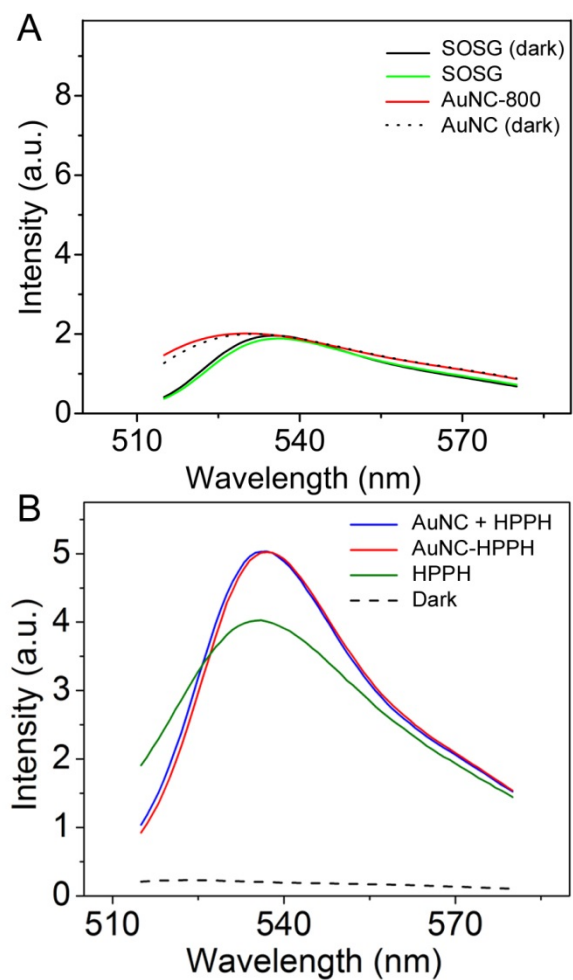
Figure S4. (A) Fluorescence spectra for PBS/D$_2$O solution of only SOSG before (black) and after (green) irradiation, as well as for PBS/D$_2$O dispersion of 10 pM AuNC and SOSG before (dashed) and after (red) irradiation. (B) Fluorescence spectra of SOSG in methanol with equimolar HPPH (green), AuNC-HPPH conjugate (red), and mixture of AuNC-PEG and HPPH (blue) with the pre-irradiation signal (dashed).
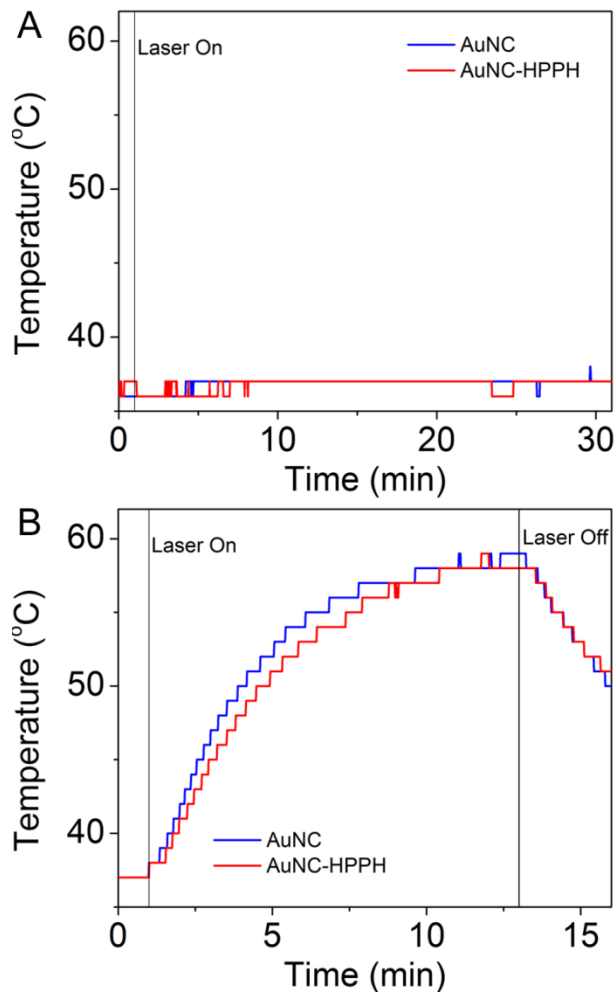
Figure S5. The temperature profile of AuNC and AuNC-HPPH that were irradiation under different conditions: (A) 0.1 nM AuNC irradiated with 665-nm laser at 75 mW/cm^2 (PDT conditions); and (B) 1 nM AuNC irradiated with 800-nm laser at 0.7 W/cm^2 (PTT conditions).
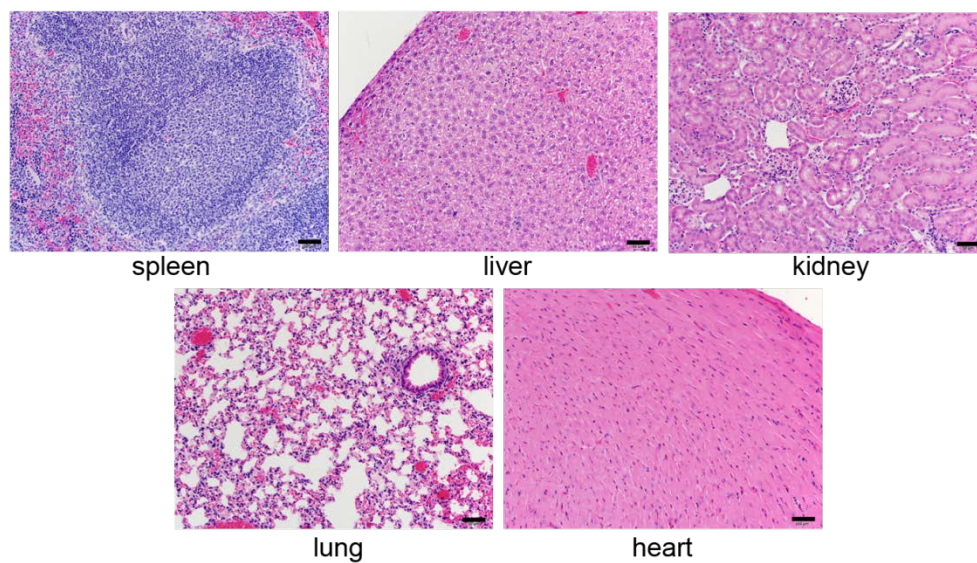
Figure S6. Photographs of representative H&E staining tissue sections of mice after 7 days post-treatment of AuNC-HPPH treated at 0.3 µmol/kg of HPPH. The scale bars are 50 µm.

Appendix B: Unpublished Data

A covalent conjugate between AuNC-PEG and HPPH was synthesized. Briefly, 1 mg of N-hydroxysuccinimide and 1 mg of 1-ethyl-3-(3-dimethylaminopropyl)carbodiimide were incubated in DMSO with 0.17 mM HPPH for 30 min. To this solution, AuNC-PEG with NH_2 terminus was added dropwise to a final concentration of 1 nM. The reaction was allowed to proceed overnight and the product was isolated by centrifugation. No significant change was observed in the UV-Vis spectrum (**Fig. B1A**) of the product, but following KCN digestion, the fluorescent signal (**Fig. B1B**) indicated that that $\sim 5 \times 10^3$ HPPH/AuNC had been conjugated. Assuming 2×10^4 PEG/AuNC,[1] the conjugation efficiency was ~ 25 %. This conjugate was then tested for its photodynamic efficacy *in vitro* using Colon-26 tumor cells (**Fig. B1C**). This construct was found to be significantly less effective than free HPPH, which was presumably due to excited state quenching by the AuNC. The IC_{50} for the conjugate was ~ 400 μM, while the IC_{50} for free HPPH was 57 μM.[2] This result stands in contrast to the noncovalent conjugate, therefore this conjugate was not investigated further.
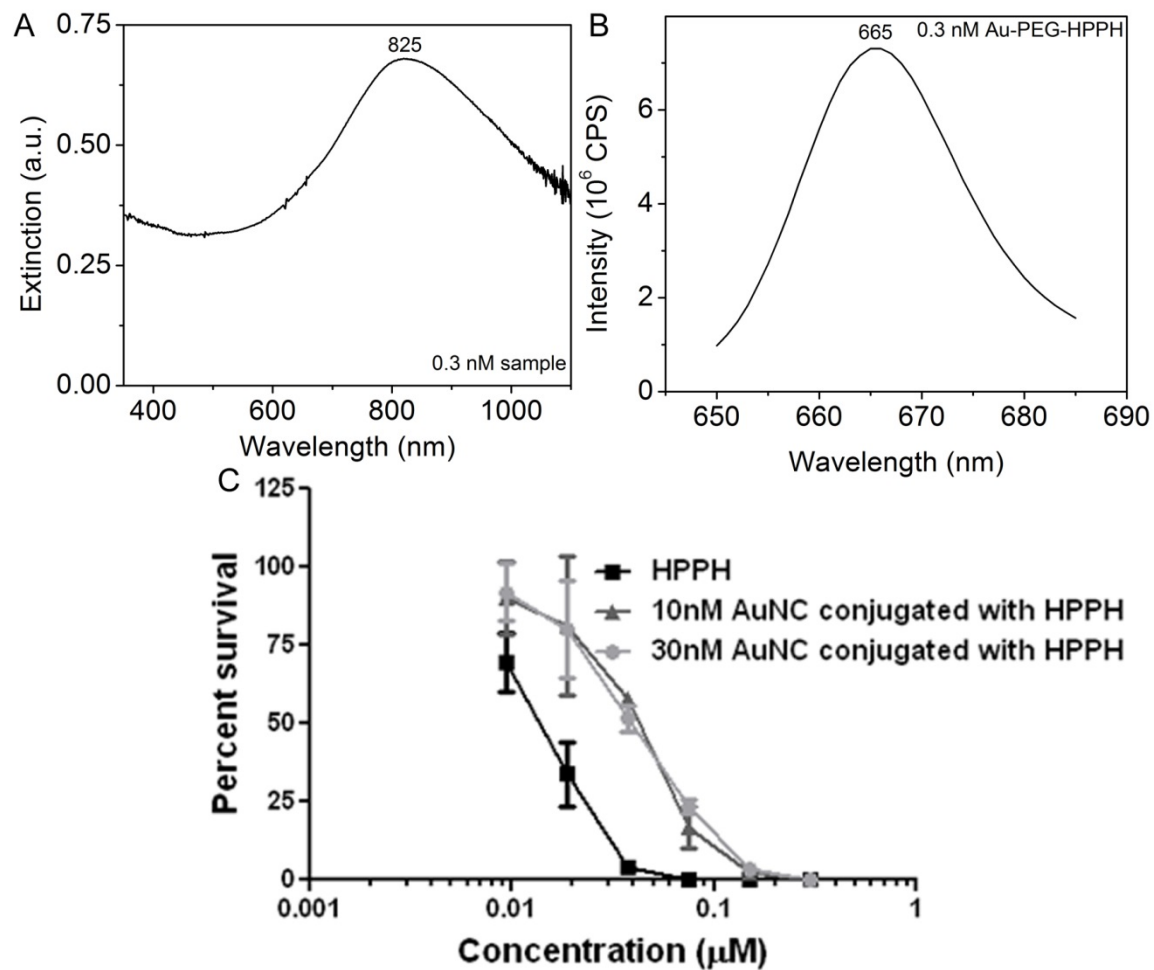
Figure B1. (A) Extinction spectrum and (B) post-KCN digestion fluorescence spectrum of covalently-conjugated AuNC-HPPH as well as (C) Viability plot of tumor cells treated with (squares) HPPH, (triangles) 10 nM AuNC-HPPH, and (circles) 30 nM AuNC-HPPH at equimolar HPPH concentration.

The role of the AuNC's LSPR in $^1O_2$ generation was investigated further. AuNCs were synthesized with LSPR at 660 nm. The edge length of AuNCs were found to be 18 ± 2.5 nm (**Fig B2A**). These AuNCs were treated with HS-PEG-NH$_2$ similar to AuNCs with LSPR at 800 nm[2] before they were noncovalently conjugated with HPPH. The loading was found to be ~10^5 HPPH/AuNC. The LSPR peak did not shift significantly (**Fig B2B**), but the absorbance peaks from HPPH emerged, resulting in a strong peak at 685 nm, the wavelength of $^1O_2$ generation. The generation of $^1O_2$ was then measured using SOSG and compared to free HPPH and AuNC-HPPH with LSPR at 800 nm (**Fig. B2C**). Interestingly, AuNC$_{665}$ conjugate showed reduced $^1O_2$ generation relative to free HPPH and the AuNC$_{800}$ conjugate. The AuNC$_{800}$ conjugate showed improved $^1O_2$ generation relative to free HPPH. This discrepancy can be attributed to two phenomena. First, the AuNC$_{665}$ LSPR overlaps with the absorbance of HPPH, thereby resulting in a lowered light dose to the photosensitizer. Second, the AuNC$_{800}$ LSPR overlaps with the phosphorescent emission of porphyrins.[3] The LSPR has been shown to stabilize the triplet state of nearby molecules in a manner similar to its enhancement of fluorescence.[4] Stabilization of the triplet state allows for a longer lifetime, increasing the likelihood of collision with ground O_2 to allow triplet-triplet annihilation to generate $^1O_2$. These results demonstrate the importance of control of the LSPR wavelength when developing a nanomaterial-photosensitizer conjugate.
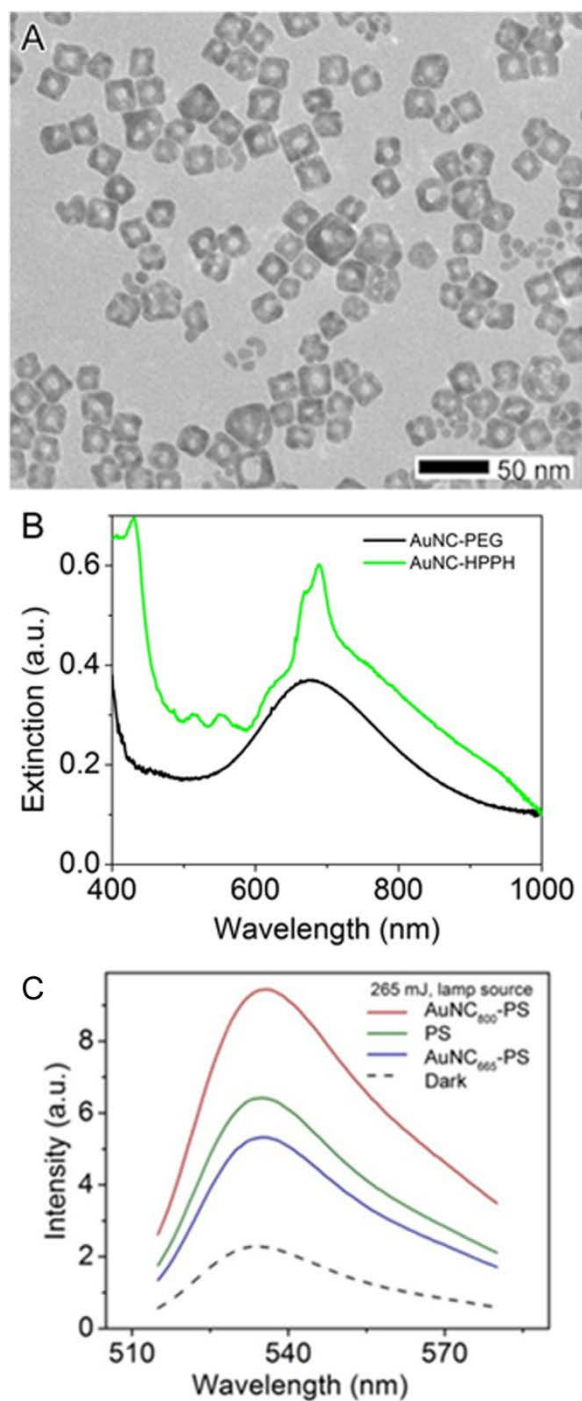
Figure B2. (A) TEM of AuNC with LSPR maximum at 665 nm and (B) extinction spectrum of AuNCs in A (black) before and (green) after loading of HPPH and (C) singlet oxygen generation of equimolar HPPH as measured by SOSG for (green) free HPPH, (blue) AuNC-HPPH with LSPR maximum at 665 nm, and (red) AuNC-HPPH with LSPR maximum at 800 nm. Dashed line indicates the SOSG signal in the absence of irradiation.

References

[1] Xia X, Yang M, Zheng Y, Li Q, Chen J, Xia Y. Quantifying the Coverage Density of Poly(ethylene glycol) Chains on the Surface of Gold Nanostructures. ACS Nano. 2012;6:512-22.

[2] Srivatsan A, Jenkins SV, Jeon M, Wu Z, Kim C, Chen J, et al. Gold nanocage-photosensitizer conjugates for dual-modal image-guided enhanced photodynamic therapy. Theranostics. 2014;4:163-74.

[3] Zhang Y, Aslan K, Previte MJR, Geddes CD. Metal-Enhanced Singlet Oxygen Generation: A Consequence of Plasmon Enhanced Triplet Yields. Journal of Fluorescence. 2007;17:345-9.

[4] Mishra H, Mali BL, Karolin J, Dragan AI, Geddes CD. Experimental and theoretical study of the distance dependence of metal-enhanced fluorescence, phosphorescence and delayed fluorescence in a single system. Physical Chemistry Chemical Physics. 2013;15:19538-44.

Chapter IV.   Understanding the Interactions between Porphyrin Photosensitizers and Polymer-Coated Nanoparticles in Model Biological Environments[*]

Abstract

Non-covalent incorporation of hydrophobic drugs into polymeric systems is a commonly-used strategy for drug delivery because non-covalent interactions minimize modification of the drug molecules, and their efficacy is retained upon release. The behaviors of the drug-polymer delivery system in the biological environment it encounters will affect the efficacy of treatment. In this report, we have investigated the interaction between a hydrophobic drug and its encapsulating polymer in model biological environments using a photosensitizer encapsulated polymer-coated nanoparticle system. The photosensitizer, 3-(1'-hexyloxyethyl)-3-devinylpyropheophorbide-a (HPPH), was non-covalently incorporated to the poly(ethylene glycol) (PEG) monolayer coated on Au nanocages (AuNCs) as AuNC-HPPH conjugates. The non-covalent binding was characterized by Scatchard analysis, fluorescence lifetime, and Raman experiments. The dissociation constant (K_d) between PEG and HPPH was found to be ~35 μM with a maximum loading of ~2.5×10^5 HPPHs/AuNC. The release was studied in a serum mimetic environment and in vesicles that models human cell membranes. The rate of the drug release mediated by proteins decreased with negatively-charged terminus of surface modified PEG or cross-linking of the terminus. Furthermore, the photothermal effect of AuNC can initiate burst release, and thus control of the release kinetics, demonstrating on-demand drug release.

Introduction

Controlled release systems for drug delivery using nanocarriers have been developed and studied for more than three decades.[1] Gold nanostructures have been used as drug delivery vehicles in chemotherapy because of their biocompatibility, facile surface modification, and robust optical properties.[2-8] While drug molecules can be covalently immobilized on the nanoparticles' surface,[2, 8-10] noncovalent interactions are particularly appealing because they minimize modification of the drug molecules, whose efficacy is then largely retained upon release. Several strategies have been developed to noncovalently tether molecules through electrostatic and hydrophobic interactions to polymer-coated nanoparticles by wrapping into layer-by-layer assembled polyelectrolytes,[11] entrapping in a polymer monolayer,[12-14] encapsulating into phospholipid bilayer,[15] or absorbing into a hydrogel.[16] Among these methods, poly(ethylene glycol) (PEG) coated nanoparticles are advantageous because PEG is generally nontoxic and possesses antifouling properties well suited for increasing circulation half-life and minimizing immunological clearance.[17] Hydrophobic phthalocyanine photosensitizers[18-20] or anti-cancer drugs[21, 22] could be delivered within the surface PEG layer or inside the hydrophobic pocket for photodynamic therapy or chemotherapy. We have recently applied a similar system to deliver a hydrophobic porphyrin-derivative (3-(1'-hexyloxyethyl)-3-devinylpyropheophorbide-a, HPPH) for image-guided photodynamic therapy with enhanced efficacy.[14]

In this work, we systematically investigate the binding affinity and the release kinetics of HPPH from PEG-coated AuNCs to further elucidate the behavior of the drug-polymer delivery system. The induced-dipole/induced-dipole interactions between the pheophorbide and the PEG backbone serve as the driving force to load molecules within the PEG layer.[23] HPPH is stably integrated within the PEG coating of AuNC-HPPH in saline solution. The release itself is

mediated by either serum proteins (specifically albumin in our model) or cell membranes (modelled here with vesicles). The serum proteins unloaded the drug over several hours and the release of entrapped molecules can be endogenously controlled by the charge and functionality of the PEG terminus. Additionally, the release rate can be exogenously controlled by utilizing the photothermal (PT) effect of Au nanostructures which allows external and temporal control of the drug release by non-invasive near-infrared light.[11, 24-27] By manipulating these variables, we are able to demonstrate on-demand unloading of the drug with minimal premature loss and were able to suggest the relative affinity of the drug for soluble proteins versus cell membranes.

Results and Discussion

The AuNC-HPPH conjugates were prepared according to the method previously reported[14] by covalently attaching HS-PEG-X to the nanoparticle surface and subsequently encapsulating HPPH into the PEG monolayer. AuNCs with an average exterior edge length of 52.6 ± 8.2 nm and interior edge length of 41.2 ± 6.2 nm were synthesized for this study. After their surface was coated with HS-PEG-NH$_3^+$, the LSPR of the AuNCs was centered at 801 nm (**Fig. 1A**), slightly redshifted from the LSPR of the "bare" AuNCs at 798 nm (**Fig. S1A**). This LSPR maximum falls within the tissue-transparent window and overlaps the 808 nm wavelength of the diode laser utilized for PT release. **Figure 1B** shows the spectral changes after loading; the LSPR of AuNCs was further redshifted to 829 nm, which can be attributed to a change in the refractive index of the local surface environment.[28] The peaks at 512, 545, 617, and 669 nm are attributed to absorption by the HPPH molecules (**Fig. S1B**). The fluorescence was quenched after loading due to static/contact quenching in the HPPH, nanometal surface energy transfer, light being absorbed by the AuNCs, or a combination thereof.[29-32] After the AuNCs were digested by KCN, the fluorescence was recovered, and then quantified by comparison to the calibration curve (**Figs.**

1C, S2A). The AuNC concentration was initially determined by flame atomic absorbance spectroscopy, from which the extinction coefficient was derived based on Beer's Law (**Fig. S2B**).

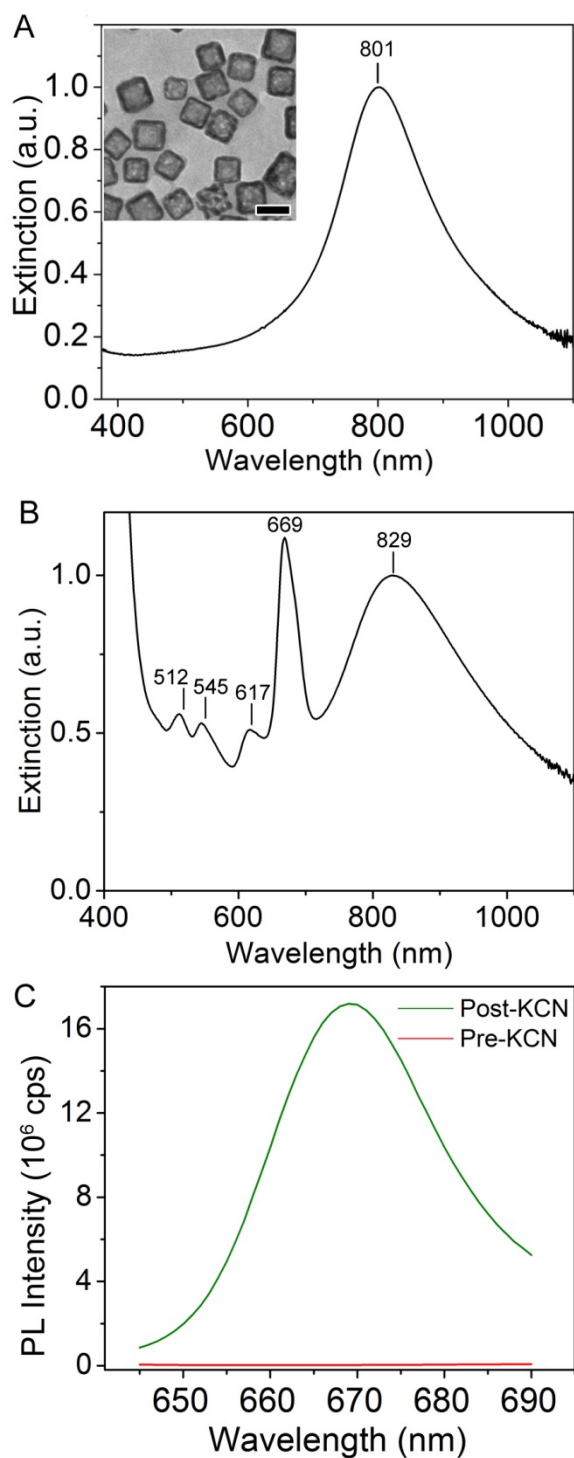**Figure 1.** Normalized UV-Vis-NIR spectra (A) AuNC before and (B) after loading with HPPH. Inset shows TEM image of AuNCs with a 50 nm scale bar. (C) Fluorescence spectra of HPPH-loaded AuNCs, before (green) and after (red) KCN digestion of AuNCs.

The loaded concentration of HPPH increased to a maximum on the order of 10^5 HPPHs per AuNC. As the loading increased, the hydrodynamic diameter (d_H) slightly increased from 98.7 ± 0.9 to 105.3 ± 2.8 nm while the zeta potential decreased from +6.4 ± 0.5 to -26.3 ± 0.8 mV (**Fig. 2A**). The d_H remained more or less constant, suggesting that HPPH was mostly entangled within the PEG monolayer on the nanocage surface rather than aggregating on top of the monolayer. Earlier theoretical work simulated that the addition of PEG to a solution of hematoporphyrin resulted in concentration-dependent porphyrin deaggregation and association with the PEG chains through strong interaction between the $-CH_2CH_2-$ region of the PEG chain and the porphyrin ring.[23] The decrease of zeta potential is likely due to the increasing amount of negatively-charged HPPH in the conjugates.

The hydrophobic interaction between PEG and HPPH was further confirmed by studying the binding affinity. Increasing amounts of HPPH were introduced to phosphate buffer (10 mM, pH 7.4) with 0 or 135 mM NaCl at constant AuNC-PEG concentration. After incubation overnight, the unbound HPPH concentration was determined by the absorbance at 669 nm upon removal of AuNCs by centrifugation. The bound HPPH (L_b) was taken to be the difference between the total (L_t) and the unbound HPPH (L_u) concentration. No loss of HPPH was seen in the absence of AuNCs. A saturation binding isotherm (**Fig 2B**) was developed, and Scatchard analysis results in a plot that is both hyperbolic and concave up, consistent with nonspecific binding between PEG and HPPH.[33] The data were fit to the equation $L_b = N \times L_u / (K_{d,ns} + L_u)$, where $K_{d,ns}$ is the dissociation constant for nonspecific binding and N is a constant loosely related to the number of available binding sites.[34] Based on the fitting, the $K_{d,ns}$ was determined to be 3.2 x 10^{-5} M and 3.7 x 10^{-5} M for 0 mM and 135 mM NaCl, respectively, which is similar to simulation results on similar molecules;[23] the respective N values increased from ~100 to ~180. These data suggest

that the NaCl does not enhance binding between HPPH and PEG, but makes available additional binding sites, increasing the packing density of HPPH. The presence of aqueous ions significantly increased the available binding sites of PEG and HPPH due to a further exposure of $-CH_2CH_2-$ of PEG to the porphyrin ring of HPPH, which ultimately caused a near doubling the N value. Moreover, the loaded HPPH reached a maximum at $\sim 2.5 \times 10^5$ HPPHs/AuNC, indicating that a finite space was available for loading within the PEG monolayer on the nanocage surface.
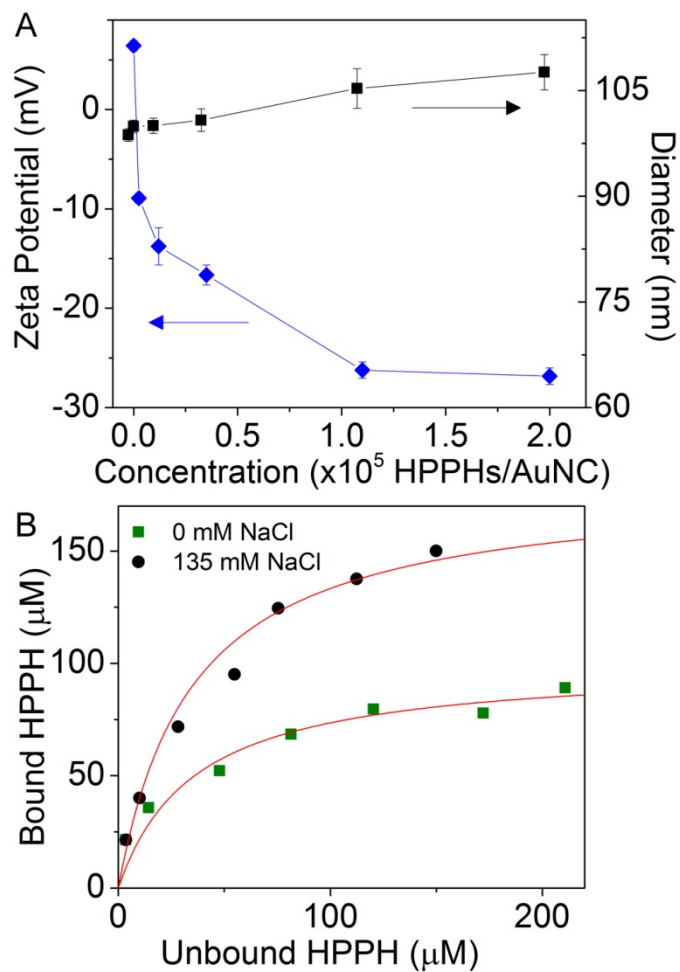
Figure 2. (A) Zeta potential (diamonds) and hydrodynamic diameter (squares) as measured by DLS for AuNC-HPPH at varying ratios of HPPH to AuNC. (B) Saturation binding isotherm between HPPH and the PEG monolayer on AuNC surface, AuNC concentration (1 nM) using 0 mM (squares) or 135 mM (circles) NaCl in 10 mM phosphate buffer (pH = 7.4). The red line indicates the fitting.

The fluorescent properties of HPPH inside the PEG layer on the AuNCs was examined by the fluorescence lifetimes of the conjugates (**Fig. 3A**). Due to quenching, the quantum yields were very low, but a weak signal was present. The HPPH lifetime (τ_{avg}) for AuNC-HPPH was measured to be 1.39 ns, comparable to that in PBS (1.51 ns) and appreciably shorter than in methanol (6.55 ns) or BSA (7.21 ns). Even when the loading concentration was reduced to 5×10^3 HPPHs per AuNC, the lifetime increased only slightly to 2.69 ns. These data suggest that the HPPH molecules in AuNC-HPPH are in close proximity to each other, similar to the small aggregates that have been generated in PBS.[35] The proximity of HPPH to the AuNC surface was characterized by Raman spectroscopy (**Fig. 3B**). Raman spectra were acquired at excitation wavelength of 488 nm and the signal intensities were compared for different forms of HPPH at a concentration of 100 nM. The samples include free HPPH, AuNC-HPPH (5×10^3 HPPHs per AuNC), and AuNC-HPPH (1×10^5 HPPHs per AuNC). The peak at 1641 cm^{-1} was assigned to the weak Raman signal from water. The C-H peaks at ~2950 cm^{-1} in these spectra likely originate from the PEG as the intensity does not change with the HPPH concentration. The broad Gaussian region from 2000 to 2500 cm^{-1} (540-555 nm) in the free HPPH was attributed to weak fluorescence of HPPH. The high loading concentration gave rise to a typical Raman peak at 1590 cm^{-1} that corresponds to the vibration of aromatic bonds in the macrocycle[36], suggesting that the pheophorbide ring is oriented somewhat perpendicularly to the surface of the metal.[37] At low concentration, the Raman signature disappeared and was replaced by a broad fluorescence peak centered at 2340 cm^{-1}. These data suggest that HPPH may be driven deeper in the monolayer and closer to the metal surface at higher concentrations. These results suggest HPPHs were densely packed within the monolayer.
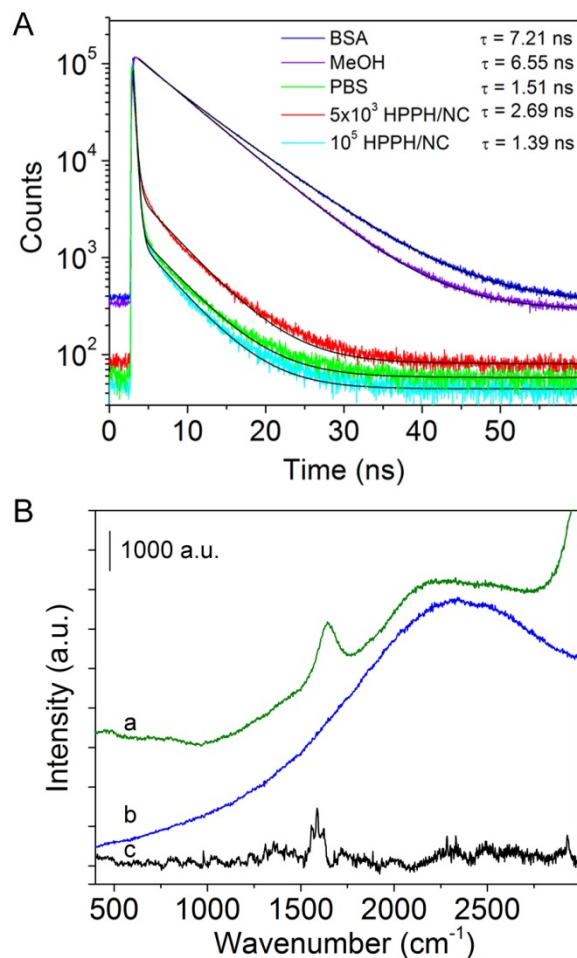
Figure 3. (A) Fluorescence lifetime measurements of HPPH under various conditions: dispersed in methanol (violet), 4% w/w BSA solution (blue), PBS (green) and as AuNC-HPPH in PBS loaded at 5000 HPPHs/AuNC (red) and 10^5 HPPHs/AuNC (cyan). (B) Raman spectra of 100 nM HPPH under various conditions: (a) free HPPH, (b) AuNC-HPPH (~5000 HPPHs/AuNC, 20 pM AuNC), and (c) AuNC-HPPH (~10^5 HPPHs/AuNC, 1 pM AuNC); spectra were acquired over 300 s using 488 nm excitation.

The release of the drug was monitored in a serum-mimetic environment to simulate intravenous injection (**Fig. 4A**).[38] Fluorescence gradually recovered over 32 h when incubated in 4 wt % BSA (~600 µM, 37 °C, pH = 7.4).[39] As a control, AuNC-HPPH was also incubated in PBS, and release was monitored using supernatant absorbance at various times compared to the maximum. It was found that 86.3 ± 7.6 % of HPPH had been unloaded in the BSA solution within 24 h, but only 4.7 ± 2.1 % of the payload had unloaded in PBS. PEG monolayers are known to resist formation of a "hard" (nonremovable) protein corona,[40, 41] therefore the release is attributable to the formation of a "soft" protein corona, which entails rapid adsorption and desorption of serum proteins on the PEG surface.[42, 43] During this transient event, BSA presumably binds HPPH, which then desorbs with the protein. The $K_{d,ns}$ of PEG-HPPH complexes is on the order of 10^{-5} M, much larger than the typical K_d values of BSA-porphyrin complexes (~10^{-9} M),[44, 45] ergo it would be energetically favorable for BSA to bind HPPH, releasing it from the PEG.

The PEG terminus was changed by conjugating AuNCs to either amine- or carboxylate-terminated PEG prior to HPPH loading (AuNC-HPPH and AuNC$_{COO}$-HPPH, respectively), which was found to significantly affect the kinetics of HPPH release. Replacing the cationic (NH_3^+) with anionic (COO^-) termini, resulted in slower unloading kinetics with only 50.1 ± 6.8 % release within 24 h. Because the isoelectric point of BSA is 4.7, it is negatively charged at pH = 7.4, and should therefore be repelled by the carboxylate terminus of the PEG,[46] which in turn retards the unloading of HPPH. The release rate could be further slowed by cross-linking the termini of the PEGs on the surface (**Fig. 4B**). Amide coupling between the cross-linker, HOOC-PEG$_{250}$-COOH (3-4 repeating units), and the NH_3^+ terminus of the PEG resulted in steric hindrance that blocked protein binding. Cross-linking with PEG$_{250}$ resulted in a dramatic reduction of the HPPH release to only 31.1 ± 8.7 % within 32 h as compared to the release of

61.2 ± 6.8 % for the non-cross-linked system.
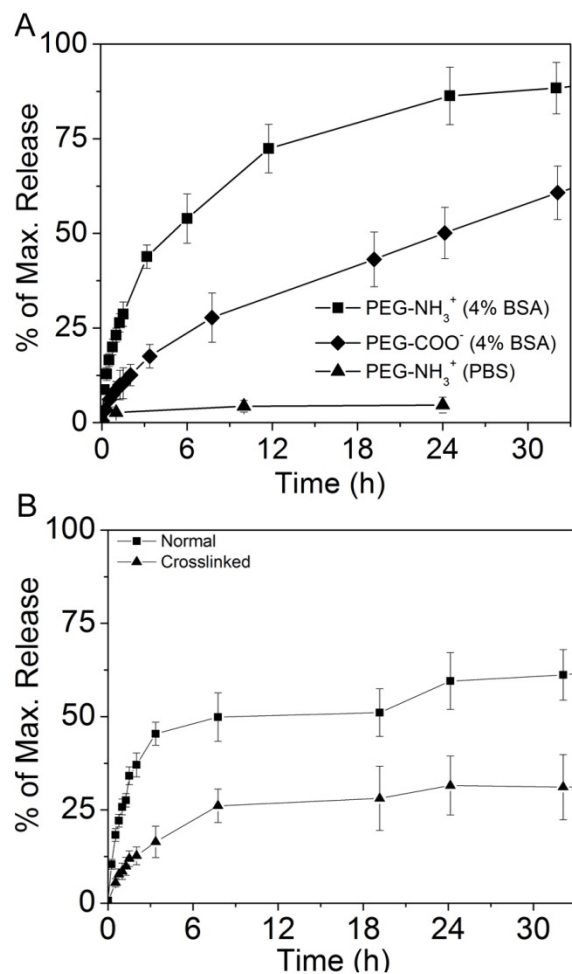
Figure 4. (A) Comparison of HPPH release kinetics at pH = 7.4, 37 °C for AuNC-HPPH using PEG-NH$_3^+$ (squares) and PEG-COO$^-$ (diamonds) with 4% w/w BSA in PBS, and in only PBS (triangles). (B) Comparison of HPPH release kinetics from AuNC-HPPH without (squares) and with (triangles) cross-linking of the polymer terminus (-NH$_2$) by HOOC-PEG-COOH. Maximum (100%) values were determined by the recovered fluorescence signal after the AuNCs were digested by KCN.

Ideally, AuNC-HPPH is anticipated to unload the HPPH in the tumor cell membrane for maximal photodynamic effect due to the short lifetime of singlet oxygen. Vesicles were prepared with a 3:1 mole ratio of DMPC and DMPG to mimic the composition of human cell membranes. Incorporation of HPPH in the vesicle membrane (1 mM lipid solution) leads to recovery of its fluorescence; therefore the release could be monitored similarly to BSA solutions. The release of HPPH to the vesicle solution was compared for free HPPH and AuNC-HPPH (**Fig 5**). Similar to the BSA solution, ~90 % of the HPPH unloaded from the AuNC-HPPH after 24 h. It is worth noting that unlike tumor cells, the vesicles were free in solution and able to interact freely with suspended particles, which would artificially inflate the kinetics of the process. Interestingly, free HPPH did not reach its maximum signal until between 2 and 4 h incubation in the vesicle solution, whereas the BSA solution of free HPPH reached a maximum within 10 min. These results imply that kinetics of HPPH adsorption are much higher for BSA than for the cell membrane. However, the release from AuNC-HPPH is comparable for both systems, which suggests that diffusion of the conjugate is a major determining factor in release. As such, following intravenous injection HPPH would be less likely to be bound by BSA when delivered as AuNC-HPPH than free HPPH. Additionally, because of its accumulation in tumors,[14] AuNC-HPPH would likely deliver a larger HPPH dose to the cell membrane itself.
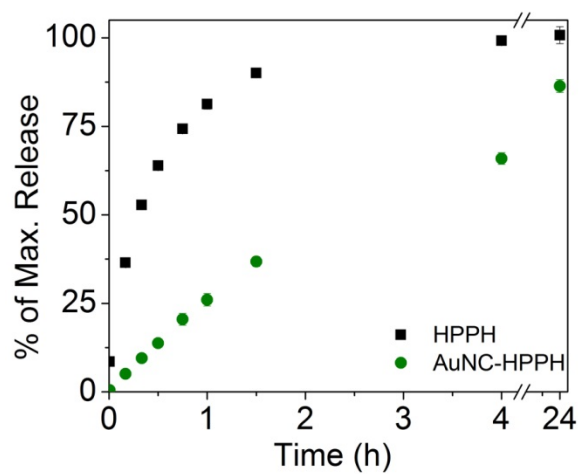
Figure 5. Kinetics of incorporation of HPPH into vesicles using (squares) free HPPH and (circles) AuNC-HPPH.

The release could be further controlled with PT heating by the AuNCs (**Fig. 6**). Under NIR irradiation by a diode laser (1 W/cm^2 at 808 nm) that overlaps with the LSPR, the solution temperature was held at 46 $^{\circ}$C for 2 h.[47, 48] In the dark, only 26.2 ± 6.7 % of the payload was released from the PEG monolayer after two hours. The slow release profile should provide enough time for the AuNC-HPPH to accumulate in the tumor prior to unloading, as demonstrated in our previous *in vivo* study.[14] Irradiation led to localized heating, which presumably increased the fluidity of the PEG layer and enabled HPPH to rapidly diffuse to the interface and interact with BSA. A linear burst release (69.2 ± 5.0 %) in the first 45 min was observed, after which the release proceeded gradually, only reaching ~75 % when the study terminated after two hours. The remaining HPPH may have been buried too deeply within the PEG monolayer to have yet interacted with BSA for release.
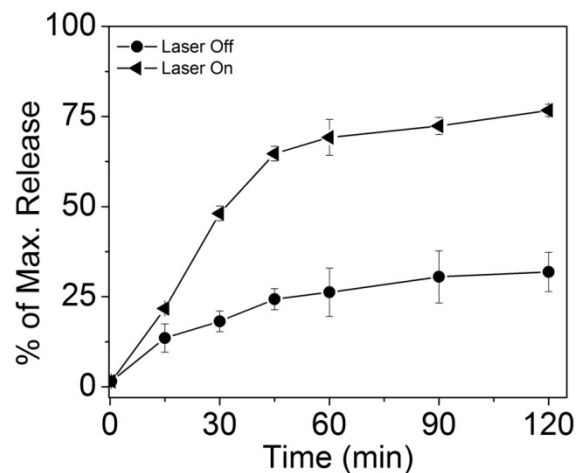
Figure 6. Comparison of HPPH release kinetics from AuNC-HPPH under irradiation by 808 nm diode laser at 1 W/cm^2 (triangles), and from AuNC-HPPH at 37 °C in the dark (squares). Maximum (100%) values were determined by the recovered fluorescence signal after the AuNCs were digested by KCN.

A finer measure of control was achieved using brief pulses of irradiation, and little release was observed during the dark time. The controlled release profiles are shown in **Figure 7A**, and the change in temperature of equimolar AuNCs in PBS is shown in **Figure 7B**. The suspension temperature rose from 37 °C to 46 °C during the 5 min irradiation period and returned to 37 °C during the 10 min dark time. AuNC$_{COO}$-HPPH and AuNC-HPPH were separately incubated in BSA for 5 min prior to the first irradiation. During the first laser pulse roughly 20 and 30 % of the respective payload was released, and only a further 5 % of the payload released in the dark time that followed. The second pulse resulted in 15 and 20 % of the respective payloads being released, and the final pulse released ~10 % of the payload. Ultimately, ~60 % and ~80 % of the payload was released from AuNC$_{COO}$-HPPH and AuNC-HPPH, respectively, during the three laser pulses. Faster release was observed for AuNC-HPPH than AuNC$_{COO}$-HPPH, similar to the dark release (**Fig. 7A**). Both samples demonstrated similar capacity for on-demand release, though AuNC$_{COO}$-HPPH seemed to be more responsive to the irradiation. The slow release observed in the absence of irradiation suggests that little premature leakage would occur during transport from the injection site to the tumor, but the extensive, controllable release of the payload suggests that extensive unloading can be accomplished quickly within the tumor. Further, release was achieved using photothermal temperatures, suggesting that added therapeutic benefit could be achieved by unloading the drug photothermally.
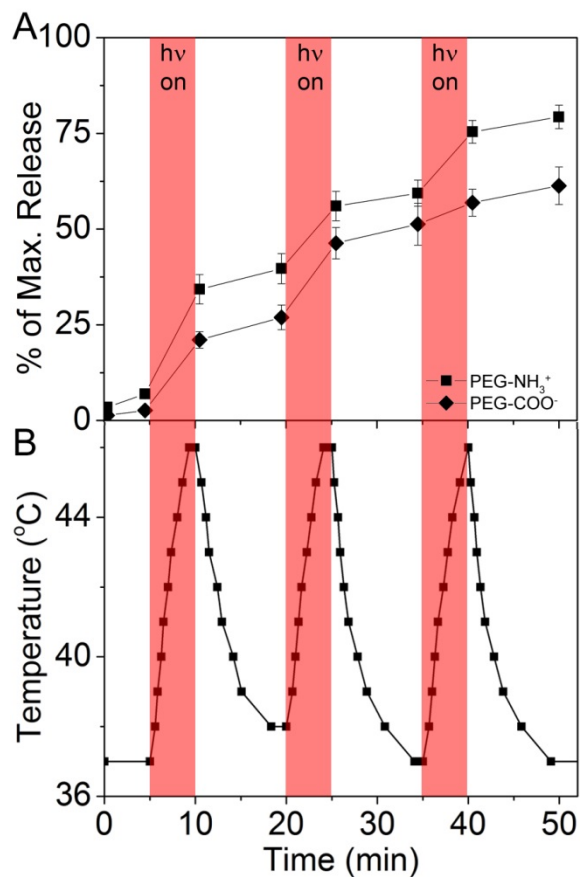
Figure 7. (A) On-demand release of HPPH from AuNC-HPPH as triggered by NIR irradiation at 808 nm (1 W/cm^2). Maximum (100%) values were determined by the recovered fluorescence signal after the AuNCs were digested by KCN. (B) Temperature change of sample solutions for cycles of 5 min irradiation and 10 min in the dark. Shaded regions indicate laser irradiation periods.

Conclusion

PEG-monolayer-covered Au nanoparticle platforms are a robust system for delivery of such hydrophobic drugs, particularly photosensitizers, in part because noncovalent conjugation minimizes changes to drug pharmakokinetics. HPPH was incorporated into such a system, characterized thoroughly, and the response to biomimetic environments investigated. The Raman, fluorescence, and physical properties of these conjugates were investigated to elucidate the nature of the binding. The loading capacity was found to be ~2×10^5 HPPHs/AuNC, the K_d was determined to be ~35 μM, and the drug was found to pack tightly within the monolayer. Release from this delivery system was studied in albumin-containing media to mimic *in vivo* delivery following intravenous injection. To mimic unloading the cell membrane, release into vesicles was also investigated. The terminus of the PEG chain significantly affected the release profile. Significantly faster release was observed from amine-terminated (cationic) PEG than carboxylate terminated (anionic) PEG. Cross-linking these termini was used to introduce steric hindrance that blocked binding of the protein with the embedded HPPH. Controllable burst release could be accomplished by using irradiation to induce the PT effect. This PEG-monolayer-covered AuNC system can potentially serve as a multifunctional platform for controlled delivery of a wide variety of hydrophobic drugs, particularly for cancer theranostics.

Methods

Exterior incorporation of HPPH to AuNC-PEG (AuNC-HPPH). HPPH (7 mg, 11 μmol) was dissolved in 2.5 mL DMSO at a concentration of 4.5 mM as stock solution. This stock solution (0.25 mL) was diluted in 4 mL of PBS via dropwise addition in ice bath to a concentration of ~183 μM. The diluted HPPH solution was flushed with Ar for 5 min and allowed to mix for 5 additional min. The AuNC-PEG suspension (3 nM, 2 mL) was added dropwise to the HPPH solution. The reaction was allowed to stir overnight under the protection of Ar in the dark. The product containing non-covalently-incorporated HPPH on AuNC-PEG was then washed three cycles of centrifugation (14,000 RPM, 15 min, 20 °C) and redispersion in PBS with a final AuNC concentration of 6 nM. The conjugated HPPH can be fully released from conjugates by methanol. UV-Vis-NIR spectroscopy was used to determine the concentration of non-covalently incorporated HPPH (extinction coefficient in methanol $\varepsilon_{HPPH} \approx 4.0 \times 10^4$ M^{-1}cm^{-1}). The concentration of AuNCs was calculated by the metal concentration from elemental analysis and size information from TEM analysis. The loading efficiency was calculated as ~1×10^5 HPPHs/AuNC. The incorporated HPPH per AuNC is readily changed by adjusting the ratio of HPPH to AuNC in the reaction. To determine the K_d, 1 nM AuNC-PEG was incubated with varying concentrations of HPPH overnight with stirring in 10 mM phosphate buffer (pH = 7.4) with 0, 135, or 1000 mM NaCl. The suspension was centrifuged and the supernatant HPPH concentration was quantified by absorbance at 665 nm. These data were used to develop a saturation binding isotherm, and fit to the equation $L_b = N*L_u/(L_u + K_d)$.

Cross-linking of AuNC-HPPH. AuNC-PEG-NH$_3^+$ was incorporated with HPPH to a concentration of ~2.5×10^4 HPPHs/AuNC using the above procedure. PEG$_{250}$, a diacidic cross-linker, was dispersed in borate buffer (pH = 9) in an ice bath with stirring to a concentration of

2.0 mM (4.2 µmol, 1.0 mg). To this solution, EDC (7.8 µmol, 1.2 mg) and NHS (10.4 µmol, 1.2 mg) were added. The solution was then flushed with Ar for 20 min. AuNC-HPPH solution (0.2 mL) was added dropwise into the solution. The reaction was allowed to stir overnight in the dark under the protection of Ar. The product was recovered by two centrifugation cycles (14,000 RPM, 15 min, 20 °C) and redispersion in PBS.

Preparation of Lipid Vesicles. 1,2-dimyristoyl-*sn*-glycero-3-phosphocholine (DMPC, 75 µmol) and 1,2-dimyristoyl-sn-glycero-3-phospho-(1'-rac-glycerol) (DMPG, 25 µmol) were dissolved in 5 mL chloroform to yield a 20 mM lipid solution. The solvent was removed under high vacuum overnight. The lipids were hydrated in 5 mL PBS with vigorous shaking for 2 h, following by 2 h in the bath sonicator, until the solution was no longer turbid. Lipid vesicles were stored at 4 °C under Ar.

Study of HPPH release kinetics. Recovered fluorescence was used to monitor the release kinetics of HPPH from AuNC-HPPH conjugates. Typically, AuNC-HPPH was diluted in PBS or BSA in PBS (4 % w/w, ~575 µM) at a final concentration of 0.1 nM. Fluorescence measurements were acquired after the dilution at various intervals throughout a 32 h period using λ_{ex} = 605 nm and λ_{em} = 668 nm. Samples were kept at room temperature, in the dark, without stirring or unnecessary agitation between measurements. At the end of the data acquisition, 10 µL of 0.5 M aqueous KCN was added to dissolve AuNCs and the fluorescence spectrum was acquired to determine the maximum (100%) HPPH signal for the sample. PBS samples were monitored using supernatant absorbance at various times following centrifugation. After measurement, the pellet was redispersed in the original supernatant.

To test the PT effect on the release kinetics, an 808-nm diode laser (Power Technology) was used to irradiate the suspension of AuNC-HPPH conjugates. The laser intensity was adjusted to

a power density of 1 W/cm^2 by changing the spot size, so the temperature of the sample was maintained at ~46 ^{o}C. The fluorescence measurement was taken at different time periods over the course of 2 h irradiation, and irradiation began within 10 s of introduction of sample into BSA. On-demand release was demonstrated using 5 min irradiation pulses followed by 10 min without irradiation.

References

[1] D. Peer, J. M. Karp, S. Hong, O. C. Farokhzad, R. Margalit, R. Langer *Nat Nano*. **2007**, 2, 751-760.

[2] P. Ghosh, G. Han, M. De, C. K. Kim, V. M. Rotello *Adv. Drug Del. Rev.* **2008**, 60, 1307-1315.

[3] P. R. Gil, W. J. Parak *ACS Nano*. **2008**, 2, 2200-2205.

[4] O. C. Farokhzad, R. Langer *ACS Nano*. **2009**, 3, 16-20.

[5] R. Bardhan, S. Lal, A. Joshi, N. J. Halas *Acc. Chem. Res.* **2011**, 44, 936-946.

[6] Y. Xia, W. Li, C. M. Cobley, J. Chen, X. Xia, Q. Zhang, M. Yang, E. C. Cho, P. K. Brown *Acc. Chem. Res.* **2011**, 44, 914-924.

[7] E. C. Dreaden, A. M. Alkilany, X. Huang, C. J. Murphy, M. A. El-Sayed *Chem. Soc. Rev.* **2012**, 41, 2740-2779.

[8] S. Rana, A. Bajaj, R. Mout, V. M. Rotello *Adv. Drug Del. Rev.* **2012**, 64, 200-216.

[9] J. Xie, S. Lee, X. Chen *Adv. Drug Del. Rev.* **2010**, 62, 1064-1079.

[10] A. M. Alkilany, S. E. Lohse, C. J. Murphy *Acc. Chem. Res.* **2012**, 46, 650-661.

[11] J. Huang, K. S. Jackson, C. J. Murphy *Nano Lett.* **2012**, 12, 2982-2987.

[12] C. K. Kim, P. Ghosh, C. Pagliuca, Z.-J. Zhu, S. Menichetti, V. M. Rotello *J. Am. Chem. Soc.* **2009**, 131, 1360-1361.

[13] F. Ren, S. Bhana, D. D. Norman, J. Johnson, L. Xu, D. L. Baker, A. L. Parrill, X. Huang *Bioconjugate Chem.* **2013**, 24, 376-386.

[14] A. Srivatsan, S. V. Jenkins, M. Jeon, Z. Wu, C. Kim, J. Chen, R. K. Pandey *Theranostics*. **2014**, 4, 163-174.

[15] N. C. M. Tam, B. M. T. Scott, D. Voicu, B. C. Wilson, G. Zheng *Bioconjugate Chem.* **2010**, 21, 2178-2182.

[16] S. R. Sershen, S. L. Westcott, N. J. Halas, J. L. West *J. Biomed. Mater. Res.* **2000**, 51, 293-298.

[17] K. Knop, R. Hoogenboom, D. Fischer, U. S. Schubert *Angew. Chem. Int. Ed.* **2010**, 49, 6288-6308.

[18] Y. Cheng, A. C. Samia, J. D. Meyers, I. Panagopoulos, B. Fei, C. Burda *J. Am. Chem. Soc.* **2008**, 130, 10643-10647.

[19] Y. Cheng, A. C. Samia, J. Li, M. E. Kenney, A. Resnick, C. Burda *Langmuir*. **2009**, 26, 2248-2255.

[20] Y. Cheng, J. D. Meyers, A.-M. Broome, M. E. Kenney, J. P. Basilion, C. Burda *J. Am. Chem. Soc.* **2011**, 133, 2583-2591.

[21] P. Ghosh, G. Han, M. De, C. K. Kim, V. M. Rotello *Advanced Drug Delivery Reviews*. **2008**, 60, 1307-1315.

[22] F. Ren, S. Bhana, D. D. Norman, J. Johnson, L. Xu, D. L. Baker, A. L. Parrill, X. Huang *Bioconjugate Chemistry*. **2013**, 24, 376-386.

[23] Y.-C. Li, S. Rissanen, M. Stepniewski, O. Cramariuc, T. Róg, S. Mirza, H. Xhaard, M. Wytrwal, M. Kepczynski, A. Bunker *J. Phys. Chem. B*. **2012**, 116, 7334-7341.

[24] M. S. Yavuz, Y. Cheng, J. Chen, C. M. Cobley, Q. Zhang, M. Rycenga, J. Xie, C. Kim, K. H. Song, A. G. Schwartz, L. V. Wang, Y. Xia *Nat. Mater.* **2009**, 8, 935-939.

[25] G. D. Moon, S.-W. Choi, X. Cai, W. Li, E. C. Cho, U. Jeong, L. V. Wang, Y. Xia *J. Am. Chem. Soc.* **2011**, 133, 4762-4765.

[26] J. You, G. Zhang, C. Li *ACS Nano*. **2010**, 4, 1033-1041.

[27] S. R. Sershen, S. L. Westcott, N. J. Halas, J. L. West *Journal of Biomedical Materials Research*. **2000**, 51, 293-298.

[28] K. A. Wilets, R. P. V. Duyne *Ann. Rev. Phys. Chem.* **2007**, 58, 267-297.

[29] C. S. Yun, A. Javier, T. Jennings, M. Fisher, S. Hira, S. Peterson, B. Hopkins, N. O. Reich, G. F. Strouse *J. Am. Chem. Soc.* **2005**, 127, 3115-3119.

[30] T. L. Jennings, M. P. Singh, G. F. Strouse *J. Am. Chem. Soc.* **2006**, 128, 5462-5467.

[31] X. Xia, M. Yang, L. K. Oetjen, Y. Zhang, Q. Li, J. Chen, Y. Xia *Nanoscale*. **2011**, 3, 950-953.

[32] L. Biczok, P. Valat, V. Wintgens *Physical Chemistry Chemical Physics*. **1999**, 1, 4759-4766.

[33] C. M. Mendel, D. B. Mendel *Biochem J*. **1985**, 228, 269-272.

[34] E. J. van Zoelen *Biochem J*. **1989**, 262, 549-556.

[35] K. Baba, H. E. Pudavar, I. Roy, T. Y. Ohulchanskyy, Y. Chen, R. K. Pandey, P. N. Prasad *Mol. Pharm.* **2007**, 4, 289-297.

[36] T. M. Cotton, S. G. Schultz, R. P. V. Duyne *J. Am. Chem. Soc.* **1982**, 104, 6528-6532.

[37] X. Gao, J. P. Davies, M. J. Weaver *J. Phys. Chem.* **1990**, 94, 6858-6864.

[38] S. V. Jenkins, H. Qu, T. Mudalige, T. M. Ingle, R. Wang, F. Wang, P. C. Howard, J. Chen, Y. Zhang *Biomaterials*. **2015**, 51, 226-237.

[39] J. P. Doweiko, D. J. Nompleggi *J. Parenteral Enteral Nutrition*. **1991**, 15, 207-211.

[40] P. Harder, M. Grunze, R. Dahint, G. M. Whitesides, P. E. Laibinis *J. Phys. Chem. B*. **1998**, 102, 426-436.

[41] E. Ostuni, R. G. Chapman, R. E. Holmlin, S. Takayama, G. M. Whitesides *Langmuir*. **2001**, 17, 5605-5620.

[42] C. D. Walkey, J. B. Olsen, H. Guo, A. Emili, W. C. W. Chan *J. Am. Chem. Soc.* **2011**, 134, 2139-2147.

[43] C. D. Walkey, W. C. W. Chan *Chem. Soc. Rev.* **2012**, 41, 2780-2799.

[44] M. Rotenberg, R. Margalit *Biochem. J*. **1985**, 229, 197-203.

[45] A. Mahammed, H. B. Gray, J. J. Weaver, K. Sorasaenee, Z. Gross *Bioconjugate Chem.* **2004**, 15, 738-746.

[46] R. A. Hartvig, M. van de Weert, J. Østergaard, L. Jorgensen, H. Jensen *Langmuir*. **2011**, 27, 2634-2643.

[47] J. Chen, C. Glaus, R. Laforest, Q. Zhang, M. Yang, M. Gidding, M. J. Welch, Y. Xia *Small*. **2010**, 6, 811-817.

[48] J. Chen, M. Yang, Q. Zhang, E. C. Cho, C. M. Cobley, C. Kim, C. Glaus, L. V. Wang, M. J. Welch, Y. Xia *Adv. Funct. Mater.* **2010**, 20, 3684-3694.

Appendix A: Supporting Information

Experimental Details:

Materials. Silver trifluoroacetate ($AgCF_3COO$), tetrachloroauric acid ($HAuCl_4$), poly(vinyl pyrrolidone) (PVP, M.W.~55,000), sodium hydrogen sulfide (NaSH), dimethylsulfoxide (DMSO), 1-(3-Dimethylaminopropyl)-3-ethylcarbodiimide hydrochloride (EDC), and N-hydroxysuccinimide (NHS) were purchased from Alfa Aesar. Ethylene glycol (EG), potassium cyanide (KCN), and sodium chloride (NaCl) were purchased from JT Baker. Hydrochloric acid (HCl, 99.999%), phosphate-buffered saline (PBS), O-(3-Carboxypropyl)-O'-[2-(3-mercaptopropionylamino)ethyl] polyethylene glycol($PEG\text{-}COO^-$, M.W.=5,000), and poly(ethylene glycol) bis(carboxymethyl) ether (PEG_{250}, M.W.=250) were purchased from Sigma Aldrich. Amine-terminated PEG thiol TFA salt ($PEG\text{-}NH_3^+$, M.W.=5,000) was purchased from JenKem. Acetone and methanol (MeOH) were purchased from EMD. Bovine serum albumin was purchased from Rockland Inc. All water used in the procedures was 18 MΩ H_2O unless specified. 2-devinyl-2-(1-hexyloxyethyl)pyropheophorbide (HPPH, marketed as Photochlor) was prepared based on the previously reported method in Dr. Pandey's laboratory.[1] All chemicals were used as received.

Synthesis of AuNCs. AuNCs were synthesized by a two-step process using Ag cubes as a sacrificial template for the galvanic replacement reaction. Briefly, Ag nanocubes were synthesized with edge length of ~40 nm and LSPR peak at 443 nm.[2] The as-prepared Ag nanocubes (96 pmol, ~8 nM) were then titrated with 1 mM $HAuCl_4$ aqueous solution at a rate of 45 mL/h at 100 °C under vigorous stirring until the LSPR of the reaction mixture reached ~800 nm.[3] The mixture remained on heat for 5 min, before being cooled to room temperature. The AuNCs were further purified with saturated NaCl solution to remove AgCl precipitate. The

product was washed twice with H_2O and redispersed in H_2O for future use. Atomic absorption data indicate that the AuNCs are 91% Au by mass with the remainder being Ag.

Conjugation of PEG to AuNCs. Details regarding AuNC synthesis can be found in the supporting information. AuNCs were synthesized with LSPR of ~800 nm to overlap with the laser used for photothermal experiments. To conjugate thiol-terminated PEG (*i.e.*, PEG-NH$_3^+$, PEG-COO$^-$) to AuNCs, based on a previously published procedure,[4] 0.4 μmol of PEG was dissolved in 4 mL H_2O in a 20 mL vial. The solution was placed in an ice bath with stirring for 5 min. Next, 8 mL of 1.0 nM AuNC suspension was added dropwise over 5 min. The vial was flushed with Ar for 10 minutes and allowed to stir overnight in dark. After conjugation, the excess PEG was removed by three cycles of centrifugation (14,000 RPM, 15 min, 20 °C) and redispersion in H_2O, and finally redispersed in PBS with a concentration of ~3 nM.

Instrumentation. Transmission electron microscrope (TEM) images were obtained using JEOL 100cx with an acceleration voltage of 100 kV. The specimens were prepared by dropping the samples onto carbon-coated copper grid and allowing the solvent to evaporate in air. UV-Vis-NIR spectra were obtained using spectrophotometer (Agilent HP8453). Fluorescence spectra were obtained using fluorimeter (Horiba FluoroLog3). The concentrations of Au and Ag were determined using atomic absorption (AA) spectrometer (GBC 932). Hydrodynamic diameter (d_H) and ζ potential of the conjugated AuNCs were determined using dynamic light scattering (Brookhaven ZetaPALS). Fluorescence lifetime measurement were acquired using MicroTime 200 microscope (PicoQuant GmbH) with $\lambda_{ex} = 640$ and $\lambda_{em} = 670$; the data were fitted using SymPhoTime software. Raman spectra were obtained using Raman Microscope (Horiba). Spectra were acquired in a 50 μL quartz cuvette using 488 nm laser with a He/Ar source and an acquisition time of 300 s.
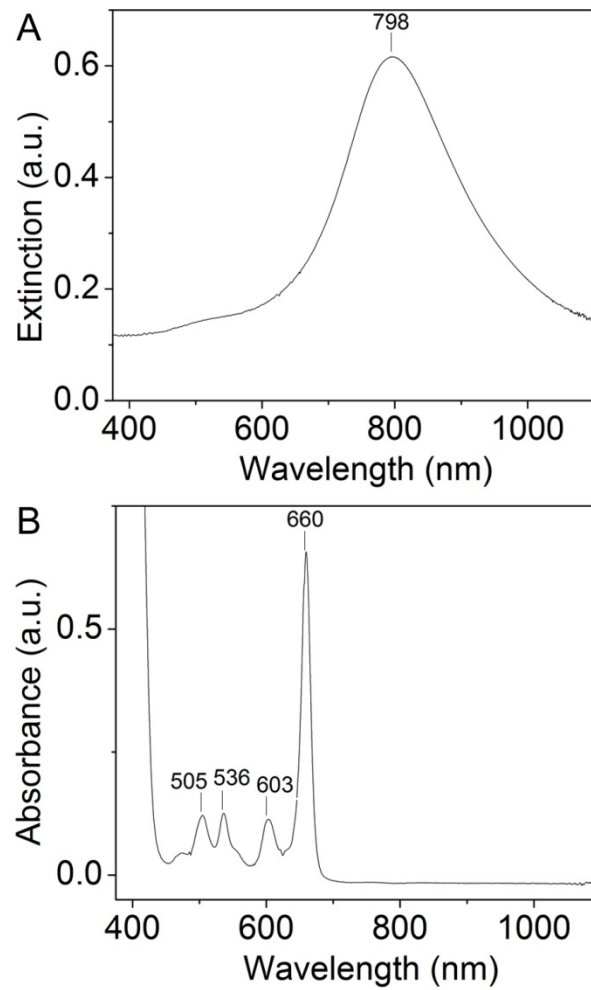
Figure S1. Extinction spectra of bare AuNCs (A) and HPPH in PBS (B).
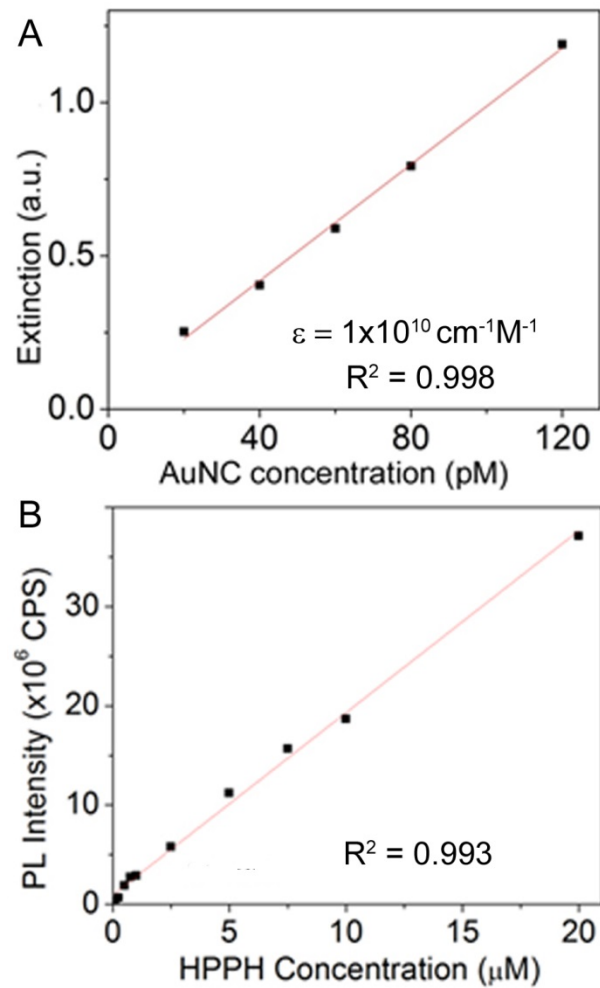
Figure S2. Calibration curves for AuNC extinction at 801 nm (A) and HPPH fluorescence at 669 nm in 4% w/w BSA (B). AuNC concentration was determined using atomic absorbance spectroscopy.

References:

[1] R. K. Pandey, A. B. Sumlin, S. Constantine, M. Aoudia, W. R. Potter, D. A. Bellnier, B. W. Henderson, M. A. Rodgers, K. M. Smith, T. J. Dougherty *Photochem. Photobiol.* **1996**, 64, 194-204.

[2] Q. Zhang, W. Li, L.-P. Wen, J. Chen, Y. Xia *Chemistry – A European Journal*. **2010**, 16, 10234-10239.

[3] S. E. Skrabalak, L. Au, X. Li, Y. Xia *Nat. Protocols*. **2007**, 2, 2182-2190.

[4] X. Xia, M. Yang, Y. Zheng, Q. Li, J. Chen, Y. Xia *ACS Nano*. **2012**, 6, 512-522.

Chapter V.   Drug-Loaded Immuno-Gold Nanoconstructs for Synergistic Photothermal and Antibiotic Killing of *Staphylococcus aureus*[*]

Abstract

Resistance to conventional antibiotics is a growing public health concern that is quickly outpacing the development of new antibiotics. This has lead the Infectious Disease Society of America to define *Enterococcus faecium, Staphylococcus aureus, Klebsiella pneumoniae, Acinetobacter baumannii, Pseudomonas aeruginosa,* and *Enterobacter* species as the ESKAPE pathogens based on the alarming lack of antibiotics useful for the treatment of infections caused by these species. This emphasizes the need for alternative therapeutic strategies to combat infections caused by these and other bacterial pathogens. In this report, we used *Staphylococcus aureus* as a proof-of-principle ESKAPE pathogen to demonstrate that therapeutic levels of an appropriate antibiotic (daptomycin) can be incorporated into polydopamine-coated gold nanocages (AuNC@PDA) and that daptomycin-loaded AuNC@PDA can be conjugated to antibodies targeting a species-specific surface protein (staphylococcal protein A) as a means of achieving selective delivery of AuNCs directly to the bacterial cell surface. We also demonstrate that laser irradiation at levels within the current safety standard for use in humans can then be used to achieve both a lethal photothermal effect and controlled release of antibiotic, thus resulting in a degree of therapeutic synergy capable of eradicating viable bacteria.

Introduction

The treatment of bacterial infections has been dramatically compromised by the persistent emergence of antibiotic resistant strains.[1-3] This has lead the Infectious Disease Society of America (IDSA) to designate *Enterococcus faecium, Staphylococcus aureus, Klebsiella pneumoniae, Acinetobacter baumannii, Pseudomonas aeruginosa,* and *Enterobacter* species as the ESKAPE pathogens based on the rapidly decreasing availability of useful antibiotics against these pathogens.[4] Although new antibiotics have been developed, the pace of development is slow by comparison to the emergence of resistant strains, and past experience has proven that the use of any conventional antibiotic will ultimately lead to the emergence of such resistance.[1] In addition, many forms of bacterial infection, specifically those associated with biofilm formation, are intrinsically resistant to antimicrobial therapy irrespective of the acquired resistance status of the offending bacteria.[5] These factors have created an urgent need for the development of alternative antibacterial strategies that would be less subject to the selective forces that drive the emergence of acquired antibiotic resistance.

Two alternatives that have been explored are photodynamic therapy (PDT) and photothermal (PT) therapy.[6] PDT utilizes a photosensitizer and visible light in the presence of oxygen to produce reactive oxygen species (ROS) capable of killing pathogenic microorganisms.[7-9] However, it is challenging to destroy the number of bacteria required to achieve the desired effect of eliminating the infection without damaging host tissues due to the short lifetime and thus limited potency of the ROS generated by this approach.[10] Instead, we and others have explored the use of PT therapy using light-absorbers such as gold nanoparticles and carbon nanotubes to generate laser-assisted PT effects capable of the targeted physical destruction of bacterial cells.[11-13] Indeed, in an experimentally amenable murine model, we confirmed that this

approach can be combined with photoacoustic (PA) flow cytometry to detect and eradicate bacterial cells in the blood.[14-15] While PT killing has great potential to treat bacteremia and potentially other forms of bacterial infection including those involving formation of a biofilm,[13] the combined use of PT with controlled antibiotic release has the potential to dramatically improve treatment efficacy compared to either therapeutic approach alone. This combined approach of using gold nanoparticles to achieve PT-mediated effects and controlled drug release has been explored to great effect in the context of cancer,[16] but to date it has not been explored in the context of infectious disease. As with cancer, this synergistic approach has tremendous potential in that the therapeutic synergy of PT-mediated killing and controlled antibiotic release has the potential to reduce both the degree of laser irradiation and the amount of antibiotic required to achieve the desired clinical effect. Evaluating this hypothesis was the focus of the experiments we report.

To this end, we examined the killing efficacy of a novel pathogen-targeted nanotherapeutic approach that allowed for both the physical, PT-mediated destruction of bacterial cells and concomitant release of an antibiotic in relatively high concentrations and in the immediate environment of the offending bacterial cells. We chose to focus on *Staphylococcus aureus* (*S. aureus*) as a proof-of-principle pathogen because it is one of the most prominent ESKAPE pathogens owing to the frequency and severity of the infections it causes, its antibiotic resistance status,[3] and its prominence as a cause of biofilm-associated infections.[17] The nanoconstruct we investigated consisted of a plasmonic hard core of gold nanocages (AuNC) and a polymer soft shell of polydopamine (PDA) assembled as a core-shell structure. This construct was loaded with the antibiotic daptomycin (Dap), which was chosen because it is active against MRSA[18] and has relatively good efficacy in the context of a biofilm.[19] Daptomycin-loaded AuNCs were

148

functionalized for targeting to *S. aureus* by conjugation to antibodies against staphylococcal protein A (anti-SPA), thereby creating a photoactivatable, highly selective nanodrug. As illustrated in **Figure 1**, the underlying concept is that when this nanodrug attaches to the *S. aureus* cell surface, irradiation with near-infrared (NIR) light will activate plasmonic AuNCs to convert photon energy to thermal energy resulting in an increase in temperature[20-21] of sufficient magnitude for the simultaneous generation of localized PT effects and expansion of the PDA coating leading to controlled antibiotic release.[22-23]
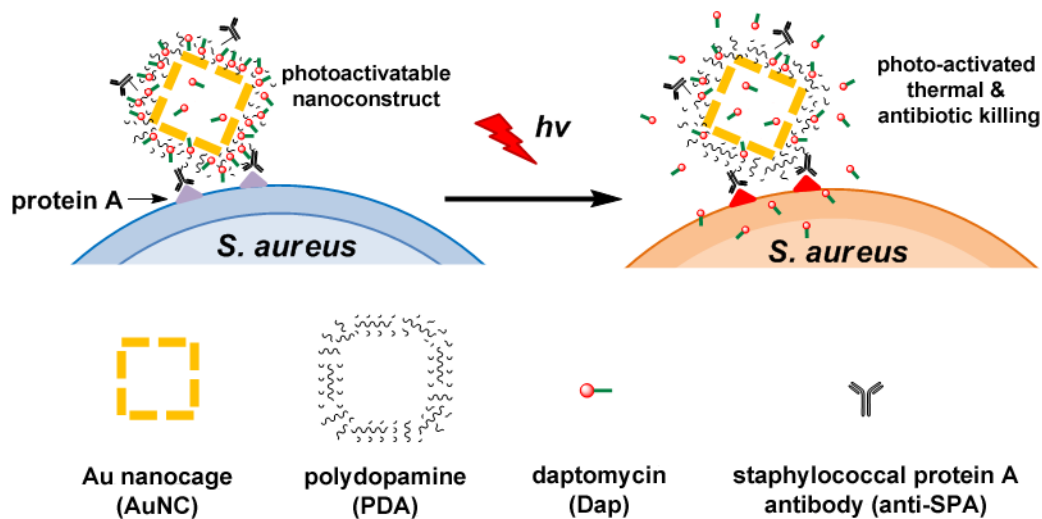
Figure 1. Schematic illustration of the working mechanism of the photoactivatable nanoconstruct as a super nanodrug for synergistic photothermal and antibiotic treatment of *S. aureus*.

Results and Discussion

The AuNCs were synthesized using a galvanic replacement reaction between Ag nanocubes and chloroauric acid as described in previous reports.[23-24] The initial AuNCs were found to contain 74.3% Au and 25.7% Ag by mass corresponding to 61.3% Au and 38.7% Ag by atomic number. The outer and inner edge lengths of the AuNCs were 54.5 ± 5.0 nm and 38.4 ± 5.3 nm, respectively, and they exhibited an extinction maximum of localized surface plasmon resonance (LSPR) at 753 nm (**Fig. S1**). The desired nanoconstruct was then prepared in three sequential steps following the reaction scheme in **Figure 2** with details described in supporting information: i) *in situ* polymerization of dopamine to deposit a layer of PDA on the AuNCs forming an intermediate core-shell structure (AuNC@PDA);[25-27] ii) loading of Dap to the PDA shell through intermolecular interactions to obtain a Dap-loaded intermediate (AuNC@Dap/PDA); and iii) covalent conjugation of anti-SPA through catechol chemistry to yield the final nanoconstruct (AuNC@Dap/PDA-anti-SPA). The intermediates obtained during synthesis were isolated, purified, and characterized prior to each subsequent reaction.
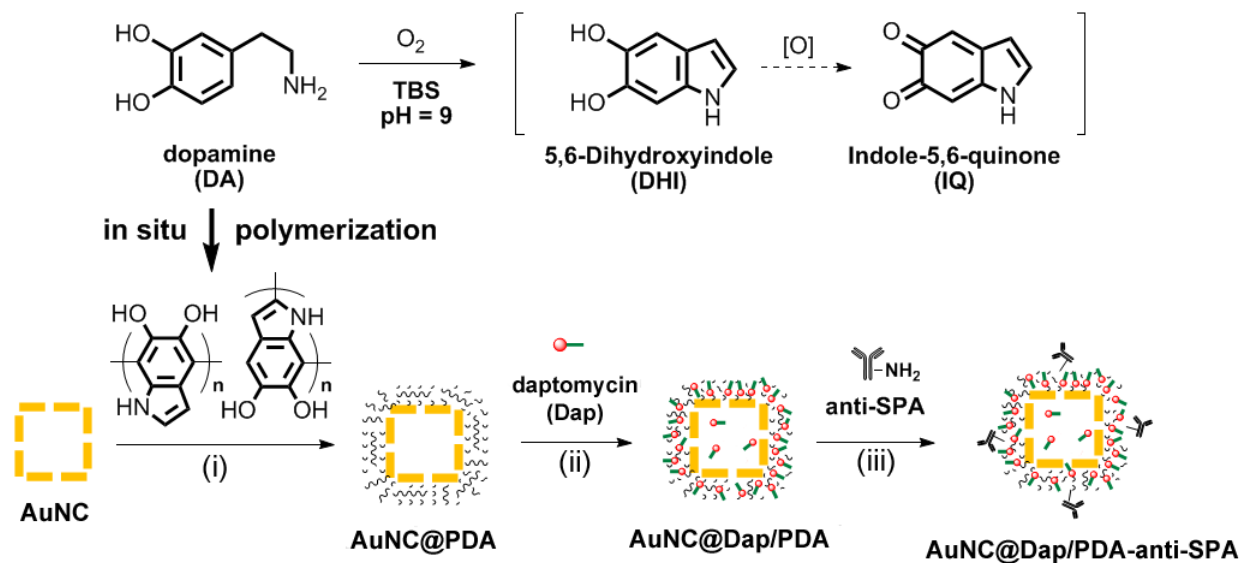
Figure 2. (A) Three-step scheme for synthesis of the nanoconstruct: (i) *in situ* polymerization of dopamine to form AuNC@PDA; (ii) loading of Dap to obtain AuNC@Dap/PDA; and (iii) conjugation of staphylococcal protein A antibody to yield AuNC@DapPDA-anti-SPA.

After self-polymerization of dopamine on the surface of AuNCs, a layer of PDA with a thickness of 20-50 nm was confirmed by TEM (**Fig. 3A**). The hydrodynamic diameter was increased from ~90 nm for AuNCs to ~200 nm for AuNC@PDA (**Fig. S2**). The LSPR peak was shifted to 824 nm (**Fig. 3B**) which is attributed to the changes in the refractive index of the medium from 1.33 for water to 1.55 for PDA as the PDA coating becomes thicker.[28-29] The PDA coating process was monitored by UV-Vis spectral analysis of the reaction solution (**Fig. S3, A and C**). During the deposition of PDA, the LSPR maxima of the AuNCs gradually shifted from 753 nm to 824 nm. Additionally, a peak at 410 nm attributable to quinone was progressively increased, indicating the oxidation of dopamine to dopamine quinone.[30] The product of AuNC@PDA was further characterized by Fourier transform infrared (FTIR) spectroscopy (**Fig. S3D**). The peak at 1611 cm^{-1} can be assigned to C-C stretching of indole or indoline structures while the peaks at 1729, 2846/2916, and 3600 cm^{-1} can be attributed to C=O, C-H, and N-H stretching on the heterocyclic molecules.[31]

The photothermal effect of AuNC@PDA suspension was measured under *in vitro* conditions used for antimicrobial studies. AuNC@PDA suspensions (200 µL) with an LSPR at ~820 nm was added to each well of a 96-well microtiter plate at concentration ranging from 0.04 to 0.4 nM (2.4×10^{10}-2.4×10^{11} AuNC@PDA/mL). Samples were sealed by a transparent film to prevent evaporation and irradiated using a diode laser centered at 808 nm with a power of 0.75 W and a spot size of 0.30 cm^2 covering the entire surface area of the well. Through the transparent film, the actual power that reached the samples was reduced to 0.50 W corresponding to 1.67 W/cm^2. Temperature changes as a function of time were recorded by an infrared thermal sensor. The results confirmed a temperature increase with increased concentration of AuNC@PDA and laser fluence that reached a plateau after 5 min (**Fig. 3, C and D**). This photo-responsive

AuNC@PDA was used for Dap loading and anti-SPA conjugation in consecutive steps to achieve a light-triggered, pathogen-specific antibiotic delivery platform.
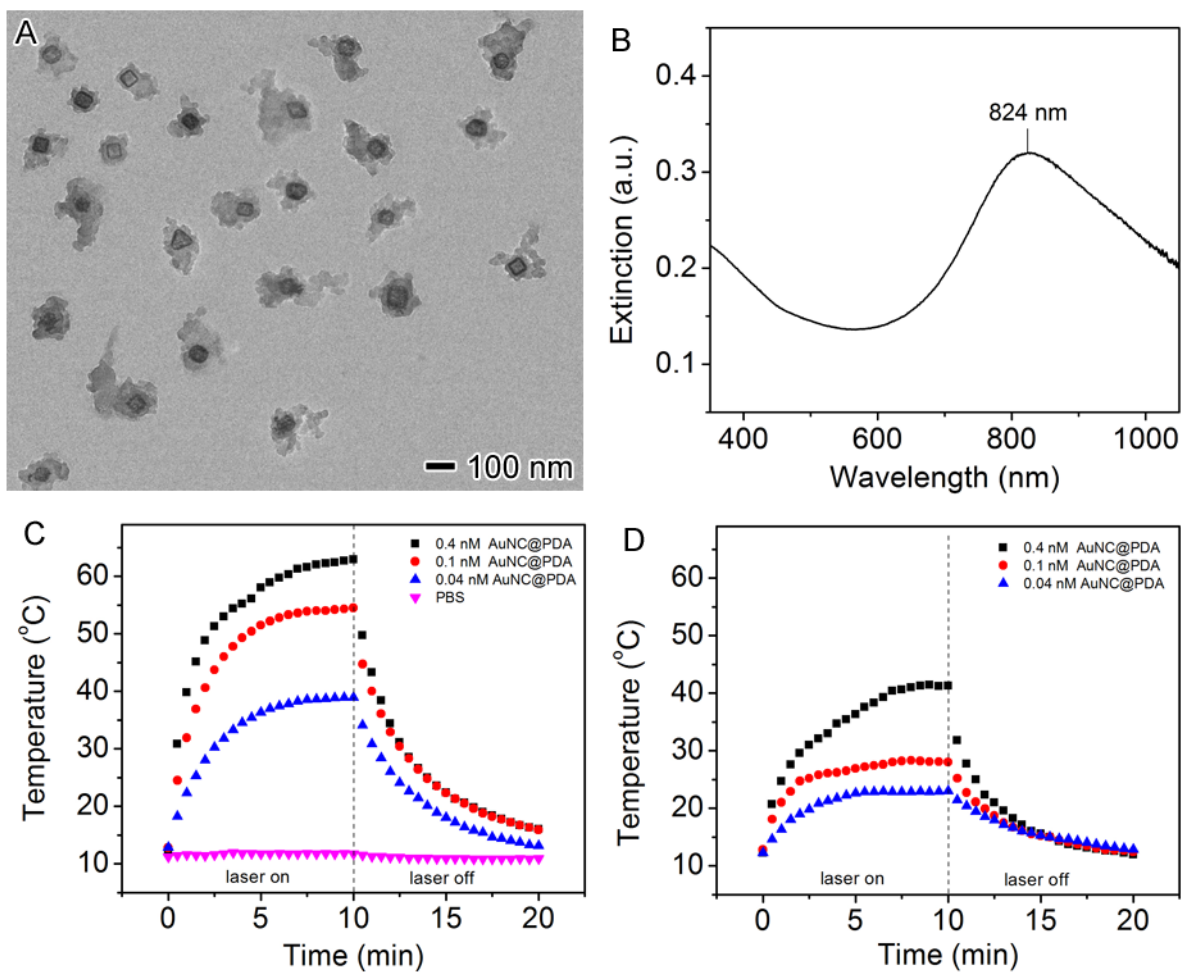
Figure 3. (A) TEM image of AuNC@PDA; (B) UV-Vis spectra of AuNC@PDA aqueous suspension. (C, D) Temperature profile of AuNC@PDA suspension in PBS as a function of time irradiated with an 808-nm diode laser at power density of (C) 1.67 W/cm^2 and (D) 0.83 W/cm^2.

Daptomycin is a cyclic lipopeptide consisting of a cyclic moiety of a 10 amino acid peptide with an N-terminal three amino acids protruding with an N-terminus containing a decanoyl fatty acyl side chain.[32] It can be loaded to AuNC@PDA through intermolecular interactions such as ionic (or electrostatic) interactions, hydrogen bonding, and dispersion forces (hydrophobic interactions). Dap has an isoelectric point (pI) of ~3.8,[33] and thus it carries a net positive charge at a pH < 3.8 while at a higher pH it carries a net negative charge. The zeta potential of AuNC@PDA is neutral at a pH ~3.0 and changes from negative to positive as pH decreases (**Fig. 4A**). At a pH above 3.0 but below 3.8, the cationic Dap and anionic PDA may form an ionic complex. On the other hand, Dap was found to aggregate *via* reversible "self-association" and the critical aggregation concentration (CAC) depends on pH.[34] At pH > 6.5, Dap remains a monomer while it forms aggregates of 16-20 molecules at a pH ≤ 5.0 with a CAC between 0.12 and 0.20 mM. Therefore, it is expected that the loading capacity increases at low pH due to the additional driving force of self-association as the concentration of Dap is higher than its CAC.

At a fixed concentration of 0.6 mM, Dap was loaded to 4 nM AuNC@PDA at pH of 7.8 or 2.2. After Dap loading, the PDA surface was functionalized with anti-SPA through catechol chemistry by conjugate addition of primary amine to the oxidized product of catechol (*o*-quinone).[35] The loading capacities of Dap were found to be 4 and 12 μg/mL of Dap in 0.4 nM of AuNC@PDA-anti-SPA using ultra-performance liquid chromatography (UPLC) (**Fig. S4A**). These values correspond to 6.2×10^3 and 1.9×10^4 Dap molecules per AuNC@PDA denoted as AuNC@Dap$_{Lo}$/PDA-anti-SPA and AuNC@Dap$_{Hi}$/PDA-anti-SPA, respectively. The UV-Vis spectra were essentially unchanged after Dap loading and anti-SPA conjugation with LSPR maxima at 819, 818, and 821 nm for AuNC@PDA-anti-SPA, AuNC@Dap$_{Lo}$/PDA-anti-SPA and AuNC@Dap$_{Hi}$/PDA-anti-SPA, respectively (**Fig. S4B**). The number of anti-SPA molecules on

the particle surface was quantified using a dye-labeled secondary IgG antibody. After dissolution

of AuNCs with KCN, the fluorescence intensity was measured and compared to a calibration

curve (**Fig. S4C**). The number of anti-SPA per AuNC was estimated to be 19, 28, and 13 for

AuNC-anti-SPA, AuNC@Dap_{Lo}/PDA-anti-SPA and AuNC@Dap_{Hi}/PDA-anti-SPA, respectively.

The efficiency of antibody conjugation averaged ~20% under the reaction conditions used. The

binding affinity was further analyzed by Scatchard plot and the disassociation constant (K_d) was

determined (**Fig. S4D**). The nonspecific interactions of Dap to AuNC@PDA are likely due to a

high affinity binding motif with K_d of 4.9 μM and a low affinity binding site with K_d of 230 μM.

Since the ionic complex of Dap and AuNC@PDA is unlikely to form at either pH, the increase

in loading capacity at low pH is likely attributable to self-association of Dap. Such aggregation is

reversible at elevated temperature, thus facilitating the photothermal release of Dap.[34, 36]

The light-triggered release of Dap was then examined under *in vitro* conditions. The Dap release

profile was established at a 0.4 nM concentration of AuNCs (**Fig. 4B**). When the laser was on,

the amount Dap released from the nanoconstructs gradually increased over time and reached

~2.6 and ~4.8 μg/mL at 10 min after irradiation at power density of 1.67 W/cm^2 for

AuNC@Dap_{Lo}/PDA-anti-SPA and AuNC@Dap_{Hi}/PDA-anti-SPA, respectively. In contrast, the

release of Dap without irradiation was <1 μg/mL for AuNC@Dap_{Lo}/PDA-anti-SPA and ~1

μg/mL for AuNC@Dap_{Hi}/PDA-anti-SPA. Additionally, the nanoconstructs were stable for at

least two months at 4°C with Dap released < 1 μg/mL. The corresponding temperature profiles of

the samples showed that the suspension temperature rapidly increased above 37 ^{o}C within 1-2

min of irradiation and reached a plateau at ~55°C 5 min after irradiation. Within the first two

minutes, the amount of Dap released was ~1 μg/mL. To rule out leakage at physiological

temperature, the samples were incubated at 37°C for 24 h and the amount of Dap released was

remained to be ~ 1 μg/mL, suggesting that this amount was likely due to background signal of the instrument.

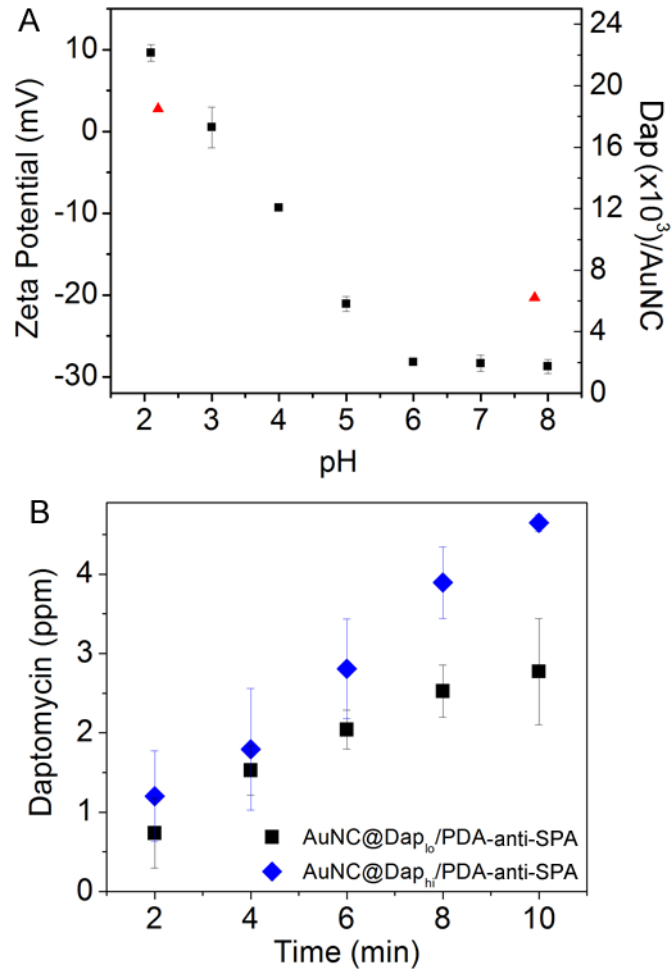**Figure 4.** (A) Zeta potential of AuNC@PDA and loading capacity of Dap as a function of pH. (B) Release profiles of Dap upon irradiation by a diode laser at 808 nm with a power density of 1.67 W/cm^2 at a concentration of 0.4 nM AuNCs with different Dap loading: 4 μg/mL or 6.2 × 10^3 Dap/AuNC (AuNC@Dap$_{Lo}$/PDA-anti-SPA, square) and 12 μg/mL or 1.9 × 10^4 Dap/AuNC (AuNC@Dap$_{Hi}$/PDA-anti-SPA, diamond).

Specific binding of the anti-SPA functionalized nanoconstructs was confirmed by two-photon luminescence imaging of *S. aureus* cells exposed to AuNC@PDA-anti-SPA by comparison to those exposed to AuNC@PDA and unexposed cells. *S. aureus* cells stained with 4',6-diamidino-2-phenylindole (DAPI) appeared blue, while AuNCs emitted light in the visible region when excited at the plasmon resonance (~800 nm) and appeared red.[37] These studies were done with the methicillin-sensitive *S. aureus* (MSSA) strain UAMS-1 and the MRSA strain LAC, which were chosen for these studies because they are distinct by comparison to each other at both the genetic and phenotypic levels, one example of the latter being that UAMS-1 produces protein A at high levels by comparison to LAC.[38-40]

For both UAMS-1 and LAC, the results confirmed co-localization of red and blue signals with *S. aureus* cells exposed to AuNC@PDA-anti-SPA (**Fig. 5, A and D**), suggesting that the AuNC@PDA-anti-SPA were attached to the cell surface. No co-localization was observed with *S. aureus* cells exposed to AuNC@PDA (**Fig. 5, B and E**). As an additional control, isogenic *spa* mutants that do not produce protein A were also examined in these experiments (**Fig. 5, C and F**). Quantitative analysis was performed by comparing the ratio of the pixel intensity from AuNC image (800 nm laser, red channel) to the pixel intensity of the DAPI image (700 nm laser, blue channel). The ratio intensities of fifty individual cells were averaged for each sample (**Fig. S5**). Significant differences were confirmed by comparing AuNC@PDA-anti-SPA to AuNC@PDA for both strains consistent with the qualitative visualization. Albeit at reduced levels, co-localization of blue and red signals was also observed in the *spa* mutants, which suggests additional biomarkers on the cell surface that bind anti-SPA. This was confirmed by western blot of conditioned medium using the same anti-SPA antibody used to produce our nanoconstructs (**Fig. S6**). In this respect it should be emphasized that SPA is an IgG-binding

160

protein and that *S. aureus* produces other such proteins, one example being Sbi.[41] More importantly, in the context of the therapeutic approach we propose, this could be viewed as an advantage as it would further enhance antibody targeting even in strains that produce relatively low levels of SPA.

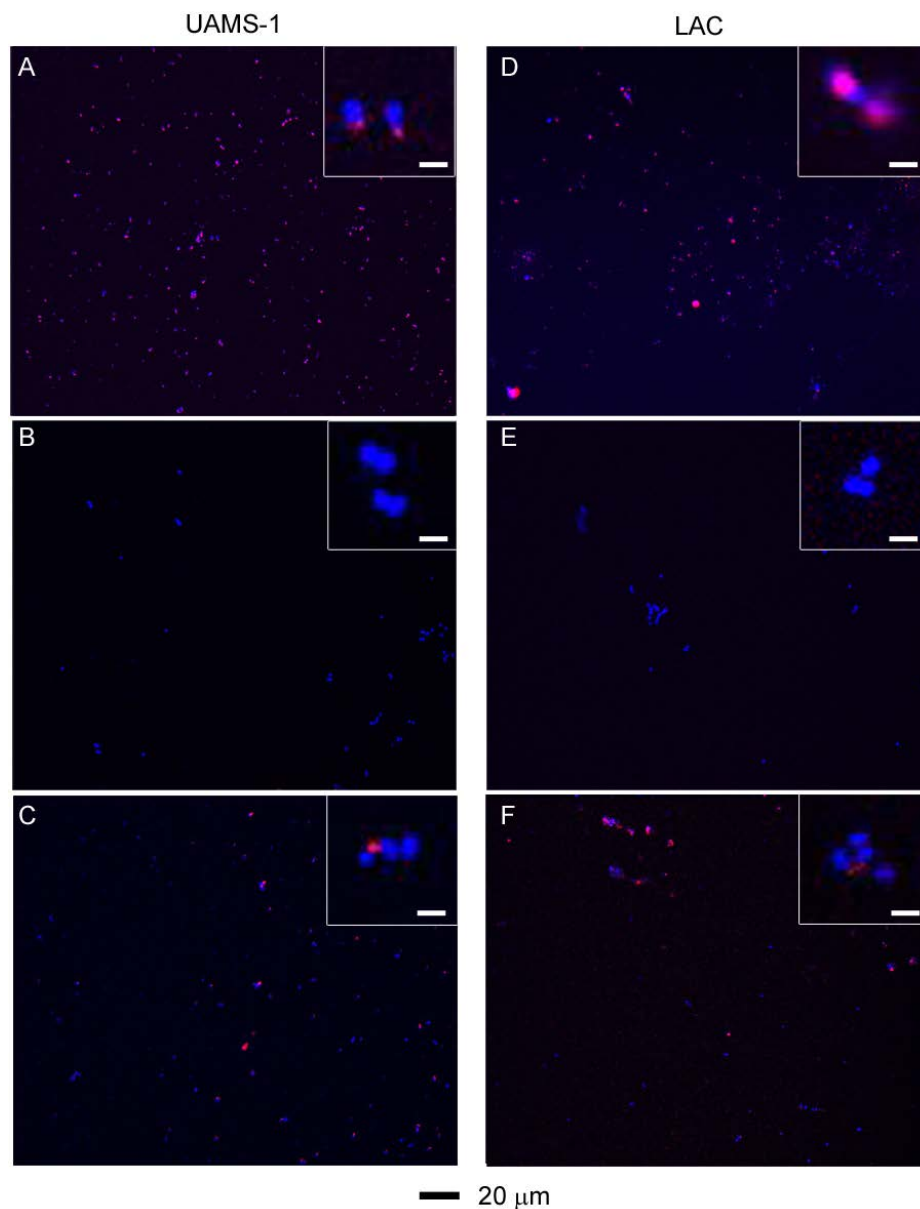**Figure 5.** Two-photon fluorescence images of *S. aureus* cells treated at different conditions: (A) UAMS-1 exposed to AuNC@PDA-anti-SPA; (B) UAMS-1 exposed to AuNC@PDA; (C) UAMS-1 *spa* mutant exposed to AuNC@PDA-anti-SPA; (D) LAC exposed to AuNC@PDA-anti-SPA; (E) LAC treated with AuNC@PDA; and (F) LAC *spa* mutant exposed to AuNC@PDA-anti-SPA;. Cells were stained with DAPI colored in blue. Luminescence of AuNCs was colored in red.

Killing efficacy of different AuNC nanoconstructs was assessed using a 96-well microtiter plate format. In control experiments carried out to establish a baseline for these studies, the *S. aureus* strain UAMS-1 was grown in tryptic soy broth (TSB) and diluted to an optical density (OD_{560}) of 0.05, which corresponds to 1×10^7 bacterial cells. As a control for the number of viable bacteria, expressed as colony-forming units or CFU, 180 µL of this suspension was placed in each well of a microtiter plate (1.8×10^6 CFU per well) without exposure to any nanoconstruct or laser irradiation. To make the volume in each well consistent with our other experiments, 20 µl of sterile TSB was then added to bring the total volume to 200 µL. A sample was then removed, appropriately diluted in TSB, and plated on tryptic soy agar (TSA) to determine the number of CFU. These studies confirmed the initial concentration of bacteria, while a sample taken after 24 h incubation at 37°C confirmed a concentration of 10^9 CFU/mL (**Fig. 6, group 1**). When *S. aureus* cells were exposed to Dap at a concentration of 5 µg/mL, which corresponds to 5 times the breakpoint minimum inhibitory concentration (MIC) that defines a daptomycin-sensitive strain of *S. aureus*,[19] the number of CFU remained unchanged at the immediate time point but decreased below the limit of detection after 24 h (**Fig. 6, group 2**).

Bacterial cells were also exposed to seven different nanoconstructs corresponding to the following experimental groups: 3) AuNC, 4) AuNC@PDA (no Dap loaded), 5) AuNC@Dap$_{Lo}$/PDA (4 µg/mL Dap loaded), and 6) AuNC@Dap$_{Hi}$/PDA (12 µg/mL Dap loaded), and 7-9) nanoconstructs 4-6 conjugated to anti-SPA antibody. The number of AuNCs used was 4.8×10^{10}, which corresponds to a ratio of $\sim 2.7 \times 10^4$ AuNCs per bacterial cell. Replicate samples (*n* = 3) confirmed little or no bacterial cell killing when *S. aureus* cells were exposed to any formulation of AuNC in the absence of laser irradiation (**Fig. 6, groups 3-9**). This confirms the absence of bacterial cell killing in the absence of irradiation even with the AuNC@Dap$_{Hi}$/PDA-

anti-SPA constructs. This is consistent with our results confirming that Dap release in the absence of laser irradiation (i.e. "dark release") was <1.0 µg/mL in the low Dap samples and ~1.0 µg/mL in the high Dap samples (see above), thus confirming minimal release of Dap in the absence of the temperature increase associated with laser irradiation. Based on these collective results, our interpretation of the studies described below in which irradiation was employed is that bacterial cell death observed immediately after exposure is indicative of PT-mediated effects, while those observed after 24 h is indicative of Dap release.

To assess bacterial cell killing as a function of laser irradiation, bacterial cells were exposed to the alternative nanoconstructs using the same concentration of bacterial cells and nanoconstructs. Replicate samples were then irradiated as detailed above in the context of assessing Dap release (10 min, 1.67 W/cm^2). Immediately after irradiation, a sample was taken to determine the relative number of CFU. The remainder of each sample was then incubated at 37°C for 24 h before taking a second sample. Significant reductions in bacterial viability were observed in all nanoconstruct-exposed cells with laser irradiation. This includes cells exposed to AuNC@PDA even without Dap loading or antibody conjugation (**Fig. 6, group 10**). However, in the absence of Dap loading, bacterial counts in one of three samples rebounded to those observed in the control group after 24 h incubation (**Fig. 6, group 1**). These results confirm a PT-mediated effect that reduced bacterial counts below the level of detection but did not completely clear all samples of viable bacteria. Support for this hypothesis comes from the observation that this rebound effect was not observed with AuNCs loaded with even the lower concentration of daptomycin (AuNC@DAP$_{Lo}$/PDA) (**Fig. 6, group 11**).

These results demonstrate a significant degree of bacterial cell killing even without antibody-mediated targeting. However, this must be interpreted in the context of the confined environment

of the wells of a microtiter plate. This is particularly true when considering the transition to *in vivo* use in which antibody-mediated localization is likely to be required to achieve selective targeting of bacterial cells within the complex milieu of the host. Based on this, we examined AuNC@PDA conjugated to anti-SPA antibodies (AuNC@PDA-anti-SPA). Based on CFU counts at the immediate time point, we achieved a 2-3 log reduction in CFU (**Fig. 6, group 12**), which for the reasons discussed above we attribute to PT-mediated effects. While significant, this reduction was less than that observed with unconjugated AuNC@PDA (**Fig. 6, groups 10 and 11**), suggesting antibody conjugation reduces bacterial cell killing due to PT effects. This is consistent with the observation that the temperature increase associated with laser irradiation was less with anti-SPA conjugated AuNCs by comparison to unconjugated AuNCs (**Fig. S7A**). As would be expected based on this, in the absence of daptomycin loading CFU counts rebounded in some samples to maximum levels after 24 hr incubation (**Fig. 6, group 12**). In contrast, this rebound effect was eliminated by daptomycin loading even at the lower concentration (**Fig. 6, groups 13 and 14**), thus confirming the therapeutic synergy of our approach.

These same trends were also observed with the methicillin-resistant *S. aureus* strain LAC, but LAC appeared to be even more sensitive to PT-mediated killing than UAMS-1. Specifically, a decrease in CFU of 3-4 logs was observed immediately after irradiation (AuNC@PDA-anti-SPA) (**Fig. 6, group 15**), while with daptomycin loading the number viable bacteria was below the level of detection at both the immediate and 24 hr time points (**Fig. 6, groups 16-17**). These results suggest that LAC is thermally more sensitive than UAMS-1 in the relevant temperature range of 50-55 $^{\circ}$C. This was subsequently confirmed in experiments in which each strain was exposed to 50 or 55 $^{\circ}$C and samples removed at 2 minute intervals to assess the decrease in CFU (**Fig. S7B**).
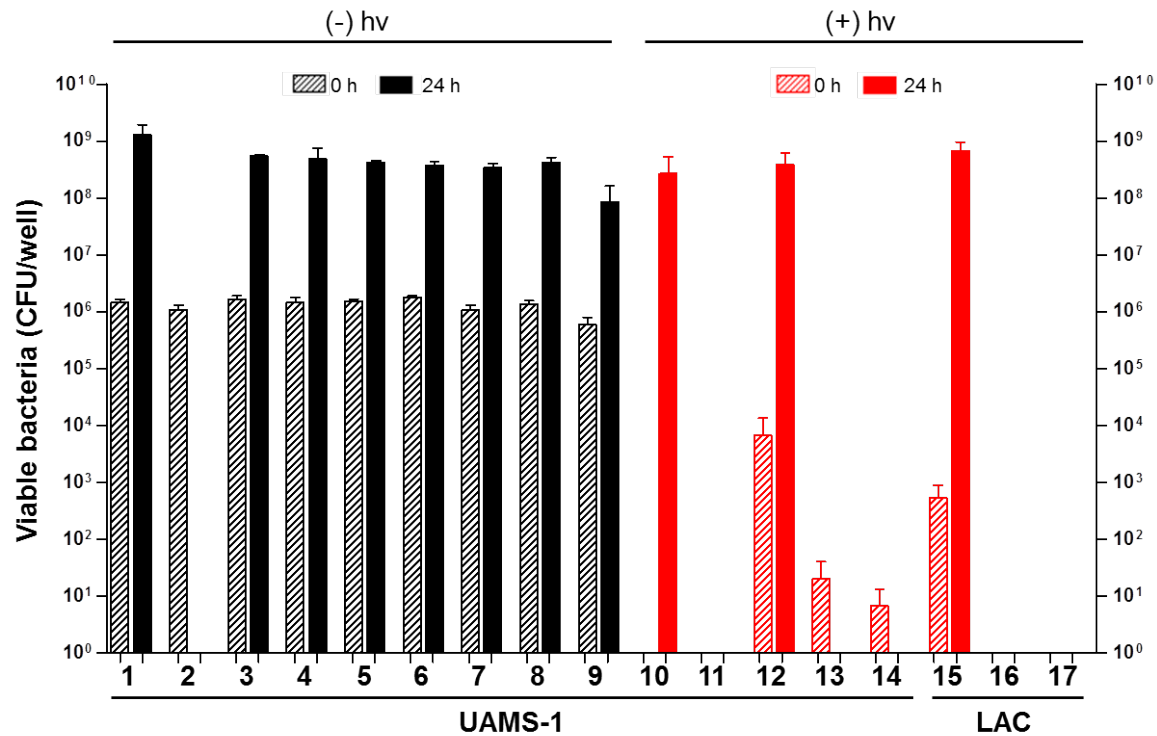
Figure 6. Viability of *S. aureus* cells exposed to different AuNC formulations without (black, groups 1-9) and with (red, groups 10-17) irradiation with a diode laser at 808 nm at a power density of 1.67 W/cm^2 for 10 min (right in red). CFU values were determined by plating samples 0 h and 24 h after treatment exposure to the indicated nanoconstructs and, where appropriate, laser irradiation. Group 1-14 were UAMS-1 cells exposed to (1) no treatment; (2) 5 μg/mL Dap; (3) AuNCs; (4) AuNC@PDA; (5) AuNC@Dap$_{Lo}$/PDA; (6) AuNC@Dap$_{Hi}$/PDA; (7) AuNC@PDA-anti-SPA; (8) AuNC@Dap$_{Lo}$/PDA-anti-SPA; (9) AuNC@Dap$_{Hi}$/PDA-anti-SPA; (10) AuNC@PDA; (11) AuNC@Dap$_{Lo}$/PDA; (12) AuNC@PDA-anti-SPA; (13) AuNC@Dap$_{Lo}$/PDA-anti-SPA; and (14) AuNC@Dap$_{Hi}$/PDA-anti-SPA. Group 15-17 were LAC cells treated with (15) AuNC@PDA-anti-SPA; (16) AuNC@Dap$_{Lo}$/PDA-anti-SPA; and (17) AuNC@Dap$_{Hi}$/PDA-anti-SPA.

Conclusion

We have demonstrated our ability to successfully synthesize antibiotic-loaded immuno-plasmonic nanoconstructs for use as novel antimicrobial agents. These AuNC-based nanoconstructs were effectively shown to convert NIR light into heat for PT killing of bacterial cells as well as thermally-controllable PDA expansion and antibiotic release. The therapeutic synergy of the nanoconstructs was confirmed for both the methicillin-sensitive *S. aureus* (MSSA) strain UAMS-1 and the methicillin-resistant *S. aureus* (MRSA) strain LAC. Although its utility against MRSA is perhaps particularly noteworthy given that these strains pose a particular clinical problem, it is also noteworthy in that LAC is representative of the USA300 clonal lineage of *S. aureus* isolates, which are characterized by high levels of expression of the accessory gene regulator (*agr*) and consequently relatively low levels of SPA production.[40] This demonstrates that this photoactivatable nanodrug provides a new platform for therapeutic synergy of PT and antibiotic treatment of diverse strains of *S. aureus* including those most commonly associated with highly-invasive community-associated infections.[2] Moreover, sensitivity and coverage for additional strains could potentially be increased even further by including additional antibodies either alone or in combination with each other.[15] Indeed, the technology we describe would be applicable to other bacterial pathogens, including the other ESKAPE pathogens, depending only on the availability of an appropriate pathogen-specific antibody and the ability to incorporate appropriate antibiotics into the AuNC formulation.

As in the treatment of cancer,[16] the dual therapeutic approach we describe has the potential to limit the amount of laser irradiation and potentially even the amount of antibiotic required to achieve the desired therapeutic effect, particularly given the highly localized nature of both PT effects and antibiotic release directly at the bacterial cell surface. Using a murine bacteremia

model, we previously demonstrated that, even without antibiotic loading, we could achieve significant bacterial killing using anti-SPA conjugated gold nanoconstructs and transdermal laser irradiation in the context of bacteria in the bloodstream.[15] However, this therapeutic synergy is likely to prove a very important consideration in the transition from *in vitro* studies to *in vivo* use in humans, particularly when attempting to achieve adequate laser irradiation through the skin in other types of infection including the deeper layers of an established biofilm. Thus, our results provide an important experimental foundation to pursue this transition in the context of diverse bacterial pathogens and diverse forms of bacterial infection, including those associated with biofilm formation.

Methods

Synthesis of antibiotic-loaded immuno-gold nanoconstructs. The AuNCs were synthesized by galvanic replacement reaction between Ag nanocubes and $HAuCl_4$ as previously described.[1] AuNC@PDA were prepared by self-polymerization of dopamine monomer on the surface of AuNCs under basic conditions in the presence of O_2. Briefly, 3 mL of 5 nM AuNCs were diluted to 200 mL using Tris-buffered saline (TBS, 20 mM Tris and 100 mM NaCl, pH = 9) in a 250-mL, 3-neck, round-bottom flask. The reaction flask was briefly flushed with O_2 and placed in a bath sonicator held at 4^oC with ice. Dopamine hydrochloride (0.2 mmol, 36.0 mg) was added to the flask, the vessel was sealed under 1 atm O_2, and the mixture was sonicated for 75 min until the LSPR had red-shifted ~50 nm. After this reaction, the product was collected by centrifugation at 7,000 rpm for 10 min, washed with H_2O twice and recovered by centrifugation at 14,000 rpm for 10 min at 4^oC. The AuNC@PDA were resuspended in H_2O at a concentration of 6 nM for characterization and future use.

Various amounts of daptomycin were loaded to the AuNC@PDA under different conditions to prepare daptomycin-loaded AuNC@PDA (AuNC@DAP/PDA). Briefly, 1 nM AuNC@PDA were incubated with 1 mg/mL of daptomycin (0.6 mM) in 10 mM citrate buffer (pH = 2.2 or 7.8) at various NaCl concentrations (0 mM, 150 mM, or 1 M). The reaction was allowed to stir overnight at 4^oC in the dark. The product was collected, purified with PBS once and H_2O 3 times, and re-collected by centrifugation at 14,000 rpm for 10 min to remove free daptomycin. The AuNC@DAP/PDA were resuspended in H_2O at a concentration of 4 nM AuNCs for characterization and future use.

Anti-SPA was conjugated to the surface of AuNC@DAP/PDA through the N-terminal amine by Michael addition reaction to form anti-SPA conjugated AuNC@DAP/PDA nanoconstructs

(AuNC@DAP/PDA-anti-SPA). Briefly, AuNC@DAP/PDA were dispersed in 1 mL of 10 mM bicene buffer (pH = 8.5) and 0.1 nmol of anti-SPA was added to the solution. The reaction was allowed to proceed at 4°C for 1 h. The nanoconstructs were collected and washed 3 times with PBS by centrifugation at 14,000 rpm for 5 min at 4°C. The nanoconstructs were dispersed in PBS for future use.

Two-photon imaging. Cultures of the *S. aureus* strains UAMS-1, LAC, and their isogenic *spa* mutants were grown to an optical density (OD_{560}) of 1.0 in tryptic soy broth (TSB), which corresponds to ~2×10^8 CFU/mL. This sample (40 μL) was applied to a glass microscope slide demarcated with a hydrophobic pen and allowed to air dry. Bacteria were heat fixed before adding 90 uL of PBS and 10 uL of AuNC@PDA-anti-SPA or AuNC@PDA. After 30 min at room temperature, reagents were removed by soaking in PBS 3 times for 10 min each time. The slide was blotted dry before adding 100 uL of 40× diluted DAPI (purchased as NucBlue Fixed Cell ReadyProbe Reagent, Molecular Probes) in PBS and incubating for 10 min. This stain was removed and the slides washed by soaking in fresh PBS 3 times for 5 min each time. The slides were blotted dry, 10 uL of PBS was used as a mounting medium, and a #2 coverslip was applied and sealed with nail polish. Two-photon images were acquired using customized, four channel, resonant scanning multiphoton microscopy platform (Thorlabs, USA) and a 40× water immersion 0.8 NA objective (Nikon). Illumination was provided by a Mai Tai HP ultra-fast Ti:Sapphire laser (Spectra Physics). DAPI fluorescence was visualized using 10 mW excitation at 700 nm and collecting from blue (466/40) channel. AuNC luminescence were visualized using 10 mW excitation at 800 nm and collecting from the red (607/70) channel. Images are the average of 200 frames and processed identically using ImageJ. The quantitative analysis was performed by comparing the ratio of the pixel intensity from AuNC image (800 nm laser, red

channel) to the pixel intensity of the DAPI image (700 nm laser, blue channel). The cells (n = 50) were analyzed and the ratio intensities were averaged for each sample.

Antimicrobial activity analysis. The *S. aureus* strains UAMS-1 and LAC were grown in tryptic soy broth (TSB) and diluted to an optical density (OD_{560}) of 0.05, which corresponds to 1×10^7 bacterial cells, using TSB supplemented with 2.5 mM $CaCl_2$, which is required for the *in vitro* bactericidal activity of daptomycin. This suspension (180 µL) was placed in each well of a microtiter plate (1.8×10^6 CFU per well). Prior to irradiation, the nanoconstruct suspension for each experimental group was sonicated (Bransonic 2800; Branson) and vortexed for 5 s to ensure homogenous dispersion. the appropriate nanoconstruct (20 µL) was then added to each well giving a final volume of 200 µL and a final AuNC concentration of 0.4 nM, which corresponds to 2.4×10^{11} AuNCs per mL. Thus, each well contained 4.8×10^{10} AuNCs, which corresponds to a ratio of ~2.4×10^5 AuNCs per bacterial cell. For irradiated groups, the contents of each well were mixed thoroughly and a Breathe-Easy gas permeable sealing membrane (Diversified Biotech) was used to seal the microtiter plate prior to irradiation, thus preventing evaporation. Plates containing irradiated groups were placed on ice and each treatment well was irradiated for 10 min by diode laser at 808 nm with a power of 0.75 W and a spot size of 0.30 cm^2 covering the surface area of a well. Immediately following irradiation, the sealing membrane was removed, the contents of each well were mixed thoroughly by pipetting, and a 50 µL aliquot was removed for bacterial quantification. For non-irradiated groups, a 50 µL aliquot was removed immediately after mixing of culture and the appropriate nanoconstruct for bacterial quantification. After removal of aliquots with or without laser irradiation, plates were re-sealed and incubated at 37 ºC with constant shaking (115 rpm). After 24 h, sealing membranes were removed, the contents of each well were mixed by pipetting, and a 50 µL aliquot was removed for bacterial quantification.

Bacterial quantification was performed by serial dilution and plate counts to enumerate viable bacteria based on colony-forming units (CFU) per well. This method allowed for simultaneous assessment of PT-mediated killing (quantification of samples immediately following irradiation) and laser-assisted daptomycin release (quantification of samples after 24 h incubation).

Acknowledgment

References

(1)   Bassetti, M.; Merelli, M.; Temperoni, C.; Astilean, A. New antibiotics for bad bugs: Where are we? Ann. Clinical Microbiology and Antimicrobials 2013, 12, 22.

(2)   Boucher, H. W.; Corey, G. R. Epidemiology of methicillin-resistant Staphylococcus aureus. Clinical Infectious Diseases 2008, 46, S344-S349.

(3)   Chambers, H. F.; DeLeo, F. R. Waves of resistance: Staphylococcus aureus in the antibiotic era. Nat. Rev. Micro. 2009, 7, 629-641.

(4)   Boucher, H. W.; Talbot, G. H.; Bradley, J. S.; Edwards, J. E.; Gilbert, D.; Rice, L. B.; Scheld, M.; Spellberg, B.; Bartlett, J. Bad bugs, no drugs: No ESKAPE! An update from the Infectious Diseases Society of America. Clinical Infectious Diseases 2009, 48, 1-12.

(5)   Römling, U.; Balsalobre, C. Biofilm infections, their resilience to therapy and innovative treatment strategies. J. Internal Medicine 2012, 272, 541-561.

(6)   Ray, P. C.; Khan, S. A.; Singh, A. K.; Senapati, D.; Fan, Z. Nanomaterials for targeted detection and photothermal killing of bacteria. Chem. Soc. Rev. 2012, 41, 3193-3209.

(7)   Hamblin, M. R.; Hasan, T. Photodynamic therapy: a new antimicrobial approach to infectious disease? Photochemical & Photobiological Sciences 2004, 3, 436-450.

(8)   Jori, G.; Fabris, C.; Soncin, M.; Ferro, S.; Coppellotti, O.; Dei, D.; Fantetti, L.; Chiti, G.; Roncucci, G. Photodynamic therapy in the treatment of microbial infections: Basic principles and perspective applications. Lasers in Surgery and Medicine 2006, 38, 468-481.

(9)   Berthiaume, F.; Reiken, S. R.; Toner, M.; Tompkins, R. G.; Yarmush, M. L. Antibody-targeted photolysis of bacteria In Vivo. Nat. Biotech. 1994, 12, 703-706.

(10)   Kharkwal, G. B.; Sharma, S. K.; Huang, Y.-Y.; Dai, T.; Hamblin, M. R. Photodynamic therapy for infections: Clinical applications. Lasers in Surgery and Medicine 2011, 43, 755-767.

(11)   Zharov, V. P.; Mercer, K. E.; Galitovskaya, E. N.; Smeltzer, M. S. Photothermal nanotherapeutics and nanodiagnostics for selective killing of bacteria targeted with gold nanoparticles. Biophys. J. 2006, 90, 619-627.

(12)   Norman, R. S.; Stone, J. W.; Gole, A.; Murphy, C. J.; Sabo-Attwood, T. L. Targeted photothermal lysis of the pathogenic bacteria, Pseudomonas aeruginosa, with gold nanorods. Nano Lett. 2008, 8, 302-306.

(13)   Levi-Polyachenko, N.; Young, C.; MacNeill, C.; Braden, A.; Argenta, L.; Reid, S. Eradicating group A Streptococcus bacteria and biofilms using functionalised multi-wall carbon nanotubes. Int. J. Hyperthermia 2014, 30, 490-501.

(14)   Zharov, V. P.; Galanzha, E. I.; Shashkov, E. V.; Kim, J.-W.; Khlebtsov, N. G.; Tuchin, V. V. Photoacoustic flow cytometry: principle and application for real-time detection of circulating single nanoparticles, pathogens, and contrast dyes in vivo. J. Biomed. Optics 2007, 12, 051503-051503-14.

(15)   Galanzha, E. I.; Shashkov, E.; Sarimollaoglu, M.; Beenken, K. E.; Basnakian, A. G.; Shirtliff, M. E.; Kim, J.-W.; Smeltzer, M. S.; Zharov, V. P. In vivo magnetic enrichment, photoacoustic diagnosis, and photothermal purging of infected blood using multifunctional gold and magnetic nanoparticles. PLoS ONE 2012, 7, e45557.

(16)   Shao, J.; Griffin, R. J.; Galanzha, E. I.; Kim, J.-W.; Koonce, N.; Webber, J.; Mustafa, T.; Biris, A. S.; Nedosekin, D. A.; Zharov, V. P. Photothermal nanodrugs: potential of TNF-gold nanospheres for cancer theranostics. Sci. Rep. 2013, 3, Artical number: 1293.

(17)   Archer, N. K.; Mazaitis, M. J.; Costerton, J. W.; Leid, J. G.; Powers, M. E.; Shirtliff, M. E. Staphylococcus aureus biofilms. Virulence 2011, 2, 445-459.

(18)   Anstead, G.; Cadena, J.; Javeri, H. Treatment of infections due to resistant

Staphylococcus aureus. In Methicillin-Resistant Staphylococcus Aureus (MRSA) Protocols, Ji, Y., Ed. Humana Press: 2014; Vol. 1085, pp 259-309.

(19)   Weiss, E. C.; Zielinska, A.; Beenken, K. E.; Spencer, H. J.; Daily, S. J.; Smeltzer, M. S. Impact of sarA on Daptomycin Susceptibility of Staphylococcus aureus Biofilms In Vivo. Antimicrobial Agents and Chemotherapy 2009, 53, 4096-4102.

(20)   Chen, J.; Wang, D.; Xi, J.; Au, L.; Siekkinen, A.; Warsen, A.; Li, Z.-Y.; Zhang, H.; Xia, Y.; Li, X. Immuno gold nanocages with tailored optical properties for targeted photothermal destruction of cancer cells. Nano Lett. 2007, 7, 1318-1322.

(21)   Chen, J.; Glaus, C.; Laforest, R.; Zhang, Q.; Yang, M.; Gidding, M.; Welch, M. J.; Xia, Y. Gold nanocages as photothermal transducers for cancer treatment. Small 2010, 6, 811-817.

(22)   Yavuz, M. S.; Cheng, Y.; Chen, J.; Cobley, C. M.; Zhang, Q.; Rycenga, M.; Xie, J.; Kim, C.; Song, K. H.; Schwartz, A. G. Gold nanocages covered by smart polymers for controlled release with near-infrared light. Nat. Mater. 2009, 8, 935-939.

(23)   Chen, J.; Yang, M.; Zhang, Q.; Cho, E. C.; Cobley, C. M.; Kim, C.; Glaus, C.; Wang, L. V.; Welch, M. J.; Xia, Y. Gold nanocages: A novel class of multifunctional nanomaterials for theranostic applications. Adv. Funct. Mater. 2010, 20, 3684-3694.

(24)   Zhang, Q.; Li, W.; Wen, L.-P.; Chen, J.; Xia, Y. Facile synthesis of Ag nanocubes of 30 to 70 nm in edge length with CF3COOAg as a precursor. Chem. Eur. J. 2010, 16, 10234-10239.

(25)   Postma, A.; Yan, Y.; Wang, Y.; Zelikin, A. N.; Tjipto, E.; Caruso, F. Self-polymerization of dopamine as a versatile and robust technique to prepare polymer capsules. Chem. Mater. 2009, 21, 3042-3044.

(26)   Dreyer, D. R.; Miller, D. J.; Freeman, B. D.; Paul, D. R.; Bielawski, C. W. Elucidating the structure of poly(dopamine). Langmuir 2012, 28, 6428-6435.

(27)   Liebscher, J.; Mrówczyński, R.; Scheidt, H. A.; Filip, C.; Hădade, N. D.; Turcu, R.; Bende, A.; Beck, S. Structure of polydopamine: A never-ending story? Langmuir 2013, 29, 10539-10548.

(28)   Loget, G.; Wood, J. B.; Cho, K.; Halpern, A. R.; Corn, R. M. Electrodeposition of polydopamine thin films for DNA patterning and microarrays. Anal. Chem. 2013, 85, 9991-9995.

(29)   Kreibig, U.; Vollmer, M. Optical Properties of Metal Clusters. Springer: Berlin, 1995; Vol. 25.

(30)   Lee, Y.; Park, T. G. Facile fabrication of branched gold nanoparticles by reductive hydroxyphenol derivatives. Langmuir 2011, 27, 2965-2971.

(31)   Osullivan, D. G. Vibrational frequency correlations in heterocyclic molecules. 7. Special features of a range of compounds possessing a benzene ring fused to a 5-membered ring. J. Chem. Soc. 1960, 3278-3284.

(32)   Zhang, T.; Muraih, J. K.; MacCormick, B.; Silverman, J.; Palmer, M. Daptomycin forms cation-and size-selective pores in model membranes. Biochim. Biophy. Acta (BBA) - Biomembranes 2014, 1838, 2425-2430.

(33)   Qiu, J.; Yu, L.; Kirsch, L. E. Estimated pKa values for specific amino acid residues in daptomycin. J. Pharm. Sci. 2011, 100, 4225-4233.

(34)   Qiu, J.; Kirsch, L. E. Evaluation of lipopeptide (daptomycin) aggregation using fluorescence, light scattering, and nuclear magnetic resonance spectroscopy. J. Pharm. Sci. 2014, 103, 853-861.

(35)   Ye, Q.; Zhou, F.; Liu, W. Bioinspired catecholic chemistry for surface modification. Chem. Soc. Rev. 2011, 40, 4244-4258.

(36)   Ferguson, W. E.; Smith, C. M.; Adams, E.; Barlow, G. H. The temperature-dependent self-association of adenosine 5'triphosphate in 0.154 M NaCl. Biophysical chemistry 1974, 1, 325-337.

(37)   Au, L.; Zhang, Q.; Cobley, C. M.; Gidding, M.; Schwartz, A. G.; Chen, J.; Xia, Y. Quantifying the cellular uptake of antibody-conjugated Au nanocages by two-photon microscopy and inductively coupled plasma mass spectrometry. ACS Nano 2009, 4, 35-42.

(38)   Beenken, K. E.; Mrak, L. N.; Griffin, L. M.; Zielinska, A. K.; Shaw, L. N.; Rice, K. C.; Horswill, A. R.; Bayles, K. W.; Smeltzer, M. S. Epistatic relationships between sarA and agr in Staphylococcus aureus biofilm formation. PLoS ONE 2010, 5, e10790.

(39)   Cassat, J. E.; Dunman, P. M.; McAleese, F.; Murphy, E.; Projan, S. J.; Smeltzer, M. S. Comparative genomics of Staphylococcus aureus musculoskeletal isolates. Journal of bacteriology 2005, 187, 576-592.

(40)   Cheung, G. Y.; Wang, R.; Khan, B. A.; Sturdevant, D. E.; Otto, M. Role of the accessory gene regulator agr in community-associated methicillin-resistant Staphylococcus aureus pathogenesis. Infection and Immunity 2011, 79, 1927-1935.

(41)   Smith, E. J.; Visai, L.; Kerrigan, S. W.; Speziale, P.; Foster, T. J. The Sbi protein is a multifunctional immune evasion factor of Staphylococcus aureus. Infection and Immunity 2011, 79, 3801-3809.

Appendix A: Supporting Information

Experimental Details

Chemicals and materials Silver trifluoroacetate (AgTFA), sodium hydrogen sulfide (NaSH), hydrochloric acid (HCl, 99.999%), tetrachloroauric acid trihydrate (HAuCl$_4$·3H$_2$O), sodium chloride (NaCl), and dopamine hydrochloride (99%) were purchased from Alfa Aesar. Poly(vinylpyrrolidone) (PVP, M.W.=55,000), phosphate-buffered saline (PBS), tris(hydroxymethyl)aminomethane hydrochloride (Tris-HCl), tris(hydroxymethyl)aminomethane (Tris), citric acid, trisodium citrate dehydrate, bicine, and anti-protein A antibody (catalog number P3775) were purchased from Sigma Aldrich. Ethylene glycol (EG) was purchased from J.T. Baker. Acetone was purchased from EMD. Daptomycin was purchased from Cubist Pharmaceuticals. All experiments were performed using 18 MΩ H$_2$O unless specified otherwise. All chemicals were used as received.

Synthesis of Au nanocages (AuNCs). The AuNCs were synthesized by galvanic replacement reaction between Ag nanocubes and HAuCl$_4$ as previously described.[1] First, Ag nanocubes were synthesized by the polyol method.[2] Briefly, 50 mL EG was added to a 250-mL round-bottom flask equipped with a stirring bar and placed in an oil bath at 150°C. After the temperature equilibrated (30~45 min), EG solutions of 0.6 mL of 3 mM NaHS, 5 mL of 3 mM HCl, 12.5 mL of PVP (0.25 g), and 4 mL of 282 mM AgTFA were sequentially added to the reaction flask. Once the LSPR peak reached ~440 nm (~35 min after addition of AgTFA), the reaction was quenched in an ice bath. Upon cooling, the product was collected by adding acetone to the reaction solution at a ratio of 5:1 and centrifuging at 7,000 rpm for 10 min. The resulting pellet was purified twice with H$_2$O and collected by centrifugation at 15,000 rpm for 10 min, and resuspended in 10 mL of H$_2$O for future use.

To synthesize AuNCs, 10 mL of H$_2$O was heated to boiling in a 50-mL round-bottom flask

equipped with a stirring bar. To the boiling liquid, 1 mL of the Ag nanocubes described above was added and subsequently 1 mM $HAuCl_4$ was added using a syringe pump at a rate of 45 mL/h until the LSPR maximum was at 750 nm. The AuNCs were purified by saturated NaCl solution to remove by-product AgCl, washed 3 times by centrifugation at 15,000 rpm for 10 min, and resuspended in H_2O at a concentration of 5 nM for future use.

Synthesis of polydopamine-coated AuNCs (AuNC@PDA). AuNC@PDA were prepared by self-polymerization of dopamine monomer on the surface of AuNCs under basic conditions in the presence of O_2. Briefly, 3 mL of 5 nM AuNCs were diluted to 200 mL using Tris-buffered saline (TBS, 20 mM Tris and 100 mM NaCl, pH = 9) in a 250-mL, 3-neck, round-bottom flask. The reaction flask was briefly flushed with O_2 and placed in a bath sonicator held at 4°C with ice. Dopamine hydrochloride (0.2 mmol, 36.0 mg) was added to the flask, the vessel was sealed under 1 atm O_2, and the mixture was sonicated for 75 min until the LSPR had red-shifted ~50 nm. After this reaction, the product was collected by centrifugation at 7,000 rpm for 10 min, washed with H_2O twice and recovered by centrifugation at 14,000 rpm for 10 min at 4°C. The AuNC@PDA were resuspended in H_2O at a concentration of 6 nM for characterization and future use.

Loading of daptomycin. Various amounts of daptomycin were loaded to the AuNC@PDA under different conditions to prepare daptomycin-loaded AuNC@PDA (AuNC@DAP/PDA). Briefly, 1 nM AuNC@PDA were incubated with 1 mg/mL of daptomycin (0.6 mM) in 10 mM citrate buffer (pH = 2.2 or 7.8) at various NaCl concentrations (0 mM, 150 mM, or 1 M). The reaction was allowed to stir overnight at 4°C in the dark. The product was collected, purified with PBS once and H_2O 3 times, and re-collected by centrifugation at 14,000 rpm for 10 min to remove free daptomycin. The AuNC@DAP/PDA were resuspended in H_2O at a concentration of 4 nM

177

AuNCs for characterization and future use. Prior to quantification of daptomycin concentration, AuNCs were digested by KCN to avoid interference. The dissociation constant (K_d) for daptomycin and AuNC@PDA in PBS was determined by Scatchard plot.

Conjugation of anti-protein A antibody (anti-SPA). Anti-SPA was conjugated to the surface of AuNC@DAP/PDA through the N-terminal amine by Michael addition reaction to form anti-SPA conjugated AuNC@DAP/PDA nanoconstructs (AuNC@DAP/PDA-anti-SPA). Briefly, AuNC@DAP/PDA were dispersed in 1 mL of 10 mM bicene buffer (pH = 8.5) and 0.1 nmol of anti-SPA was added to the solution. The reaction was allowed to proceed at 4°C for 1 h. The nanoconstructs were collected and washed 3 times with PBS by centrifugation at 14,000 rpm for 5 min at 4°C. The number of anti-SPA per nanoconstruct was determined by the use of the secondary antibody, fluorescein isothiocyanate-labeled IgG (FITC-IgG). The nanoconstructs were dispersed in PBS for future use.

Characterization of nanoconstructs. Transmission electron microscopy (TEM) images were captured using a TEM microscope (JEOL 100cx) with an accelerating voltage of 100 kV. The hydrodynamic diameters and zeta potentials of nanoconstructs were determined using a dynamic light scattering instrument (Brookhaven ZetaPALS). The concentration of metals was determined using an atomic absorption (AA) spectrometer (GBC 932). UV‑Vis spectra were taken on a UV‑Vis spectrophotometer (Agilent Cary 50). Fluorescence spectra were recorded on a fluorimeter (Horiba FluoroLog3). Infra-red spectra were collected on Fourier Transform infra-red spectrometer (FTIR, Bruker Tensor 27).

Two-photon imaging. Cultures of the *S. aureus* strains UAMS-1, LAC, and their isogenic *spa* mutants were grown to an optical density (OD_{560}) of 1.0 in tryptic soy broth (TSB), which corresponds to ~2×10^8 CFU/mL. This sample (40 μL) was applied to a glass microscope slide

demarcated with a hydrophobic pen and allowed to air dry. Bacteria were heat fixed before adding 90 uL of PBS and 10 uL of AuNC@PDA-anti-SPA or AuNC@PDA. After 30 min at room temperature, reagents were removed by soaking in PBS 3 times for 10 min each time. The slide was blotted dry before adding 100 uL of 40× diluted DAPI (purchased as NucBlue Fixed Cell ReadyProbe Reagent, Molecular Probes) in PBS and incubating for 10 min. This stain was removed and the slides washed by soaking in fresh PBS 3 times for 5 min each time. The slides were blotted dry, 10 uL of PBS was used as a mounting medium, and a #2 coverslip was applied and sealed with nail polish. Two-photon images were acquired using customized, four channel, resonant scanning multiphoton microscopy platform (Thorlabs, USA) and a 40× water immersion 0.8 NA objective (Nikon). Illumination was provided by a Mai Tai HP ultra-fast Ti:Sapphire laser (Spectra Physics). DAPI fluorescence was visualized using 10 mW excitation at 700 nm and collecting from blue (466/40) channel. AuNC luminescence were visualized using 10 mW excitation at 800 nm and collecting from the red (607/70) channel. Images are the average of 200 frames and processed identically using ImageJ. The quantitative analysis was performed by comparing the ratio of the pixel intensity from AuNC image (800 nm laser, red channel) to the pixel intensity of the DAPI image (700 nm laser, blue channel). The cells (n = 50) were analyzed and the ratio intensities were averaged for each sample.

Release of daptomycin. The release of daptomycin from the AuNC@DAP$_{Lo}$/PDA and AuNC@DAP$_{Hi}$/PDA was carried out at neutral pH under the near-infrared irradiation. Briefly, each construct was suspended in 200 μL PBS (pH = 7.4) at a concentration of 0.4 nM on ice. Samples were irradiated by an 808-nm diode laser at a power density of 1.66 W/cm^2 for different periods of time up to 10 min. After irradiation, the samples were centrifuged briefly at 14,000 rpm for 3 min at 4°C and the supernatants were collected. The concentration of daptomycin was

then analyzed by ultra-performance liquid chromatography (UPLC, Waters Acquity). As controls, a solution containing daptomycin and, if applicable, nanoconstructs digested with KCN, were also evaluated by UPLC. Elution was performed using a mobile phase consisting of a gradient (90:10 to 10:90) of H_2O and acetonitrile (1% trifluoroacetate) through a phenyl stationary phase (BEH phenyl, Acquity) at a flow rate of 0.2 mL/min with ultraviolet detection at 262 nm. Daptomycin eluted after 3.5 min and peak integral was linear over the concentrations tested.

Thermal curve assessment. The temperature measurement was performed under the same conditions described above for assessment of daptomycin release, with temperature changes as a function of time recorded by a thermal couple inserted into the 200 µL suspension or an infrared sensor .

Western blot analysis. Relative amounts of extracellular protein A (eSpa) was assessed using standardized cell-free supernatants as previously described.[3] Briefly, eSpa was detected by Western blot using rabbit anti-Protein A (Sigma Chemical Co., St. Louis, MO) at a 1:4000 dilution as primary antibody. Secondary antibody was horseradish peroxidase (HRP)-conjugated goat anti-rabbit IgG (Sigma Chemical Co., St. Louis, MO). Blots were developed using SuperSignal West Femto Chemiluminescent Substrate kit (Thermo Fisher Scientific, Rockford, IL).

Antimicrobial activity analysis. The *S. aureus* strains UAMS-1 and LAC were grown in tryptic soy broth (TSB) and diluted to an optical density (OD_{560}) of 0.05, which corresponds to 1×10^7 bacterial cells, using TSB supplemented with 2.5 mM $CaCl_2$, which is required for the *in vitro* bactericidal activity of daptomycin. This suspension (180 µL) was placed in each well of a microtiter plate (1.8×10^6 CFU per well). Prior to irradiation, the nanoconstruct suspension for

each experimental group was sonicated (Bransonic 2800; Branson) and vortexed for 5 s to ensure homogenous dispersion. the appropriate nanoconstruct (20 µL) was then added to each well giving a final volume of 200 µL and a final AuNC concentration of 0.4 nM, which corresponds to 2.4×10^{11} AuNCs per mL. Thus, each well contained 4.8×10^{10} AuNCs, which corresponds to a ratio of ~2.4×10^5 AuNCs per bacterial cell. For irradiated groups, the contents of each well were mixed thoroughly and a Breathe-Easy gas permeable sealing membrane (Diversified Biotech) was used to seal the microtiter plate prior to irradiation, thus preventing evaporation. Plates containing irradiated groups were placed on ice and each treatment well was irradiated for 10 min by diode laser at 808 nm with a power of 0.75 W and a spot size of 0.30 cm^2 covering the surface area of a well. Immediately following irradiation, the sealing membrane was removed, the contents of each well were mixed thoroughly by pipetting, and a 50 µL aliquot was removed for bacterial quantification. For non-irradiated groups, a 50 µL aliquot was removed immediately after mixing of culture and the appropriate nanoconstruct for bacterial quantification. After removal of aliquots with or without laser irradiation, plates were re-sealed and incubated at 37 ºC with constant shaking (115 rpm). After 24 h, sealing membranes were removed, the contents of each well were mixed by pipetting, and a 50 µL aliquot was removed for bacterial quantification. Bacterial quantification was performed by serial dilution and plate counts to enumerate viable bacteria based on colony-forming units (CFU) per well. This method allowed for simultaneous assessment of PT-mediated killing (quantification of samples immediately following irradiation) and laser-assisted daptomycin release (quantification of samples after 24 h incubation).

Figure S1. (A) TEM image of AuNCs synthesized by galvanic replacement of Ag nanocubes with chloroauric acid; and (B) UV-Vis spectrum of the AuNC aqueous suspension corresponding to the sample shown in (A).
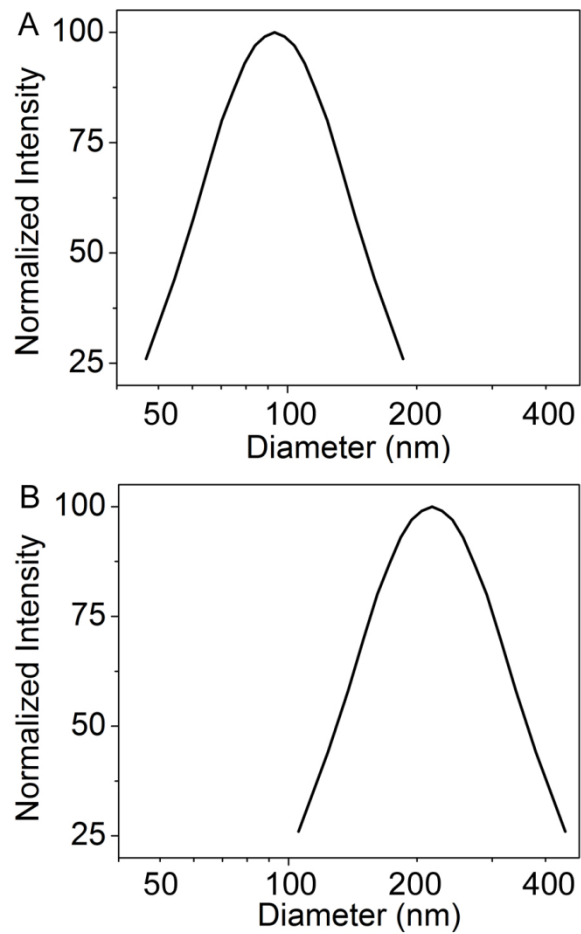
Figure S2. Histogram of hydrodynamic diameter of aqueous suspensions measured by dynamic light scattering: (A) AuNCs; and (B) AuNC-PDA.
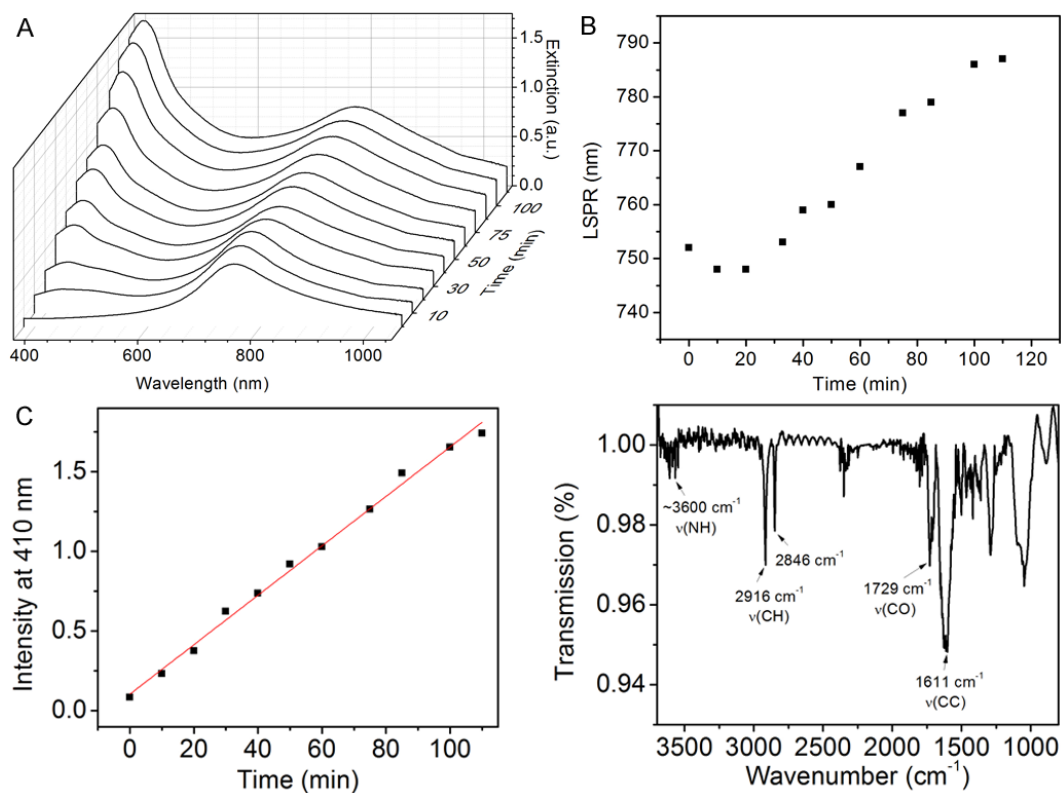
Figure S3. (A) UV-Vis spectroscopic monitoring of the reaction solution during self-polymerization process of dopamine on the surface of AuNCs; (B) LSPR shift of AuNCs as a function of reaction time; (C) Absorbance change at 410 nm as a function of time with the red line indicated a linear fit of $y = 0.0155x + 0.105$ ($R^2 = 0.994$).
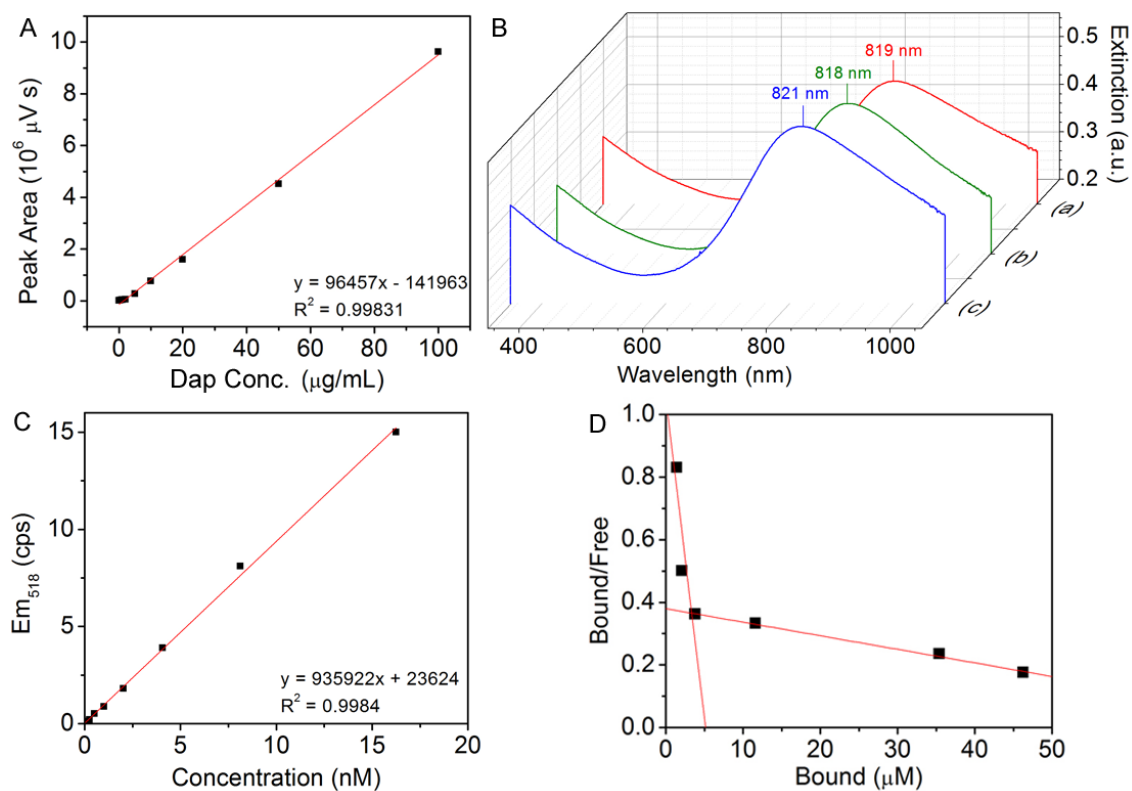
Figure S4. (A) Calibration curve of Dap concentration using UPLC; (B) UV-Vis spectra of AuNC@PDA-anti-SPA (blue), AuNC@Dap$_{Lo}$/PDA-anti-SPA (green) and AuNC@Dap$_{Hi}$/PDA-anti-SPA (red); (C) Calibration curve of dye-labeled IgG using fluorometer; and (D) Scatchard plot to analyze binding affinity of Dap to PDA (ratio of bound Dap to free Dap versus bound Dap).
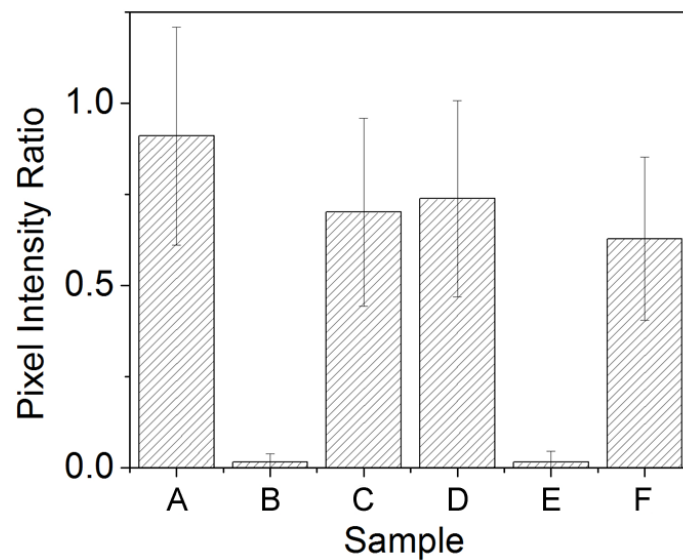
Figure S5. Quantitative analysis of two-photon fluorescence images by pixel intensity ratio of AuNCs (red channel) to DAPI (blue channel) for each sample corresponding to the images in **Figure 5**, A-F.
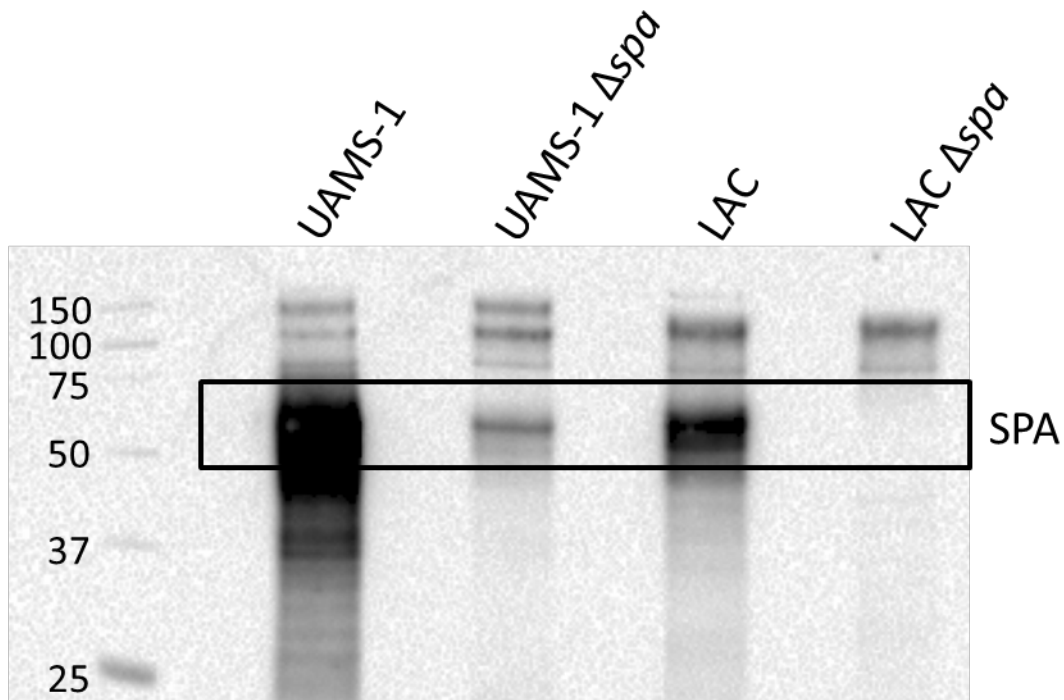
Figure S6. Western blot analysis of *spa* mutants. Supernatants from stationary phase cultures of the indicated strains were resolved by SDS-PAGE, transferred to nitrocellulose, and blotted with anti-Spa antibody. The boxed region indicates the molecular weight range expected of protein A (SPA). Although protein A is an LPXTG-anchored surface protein, supernatants were used for this experiment because it is also known to be released into the supernatant in amounts that quantitatively reflect its overall production level in different strains.[3]
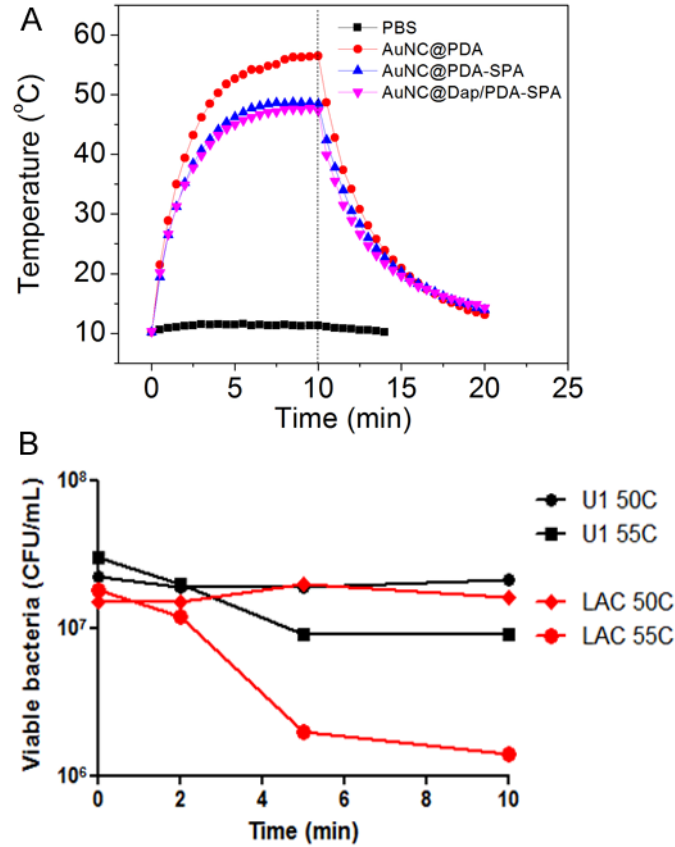
Figure S7. (A) Temperature profile of 0.4 nM suspensions of the indicated AuNC formulations as a function of time of irradiation with an 808-nm diode laser at power density of 1.67 W/cm^2. (B) Relative thermal sensitivity of UAMS-1 (U1) and LAC. Bacterial cells were suspended in PBS and exposed to the indicated temperatures before removing aliquots to assess viability.

References:

(1) Chen, J.; Yang, M.; Zhang, Q.; Cho, E. C.; Cobley, C. M.; Kim, C.; Glaus, C.; Wang, L. V.; Welch, M. J.; Xia, Y. Gold nanocages: A novel class of multifunctional nanomaterials for theranostic applications. Adv. Funct. Mater. 2010, 20, 3684-3694.

(2) Zhang, Q.; Li, W.; Wen, L.-P.; Chen, J.; Xia, Y. Facile synthesis of Ag nanocubes of 30 to 70 nm in edge length with CF_3COOAg as a precursor. Chem. Eur. J. 2010, 16, 10234-10239.

(3) Mrak, L. N.; Zielinska, A. K.; Beenken, K. E.; Mrak, I. N.; Atwood, D. N.; Griffin, L. M.; Lee, C. Y.; Smeltzer, M. S. saeRS and sarA act synergistically to repress protease production and promote biofilm formation in Staphylococcus aureus. PLoS ONE 2012, 7, e38453.

Chapter VI. Gold-Copper Alloyed Nanorods for Metal-catalyzed Organic Reactions: Implication of Surface Ligands on Nanoparticle-based Heterogeneous Catalysis[*]

Abstract

Recent advances in nanoparticle synthesis have created new potential avenues for aqueous catalysis of organic reactions. Morphological control of metal nanoparticles often involves the use of surface ligands, which in turn affect the catalytic activity of nanocatalysts. This Letter demonstrates that surface anchoring group, chain length, and configuration of the water-soluble, polymeric ligands influence the catalytic properties of alloyed $AuCu_3$ nanorods for metal-catalyzed organic reactions. Due to the binding affinity of the surface-anchoring groups, a thiol anchor was found to be detrimental the Au-catalyzed reduction of *p*-nitrophenol while the Cu-catalyzed azide–alkyne cycloaddition was severely inhibited by amine anchors. Furthermore, the catalytic activity of nanorods increased with increased dimension of the ligands with the same anchoring group due to the reduction of graft density. Elevated temperature facilitates the mobility of surface ligands in benzonitrile hydration to benzamide, resulting in the enhancement of catalytic activity. This work highlights the paramount importance of surface ligand selection in the design of nanocatalysts for catalytic organic reactions.

Introduction

Metal nanoparticles have received considerable attention as heterogeneous catalysts in the past two decades due to their extremely large surface-to-volume ratio compared to their bulk counterparts.[1] Uniform nanoparticle suspensions are considered as the bridge between traditional homogenous and heterogeneous catalysis. Nanoparticle catalysts have demonstrated the capacity to catalyze reactions in H_2O, at relatively low temperatures, under normal atmosphere.[2] These catalysts can be readily recovered by centrifugation, therefore they can be recycled. Numerous efforts have been made to synthesize metal nanoparticles with controllable size and shape which, in turn, tune their catalytic activity.[3] In order to manipulate the morphology, surface ligands are deployed in the synthesis and the resultant nanoparticles are capped by a monolayer of these ligands. The binding affinity of these ligands to the surface plays an important role in the catalytic activity of the nanoparticles in heterogeneous catalysis because the reactant molecules are activated on the nanoparticle surface.[4–6]

Ligand exchange is used as the first step in many phase transfer processes designed to retain surface activity of nanomaterials. In this Letter, we correlate the catalytic activities of aqueous, surface-capped Au–Cu alloyed nanorods to polymeric ligands with different functional groups, molecular weights, and configurations for organic reactions. This correlation allows us to choose and design surface ligand to retain and further enhance the catalytic activity of the nanoparticles. Coinage metals, such as Au and Cu, have been demonstrated for numerous catalytic processes.[1] Alloying Au and Cu enables synergy of their catalytic properties, and thus Au–Cu alloys are better catalysts than Au or Cu alone for many important reactions such as CO oxidation,[7] propene epoxidation,[8] and benzyl alcohol oxidation.[9]

Additionally, using these alloys can defray the cost of pure Au materials and reduce the

reactivity of Cu with air.[10] The catalytic activity can be further altered by modifying the morphology of the nanoparticles. For example, we have demonstrated that the rod-shaped $AuCu_3$ nanoparticles are approximately ten-fold more active than spherical nanoparticles with the same composition and surface area.[11] The $AuCu_3$ nanoparticles absorb visible or near-infrared light, which may generate singlet oxygen,[12] which could be used in an alternative approach for organic syntheses developed by Prof. Harry Wasserman,[13] including bipyrrole aldehyde,[14] an intermediate in the total synthesis of prodigiosenes.[15,16] Herein, we use the $AuCu_3$ nanorods ($AuCu_3NRs$) as model catalysts to study the influence of surface ligands on their catalytic activity. Three metal-catalyzed reactions are chosen for this study: Au-catalyzed *p*-nitrophenol reduction, Cu-catalyzed alkyne–azide 'click' cycloaddition, and metal-catalyzed nitrile hydration, all of which are important reactions for the synthesis of intermediates in drug discovery. The binding affinity of polymeric ligands to Au and Cu surfaces is correlated to their catalytic activity for these three reactions.

Results and Discussion

The $AuCu_3NRs$ were synthesized by alkylamine reduction as previously described.[11] Briefly, $HAuCl_4$ was reduced at 140 °C for 20 min in tetradecylamine under protection of Ar to generate Au seed particles. The reaction temperature was increased to 210 °C and copper acetylacetonate (4:1 mol ratio Cu–Au) dissolved in oleylamine was injected. The reaction was allowed to proceed for another 20 min to form $AuCu_3NRs$. **Figure 1A** shows the transmission electron microscopy (TEM) image of typical $AuCu_3NRs$, having an average length of 25.0 ± 2.1 nm and diameter of 11.2 ± 1.0 nm, equal to an aspect ratio of ~2. The powder X-ray diffraction (XRD) pattern verified that the $AuCu_3NRs$ adopted face-centered-cubic (fcc) crystal structure, suggesting a random alloy of Au and Cu (**Fig. 1B**). The peaks at 42.1, 48.2, and 71.3 ° were

assigned to (1 1 1), (2 0 0), and (2 2 0) crystallographic planes of fcc structure. The composition (1:3 ratio Au to Cu) of the AuCu$_3$NRs was confirmed by analyzing the most prominent peak of the (1 1 1) plane using Vegard's law. **Figure 1C** shows the optical spectrum of the AuCu$_3$NRs with an extinction peak at 670 nm. To obtain water-soluble catalysts, ligand exchange was performed in CHCl$_3$, followed by transferring into aqueous solution using ethanol as a phase transfer intermediary.[11,17] After phase transfer, the AuCu$_3$NRs were well-dispersed in aqueous solution and there was little change in their optical spectra. The concentrations of Au and Cu were measured by flame atomic absorbance spectroscopy.
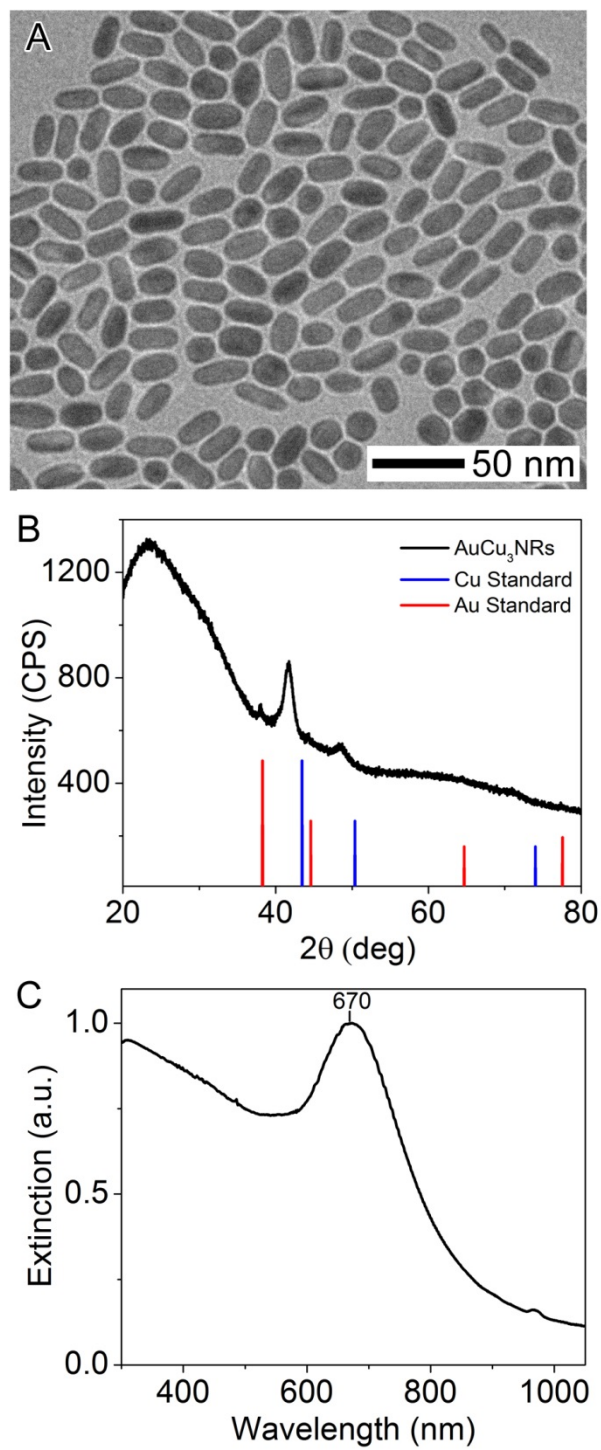
Figure 1. Characterization of AuCu₃NRs: (A) TEM image; (B) XRD pattern; and (C) extinction spectrum.

Water-soluble polymers were used to replace the alkylamines capping the surface of the AuCu$_3$NRs, yielding water-soluble catalysts. **Table 1** lists the water-soluble polymers including linear poly(ethylene glycol) (PEG) and branched poly(ethyleneimine) (PEI). PEG (M.W. = 5000) terminated with amine (–NH$_2$), thiol (–SH), and carboxylic acid (–COOH) functional groups were chosen for the study, named as PEG-NH$_2$, PEG-SH, or PEG-COOH. The amine group has a high affinity to coordinate with Cu while the thiol group strongly interacts with Au surface. The carboxylic acid group loosely attaches to both Cu and Au surfaces. The effect of multidentate binding to the surface is compared using PEI which contains multiple amino groups. The influence of steric hindrance is studied using PEG and PEI with different molecular weights. To investigate the effects of capping-ligand effects on the catalytic properties, Au-catalyzed *p*-nitrophenol reduction, Cu-catalyzed alkyne–azide 'click' cycloaddition, and metal-catalyzed nitrile hydration were selected to test the hypotheses.

Table 1. Summary of aqueous AuCu$_3$NRs capped by different polymeric ligands

AuCu$_3$NR sample name	Ligand	Terminus	M.W. (Da)	Au/Cu (mol/mol)
PEG-NH$_2$	poly(ethylene glycol)	-NH$_2$	5000	0.41
PEG750	poly(ethylene glycol)	-NH$_2$	750	0.40
PEG-SH	poly(ethylene glycol)	-SH	5000	0.46
PEG-COOH	poly(ethylene glycol)	-COOH	5000	0.43
PEI10000	poly(ethyleneimine)	branched, -NH$_2$	10000	0.55
PEI600	poly(ethyleneimine)	branched, -NH$_2$	600	0.54

The NaBH$_4$ reduction of *p*-nitrophenol (more accurately, *p*-nitrophenolate) is a well-studied model reaction for nanoparticle-based catalysis (**Scheme 1**).[18] Compared to Cu, Au can catalyze the p-nitrophenol reduction more efficiently.[19] The reduction process can be monitored by the loss of absorbance at 400 nm corresponding to the disappearance of *p*-nitrophenolate.[19] The reaction proceeds through two steps: an induction period (t_0) wherein the surface of the particle is reconstructed to activate the adsorbed reactant molecules and a catalytic period (k_{cat}) where the reaction follows first-order kinetics with respect to *p*-nitrophenol concentration.[20] In the absence of metal nanoparticles the reaction had not proceeded after 2 h incubation (**Fig. S1**). **Table 2** lists the results derived from the UV–Vis spectroscopic analysis. **Figure 2** shows the UV–Vis spectroscopic monitoring of the reaction process in the presence of ligand-capped AuCu$_3$NRs. The induction period was found to be 3.7, 3.9, and 17.7 min for the PEG-NH$_2$, PEG-COOH, and PEG-SH and the k_{cat} (s^{-1}) was determined to be 0.0048, 0.0033, and 0.0022, respectively, for 1 ppm Au samples (catalyst loading 1% by Au atom). The strong binding between the thiol and Au prevents access of reactant molecules to the metal surface.[6] As a result, the induction time is increased and the k_{cat} reduces. On the other hand, the AuCu$_3$NRs with weakly-bound PEG-NH$_2$ and PEG-COOH show much shorter induction times and larger catalytic rate constants than those with tightly-bound PEG-SH.
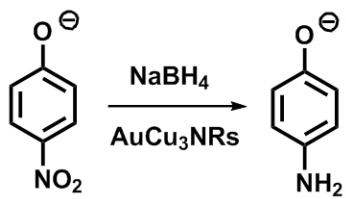
Scheme 1. Au-catalyzed *p*-nitrophenol reduction.

Table 2. Catalytic efficiency of ligand-capped AuCu$_3$NRs for *p*-nitrophenol reduction

Sample	[Au] (ppm)	k_{cat} (s^{-1})[a]	t_0 (min)[b]
PEG-NH$_2$	1.0	0.0048	3.7
PEG-COOH	1.0	0.0033	3.9
PEG-SH	1.0	0.0022	17.7
PEG-NH$_2$	2.0	0.0101	0.9
PEG750	2.0	0.0062	1.4
PEI10000	2.0	0.0071	2.3
PEI600	2.0	0.0064	2.0

[a]determined by taking the slope of the linear portion of ln(Abs$_0$/Abs)
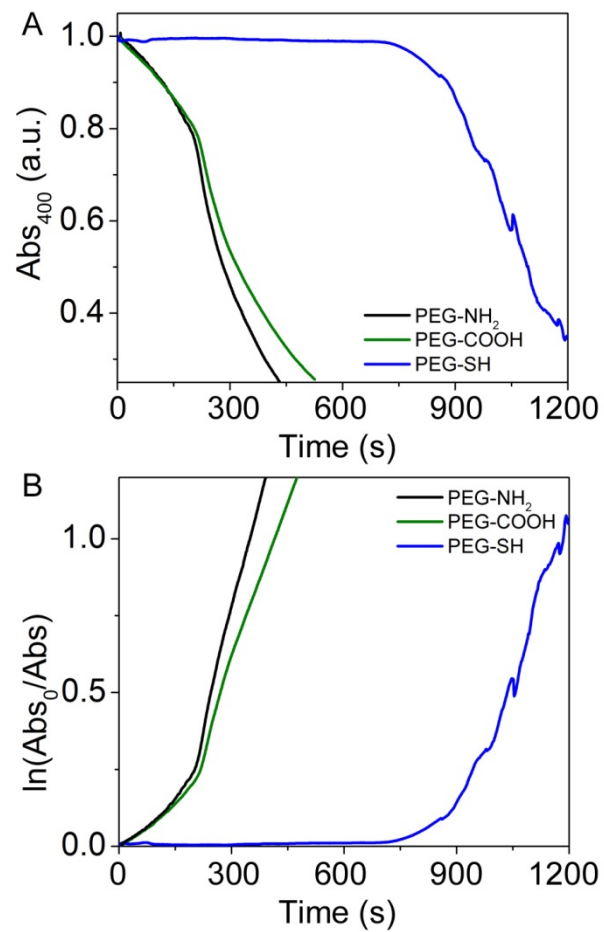[b]determined by minimum in 1st derivative of Abs vs. time.

Figure 2. Nitrophenol reduction catalyzed by (black) PEG-NH₂, (green) PEG-COOH, and (blue) PEG-SH monitored as (A) absorbance at 400 nm, and (B) natural log of the ratio of absorbance at 400 nm at time = 0 and time = t.

Several different polymers with amine groups were used to investigate the effects of multidentate binding and steric hindrance, as shown in **Figure 3**. Both PEG750 and PEG-NH$_2$ provide a single anchor to the AuCu$_3$NR surface, while the PEIs allow multidentate binding to the metal surface. Using 2 ppm Au (2% catalyst loading) the induction times were 1.4 and 0.8 min and the k$_{cat}$ were 0.0062 and 0.0101 s^{-1} for PEG750 and PEG-NH$_2$ capped AuCu$_3$NRs, respectively. This discrepancy can be attributed to the increased graft density of shorter polymers relative to longer polymers,[21] thereby inhibiting the access of reactants to active sites on the surface. The PEI-capped AuCu$_3$NRs showed induction times of 2.3 and 2.0 min and kcat of 0.0064 and 0.0071 s^{-1} for PEI600 and PEI10000, respectively. One would expect that the multidentate binding ligands should greatly reduce the catalytic activity; however, the catalytic activity of PEI600-capped AuCu$_3$NRs is comparable to that of PEG750-capped ones. Coincidently, it was found that a blue supernatant was recovered during the phase transfer process with PEIs, suggesting that Cu^{2+} ions had been released from the AuCu$_3$NRs. The FAAS results confirmed the substantial increase in the mole fraction of Au and Cu in the AuCu$_3$NRs while XRD pattern revealed the composition remained to be AuCu$_3$. These data imply that the PEI-capped AuCu$_3$NRs are covered by a skin of pure Au, which promotes the catalytic properties of the AuCu$_3$NRs and compensates the detrimental effect of multidentate binding to the surface. The PEI etching of Cu from the AuCu$_3$NRs is akin to the Tumbaga processing that Native Americans used to produce alloyed AuCu$_3$ pots with a pure Au surface.[22] Similar to the case of PEG, the catalytic activity increased with increased chain length, suggesting that the bulky PEI10000 configuration wrapping around the AuCu$_3$NRs creates more available reaction sites compared to the smaller ligand.
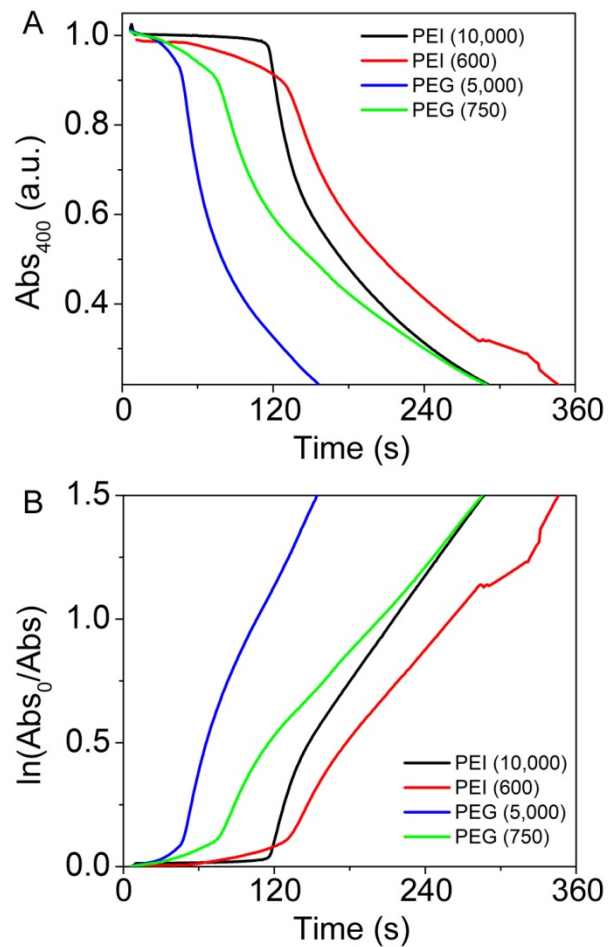
Figure 3. Nitrophenol reduction catalyzed by (black) PEI10000, (red) PEI600, (blue) PEG-NH$_2$, and (green) PEG750 monitored as (A) absorbance at 400 nm, and (B) natural log of the ratio of absorbance at 400 nm at time = 0 and time = t.

To further elucidate the surface ligand effects on the bimetallic catalysts, the catalytic activity of AuCu$_3$NRs was investigated for the Cu-catalyzed 'click' reaction between benzylazide and phenylacetylene yielding a triazole (**Scheme 2**).[23] Pure Cu nanoparticles have been demonstrated for this reaction in THF;[24] however, the possibility of surface oxidation of the Cu nanoparticles could not be ruled out. This reaction has been demonstrated on the Au (1 1 1) surface, but the Au acts as a two-dimensional constraint rather than as a catalytic participator.[25] In this study, the click reaction was carried out in 1:1 t-butanol–H$_2$O at room temperature for 0.5, 2, and 18 h with 1 $equiv$. phenylacetylene, 1.2 $equiv$ benzylazide, 0.1 $equiv$ sodium ascorbate, and 0.005 $equiv$. Cu (as AuCu$_3$NR or CuCl, 0.5% catalyst loading). The product was isolated by extraction with dichloromethane and the conversion was quantified by ^{1}H NMR by monitoring the loss of alkyne peak (2.9 ppm) and the emergence of the vinyl peak (7.65 ppm), as listed in **Table S1**. No reaction was observed in the absence of Cu-based catalysts. The conversion efficiencies of the different ligand-capped AuCu$_3$NRs are included in **Table 3**. Comparable to the CuCl salt as a positive control catalyst, PEG-SH and PEG-COOH capped AuCu$_3$NRs demonstrated nearly a complete conversion of phenylacetylene because the weak-ligand bound surface are accessible to the reactants. The amine terminated PEG750 capped AuCu$_3$NRs only demonstrated approximately 50% conversion and PEG-NH$_2$ capped AuCu$_3$NRs showed almost no catalytic activity. This result indicates that the strong interaction between amines and Cu prevents successful adsorption of the reactants to the nanoparticle, thereby inhibiting the reactions. Surprisingly, both PEI750 and PEI10000, which contain numerous primary, secondary, and tertiary amines, did not seem to interfere with the catalytic process, suggesting that the leaching of Cu from AuCu$_3$NR surface weakens the binding of branched PEI to the surface and makes it available for reactants to adsorb over a prolonged reaction time. Similar trends for the ligand

effects were found at the time points of 0.5 and 2 h compared to the results from 18 h.
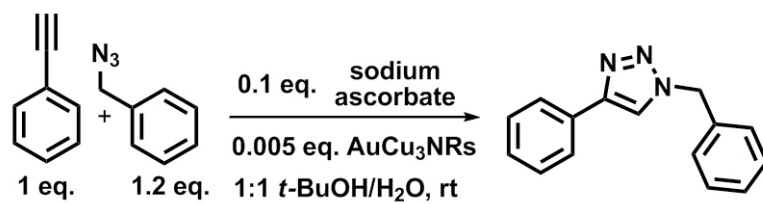
Scheme 2. Cu-catalyzed alkyne-azide 'click' cycloaddition

Table 3. Catalytic efficiency of ligand-capped AuCu$_3$NRs for azide-alkyne cycloaddition

Catalyst	0.5 h Conversion[a]	2 h Conversion[a]	18 h Conversion[a]
No Catalyst	<5 %	<5 %	<5 %
CuCl	5 %	20 %	>98 %
PEG-NH$_2$	<5 %	<5 %	5 %
PEG-750	<5 %	6 %	51 %
PEG-SH	<5 %	15 %	>98 %
PEG-COOH	<5 %	11 %	>98 %
PEI10000	<5 %	16 %	>98 %
PEI600	6 %	19 %	>98 %

[a]determined by ^{1}H NMR peak integrals. The reaction proceeded according to **Scheme 2.**

The binding affinity of ligand to the surface is weakened as the temperature increases. To study the temperature effects on the ligand binding, the metal-catalyzed hydration of benzonitrile to benzamide was investigated (**Scheme 3**).[26] The reaction was run at both 75 °C and 95 °C and catalyzed using AuCu$_3$NRs (0.5% catalyst loading by metal atom) capped by all six different ligands and results are listed in **Table 4**. The initial concentration of benzonitrile was 1 mg/mL (~9.3 mM) and ultra-performance liquid chromatography (UPLC) was used to quantify the conversion by monitoring absorbance at 254 nm as listed in **Tables S2** and **S3**. In the absence of AuCu$_3$NRs, no reaction took place at 75 °C and complete conversion from benzonitrile was observed at 95 °C after 24 h. Both of PEI600 and PEG750 capped AuCu$_3$NRs showed the highest turnover frequency and greatest conversion at either temperature among all catalysts studied. The 5000 Da PEG-capped AuCu$_3$NRs showed roughly similar, low catalytic activity, suggesting steric interference preventing access to the AuCu$_3$NR surface to catalyze the reaction. The elevated temperature provides surface lability, which reduced the graft density of the ligands. At high temperatures, the PEI10000 showed similar activity to the small ligands (*i.e.*, PEG750 and PEI600) because the elevated temperature aided surface lability and fluidity of the ligand coating. The turnover number was found to increase by two orders of magnitude at the elevated temperature. After 24 h at 75 °C in the presence of only ligands (1 mg/mL) without AuCu$_3$NRs, no significant conversion was observed for linear polymers, while the branched ligands showed slight conversion (<5 %), suggesting that the presence of the metal particles significantly enhances the rate of reaction.
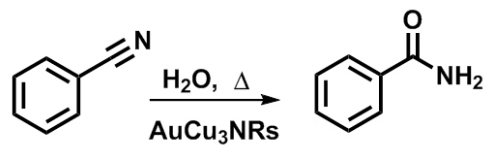
Scheme 3. Metal-catalyzed nitrile hydration.

Table 4. Catalytic efficiency of AuCu$_3$NRs for benzonitrile hydration

Catalyst	24 h, 75 °C[a,b]	3 h, 75 °C[b]	24 h, 75 °C[b]	TOF (mol/mol$_{cat}$*h)[c]	3 h, 95 °C[b]	TOF (mol/mol$_{cat}$*h)[d]
No Catalyst		<2 %	<2 %	N/A	20.7 %	1380
PEG-NH$_2$	<2 %	3.1 %	14.5 %	121	26.7 %	1780
PEG750	<2 %	8.6 %	25.0 %	209	40.0 %	2670
PEG-SH	<2 %	2.4 %	10.1 %	84	23.1 %	1540
PEG-COOH	< 2 %	<2%	12.5 %	104	21.2 %	1420
PEI10000	3.0 %	3.0%	15.1 %	180	39.6 %	2640
PEI600	4.6 %	6.5 %	21.7 %	126	43.3 %	2890

[a]Controls performed without AuCu$_3$NRs using 1 mg/mL ligand concentration.
[b]Conversion determined by UPLC monitoring 254 nm. Reaction proceeded according to **Scheme 3** with 9.3 mM benzonitrile and 0.5 % catalyst loading.
[c]Turnover frequency calculated based on 24 h incubation.
[d]Turnover frequency calculated based on 3 h incubation.

Conclusion

In summary, we have demonstrated the effects of surface ligands on the catalytic properties of alloyed AuCu$_3$NRs. The surface anchoring group, chain length and configuration of the water-soluble, polymeric ligands were found to affect the catalytic properties of the nanoparticles. The Au-catalyzed reduction of *p*-nitrophenol was found to be detrimentally affected by thiol anchors, presumably due to the strength of the Au–thiol bond. In contrast, the Cu-catalyzed azide–alkyne cycloaddition was severely inhibited by amine functional groups because of the strong interaction between amine and Cu. Additionally, smaller ligands were found to have reduced catalytic activity relative to larger ligands owing to the decrease of graft density. From benzonitrile hydration to benzamide, elevated temperature was found to increase the mobility of ligands and result in the enhancement of catalytic activity of the ligand-capped nanocatalysts. This work reveals the potential of AuCu$_3$NRs for a variety of catalytic organic reactions, yet underscores the paramount importance of surface ligand selection in the design of nanocatalysts.

References

1. Yan, N.; Xiao, C.; Kou, Y. *Coord. Chem. Rev.* **2010**, *254*, 1179–1218.

2. Polshettiwar, V.; Varma, R. S. *Green Chem.* **2010**, *12*, 743–754.

3. Wang, D.; Li, Y. *Adv. Mater.* **2011**, *23*, 1044–1060.

4. Schrinner, M.; Ballauff, M.; Talmon, Y.; Kauffmann, Y.; Thun, J.; Möller, M.; Breu, J. *Science* **2009**, *323*, 617–620.

5. Coppage, R.; Slocik, J. M.; Sethi, M.; Pacardo, D. B.; Naik, R. R.; Knecht, M. R. *Angew. Chem., Int. Ed.* **2010**, *49*, 3767–3770.

6. Biswas, M.; Dinda, E.; Rashid, M. H.; Mandal, T. K. *J. Colloid Interface Sci.* **2012**, *368*, 77–85.

7. Kameoka, S.; Tsai, A. P. *Catal. Lett.* **2008**, *121*, 337–341.

8. Chimentão, R. J.; Medina, F.; Fierro, J. L. G.; Llorca, J.; Sueiras, J. E.; Cesteros, Y.; Salagre, P. *J. Mol. Catal. A: Chem.* **2007**, *274*, 159–168.

9. Della Pina, C.; Falletta, E.; Rossi, M. *J. Catal.* **2008**, *260*, 384–386.

10. Bracey, C. L.; Ellis, P. R.; Hutchings, G. *J. Chem. Soc. Rev.* **2009**, *38*, 2231–2243.

11. Chen, S.; Jenkins, S. V.; Tao, J.; Zhu, Y.; Chen, J. *J. Phys. Chem. C* **2013**, *117*, 8924– 8932.

12. Vankayala, R.; Sagadevan, A.; Vijayaraghvan, R.; Kuo, C.-L.; Hwang, K. C. *Angew. Chem., Int.* Ed. **2011**, *50*, 10640–10644.

13. Wasserman, H. H.; Ives, J. L. *Tetrahedron* **1981**, *37*, 1825–1852.

14. Wasserman, H. H.; Petersen, A. K.; Xia, M.; Wang, J. *Tetrahedron Lett.* **1999**, *40*, 7587–7589.

15. Wasserman, H. H.; McKeon, J. E.; Smith, L.; Forgione, P. *J. Am. Chem. Soc.* **1960**, *82*, 506–507.

16. Jenkins, S.; Incarvito, C. D.; Parr, J.; Wasserman, H. H. *CrystEngComm* **2009**, *11*, 242–245.

17. Yang, J.; Sargent, E.; Kelley, S.; Ying, J. Y. *Nat. Mater.* **2009**, *8*, 683–689.

18. Herves, P.; Perez-Lorenzo, M.; Liz-Marzan, L. M.; Dzubiella, J.; Lu, Y.; Ballauff, M. *Chem. Soc. Rev.* **2012**, *41*, 5577–5587.

19. Pozun, Z. D.; Rodenbusch, S. E.; Keller, E.; Tran, K.; Tang, W.; Stevenson, K. J.; Henkelman, G. *J. Phys. Chem. C* **2013**, *117*, 7598–7604.

20. Gu, S.; Wunder, S.; Lu, Y.; Ballauff, M.; Fenger, R.; Rademann, K.; Jaquet, B.; Zaccone, A. *J. Phys. Chem. C* **2014**, *118*, 18618–18625.

21. Xia, X.; Yang, M.; Zheng, Y.; Li, Q.; Chen, J.; Xia, Y. *ACS Nano* **2012**, *6*, 512–522.

22. Guisbiers, G.; Mejia-Rosales, S.; Khanal, S.; Ruiz-Zepeda, F.; Whetten, R. L.; José-Yacaman, M. *Nano Lett.* **2014**, *14*, 6718–6726.

23. Kolb, H. C.; Finn, M. G.; Sharpless, K. B. *Angew. Chem., Int. Ed.* **2001**, *40*, 2004–2021.

24. Alonso, F.; Moglie, Y.; Radivoy, G.; Yus, M. *Tetrahedron Lett.* **2009**, *50*, 2358–2362.

25. Díaz Arado, O.; Mönig, H.; Wagner, H.; Franke, J.-H.; Langewisch, G.; Held, P. A.; Studer, A.; Fuchs, H. *ACS Nano* **2013**, *7*, 8509–8515.

26. Downs, E. L.; Tyler, D. R. *Coord. Chem. Rev*. **2014**, *280*, 28–37.

Appendix A: Supporting Information

Materials and Methods

Chemicals

Tetrachloroauric acid trihydrate (HAuCl$_4$·3H$_2$O), copper acetoacetonate (Cu(acac)$_2$), oleylamine (70%), branched poly(ethyleneimine) (m.w. 10,000, PEI10000), branched poly(ethyleneimine) (m.w. 600, PEI600), sodium borohydride (NaBH$_4$), benzonitrile, benzylbromide, sodium ascorbate, trifluoroacetic acid, and dimethylsulfoxide (DMSO) were purchased from Alfa Aesar. Choloroform (CHCl$_3$), dichloromethane, diethyl ether, hexanes, toluene, acetonitrile, and t-butanol were purchased from EMD. Sodium azide (NaN$_3$), methoxypolyethyleneglycol 5000 acetic acid (m.w. 5000, PEG-COOH), poly(ethylene glycol) monomethyl ether thiol (m.w. 5000, PEG-SH), and phenylacetylene were purchased from Sigma Aldrich. Methoxypolyethylene glycol amine (m.w. 5000, PEG-NH$_2$), O-(2-aminoethyl)-O'-methylpolyethylene glycol (m.w. 750, PEG750), and p-nitrophenol were purchased from Fluka. Tetradecylamine was purchased from TCI. Octadecylamine was purchased from Acros. Ethanol (EtOH, 200 proof) was purchased from Koptec. Deuterated chloroform (CDCl$_3$) was purchased from Cambridge Isotope Labs. Ultrapure H$_2$O (18 MΩ) generated with an Elga PurelabUltra was used in all experiments. All chemicals were used as received.

Synthesis of AuCu$_3$ Nanorods (AuCu$_3$NRs)

To a 25 mL 3-neck round-bottom flask, 17.9 mg HAuCl$_4$·3H$_2$O was added directly, followed by addition of 2.1 g tetradecylamine and 2.7 g octadecylamine. The flask was placed on a heating mantle at 80 °C with magnetic stirring and purged with Ar for 5 min. The temperature was then increased to 140 °C and the reaction allowed to proceed for 20 min. In a separate vial, 47.6 mg Cu(acac)$_2$ was added and dissolved in 2 ml oleylamine. The reaction temperature was increased

to 210 °C and the Cu precursor solution was quickly injected. The reaction was allowed to proceed for an additional 20 min. The reaction was removed from heat and allowed to cool. Once the temperature had reached ~120 °C, the reaction mixture was separated into two 2 dr. vials, and the vials were then filled with toluene. The mixture was centrifuged at 3,300 g for 2 min and the supernatant removed quickly. The pellet was redispersed in ~0.1 mL toluene *via* sonication, and the remaining volume of the vial was filled with EtOH, and centrifuged for 3 min at 3,300 g. The AuCu$_3$NRs were redispersed in toluene, washed with ethanol, and centrifuged 3 additional times. The product was finally dispersed in 4 mL toluene.

Phase Transfer of AuCu$_3$NRs

To a 20 mL scintillation vial, 10 mg of ligand (see **Table 2** in main text) was added and dissolved in 10 mL CHCl$_3$. This solution was placed in an ice bath under magnetic stirring. To this solution, 0.5 mL of AuCu$_3$NRs in toluene was added, and the ligand exchange was allowed to proceed overnight in the dark. The samples were then diluted with 5 mL hexanes and centrifuged for 5 min at 7,000 RPM. The supernatant was removed and the particles redispersed in 3 mL EtOH *via* sonication. Particles were then centrifuged at 14,000 RPM for 10 min at 20 °C. The supernatant was discarded and the particles were redispersed in 3 mL H$_2$O. The particles were then centrifuged and redispersed in H$_2$O three times, being dispersed in a final volume of 0.5 mL.

Nitrophenol Reduction

A stock solution of 7 mM *p*-nitrophenol was prepared using H$_2$O. This solution was then diluted 120 fold in H$_2$O and degassed under vacuum for 2 h. A solution of 15.8 mg/mL NaBH$_4$ was prepared fresh and stored in an ice bath. Into a quartz cuvette, 2 mL of the nitrophenol solution was added followed by addition of 100 μL NaBH$_4$, which resulted in a change from clear to

yellow, indicating formation of the nitrophenolate anion. The absorbance at 400 nm of this solution was ~1.2, and stable for several hours (**Fig. S1**). To this solution, $AuCu_3NRs$ were added to a final concentration of 1 or 2 ppm Au. The $AuCu_3NRs$ were diluted prior to addition, so that 200 μL was added to the solution, dropping the absorbance to ~1.1. Addition of the catalyst was defined as time 0 s. The reaction progress was monitored *via* absorbance at 400 nm, with data points taken every 1 s. The reaction was allowed to proceed until the absorbance had dropped below 0.2.

Azide-Alkyne Cycloaddition

Benzylazide was prepared by S_N2 reaction between NaN_3 (11 mmol) and benzylbromide (10 mmol) in 20 mL DMSO. The reaction was allowed to proceed overnight at room temperature with vigorous stirring. Then 20 mL H_2O was added and the product was extracted three times with 95:5 diethyl ether: hexane. The product was washed twice with H_2O, once with brine, dried over Na_2SO_4, purified on a silica column, and collected *via* rotary evaporator. The neat IR of the resulting oil confirmed the presence of azide (2100 cm^{-1}). For the alkyne-azide cycloaddition, phenylacetylene was dissolved in 1:1 H_2O:*t*-butanol. To this solution, 1.2 eq. benzylazide, and 0.1 eq. sodium ascorbate was added. This solution was then dispersed in 1 dr. vials containing stir bars. To this, $AuCu_3NRs$ were added to a final Cu concentration of 0.5 % catalyst loading (31 ppm Cu). The reaction was allowed to proceed with magnetic stirring overnight. The reaction mixture was extracted with dichloromethane, dried, and collected under rotary evaporation. The resulting sample was then dispersed in 1 mL CDCl$_3$ and ^{1}H NMR spectra were acquired. The conversion was determined by comparing the integral of the singlet acetylene peak (2.9 ppm) and the singlet vinyl peak (7.6 ppm) (**Table S1**).

Benzonitrile Hydration

Benzonitrile was dissolved in H_2O at a concentration of 1 mg/mL. A total of 1 mL of this solution was added to 1 dr. vials and $AuCu_3NRs$ were added to a final concentration of 47 μM metal atoms (0.5 % catalyst loading). The reaction was then allowed to incubate at 75 °C or 95 °C. Aliquots were taken after 3 h and 24 h on heat. The aliquots were centrifuged for 10 min at 20 °C and 14,000 RPM to sediment the particles. The supernatant was removed and analyzed by UPLC. UPLC measurements were performed using a C18 column, The mobile phase was a gradient between 90:10 to 60:40 H_2O:acetonitrile (0.1% trifluoroacetic acid) with a flow rate of 0.1 mL/min. Relative peak areas based on absorbance at 254 nm was used to determine conversion from benzonitrile (**Tables S2** and **S3**).

Table S1. NMR Peak areas following azide-alkyne cycloaddition

	Time (h)	Integral at 2.9 ppm[a]	Integral at 7.6 ppm[b]	Relative Area[c]
No Catalyst	0.5[d]	1.0	<0.05	<0.05
	2[d]	1.0	<0.05	<0.05
	18[d]	1.0	<0.05	<0.05
CuCl	0.5	18.63	1.0	0.5
	2	4.91	1.0	0.203
	18	<0.05	1.0	<0.95
PEG-NH$_2$	0.5[d]	1.0	<0.05	<0.05
	2[d]	1.0	<0.05	<0.05
	18	17.59	1.0	0.055
PEG750	0.5[d]	1.0	<0.05	<0.05
	2	16.89	1.0	0.059
	18	0.98	1.0	0.505
PEG-SH	0.5[d]	1.0	<0.05	<0.05
	2	6.78	1.0	0.147
	18	<0.05	1.0	<0.95
PEG-COOH	0.5[d]	1.0	<0.05	<0.05
	2	9.32	1.0	0.107
	18	<0.05	1.0	<0.95
PEI10000	0.5[d]	1.0	<0.05	<0.05
	2	6.43	1.0	0.155
	18	<0.05	1.0	<0.95
PEI600	0.5	17.39	1.0	0.058
	2	5.21	1.0	0.192
	18	<0.05	1.0	<0.95

[a]Peak corresponding to alkynyl proton in phenylacetylene
[b]Peak corresponding to vinyl proton in the product, defined as having an area of 1.
[c]Calculated as (integral at 7.6 ppm)/(total area)
[d]Normalized to alkynyl proton (2.9 ppm)

Table S2. UPLC peak areas at 254 nm for benzonitrile hydration at 75 °C

	Area at 3.0 min $(\mu V*s)^a$	Area at 1.4 min $(\mu V*s)^b$	Conversion[c] after 3 h	Area at 3.0 min $(\mu V*s)^a$	Area at 1.4 min $(\mu V*s)^b$	Conversion[c] after 24 h
No Catalyst	25050386	<50000	<0.02	24966032	<50000	<0.02
PEG-NH$_2$	12603218	409357	0.031	7278057	1238610	0.145
PEG750	8804162	828996	0.086	4137633	1380175	0.250
PEG-SH	17635751	442479	0.024	13707896	1533068	0.101
PEG-COOH	8241617	<50000	<0.02	9346510	1337964	0.125
PEI10000	8443388	257259	0.030	6642599	1179692	0.151
PEI600	6577224	455784	0.065	4367036	1206915	0.217
PEG-NH$_2$[d]				34230875	226339	<0.02
PEG750 [d]				65398610	1225891	<0.02
PEG-SH [d]				39334888	599548	<0.02
PEG-COOH [d]				36421496	648182	<0.02
PEI10000 [d]				52874798	1575178	0.029
PEI600 [d]				38560311	1869462	0.046

[a]Retention time corresponding to benzonitrile
[b]Retention time corresponding to benzamide
[c]Calculated as (Area at 1.4 min)/(Total peak area)
[d]Reaction at 1 mg/mL ligand concentration in the absence of AuCu$_3$NRs

Table S3. UPLC peak areas at 254 nm for benzonitrile hydration at 95 °C

	Area at 3.0 min (μV*s)[a]	Area at 1.4 min (μV*s)[b]	Conversion[c] after 3 h	Area at 3.0 min (μV*s)[a]	Area at 1.4 min (μV*s)[b]	Conversion[c] after 24 h
No Catalyst	9860902	2575553	0.207	<50000	2793647	>0.98
PEG-NH$_2$	2793647	1015591	0.267	<50000	12654549	>0.98
PEG750	4569382	3045214	0.400	<50000	7363029	>0.98
PEG-SH	7981371	2400009	0.231	<50000	12550753	>0.98
PEG-COOH	7737616	2085718	0.212	<50000	15718987	>0.98
PEI10000	3403694	2229391	0.396	<50000	11141310	>0.98
PEI600	3718736	2838742	0.433	<50000	11141310	>0.98

[a]Retention time corresponding to benzonitrile
[b]Retention time corresponding to benzamide
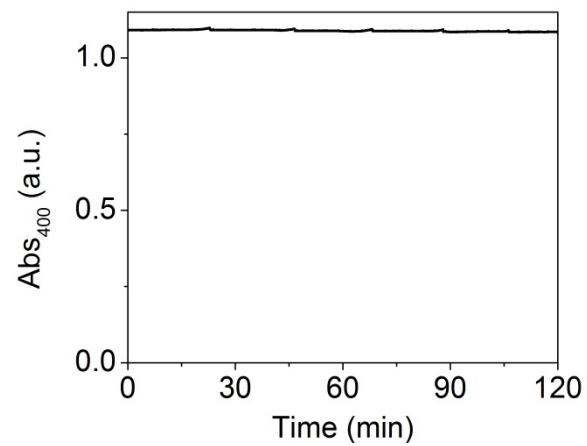[c]Calculated as (Area at 1.4 min)/(Total peak area)

Figure S1. Absorbance at 400 nm over time for NaBH$_4$ reduction of *p*-nitrophenol without added metal catalyst.

Chapter VII. Conclusion

The surface of metal nanoparticles dictates much of its biological response. Changes to the surface can affect its pharmacokinetic profile. Additionally, the surface can be used to load drugs and targeted delivery to tumors or microbial infections and the surface can be used as a catalyst for organic reactions under extremely mild conditions.

A major surface consideration is the agglomeration status of nanoparticles *in vivo*. Blood is an extremely complex fluid, and it can induce nanoparticle agglomeration, which may induce significant changes in the toxicity and biodistribution of these materials. These changes introduce complications to any regulatory mechanisms that will be implemented to deal with nanomedicine. Toward this end, Au nanoparticles were synthesized and agglomerated to varying degrees. These particles and agglomerates were introduced to whole blood. Darkfield microscopy with hyperspectral imaging was used to distinguish between the primary particles and agglomerates with minimal samples preparation based on their scattering spectra. Additionally, single particle ICP-MS was developed as a complementary method to further distinguish particles and agglomerates. These developments represent an important step toward the clinical application of nanomaterials, but additional research needs to be performed. Specifically, application of these methods to cells will further advance the ability to characterize nanomedicines. For these studies, it will be important to investigate a wide range of cell lines, the rapid nature of the methods developed here will facilitate the broad investigation of nano-bio interactions. Additionally, extraction and characterization of materials following *in vivo* injection, using methods such as these, will be an important step toward the full application of these materials.

One potential application of noble metal nanomaterials is their use as a drug delivery vehicle for

photodynamic therapy of tumors. A photosensitizer was loaded into the PEG coating of Au nanocages. The PEG surface coating increased the systems biocompatibility and created an area of reduced polarity that could be used to load the extremely hydrophobic photosensitizer. This conjugate was tested in mice against implanted tumors, and was found to be more effective than the free drug. Ultimately, the conjugate accumulated more efficiently in the tumor than the free drug. The drug was progressively unloaded into the tumor interstitium by albumin, and some of the drug presumably became embedded in cell membranes. Laser activation of the photosensitizer was also found to generate more therapeutic singlet oxygen in the presence of nanocages. Photoacoustic tomography was also used to visualize accumulation of the conjugate in the tumor site, to better enable guidance of the irradiation. The surface of the conjugate was further modified; charge and steric hindrance were used to adjust the release rate of these conjugates in a model blood environment. Irradiation was also shown to increase the solution temperature and facilitate controllable release of the drug.

The recent rise in antibiotic-resistant infections has created a growing need for nontraditional antimicrobial therapy. Toward this end, daptomycin was loaded into polydopamine coated Au nanocages. Photothermal heating was used to release the antibiotic from the construct. After loading, an antibody to unique Staphylococcal membrane proteins was conjugated to the surface. This construct was shown to bind to both a methicillin resistant and methicillin sensitive *S. Aureus* strain. Incubation of these constructs with either strain, followed by laser irradiation demonstrated complete elimination of live bacteria in planktonic culture, which was attributed to a synergistic photothermal and chemotherapeutic effect. In the absence of irradiation, little difference was observed relative to the negative control. A nontraditional construct such as this presents a possible solution to the growing crisis of antibiotic resistance. Several important

studies still need to be performed. Most important, the construct must be tested in a biofilm model, as biofilms present a significant impediment to antimicrobial therapy relative to planktonic cultures. Additionally, optimization of the construct has yet to be accomplished; specifically the best antibiotic to use and the targeting ligand has yet to be determined. Further conclusive investigation into the polymer's composition also needs to be performed.

Surface modifications have made possible the targeted delivery of both hydrophobic and hydrophilic drug molecules. The nanoparticle surface can also be extremely catalytically active. In theory, the surface can also be used to activate prodrugs *in situ*. Toward this end, the catalytic properties of $AuCu_3$ nanorods were investigated following changes of the surface ligands. Au-catalyzed reactions were significantly inhibited by thiol anchoring groups, while Cu-catalyzed reactions were inhibited by primary amine anchoring groups. The selection of ligand on the nanoparticle surface is an important consideration for the design of novel nanoparticle catalysts. Further work in this area will include the development of optimal prodrugs for *in situ* catalysis. Additionally, preliminary data suggests the LSPR can increase the surface lability of ligands, which may impart controllable catalytic properties to the surface of these types of particles.

Noble metal nanostructures possess great biomedical potential. There are major concerns that much be addressed prior to their implementation, particularly full characterization of these systems following injection into an organism. They also have great potential as drug delivery vehicles – they can be used to deliver hydrophobic drugs to tumors and hydrophilic drugs to bacterial infections. The surface can also be theoretically used to catalyze reactions at the target site. Further investigation must be performed to optimize these systems to make the least toxic and most effective theranostics agent possible. These materials, however, have the potential to enable new and significantly more effective therapeutic and diagnostic modalities.